**UNIVERSITY OF SOUTHAMPTON**

FACULTY OF ENGINEERING AND THE ENVIRONMENT

Institute of Sound and Vibration Research

# Wave propagation in reinforced concrete beams with application to non-destructive testing

by

**Evelyne El Masri**

Thesis for the degree of Doctor of Philosophy

September 2018

UNIVERSITY OF SOUTHAMPTON

ABSTRACT

FACULTY OF ENGINEERING AND THE ENVIRONMENT
Institute of Sound and Vibration Research

Doctor of Philosophy

# WAVE PROPAGATION IN REINFORCED CONCRETE BEAMS WITH APPLICATION TO NON-DESTRUCTIVE TESTING

by Evelyne El Masri

Steel reinforcements bars (rebars) are vital to reinforced concrete (RC) structures and their damage leads to catastrophic failure. Most damage occurs due to corrosion and delamination, and an early detection is necessary. Wave based methods are popular for detecting the damage remotely. However, most of these techniques require direct contact with the rebars. The aim of this project is to exploit guided waves to detect damage of the rebars via measurements only on the concrete surface.

The Wave Finite Element (WFE) is well suited to predict the wave characteristics of RC waveguides. It requires knowledge of the mass and stiffness matrices of only a segment of the waveguide which can be obtained from conventional FE analysis. A new RC model approach using embedded reinforcements is suggested and compared to conventional FE models. Next, the WFE methodology is discussed including associated numerical and ill conditioning errors. Wave solutions for RC beams with and without prestress, in the form of dispersion curves and mode shapes, were found to be similar.

Having established free wave solutions for an undamaged RC waveguide, one can couple it to a damaged segment that can be modelled in FE. Alternatively, if the damage is modelled as a reduction in rebar diameter over a certain length, then this permits the WFE coupling approach to couple damaged and undamaged RC models for better computational efficiency. High magnitudes for the reflection coefficients due to damage are found, which are associated with evanescent waves at their cut-on frequencies.

Based on these findings, a new damage identification algorithm is proposed in which the amplitudes of left and right propagating waves are estimated from surface measured forced responses. The experimental based methodology was successful in detecting rebar reduction without any prior knowledge of the dispersion relations. Experimental validation of the algorithm is found to be successful and in good agreement with simulations. The potential and limitations of the algorithm for practical structures are discussed.

# Contents

# List of Figures

# List of Tables

# Declaration of Authorship

I, Evelyne El Masri , declare that the thesis entitled *Wave propagation in reinforced concrete beams with application to non-destructive testing* and the work presented in the thesis are both my own, and have been generated by me as the result of my own original research. I confirm that:

- this work was done wholly or mainly while in candidature for a research degree at this University;
- where any part of this thesis has previously been submitted for a degree or any other qualification at this University or any other institution, this has been clearly stated;
- where I have consulted the published work of others, this is always clearly attributed;
- where I have quoted from the work of others, the source is always given. With the exception of such quotations, this thesis is entirely my own work;
- I have acknowledged all main sources of help;
- where the thesis is based on work done by myself jointly with others, I have made clear exactly what was done by others and what I have contributed myself;
- parts of this work have been published as: (El Masri et al., 2017), (El Masri et al., 2016b) and (El Masri et al., 2016a)

Signed:.....

Date:.....

# Acknowledgements

I praise and thank Allah SWT for his greatness and for giving me the strength, patience and courage to complete this thesis.

I would like to extend thanks to the many people who so generously contributed to the work presented in this thesis.

Special mention goes to my enthusiastic and dedicated supervisors Dr. Neil Ferguson and Dr. Timothy Waters. I would like to thank you both for encouraging my research and for allowing me to grow as an independent researcher. Your advice on both research as well as on my career have been invaluable. This opportunity was not only focused on tremendous academic support, but as well on so many teaching, lab tutorials and public engagement opportunities.

I would especially like to thank my family. Words cannot express how grateful I am to my mother for all of the sacrifices that you have made on my behalf. Your prayer for me was what sustained me thus far. I would also like to thank my brother Youssef for supporting me for everything, and especially I cannot thank you enough for encouraging me throughout this experience.

Finally, special thanks to my friends in Southampton that made this experience an unforgettable one. Dr. Istebreq Saeedi that made the last two years an amazing adventure through the continuous support in my good and bad times. I sincerely appreciate all the effort she made to guide me through this journey. In addition, I am grateful to Dr. Amina Seylani and Dr. Nhima Sanha that believed in my potentials, and with whom I have shared moments of deep anxiety but also of big excitement.

# Nomenclature

| | |
|---|---|
| $\mathbf{e}$ | Amplitudes of directly excited waves |
| $\boldsymbol{f}$ | Nodal forces |
| $f'$ | Compressive strength |
| $f_y$ | Yield stress |
| $j$ | $\sqrt{-1}$ |
| $k$ | Wavenumber |
| $k_b$ | Bending wavenumber |
| $k_s$ | Small wavenumber |
| $k_{tx}$ | Trial wavenumber |
| $l_x$ | Length of the spacial array |
| $n$ | Number of DOFs at the element interface |
| $\boldsymbol{q}$ | Nodal displacements |
| $\mathbf{r}$ | Reflection coefficients matrix |
| $t$ | Time |
| $w/c$ | Water cement ratio |
| $x_e$ | Excitation position |
| $x_r$ | Response position |

| | |
|---|---|
| $A$ | Cross-sectional area |
| $\mathbf{A}$ | Wave amplitudes vector |
| $\mathbf{C}$ | Damping matrix |
| C$frequency$ | Complex wave mode with its associated cut-on frequency in Hz |
| $\mathbf{D}$ | Dynamic stiffness matrix |
| $E$ | Young's Modulus |
| E$frequency$ | Evanescent wave mode with its associated cut-on frequency in Hz |
| $E_k$ | Kinetic energy |
| $E_p$ | Potential energy |
| $\mathbf{F}$ | Propagation matrix between edges of coupling joint |
| $G$ | Shear modulus |
| $I$ | Second moment of the cross-sectional area |
| $\mathbf{I}$ | Identity matrix |
| $L$ | Length of a waveguide |

| | |
|---|---|
| $\mathbf{M}$ | Mass matrix |
| $\mathbf{R}$ | Matrix for dynamic condensation on internal DOFs |
| $\mathbf{R}_{ij}$ | Reflection matrix of waves travelling from waveguide $i$ to $j$ |
| $\mathbf{R}_T$ | The net reflection matrix due to the full finite length of the discontinuity via WFE-WFE-WFE coupling approach |
| $\mathbf{S}$ | Scattering matrix |
| $\mathbf{T}$ | Transfer matrix |
| $\mathbf{T}_{ij}$ | Transmission matrix of waves travelling from waveguide $i$ to $j$ |
| $V_b$ | Total volume of batch |
| $V_{abs}$ | Volume of water absorbed |
| $V_w$ | Total volume of water |
| $V_{wf}$ | Volume of free water |
| $\mathbf{W}$ | FRF measured output vector |
| | |
| $\Delta$ | Length of an element |
| $\varepsilon$ | Strain |
| $\varepsilon_0$ | Strain at the ultimate compressive strength |
| $\zeta$ | Constant damping ratio |
| $\eta$ | Loss factor |
| $\kappa$ | Shear correction factor |
| $\lambda$ | Eigenvalue |
| $\mathbf{\Lambda}$ | Propagation matrix associated with the WAD approach |
| $\nu$ | Poisson's ratio |
| $\rho$ | Density |
| $\sigma$ | Stress |
| $\boldsymbol{\tau}$ | Wave propagation matrix |
| $\mathbf{\Phi}$ | Right eigenvector matrix |
| $\mathbf{\Psi}$ | Left eigenvector matrix |
| $\omega$ | Angular frequency |

**Superscripts**

| | |
|---|---|
| $+$ | Positive-going waves |
| $-$ | Negative-going waves |
| $*$ | Dynamically condensed matrix |
| $inc$ | Incident wave at the coupling joint interface |
| $ref$ | Reflected wave at the coupling joint interface |

**Subscripts**

| | |
|---|---|
| $c$ | Concrete |
| $ext$ | External force |
| $f$ | Forces |

| | |
|---|---|
| $I, i$ | Internal nodes of a section |
| $L, l$ | Left hand side of a section |
| M | Master nodes |
| $q$ | Displacements |
| $s$ | Steel |
| $R, r$ | Right hand side of a section |
| 12 | Wave travelling from waveguide 1 to 2 |

**Operator**

| | |
|---|---|
| $H$ | Hermitian, complex conjugate transpose |
| T | Transpose |

**Abbreviations**

| | |
|---|---|
| DOF | Degree of freedom |
| FE | Finite element |
| NDT | Non-destructive testing |
| SVD | Singular value decomposition |
| TOF | Time of flight |
| UGW | Ultrasonic guided waves |
| WAC | Wave assurance criterion |
| WAD | Wave amplitude decomposition |
| WFE | Wave finite element |

# Chapter 1

# Introduction

## 1.1 Background

Repair of concrete structures is essential both to increase their lifetime and for them to remain serviceable. One major step before the repair is to investigate the potential damage of the structure and to decide upon a proper procedure. By practical testing and laboratory observations, it has been shown that the majority of cracking in concrete and premature failures are dominated by corrosion of the reinforcement rebars. The loss of structural strength is due to delamination of its concrete cover. Although these failures do not imply the structural breakdown, essentially it affects the structural serviceability due to such damage.

The appearance and sustainability of concrete structures are disturbed by cracking, and the repairs of infrastructure impose a serious issue related to maintenance that costs around $100 billion annually worldwide Li et al. (2007). Obviously, a serious investigation of corrosion and delamination of reinforced concrete is essential to cut down the renovation expenses and sustain the serviceability of these constructions. The incidence of this type of damage is random and its pattern irregular. Normally concrete delamination is a most complex issue and is related to corrosion of the reinforcement rebars. Many methods and factors have though been suggested to quantify these problems.

The principal origin of premature corrosion of the steel reinforcement is due to exposure to chloride ions. Existing in de-icing salts and seawater, with the presence of oxygen and moisture, the intrusion of chloride ions enhances corrosion of the steel reinforcement. Also, chloride ions can exist in water or admixtures, and can be dissolved from sound concrete to reach internal steel and cause corrosion. Another key reason for steel reinforcement corrosion is the freeze-thaw effect. Once the water in moist concrete freezes, it expands by 9% which produces stresses in the capillary voids of concrete. When these stresses exceed the tensile strength of concrete, the cavities will crack. In addition,

some chemical exposures deteriorate the structure. Portland cement concrete does not possess good resistance to acid environments. Also, mineral acids and acid-containing substances like industrial waste and silage cause damage to concrete PCA (2002).

Consequently, there are many causes of cracking of reinforced concrete that produce a higher probability of environmental and chemicals attacks. Thus, these attacks lead to corrosion and delamination at a later stage. For these reasons, detection and localization of the damage especially at early stages are important before any repair strategy takes place.

Non-destructive testing (NDT) of concrete structures has proven to be an efficient technique to detect the damage without any additional harm to the structure. Many techniques have been applied to reinforced concrete, and these can be classified into different categories based on the concept behind their approach and their application as shown in Figure 1.1. This chapter discusses these general approaches, including their advantages and limitations.

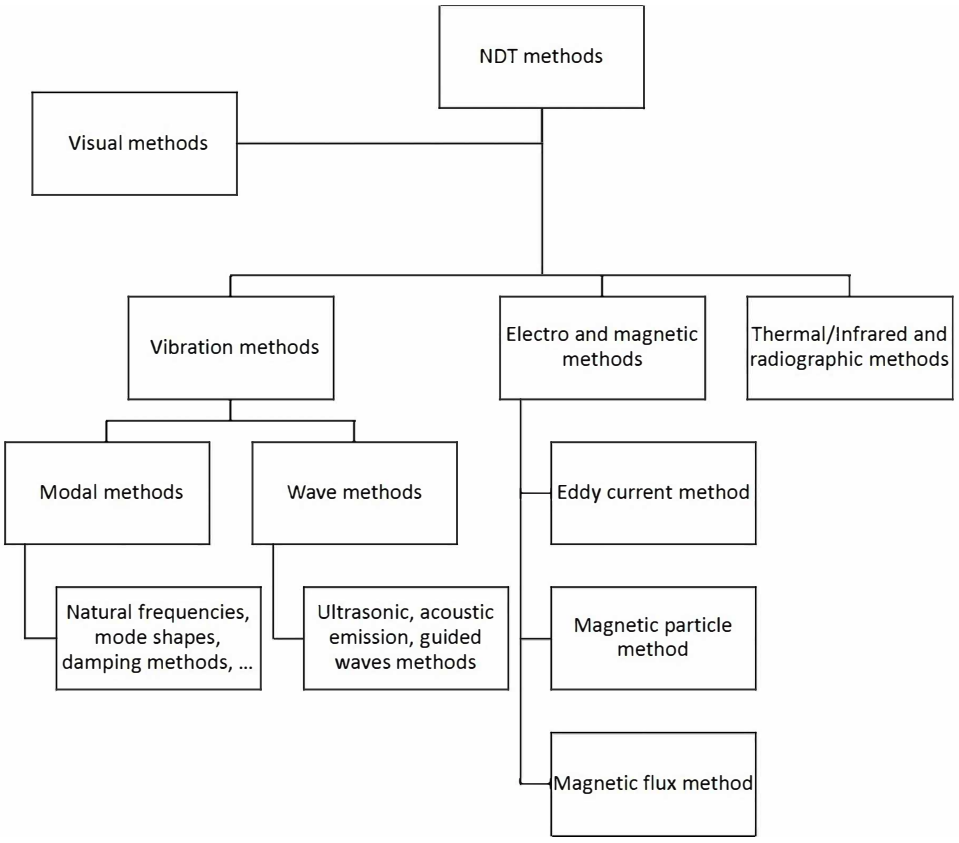


Figure 1.1: Diagram of NDT techniques classification based on The American Society of Non-destructive Testing ASNT (2015).

## 1.2 Literature review

### 1.2.1 RC beams

A reinforced concrete beam is a composite medium comprising concrete material surrounding steel reinforcements (rebars) at the top and bottom of the beam. The concrete is designed to take compression and partial shear stresses; however, steel reinforcements (horizontal rebars) are designed to handle the tensile stresses. The remaining shear stresses are taken by the stirrups (vertical rebars). The number, diameter and position of the horizontal rebars are designed based on the bending moment distribution along the beam. A typical RC beam is illustrated in Figure 1.2.

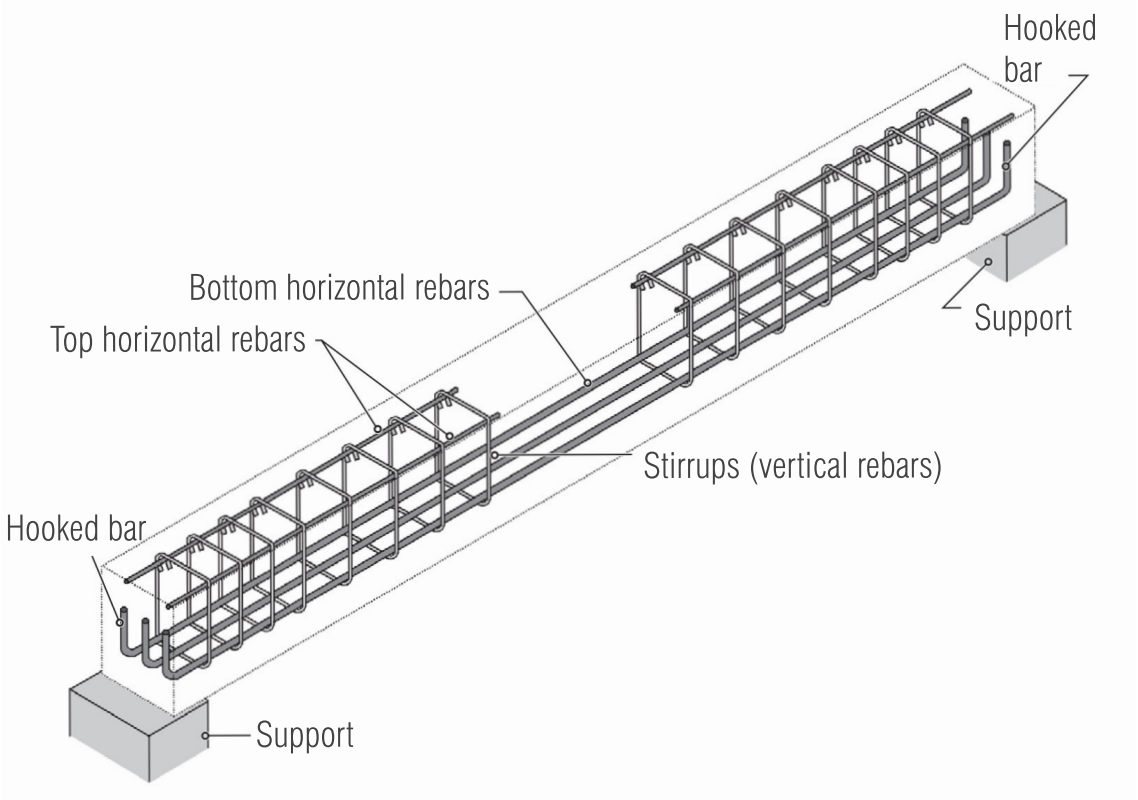


Figure 1.2: Typical RC beam with horizontal and vertical reinforcements (rebars).

Prestressed concrete is a type of reinforced concrete in which at least part of the steel reinforcement has been tensioned against the concrete. While concrete is strong and ductile in compression it is weak and brittle in tension, and hence its response to external loads is improved by applying precompression. This approach substantially increases the external load required to crack the concrete.

In the pretensoning system, steel rods or tendons (individual wires or strands) are first tensioned on a casting bed using jacks, and then concrete is poured as shown in Figure 1.3. However, in post-tensioning system, the concrete is first cast by taking into

account grooves to include the tendons. When the concrete achieves enough strength, the tendons are tensioned using jacks Raju (2007). In both cases, one should assure good bonding between steel and concrete in order for the prestress effect to transmit from steel to surrounding concrete.

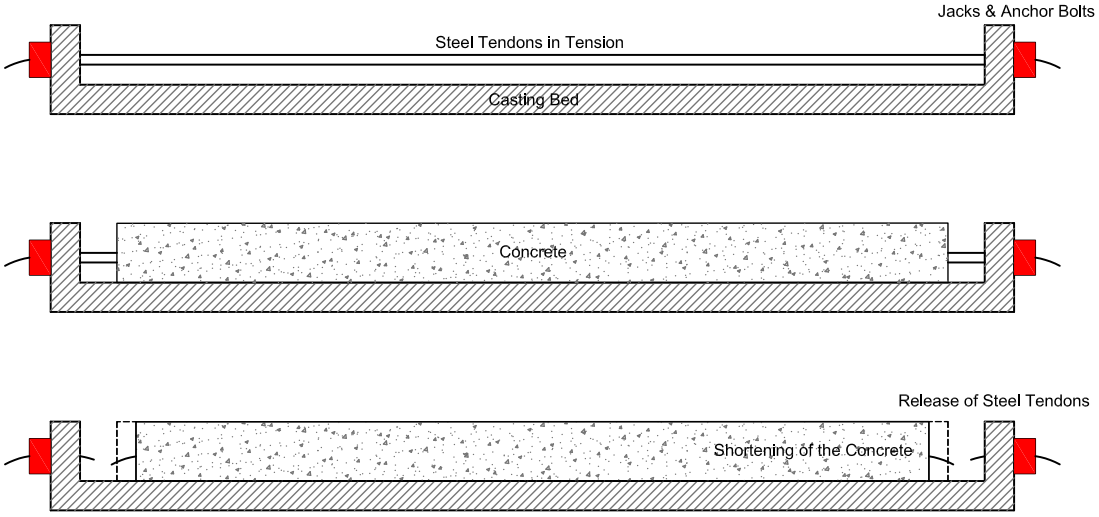


Figure 1.3: A diagram illustrating a procedure for introducing prestress in a reinforced concrete beam.

The prestressing of concrete has several advantages as compared to traditional reinforced concrete. A fully prestressed concrete member is usually subjected exclusively to compression throughout its service life. This remedies or rectifies several deficiencies of concrete. This results in many advantages for prestress of concrete compared to usual RC.

First, due to the prestress effect, the concrete section remains uncracked under service load. This produces a reduction of the steel corrosion and an increase in durability. In addition, the full section is applied under the load effect since no cracking occurs under service loads. This leads to a higher stiffness due to higher second moment of area, and lower deformation and deflection causing improved serviceability. Besides, an increase in shear capacity is resolved. Second, prestressed concrete allows high values of the span-to-depth ratio, which is more suitable for bridges and high-rise buildings. This capability gives a positive advantage for prestressed RC compared to usual RC when it comes to architectural concepts for open area structures where longer spans are required. Third, prestressed RC is more suitable for precast construction. This facilitates rapid construction, better quality control, reduced repair and multiple use of the formwork.

The force applied to prestressing strands is normally 70 - 80% of the ultimate tensile strength. There are a number of factors affecting the loss of force within the strands. Furthermore, the degree to which these factors affect the prestressing force varies with

time. For example, elastic shortening occurs at the moment of transfer, but relaxation of the steel is assumed to have reached its peak after one thousand hours have passed since prestressing.

Despite all the advantages of prestressed reinforced concrete versus conventional RC, the circumstances of any damage in the reinforcement steel in prestressed RC is more disastrous than in RC. This due to the fact that stress is present inside the steel strands. For example, corrosion of these strands causes degradation of their diameter, and a consequent increase in the stress within it. For a high level of corrosion, this phenomenon leads to complete failure of the steel strands at the point where the stress exceeds the ultimate tensile strength of the strands. For these reasons, an early detection of corrosion in steel reinforcement in prestressed RC is crucial to prevent the subsequent damage at later stages.

### 1.2.2 Overview of NDT methods

Non-destructive testing methods has been widely used in order to detect various types of damage in structures. Based on the concepts behind their application, these methods are classified into the following four main types shown as in Figure 1.1.

Visual methods involve the visual observation by the operator during inspection of the structure whereby only visible damage can be identified. Vibration methods use the vibration characteristics as a mean to detect damage, where either a modal or a wave approach can be adopted. The modal methods consider modal vibration parameters, such as natural frequencies, mode shapes and damping. However, wave methods focus on wave features while waves are travelling in a waveguide. It includes ultrasonic, acoustic emission and guided waves. Ultrasonic approaches are local methods to detect the damage through the thickness of a beam. Guided waves apply the change in the wave scattering properties to identify the damage. In addition, the acoustic emission methods are considered passive techniques that track down on the generation of waves produced by a sudden redistribution of stress in a material. Other NDT techniques are possible, such as electromagnetic methods applied to metallic materials, where resistance of the metal and changes in the magnetic fields are associated with discontinuities and damage. Finally, another method comprises a map surface scanning of the structure using thermal/infrared or radiation approaches.

Most non-destructive assessment methods need advance knowledge of the likely locality of the damage in the structure, and also require it to be humanly accessible. Thus, these techniques only provide a local assessment of the structure Zou et al. (2000). Another limitation concerns aging structures where built specifications are not available (design drawings and building records). In this case, the structure ratings are provided by the use of finite element models where these numerical models are based on the best assumed

properties of the structure under investigation. Furthermore, most of these techniques are time-consuming and expensive to apply. They are based on the principle of local health monitoring. Eddy current testing, for example, requires pre-knowledge of the crack location to determine the damage extent Chang et al. (2003).

Many techniques are presented in the literature for damage detection in reinforced concrete such as corrosion and delamination of the steel reinforcement. However, most of these techniques are electrochemical techniques like electrical resistance probe, half-cell potential and linear polarization that are only effective for small distances and are considered as local methods. For instance, an electrical resistance (ER) probe can monitor corrosion by embedding a particular type of sensor in reinforced concrete. The resistance can be expressed by a balancing bridge that is inversely proportional to the steel reinforcement cross section. As a result, corrosion is attributed to cross section reduction due to corrosion by tracking the change in the resistance measured by the probes. Since the ER method is directly related to the physical effect of carrion on steel reinforcement and not vulnerable to electrochemical parameter variations, it is only effective for long-term corrosion detection in reinforced concrete Lei and Zheng (2013).

Consequently, global health monitoring methods are essential to establish that damage is occurring at the first stage before locating it and to avoid further deterioration. Examples of these methods include visual inspection and tap tests that are limited to locating voids near the surface of concrete, de-bonding, spalling of cover, and major cracks due to audible variations. These methods are only feasible when the damage is severe. Hence, these type of evaluation methods are not feasible for large area structures such as slabs and bridge decks. In contrast, the vibration based damage identification techniques can work as both global and local health assessment methods.

Vibration-based methods can be divided into modal and wave based methods. The modal methods require the modal characteristics, and the wave-based methods typically require the wave characteristics of the structure. The majority of vibration methods are model based methods where an intact structure is used as a baseline for comparison in order to detect damage. For instance, guided waves are defined as stress waves forced to follow a path defined by the material boundaries of the structure. Generally, when a guided wave is incident on a structural discontinuity, it scatters in all directions. The structural discontinuity could be damage in the structure such as a crack, delamination or boundary. The pulse-echo and pitch-catch are the two approaches commonly used in the guided wave techniques. In the pulse-echo method, the structure is excited with a narrow bandwidth pulse, and a sensor collocated with the actuator is used to detect the returning pulse coming from discontinuities. Using the wave speed and the boundary locations, the the signals from the boundaries can be filtered out. Subsequently, the remaining signal is employed to locate the damage. In the pitch-catch method, a pulse signal is sent across the specimen where the receiver is located at the other end. From

various characteristics of the received signal, such as delay in time of transit, amplitude, frequency content, etc., information about the damage can be inferred.

In this chapter both modal and wave based methods are discussed, focusing on the advantages and limitations of each. Then, methods for modelling reinforced concrete sections via FE are reviewed for different approaches. The FE modelling comprises both reinforced concrete and prestressed reinforced concrete. In addition, the WFE method is introduced, showing different applications especially for composite waveguides. Later, coupling of damaged and undamaged waveguides using WFE solution is reviewed in detail.

### 1.2.3 Modal damage identification techniques

Modal domain methods can provide global and local characterisation. Since the modal parameters are functions of the physical characteristics of the structures (stiffness, mass, damping and the boundary conditions), any variation of these features will lead to a change in the modal features. Typically, damage decreases the stiffness of the structures locally but increases damping. These methods are divided into natural frequency based methods, mode shapes based methods and damping properties based methods.

#### Natural frequency based methods

Variations in the natural frequency is one of the main characteristics considered in modal domain methods. One main limitation regarding the natural frequency based methods relates to the lack of sensitivity to small cracks. Besides, the crack is often modelled as a rotational spring using fracture mechanics that is not applicable for the high-frequency modes and deep crack identification. As a result, these assumptions make the methods limited to a particular type of beam and damage, and applicable to the first few lower order modes based on the assumptions.

Another limitation is that the frequency shift due to damage can be small and hidden due to environmental effects and errors. That is why this method works better under controlled laboratory operating conditions. To account for this limitation, Ni et al. (2005) introduced a method that quantifies the effect of temperature on modal frequencies based on mapping the two features. Additionally, Kim et al. (2007) proposed a warning model that identifies the damage using the changes in the natural frequencies and by introducing temperature effects. Also, it was demonstrated that the damage could be detected using frequency shifts of more than 1% once the environmental impacts are filtered out.

Moreover, even with no measurement noise effects, damage identification suffers from non-uniqueness in the possible solution. Obviously symmetric structures with symmetric damage locations produce similar natural frequency shifts. Also, different crack

severities and locations produce the same changes in the fundamental frequencies. This phenomenon poses a problem for detecting various damage types and sizes. Dilena and Morassi (2004) proposed the use of resonances and anti-resonances, when the frequency measurements are limited, to detect a single crack and avoid non-uniqueness. Another critical limitation is that changes in frequencies due to the presence of damage might be undetectable or insignificant in comparison with changes resulting from environmental and temperature conditions. For in situ applications, it is necessary that one has at least a 10% change in the natural frequency due to damage in order for it to be detected. Subsequently, a statistical damage detection model using pattern recognition technique was developed to distinguish damage-induced changes from temperature-induced changes (Ni et al. (2005), Kim et al. (2007)).

The forward problem is to determine the resonance changes based on the location and severity of the damage. Gudmundson (1982) used an energy-based perturbation approach to derive an explicit expression for the resonance frequencies of damaged structures where this method expresses the losses in stiffness. Due to the fact that the frequency sensitivity is proportional to the potential energy stored in the cracked cross section of the undamaged beam, Liang and Choy (1992) developed the relationship between the fundamental natural frequencies and the location and the severity of the damage for a simply supported or cantilevered beam based on a frequency sensitivity method. Also, Morassi (1993) showed that the frequency sensitivity approach can be used for a cracked beam using a general perturbation approach. Kasper et al. (2008) derived the explicit expressions for frequency shifts for a cracked symmetric uniform beam that can be applied for shallow and deep cracks. These expressions are based on a high-frequency approximation and are not effective for the fundamental frequencies.

On the other hand, the inverse problem method is the identification of the damage based on the natural frequency measurements. Liang and Hu (1991) developed a method for detecting the crack in a uniform cantilevered or simply supported beam using three bending natural frequencies. Based on fracture mechanics, the crack size is related to its stiffness. Nandwana and Maiti (1997) had extended this method to stepped beams, and Chaudhari and Maiti (2000) to segmented beams using the Frobenius method to solve an Euler-Bernoulli type differential equation. Then, Lele and Maiti (2002) extended Nandwana and Maiti's method to cover a short beam; the shear and rotational inertia effects are provided through the Timoshenko beam theory.

Using shifts in a pair of the natural frequencies, Morassi (2001) identified a single crack in a vibrating rod based on an explicit expression for the frequency sensitivity to damage. Later, Morassi and Rollo (2001) extended the method to cover two cracks of the same severity in a simply supported beam under flexural vibrations. In addition, cracks with different severity in symmetrical positions and in various locations produce identical changes in the first three natural frequencies. By relating fractional changes in the modal energy to changes in natural frequencies due to damage, Kim and Stubbs

(2003) presented a single damage indicator (SDI) method to locate the crack in a beam using a few fundamental frequencies. Zhong et al. (2008) introduced the spectral centre correction method (SCCM) that provides a simple solution to damage identification using output only time histories of the beam's response. However, only finite element verification was presented in free noise setup for detecting small changes in the natural frequencies. Also, Pawar and Ganguli (2016) applied the fuzzy genetic system to detect a matrix crack in thin-walled composite structures. Nevertheless, in concrete structures the deterioration of steel reinforcement has a small effect on the changes in the natural frequencies since the majority of the structural stiffness is related to the concrete.

**Mode shape based methods**

The use of mode shapes and their derivatives for damage detection is considered more advantageous than natural frequencies. First, the mode shapes represent local information. Second, mode shapes are less affected by the environmental effects such as temperature. On the other hand, mode shape measurements require a set of sensors, and are more sensitive to noise contamination than natural frequency measurements (Wei and Pizhong (2010)).

Methods based only on the mode shapes are not too sensitive to damage and suffer many limitations. Without applying signal processing or pattern recognition techniques, these methods seem more applicable as a preliminary damage detection approach rather than specific localization for damage. Therefore, these methods are limited when it comes to in situ testing especially for experiments on undamaged structures. In fact, mode shape based methods require measurements at multiple locations that necessitate a high spatial resolution, and a high signal to noise ratio should be provided for the measurements to be valid. Also, changes due to the damage should be distinguished from those due to environmental effects (Burcu and Oguz (2013)).

Methods based only on mode shapes are not effective for detecting damage due to corrosion, connection problems, degradation and delamination that provoke small changes and they are usually contaminated with measurement noise. Also, it uses the baseline data from the intact structure or its accurate finite element model and compares it to the mode shapes of the damaged structures for damage identification. Shi et al. (2000) extended the damage localisation method based on multiple damage location by using a two-step damage detection: using mode shape data first as a preliminary step to localise the damage region, and then using the natural frequency changes to precisely identify the damage location and size. Abdo and Hori (2002) showed that the rotation (first derivative of displacement) is more sensitive to damage and shows better sensitivity to multiple damage than the displacement modes, that do not have a good performance when it comes to small damage even with high spatial resolution measurements. The mode shape curvature (MSC) is a second derivative method, and it is more efficient at

recognising stiffness loss of the damaged member rather than the mode shapes themselves. However, the MSC method is very sensitive to noise.

Using Euler-Bernoulli beam theory, the strain at the top surface of the beam under bending is proportional to the curvature. As a result, the curvature mode shape of a slender beam can be measured by strain mode shapes. On the other hand, this method is not quite valid if the damage is distributed along the structure and if no baseline is available for the undamaged structure. However, even with no baseline, by observing anomalies in the deflection profile or curvature, one can locate possible damage. Abdel Wahab and De Roeck (1999) suggested the use of a fine mesh to derive the modal curvature for high order modes and that the first mode will provide the most accurate curvature in practical applications due to the limited number of sensors. Subsequently, the curvature damage factor was established as a damage indicator, that is the absolute average difference between the intact and damaged curvature mode shapes. This technique was applied to a bridge and proved its effectiveness for multiple damage locations. Rahai et al. (2007) subsequently developed a finite element based approach using incomplete measured mode shapes and natural frequencies to detect the damage in structures.

#### Damping based methods

Damping properties have been rarely used for damage detection due to the high error and variability associated with damping measurements and the variety of damping definitions. Reliable measurement and accurate modelling of damping are difficult. Farrar and Doebling (1999) presented large differences in the measured damping values under laboratory tests. In the case of a long suspension bridge, damping ratios were overestimated due to bias errors.

Undetectable cracks exist, because the effect is to produce very small changes in the natural frequencies and hence it is necessary for higher order mode shapes to be examined. However, they lead to larger changes in the levels of damping. Kawiecki (2000) has suggested that damping can be a real damage indicator when it comes to lightweight structures and microstructures. Also, Curadelli et al. (2008) used wavelet transforms to obtain the instantaneous damping coefficients. The experiment was conducted on a simply supported reinforced concrete beam and a one-bay six-story aluminum frame, and the results showed that damping is more sensitive to damage than natural frequency.

### 1.2.4 Wave based methods and damage detection in RC beams

All modal based techniques are dependent on the boundary conditions of the structure, since they involve resonances produced by wave reflections in the waveguide. In reinforced concrete structures, structural members like beams and columns are not completely fixed nor completely pinned. For this reason, the use of modal based techniques

for damage detection is not always very robust, since the boundary conditions are not well categorised. In contrast to modal based techniques, wave based techniques are inherent characteristics that are independent of the boundary conditions and are therefore more feasible to detect damage in reinforced concrete structures with uncertain boundary conditions.

By tracking the changes in the wave characteristics throughout the waveguide, or by comparing wave propagation features, damage can be detected. For instance, flexural wave reflection coefficients in a cracked isotropic uniform beam are proven as a feature for damage detection since they depend on frequency and the size of the damage Shone et al. (2007). To present a dynamic model of the cracked beam, a combination of the finite element method and spectral element method was used. The dynamic stiffness matrix of a section of the beam introducing a single-edge transverse crack was determined via finite element analysis. Then, by combining finite element analysis with a spectral element model, reflection and transmission matrices for the crack were derived. It was shown that certain cracks provide considerable wave reflection.

Also, locating discontinuities (known boundaries or unknown damage) using two or more point frequency response functions (FRFs) has also been used (Shone et al. (2009)). By plotting against the flexural wavenumber, the FRF phase shows variations due to wave interference between incident and reflected waves. Thus, this is related to the distance of the excitation source from these discontinuities, that are allocated after using an inverse Fourier transform to translate from the wavenumber domain to the spatial domain. Several uniform isotropic beams damaged by sawing transverse slots produced successful results during experiments.

Different wave-based techniques have been used as potential methods for locating damage. However, difficulties arise when it comes to composite structures due to coupling and energy leakage between two or more media. Another limitation is present due to the correct modelling of the composite media and the proper coupling of different degrees of freedom associated with each material. Potential solutions and limitations of detecting corrosion and delamination in steel reinforcements were reported in the use of the guided waves approach (Lei and Zheng (2013)). For instance, these approaches were demonstrated to detect corrosion effectively via tracking the interface roughness or debonding between the steel reinforcement bar and the surrounding concrete. However, it is still a challenge to develop an efficient technique for monitoring both combined effects.

Furthermore, due to expansion stresses induced by corrosion of the reinforcement steel, the surrounding concrete cracks and releases energy in the form of sound waves. Consequently, these waves can be pursued using acoustic emission sensors. Although acoustic emission methods are efficient to detect corrosion in reinforced concrete, they are passive method and only applicable in structural health monitoring while the structure is under service and loading and not structural inspection conditions. Moreover, none of the

techniques already presented focus on corrosion detection directly through assessment of the steel reinforcement. These latter based methods are known as physical based techniques and compared to other methods, proposed to be more precise in early term detection of steel corrosion. Ultrasonic guided waves (UGW) were among the early proposed physical based techniques (Lei and Zheng (2013)).

When mechanical vibrations propagate in elastic media, they produce elastic waves and when the frequency is greater than 20 kHz these are called ultrasonic waves. Bulk waves propagate in an infinite media and are associated with longitudinal and shear waves, and guided waves are like Rayleigh and Lamb waves in finite media that are in accordance with boundary reflections and refraction. The guided waves are compatible with the elastic theory when propagating in elastic media, and with viscoelastic theory in non-elastic media. By considering a steel rebar as an elastic media, the guided waves propagating are associated with the elastic theory (Li et al. (2012)).

In detecting corrosion in steel reinforcement, guided waves are based on two main principles. Due to corrosion, the surface of the rebar becomes rougher which increases the friction and bonding with the surrounding concrete. Consequently, energy leakage from the rebar to the concrete arises, and implies a decrease in the strength of the recorded guided waves signal. In contrast, delamination of concrete caused by corrosion leads to separation between the rebar and the surrounding concrete. As a result, energy leakage from the rebar to the concrete decreases, and implies an increase in the strength of the recorded guided waves signal (Miller et al. (2012)).

By considering the steel rebar as a solid cylindrical waveguide, there are three types of propagating waves: longitudinal L (0, $m$), torsional T ($n$, $m$), and flexural waves F ($n$, $m$). The notation $m$ is associated with the circumferential displacement, and $n$ with the sequential order of the mode. When $n = 0$, the displacement is axisymmetric. However, when $n$ = 1,2,3 ... the displacement is asymmetrical. For instance, L (0, $m$) and T (0, $m$) are axisymmetrical nodes, while F ($n$, $m$) is an asymmetrical mode.

As shown by Lei and Zheng (2013), the two main parameters for wave propagation are the phase and group velocities as shown in Figure 1.4 and Figure 1.5 respectively. The numerical results are for a 22 mm diameter steel bar in air with density 7932 kg/m$^3$. The first is the speed of the wave propagation at each discrete frequency in the waveguide, whereas the second is the speed of the wave envelope propagation. Both plots are called dispersion curves and show the variation of the velocities with respect to frequency for all wavetypes (axisymmetrical and asymmetrical). Clearly different modes are present at a single frequency, which indicates the possibility of multiple modes propagating in UGWs. Furthermore, the cut-off frequency is clear for all modes except for L (0, 1) and F (1, 1), which are the only modes to be excited and propagate below 87 kHz. This limit is critical when selecting the excitation frequency of the guided wave in a rebar.

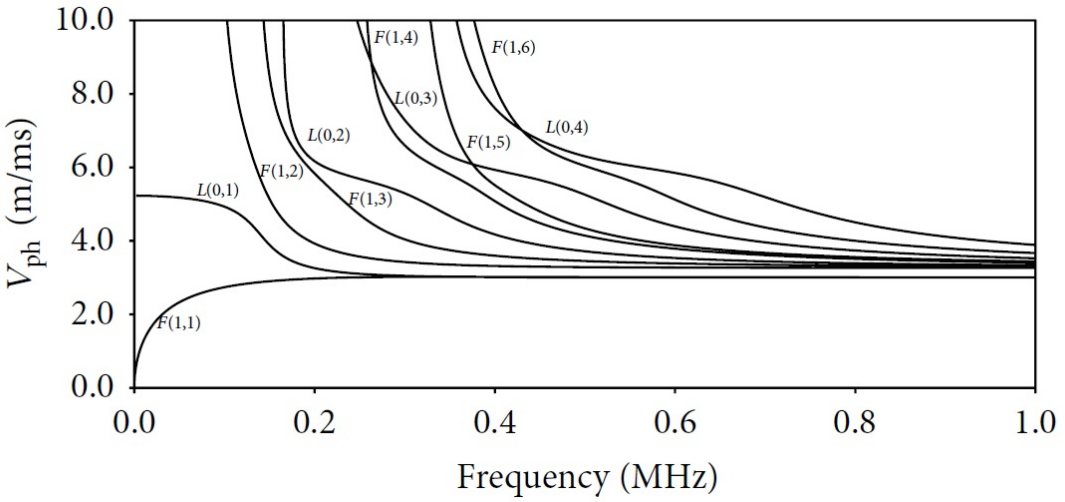


Figure 1.4: Phase velocity dispersion curve of steel reinforcement rebar Lei and Zheng (2013).

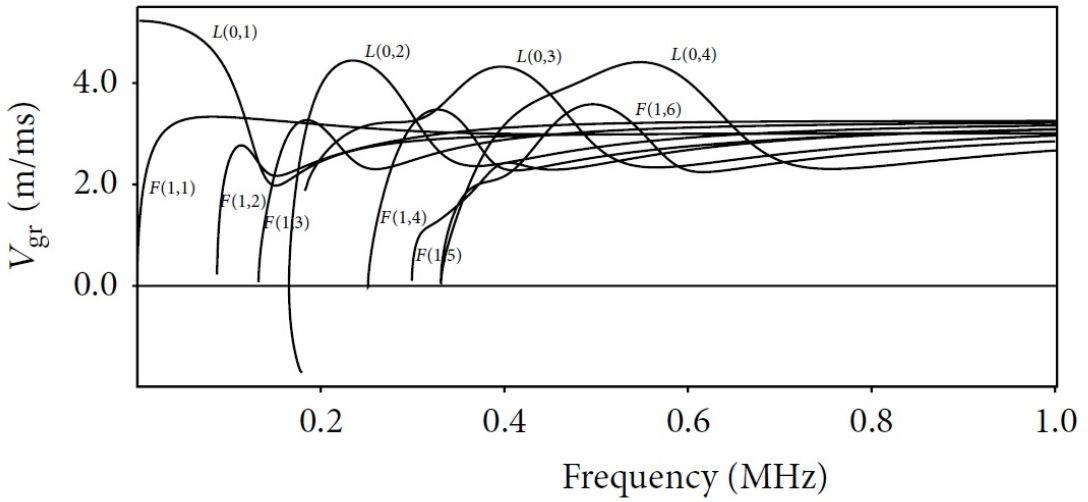


Figure 1.5: Group velocity dispersion curve of steel reinforcement rebar Lei and Zheng (2013).

The effects of stress, temperature and concrete strength on the guided waves through the steel reinforcement are presented in Li et al. (2012). Although the wave velocity of the guided waves changes with external stress according to elasticity theory, it has been shown that the group velocity of the L (0, 1) mode remains approximately unchanged at the same frequency. As a result, in the concrete interface delamination detection, the stress effects can be ignored via the UGW method. In addition, a set of different concrete strength specimens were tested in a chamber with the typical ambient temperature of civil engineering structures ranging from -40 °C to 60 °C. It has been shown that these specimens with different strength have similar group velocities for the L (0, 1) mode.

Thus, this group velocity remained stable for the selected temperature range. Moreover, concrete with higher strength corresponds to having a higher bonding strength with the steel reinforcement, leading to higher energy leakage from the rebar to the surrounding concrete. This has been proved by comparing concrete strengths of different specimens with the received UGW signal at the first wave peak value. It has been found that an increase in the concrete strength is associated with a decrease of this peak value and vice versa.

Despite the fact that UGWs are effective techniques to detect damage in steel reinforcement, they face three main difficulties as presented in Miller et al. (2012). First, since during corrosion both roughnesses of the steel section and separation from surrounding concrete occur simultaneously, the net signal strength might either rise or fall based on which effect is dominant at that time. Thus, a change in the net signal strength is not always associated with increased corrosion. Second, there are two energy profiles associated with two modes A and B related to the guided waves through the rebar from transmitter T to receiver R. It should be distinguished that both longitudinal and flexural modes can be of type A or B. In Figure 1.6, since mode A is associated with the energy profile propagating near the circumference of the steel rebar, it is more sensitive to corrosion at the interface between steel and concrete. While for mode B, the energy is restricted to be located near to the core of rebar and thus it is less affected by interface corrosion, but it causes the wave to propagate longer distances through the rebar. Therefore, mode B is preferably used in UGW due to the low level of energy leaking from steel rebar into the concrete. Finally, when the plain steel bar is replaced by a rebar, mode A cannot be used as a propagating wave through the rebar since it is sensitive to its non uniform surface texture that increases wave attenuation significantly.

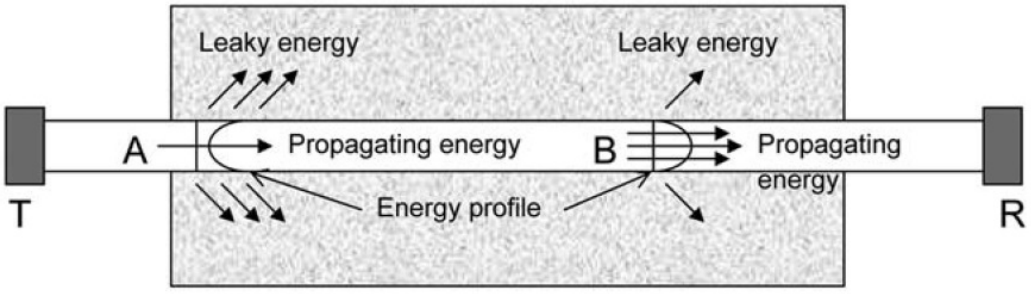


Figure 1.6: Two types of guided wave modes A and B can propagate from the transmitter T to the receiver R Miller et al. (2012).

In Li et al. (2012), the longitudinal UGW has been validated experimentally to detect interface corrosion. Proper signal length and modes are selected after plotting the dispersion curves of a steel rebar via numerical calculation. Small defects are recognised through numerical simulation, and modes are separated via a 2D FFT based on

the coupled waveforms. The peak signal value decreases with an increase in the concrete strength, and the condition of the steel-concrete interface is analysed in both the time and frequency domain. Consequently, energy attenuation is found as an accurate factor for defining the bonding condition. Miller et al. (2012) proposed a new guided wave-based technique for corrosion detecting in reinforced concrete, which expresses the change in the time of flight (TOF) of the propagating wave in loaded reinforced concrete structures with different corrosion levels. Unlike other UGWs techniques in steel reinforcement, this method is insensitive to the binding condition between the sensors and the specimen. Moreover, experimental results verify that the degree of corrosion affects both the recorded signal strength and TOF and that interface corrosion increases the signal strength while induced corrosion in bars reduces it. For in situ applications, a TOF shift between a corroded and non-corroded rebar is considered to obtain the level of corrosion.

All of the reported UGW experiments in reinforced concrete are based on the configurations shown in Figure 1.7 and Figure 1.8, where the transmitter and receiver of longitudinal guided waves are attached to the exposed ends of steel reinforcement that are offset from the sides of the concrete beam. These two configurations are not feasible for practical civil engineering structure conditions where steel reinforcement offset is not present. In addition, from reinforced concrete design theory, a rebar is added to concrete to take tension stresses induced by transverse load. Thus, no rebar exists in the central section in the concrete beam where the flexural stresses are zero.

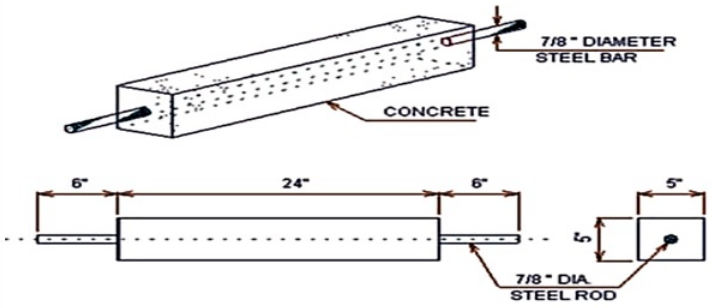


Figure 1.7: Concrete beam with central reinforcement rebar Miller et al. (2012).

As a result, the experimental configuration in the current UGWs used for corrosion detection in reinforced concrete is only feasible in laboratory conditions, where longitudinal guided waves are introduced in the rebar by directly attaching the transducers to the offset part of it. However, for typical reinforced concrete beams, this installation is impossible since no steel reinforcement is visible outside the concrete section. Thus, an alternative solution is needed where all these structural limitations are considered. So, this project will adopt vibration-based techniques and more precisely guided waves in

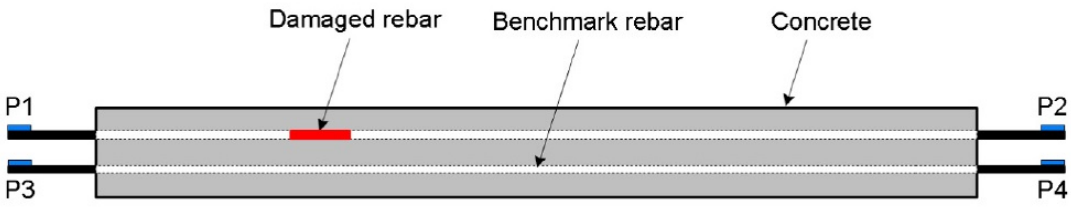


Figure 1.8: Schematic diagram of concrete beam with two reinforcement rebar and PZT positions Lu et al. (2013).

detecting corrosion in steel reinforcement embedded in concrete beams. The challenge is to develop these methods which can be adapted on reinforced concrete beams without direct contact between the transmitter and steel reinforcement. One step towards this goal is to identify the wave types present. Since it is a composite medium, a numerical approach is needed and WFE method has been adopted. However, it is necessary first to model a reinforced concrete section via FE in order to extract the associated mass and stiffness matrices. A review of the WFE approach is presented in the subsequent section.

### 1.2.5 Modelling RC using Finite Element method

Before applying the WFE approach to an RC beam, the reinforced and prestressed concrete section should be modelled via FE in order to extract the associated mass and stiffness matrices. An FE model is required with the least number of DOFs to decrease the computational time and cost. Across the literature, different scenarios have been used to model RC and prestressed RC. However, all of the methods modelled concrete using solid elements and the publications differed in how they modelled the steel reinforcements. Modelling of damage as pitting corrosion in a steel rebar was modelled using a finite element model by removing elements along the circumference as presented in Subsection 1.2.4 via Lu et al. (2013) and Zheng et al. (2014).

One approach is to model a reinforcement as bar or link element. To ensure bonding between the steel reinforcement and concrete, combined elements are used alongside the linked elements. Another approach is to use smeared elements, representing as a percentage reinforcement in the concrete solid elements, and therefore no bonding slip is assured. The smeared reinforcing method is suitable for modelling clusters of reinforcing fibres appearing in group or layer form. Each is simplified as a homogeneous membrane having unidirectional stiffness, and must have uniform cross-section, material, spacing and orientation (ANSYS (2013)). In addition, modelling of a prestressed RC is similar to a typical RC model except that one needs to introduce the effect of prestressing in the reinforcement rebars.

**Modelling RC using linked or smeared elements**

In most of the literature, concrete was modelled using 3D eight node brick elements. In the latest version of ANSYS for example, concrete corresponds to the SOLID65 element, and the steel reinforcements are present using two node elements, via LINK8 or LINK180. The latter connects nodes of adjacent concrete solid elements with a steel reinforcement location to ensure that the two materials shared the same nodes. Another approach is to model steel reinforcements as smeared elements and introduced them as a percentage change in the properties of the concrete element.

For an example of using linked elements in modelling RC, Ibrahim and Mahmood (2009) presented a finite element model of a reinforced concrete beam using ANSYS, where it was additionally reinforced with fibre reinforced polymer laminates (FRP) on the external bottom surface. The results obtained from the finite element model as load-deflection curves at mid-span and failure load were compared to experimental data, and good agreement was shown between the two. Ravi and Arulraj (2010) introduced an FE model for the behaviour of reinforced concrete beam-column joints retrofitted with carbon fibre reinforced polymer sheet. In order to validate the model, the performance of the retrofitted beam-column joint to static load was compared to the control specimens. Fathelbab et al. (2011) published a parametric study of the strengthening of reinforced concrete beams due to excessive uniform loads in flexure, shear and a combination of flexure and shear, using externally introduced bonded FRP sheets. ANSYS models have been used to perform many structural linear and non-linear predictions using several FRP configurations. The models demonstrated that the beam is strengthened in both flexure and shear, gave a higher ultimate load capacity and helped in delaying the failure and preventing debonding.

In addition, Jayajothi et al. (2013) applied a nonlinear finite element analysis to simulate the behaviour of failure modes of strengthened FRP RC beams. This is accomplished by selecting the large displacement option in the solution control. Four beams were modelled using ANSYS. A quarter of the full beam was used for modelling, taking advantage of the beam symmetry, loading and boundary conditions. From analysing the load deflection relationships until failure, the crack patterns were obtained from plotting results and compared with the experimental results available in the literature.

Another ANSYS based investigation tried to identify a crack in RC beams. Dahmani et al. (2010) presented a three-dimensional nonlinear finite element model of a reinforced concrete beam, where the concrete was again modelled using SOLID65 elements. However, the steel reinforcements were modelled as smeared reinforcements and introduced as a percentage of the steel embedded in concrete. Convergence between analytical and simulation results was illustrated including critical crack regions, reaction loads and deflections for various types of loadings. Al-Amin and Ahsan (2012) conducted the performance of an RC column under monotonic lateral loads via finite element modelling.

Cantilever columns modelled using ANSYS considered the nonlinear stress-strain relationship of the concrete and bilinear behaviour of steel. The results were in agreement with field experimental data, and the sensitivity of the load-deflection curve to changes in the column geometry was discussed.

**Modelling RC using linked and combine elements**

Combine elements ANSYS (2013) are used alongside the linked elements in order to model reinforcements and to insure bondage with the concrete. They are unidirectional springs with generalized force-deflection capability that can be used in any analysis. They have longitudinal or torsional capability in 1-D, 2-D or 3-D applications. The longitudinal option is a uniaxial tension-compression element with up to three degrees of freedom at each node i.e. translations in the nodal x, y, and z directions. No bending or torsion is considered. The torsional option is a purely rotational element with three degrees of freedom at each node i.e. rotations about the nodal x, y, and z axes. No bending or axial loads are considered. The element has large displacement capability for which there can be two or three degrees of freedom at each node ANSYS (2013).

For instance, Ghods et al. (2014) studied the effect of rebar corrosion on the behaviour of a reinforced concrete beam using modelling and experimental results. A corroded reinforced concrete beam, whose experimental results are available, was modelled in FE using ANSYS. The concrete was modelled using SOLID65 elements, and the steel reinforcements were present via LINK8 elements. In addition, the COMBIN39 element was applied for modelling the cohesion between the concrete and the rebar. This element can have zero length, and the start and end nodes between the steel and concrete can be defined as coincident as shown in Figure 1.9. The results show that a reduction in the steel reinforcement area and a change in the bond strength between the concrete and the reinforcement were seen in the model. The effect of reinforcement corrosion on the force-displacement curve and the modelled beam were also studied and compared with the results from actual reinforced beams tested.

Badiger and Malipatil (2014) undertook a parametric study of a four bending point analysis. Their ANSYS model, with nonlinear static analysis, modelled the concrete using SOLID65 elements, and the steel reinforcements were represented via LINK180 elements. The results with respect to mesh density, varying depths, use of steel cushions for support and loading points, effect of shear reinforcement on flexure behaviour and impact of the tension reinforcement on the behaviour of the beam were analysed and discussed. More recently, Jnaid and Aboutaha (2015) predicted the behaviour of reinforced concrete beams with unbonded reinforcement using a nonlinear FE ANSYS model. Loss of bond between the reinforcing steel and surrounding concrete was modelled using vertical spring elements COMBIN14, where the longitudinal spring-damper option was activated and the element was considered as a uniaxial tension-compression

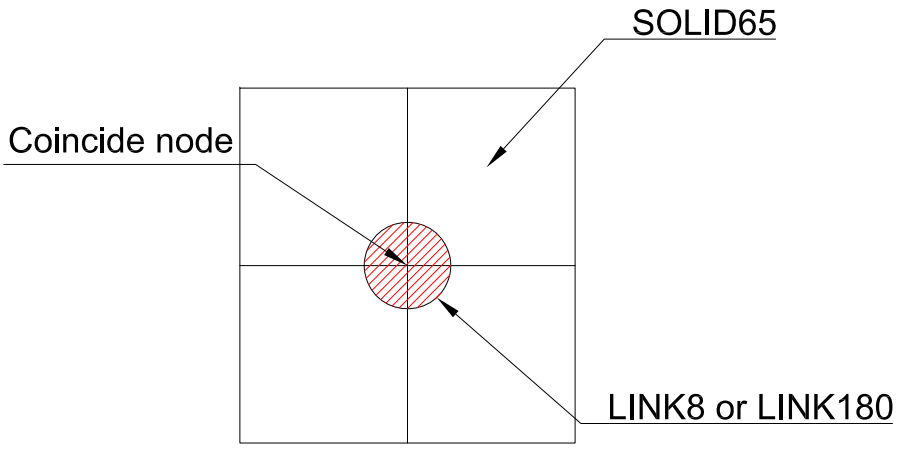


Figure 1.9: RC section model in ANSYS using SOLID65 (solid element for concrete) and LINK8/180 (beam element for steel).

element with up to three degrees of freedom at each node. The FEA model was compared to existing experimental data. The model was able to predict the ultimate flexural strength, load-deflection curve and crack pattern of concrete beams with unbonded reinforcement.

**Modelling prestressed RC using linked and combine elements**

Similar to RC beams, prestressed reinforced concrete beams need to be modelled via FE before applying the WFE approach. In most of the ANSYS based models in the published literature, the concrete was modelled using SOLID65 elements, and the steel reinforcements and prestressed tendon were represented via LINK8 or LINK180 elements. The post-tensioning was modelled via an initial strain in the tendon elements, corresponding to tendon tensile forces in a preliminary load stage. For this reason, smeared elements cannot be used to model prestressed RC since they are introduced as a percentage change in the concrete solid element and one cannot assign an initial strain to this kind of representation.

Fanning (2001) introduced nonlinear models of reinforced and post-tensioned concrete beams using ANSYS. Appropriate numerical modelling strategies were recommended and comparisons with experimental load-deflection responses were discussed for ordinary reinforced and post-tensioned concrete T-beams. Following on from this, Kim et al. (2010) undertook nonlinear finite element analysis of unbonded post-tensioned concrete beams. A 3-D finite element model using ANSYS was developed for simulating the nonlinear flexural behaviour and comparisons made with experimental results. The effects of various prestressing forces on the flexural behaviour of post-tensioned beams were investigated. In these models the concrete was modelled using SOLID65 elements, the steel reinforcements represented via LINK8 elements with prestress effect introduced

via initial strain in the latter. Li and Zhang (2011) identified natural frequencies and mode shapes of a prestressed concrete beam using ANSYS. Kote et al. (2014) illustrated the analysis of a prestressed concrete beam for determination of the physical responses such as deflection and stress distribution under a static concentrated load at the centre of the beam, also using ANSYS.

Joshuva et al. (2014) studied load-deflection responses, variations in the stresses in the concrete and steel and the crack patterns at critical stages of loading for reinforced and prestressed RC beams. The numerical predictions were compared to the data obtained using the theories of structural analysis. Padmarajaiah and Ramaswamy (2002) assessed flexural strength of prestressed concrete beams with fibre reinforcement. A three-dimensional nonlinear finite element analysis was conducted using ANSYS to study the flexural behaviour of both fully and partially prestressed fibre reinforced concrete beams. The interface behaviour between the concrete and reinforcement was modelled using COMBIN14 spring elements, with different properties to capture the effect of bond, bond-slip and peel-off. Each prestressing/deformed bar LINK8 contains two springs at each end (COMBIN14 elements), one acting perpendicular to the prestressing/bar steel to maintain concrete-steel bondage and one acting parallel to prestressing/bar steel to express the effect of prestress. A comparison of the results from both test and analysis on all 15 specimens, confirm that inclusion of fibres over a partial depth on the tensile side of the prestressed flexural structural members was economical and led to considerable cost saving without sacrificing the desired performance.

Subsequently, most of the literature reported follows a representation of the concrete as solid elements in the FE model approach. However, steel reinforcements can be modelled as linked with combine elements or a smeared element in the concrete media. In the prestressed RC model, the prestress effect is introduced as an initial strain in the linked elements. That is why the smeared approach cannot be used for prestressed RC in FE.

**Modelling of damaged rebar due to corrosion**

The two most common types of corrosion phenomena that affect reinforcing steel are general and pitting (localised) corrosion. General corrosion is found when there is a relatively uniform surface attack on the steel. This rarely happens for steel embedded in concrete exposed to an aggressive chloride environment, but is more likely a result of carbonation.

On the other hand, in a chloride environment, pitting corrosion is the most likely corrosion phenomena to occur in RC structures. Attacked by the chlorides ions, the metal protective layer is damaged and corrosion starts to develop. Chloride sources vary, such as salt spray in marine environments from the application of de-icing salts and in some cases from concrete admixtures Darmawan (2010).

In Lu et al. (2013), the characteristics of UGWs were investigated for detection of corrosion in reinforced concrete beams where damage was represented experimentally by the partial removal of different lengths of the rebar. Due to leakage of energy from the steel to the surrounding concrete, the guided wave's magnitude and velocity decrease along the steel reinforcement. To compensate for this effect, statistical parameters representing the wave characteristics were extracted from the captured signals to identify the rebar conditions.

Subsequently, in Mustapha et al. (2014), the propagation properties of UGWs in steel reinforcement were investigated. Also, to reduce the noise in the captured wave and to overcome the difficulty of wave conversion, a wavelet transform was adopted. Afterwards, in Zheng et al. (2014), pitting corrosion in a steel rebar was modelled using a finite element model by removing elements around the circumference. Numerical simulations show the feasibility of corrosion prediction via UGWs by tracking the characteristic of the time-frequency localization using a wavelet transform. Due to energy leakage from the steel rebar to the surrounding concrete, the wavelet analysis was used for extremely weak signals.

In this thesis, different amounts of damage representing corrosion of the steel reinforcement in the RC members are considered. Corrosion is modelled as a percentage reduction in a reinforcement diameter over a specified length. Moreover, this reduction is localised over a small length in order to represent the pitting corrosion effect.

### 1.2.6 Wave Finite Element method and coupling of waveguides

After modelling a reinforced and prestressed concrete section using an FE model, and after extracting the corresponding mass and stiffness matrices, the WFE approach can be applied to each waveguide. Throughout the literature, the WFE method has been applied to both simple and complex waveguides in order to identify the wave characteristics. The WFE concept relies on the notion of predicting the wave characteristics of a repetitive structure through analysing the wave propagation within a periodic element. By taking a short section of the waveguide, and by expressing the continuity of displacements and equilibrium of forces between the boundaries, an eigenvalue problem is posed in terms of a transfer function. By solving this problem at each specified frequency, the eigenvalues are related to the wavenumbers of the waveguide that relate the variables to the right and left side of the section, and the eigenvectors are associated with the internal displacements and forces.

Duhamel et al. (August 2003) presented the WFE method for simple homogeneous one dimensional waveguides. The efficiency of this method was compared to the spectral FE method via the forced response of a finite beam and plate-strip. In Mace et al. (2005), wavenumbers, energy and group velocity were presented and discussed for a beam, a

simply supported plate strip and a viscoelastic laminate. Mencik and Ichchou (2007) formulated and solved wave propagation in guided elastodynamic structures filled with acoustic fluid using WFE. Free and forced frequency responses of the waveguide were presented, and comparisons between the proposed method and classical theories were formulated showing that this method is not limited to low frequencies. Arrud et al. (2007) also compared the wave finite element and spectral element method. A simple Timoshenko beam and Kirchhoff Levy plates were used as an illustration. In a later application, Waki et al. (2009b) expressed free and forced vibrations of a tyre using the WFE formulation on a short circumferential segment, and results were compared to experiments. Then, Waki et al. (2009a) considered numerical issues concerning the wave and finite element method for free and forced vibrations of waveguides, and a robust procedure was proposed.

Manconi and Mace (2009) applied the WFE approach to identify the wave characteristics in cylindrical and curved panels. These include isotropic, orthotropic, and laminated sandwich constructions. Despite the complexity of these sandwich panels, accurate dispersion curves were found at a small computational cost. Later, Manconi and Mace (2010) employed the approach to predict wave dispersion, wave attenuation and dissipation in viscoelastic laminated panels. In addition, a formulation to calculate the average loss factor of an anisotropic component was proposed. Dispersion curves for different damped laminated panels were evaluated. Renno and Mace (2010) formulated a rectangular segment as a waveguide via WFE. Then, the forced response to a convected harmonic pressure (CHP) was formulated, where a comparison was presented between FE and WFE predictions of a frequency response function for a cantilevered laminated beam. Furthermore, Renno and Mace (2011) calculated the forced response of two-dimensional homogeneous media via WFE. Numerical examples covered isotropic, orthotropic and laminated plates. Zhou et al. (2011) compared the wave propagation between the semi-analytical finite element (SAFE) method and WFE for a steel pipe. Efficiency and accuracy of both methods were examined.

Following this, Manconi et al. (2013) predicted the effect of pre-stress on the damping of curved panels through the waves solution via WFE. It has been shown that prestress reduces the global loss factor especially for radial displacement modes. Renno et al. (2013) modelled the dynamic behaviour of plane and axisymmetric laminated structures via WFE. Numerical examples were presented, including anisotropic, plane and cylindrical foam-cored laminated sandwich constructions with pre-stress.

One of the major advantages of the WFE method is that the solutions produce the displacement and forces at each DOF, which can be used to couple damaged and undamaged waveguides to predict the reflection and transmission coefficients due to a defect. One method is to implement the continuity and force equilibrium conditions between the damaged and undamaged section. In this case, the coupling of a WFE-FE-WFE model approach is used where the damaged waveguide is only modelled via FE.

For instance, Ichchou et al. (2009) formulated the WFE method to obtain the eigenvalues/eigenvectors solutions for rectangular cross section waveguides. The diffusion matrix prediction model (DMM) was used to couple damaged and undamaged waveguides, where higher modes show sensitivity to damage modelled as a notch within the section. In addition, Zhou and Ichchou (2010a) expressed wave excitation and scattering using the eigensolutions from WFE of coupled structures comprising damaged and undamaged plates. Then, Zhou and Ichchou (2010b) used the WFE method to obtain the wave characteristics of a curved beam. Mode conversion, reflection and transmission coefficients were used to localise damaged portions.

Renno and Mace (2013) calculated the reflection and transmission coefficients of joints using a hybrid finite element/wave and finite element approach, where the joint was modelled via FE and a small portion of the waveguide is described via a WFE model. The two waveguides are coupled in order to get the reflection and transmission coefficients of the joint. Forced response examples were presented for two rods connected at a point mass, an L-frame configuration and lap-jointed laminated beams with a slot. Kharrat et al. (2011) proposed the identification and sizing of defects in pipelines by the wave finite element method using torsional guided waves. Reflections from cracks are expressed as a methodology to identify damage sizing. WFE was adapted to predict the wave characteristics of hollow cylinders, and good agreement was found with respect to full finite element simulation. Later, Kharrat et al. (2014) used WFE to construct a numerical database of reflection coefficients by varying the dimensions of the damage in pipelines. Torsional guided waves were also proposed for pipeline inspection. Furthermore, Kessentini et al. (2016) used the evolution of the scattering coefficients via the dynamic stiffness matrix of the coupling elements in order to illustrate the forced response to pressure excitations for both single and coupled waveguides with and without damping effects.

Another method is to model each waveguide via WFE, and couple damaged and undamaged sections via a wave approach by considering a junction between the waveguides of different types. In this case, the coupling of a WFE-WFE-WFE model methodology is used. For instance, Harland et al. (2001) presented the reflection and transmission coefficients of waves passing through two different beam waveguides. By considering the continuity and equilibrium equations at the junction, incident, reflected and transmitted waves can be related through WFE solutions as displacement and forces of each waveguide. Next, Lee et al. (2007) introduced the reflection and transmission calculation through a finite length connector separating two beams by expressing the incident, reflected and transmitted waves at each junction. Comparison of an exact solution with discrete models were presented as well.

To summarise, the WFE method has been applied to both simple and complex waveguides. The solution can be used to couple damaged and undamaged waveguides. Scattering properties can be identified and subsequently, potential damage-sensitive modes

associated with high reflection features can be classified. However, the WFE approach has not been applied to RC sections in any of the literature. In this thesis, the approach is applied to RC sections with different damage scenarios. Then, the solution is employed to define a damage sensitive criteria based on the high reflection of particular wave modes.

### 1.2.7 Conclusions

In summary, damage detection due to delamination in composite structures is not detected effectively and precisely using a single vibration-based methodology. In reinforced concrete structures, the stiffness of the structures is dominated by the concrete. Therefore, the delamination/corrosion or debonding in the steel reinforcement is not accurately identified by using only a single vibration-based method. Also, damage should be detected at earlier stages to increase the durability and life cycle of the structure. Furthermore, a reinforced concrete section cannot be modelled as a thin beam to be completely consistent with Euler-Bernoulli theory. That is why it is preferable for the reinforced concrete beam to be modelled as a deep beam, and consequently compatible with a Timoshenko beam theory model.

Moreover, none of the techniques already presented focuses on corrosion detection directly through assessment of the steel reinforcement. These latter methods are known as physical based techniques and are compared to other methods. Ultrasonic guided waves (UGW) was among the proposed physical based techniques. In detecting corrosion in steel reinforcement, guided waves are based on two main principles: roughness of interference and separation of the steel and concrete. However, in all UGW experiments on reinforced concrete, the transmitter and receiver for longitudinal guided waves are attached to the steel reinforcement that are offset from the ends of the concrete beam. This arrangement is only feasible in the laboratory and not in situ conditions. Local methods are time and cost consuming, and methods that can act both globally and locally are more highly appreciated. For all these reasons, a mix of vibration-based methodologies is preferable for the examination of deep reinforced concrete beams.

By using wave-based methods, identification of the wave characteristics is essential in reinforced concrete. Before applying the WFE approach for the waveguide, the reinforced and prestressed concrete section should be modelled via FE in order to extract the associated mass and stiffness matrices. A proper FE model is required with the least number of DOFs to decrease the computational time and cost. Across the literature, different scenarios have been used to model RC and prestressed RC. However, all of the methods modelled the concrete using solid elements and the differences occurred on how to model the steel reinforcements. One approach is to model the reinforcement as a bar or link elements. To ensure bonding between the steel reinforcement and concrete, combine elements are used alongside the linked elements. Another approach is to use

smeared elements presented as percentage reinforcement in concrete solid elements, and therefore no bonding slip is assured. In addition, the modelling of prestressed RC is similar to typical RC except that one needs to introduce the effect of prestressing in the reinforcement rebars. However, this is only accomplished by using linked elements, and not through smeared elements, that requires the presence of nodes at the location of the rebars to be assigned.

After modelling reinforced and prestressed concrete section in FE, and after extracting the corresponding mass and stiffness matrices, a WFE approach could be applied to each waveguide. Throughout the literature, the WFE method has been applied to simple and complex waveguides in order to identify the wave characteristics. WFE solutions as displacements and forces associated with each DOF have been employed to couple damaged and undamaged waveguides. One approach is to implement the continuity and force equilibrium conditions between the damaged and undamaged section, via a WFE-FE-WFE model where the damaged part is only modelled via FE. For computational efficiency, this coupling approach is more feasible for discontinuities covering a small length of a section.

## 1.3 Aims of the thesis

The aims of this thesis are summarised as follow.

1- Develop accurate and numerical efficient static and dynamic models for RC beams.

2- Determine the type of wave propagation and their characteristics in deep RC beams with and without prestress.

3- Quantify the dynamic effect of damage in the embedded rebars of RC beam on wave propagation in the beam.

4- Identify a damage detection algorithm which is particularly sensitive to rebar thickness reduction. It should not require direct excitation of the embedded rebar.

5- Perform and evaluate the success of the detection algorithm using experimental validation.

## 1.4 Outline of the thesis

In Chapter 1, discussions including advantages and limitations of different NDT techniques to detect corrosion of the reinforcement in reinforced concrete have been presented. Modal damage identification techniques and wave based methods for reinforced concrete are compared. In this project, the focus is on a wave based approach and more

specifically into guided waves. In order to identify the waves characteristics within the reinforced concrete waveguide, the wave finite element method is applied. This method requires the knowledge of the mass and stiffness matrices of the waveguide. That is why a finite element model of a section is needed. Subsequently, a literature review of the finite element modelling of reinforced concrete structures is presented in addition to the application of wave finite element methods for composite waveguides and its role in coupling different waveguides.

Chapter 2 presents the methodology of modelling reinforced concrete and prestress reinforced concrete section using the finite element method. A new approach using embedded reinforcements is suggested and compared to conventional models and published results in the literature covering static and dynamic analysis.

Chapter 3 covers a review of the wave finite element methodology including the numerical and ill conditioning errors associated with it. Also, the formulation for the forced response using WFE is presented. Furthermore, Chapter 4 covers the wave solutions using wave finite elements for reinforced, prestress and post-tensioned reinforced concrete as dispersion curves and wave mode shapes. In addition, the forced response generated via FE and WFE solutions are compared.

In Chapter 5, the wave finite element solution uses nodal displacements and forces to couple damaged and undamaged reinforced concrete waveguides. Two coupling approaches are compared with respect to their advantages and limitations. One approach is then chosen to couple different damaged and undamaged models. The magnitude of the reflection coefficients associated with the least attenuated modes are plotted for reinforced concrete. A potential damage criterion is then identified.

Subsequently, Chapter 6 defines a damage identification algorithm based on the findings of the previous chapters. The algorithm is demonstrated via simulations on damaged and undamaged RC beams possessing different boundaries. The potential and accuracy of the algorithm to locate the damage is tested.

In Chapter 7, the damage detection algorithm is validated experimentally on specifically designed RC beams with no discontinuities and various level of rebar reduction. Fabrication of the specimens is briefly described. In addition, the wavenumbers are estimated experimentally using a correlation method. The potential of the algorithm to detect and locate the damage is validated and quantified.

Finally, in Chapter 8, conclusions are presented covering the main outcomes of this thesis, and suggestions for further research and potential limitations are outlined. In addition, the details of some of the calculations and analysis are presented in Appendix A and B.

## 1.5 Contributions of the thesis

The original contributions of this thesis are as follows.

1- Modelling of reinforced concrete sections using embedded reinforcements is proven accurate and possible rather than using the LINK element typically available in FE software. The new model requires less mesh than the conventional one, and no coupling elements are needed between the rebar and the adjacent concrete solid nodes.

2- The WFE method is successfully applied to obtain the dispersion relations and the corresponding wave mode shapes of an RC beam. Sensitivity of the free wave propagation to the rebar geometry and properties is presented.

3- A new approach to coupling damaged and undamaged waveguides using WFE-WFE-WFE is presented and compared to the WFE-FE-WFE technique present in the literature.

4- Significant scattering of high order wave modes, where cross sectional deformation occurs, is shown to occur at the junction between damaged and undamaged waveguides, due to wave propagation in one waveguide not propagating in the other at a specific frequencies.

5- A damage detection algorithm to identify and locate the loss of thickness in a rebar is proposed which requires no benchmark or numerical model for the intact structure.

6- Experimental validation and implementation of the damage detection algorithm is performed based on identifying and measuring the cross section wave modes at their cut-on frequencies. The potential benefits and limitations of the novel wave based damage detection method are discussed.

# Chapter 2

# Finite Element modelling of reinforced concrete beams

## 2.1 Introduction

Reinforced concrete is a major structural component in civil structures such as buildings and bridges. Understanding its behaviour under loading service is important for the development of an overall feasible and safe structure. For this purpose, different methods had been used to study the performance of concrete structural members.

Finite Element (FE) modelling has become more attractive in recent years especially with the progressing knowledge and capabilities of computer software and hardware. It is used in simulations of many reinforced concrete structures in order to understand the response of individual structural components and their contribution to a structure as a whole, in addition to the behaviour under different loading/analysis scenarios.

Since reinforced concrete is a composite medium where the steel bars are embedded within concrete, it has always been a challenge to model the RC section correctly in FE software with the most effective mesh size, number of nodes and degree of freedoms. In addition, it is necessary to incorporate the bond accurately between the steel reinforcements and the surrounding concrete. In this research, a new approach is presented for modelling RC beams using new features in the ANSYS FE software, and then it is compared to existing conventional techniques.

Before identifying the RC wave characteristics by applying the Wave Finite Element (WFE) method to reinforced and prestressed concrete waveguides, the two sections should be modelled via FE in order to extract the associated mass and stiffness matrices. In this chapter, two FE modelling approaches for a reinforced concrete section with and without prestress using FE are compared statically and dynamically. The approaches differ in their modelling of the steel reinforcements: linked elements are applied as bars

connecting nodes where the reinforcements are present, and embedded elements are modelled as beams inside the concrete solid elements. Subsequently, one approach is selected for the subsequent simulation models.

## 2.2 Finite Element modelling of RC beams using embedded reinforcements

As seen in the literature review, typically the concrete is modelled using SOLID65 elements and the steel reinforcements are modelled via LINK8 or LINK180 in the current version of ANSYS. This model is assigned as Model A. The alternative, proposed here, is assigned as Model B where the reinforcement rebars are modelled via the 3D discrete element REINF264 embedded in the SOLID65 element. Both models' cross sections are plotted in Figure 2.1.

**FE model properties**

Both beams share the same dimensions. They are 2 m long with fixed boundary conditions. All the steel reinforcements are of 25 mm diameter. In addition, the two cross-sections have the same geometry and rebars location as shown in Figure 2.1. Due to the difference in defining the LINK180 and REINF264 elements in the model, the mesh attributes are different for the two cross-sections. This will be clearly explained in the elements description.

SOLID65 is a 3D eight nodes brick solid element, and it has three DOFs per node, which are translations in the X, Y and Z directions. The solid is capable of cracking in tension and crushing in compression representing the concrete material behaviour ANSYS (2013). This is essential for the FE static analysis validation to represent the brittle behaviour of the concrete. The geometry and node locations are shown in Figure 2.2.

LINK180 is a 3-D spar that is useful in a variety of engineering applications. The element can be used to model trusses, sagging cables, links and springs. It is a uniaxial tension-compression element with three degrees of freedom at each node in the X, Y and Z directions. As in a pin-jointed structure, no bending of the element is considered. Plasticity, creep, rotation, large deflection and large strain capabilities are included ANSYS (2013). It is defined via two nodes, and in modelling the RC section it is used in connecting nodes of adjacent concrete solid elements with a steel reinforcement location to ensure that the two materials share the same coincident common nodes as illustrated in Figure 2.1. The geometry and node locations are shown in Figure 2.3. The diameter of the reinforcement is identified as a real constant for the element.

The REIN264 element is used to model the reinforcement in Model B. REINF264 is embedded in the SOLID65 element (referred to here as the base element). The element

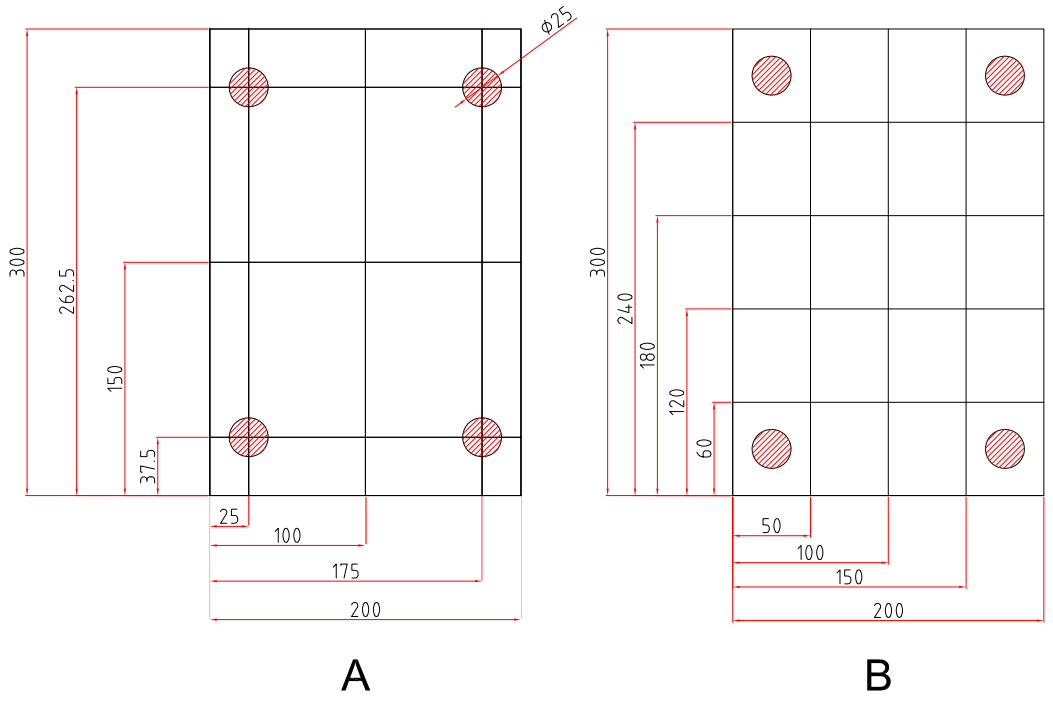


Figure 2.1: RC section meshes using (A) linked and (B) embedded reinforcements.

Model A comprises 16 SOLID65 elements per cross-section compared to 25 elements for Model B. Dimensions are in mm.

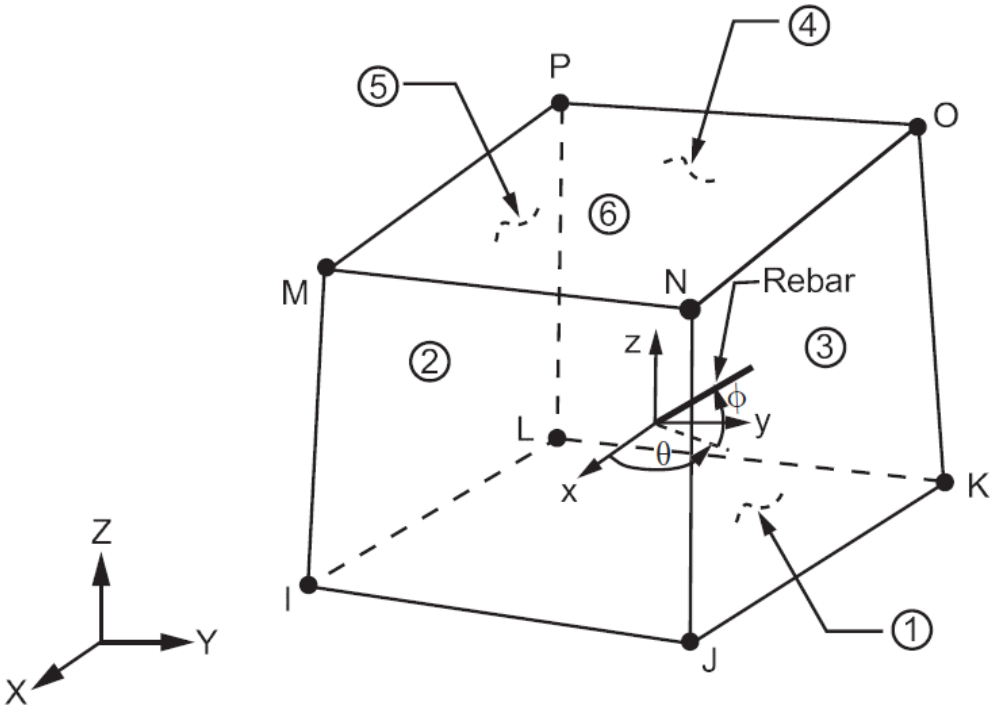


Figure 2.2: SOLID65 geometry and nodes locations ANSYS (2013).

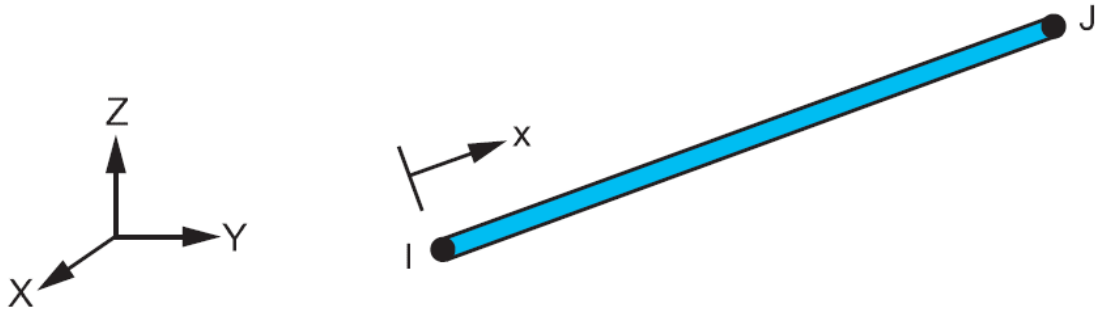


Figure 2.3: LINK180 geometry and nodes locations ANSYS (2013).

is suitable for simulating reinforcing fibres with arbitrary orientations. Each fibre is modelled separately as a spar that only has uniaxial stiffness. The nodal locations, degrees of freedom and connectivity of the REINF264 element are identical to those of the base element. REINF264 has plasticity, stress stiffening, creep, large deflection and large strain capabilities. The location of the rebar is defined as an offset distance from the edges of the base element selected ANSYS (2013). The geometry and node locations are shown in Figure 2.4. The diameter of the reinforcement is identified in the reinforcing window in ANSYS. The associated shapes functions of REINF264 are presented in Appendix C.

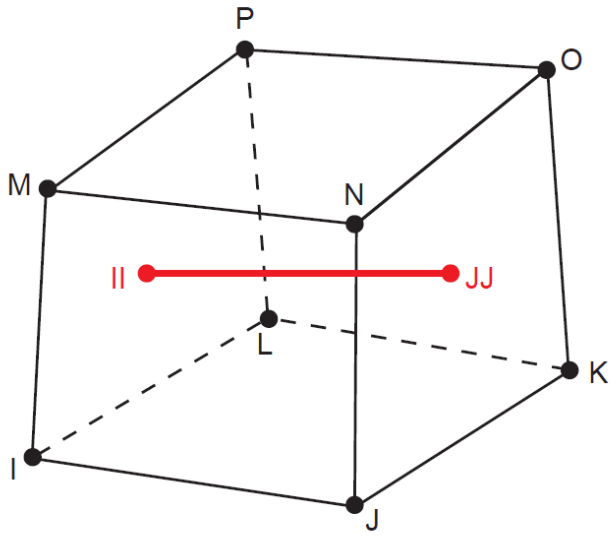


Figure 2.4: REINF264 geometry and nodes locations ANSYS (2013).

SOLID65 element (nodes: I-J-K-L-M-N-O-P) representing the concrete with embedded REINF264 (nodes: II-JJ) representing the discrete reinforcement.

In this chapter, RC and prestressed RC beams are considered and analysed under static and dynamic loading as shown in Figure 2.5.Considering the RC beam, when the load

state is large then a nonlinear analysis is more suitable. However, the dynamic analysis is associated with small deformations about the statically loaded equilibrium position. The latter is the solution of either a linear or non-linear static FE solution. Subsequently, a linear analysis is suitable and accurate for the dynamic analysis simulation. Similarly in the case of dynamic analysis of prestressed RC beams where the prestress load keeps the RC beam within the linear behaviour for the dynamic response.

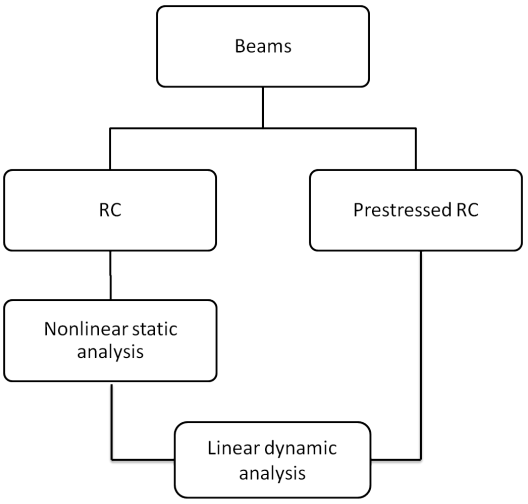


Figure 2.5: Analysis types to be conducted on RC and prestressed RC beams.

### Material properties

Concrete material is considered non-linear in this chapter only when its is under static analysis. The nonlinear behaviour of the concrete originates from the crack growing along the concrete since the load is large. The crack produces a reduction of the material stiffness as a function of the levels of the strain. However, in the next chapters, free and forced wave propagation are considered and the cross section of the RC section is uncracked. Therefore, concrete is linear in the latter case.

The SOLID65 element requires linear isotropic and multilinear isotropic material properties to model concrete properly. The multilinear isotropic material uses the von Mises failure criterion along with the Willam and Warnke model to define the failure of the concrete Willam and Warnke (1974). In ANSYS, EX is the modulus of elasticity of the concrete ($E_c$), and PRXY is the Poisson's ratio ($\upsilon$). The modulus is based on the equation,

$$E_c = 4700\sqrt{f'_c} \quad (MPa) \tag{2.1}$$

with $f'_c$ as the compressive strength of concrete of value equal to 33 MPa. The Poisson ratio $\upsilon$ is assumed to be 0.3. The compressive uniaxial stress-strain relationship for the concrete model was obtained using the following equations to compute the multilinear

isotropic stress-strain curve for the concrete by MacGregor (2012).

$$f = \frac{E_c\,\varepsilon}{1 + (\frac{\varepsilon}{\varepsilon_0})^2} \tag{2.2}$$

$$\varepsilon_0 = \frac{2f'_c}{E_c} \tag{2.3}$$

$$E_c = \frac{f}{\varepsilon} \tag{2.4}$$

where $f$ is the stress at any strain $\varepsilon$ in MPa, and $\varepsilon_0$ is the strain at the ultimate compressive strength $f'_c$. The multilinear isotropic stress-strain implemented requires the first point of the curve to be defined by the user. It must satisfy Hookes Law, i.e

$$E = \frac{\sigma}{\varepsilon} \tag{2.5}$$

The multilinear curve is used to help with convergence of the nonlinear solution algorithm. Figure 2.6 shows the stress-strain relationship used for this study which is based on work reported in Kachlakev et al. (2001). Point 1 is defined as 0.30 $f'_c$, and it is calculated in the linear range by Equation 2.4. Points 2, 3 and 4 are calculated from Equation 2.2 with $\varepsilon_0$ obtained from Equation 2.3. Strains are selected and the stress is calculated for each strain. Point 5 is defined at $f'_c$ with $\varepsilon_0 = 0.003$ indicating traditional crushing strain for unconfined concrete.

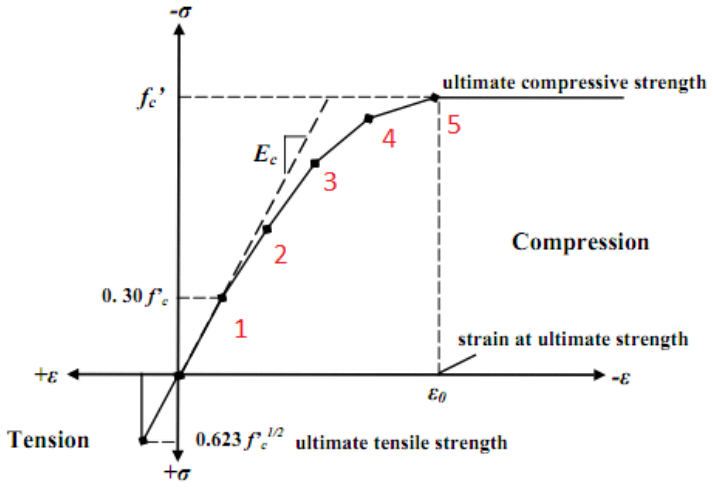


Figure 2.6: Uniaxial stress-strain curve for concrete MacGregor (2012).

Implementation of the Willam and Warnke material model Willam and Warnke (1974) in ANSYS requires different constants to be defined: (to express the non-linearity of concrete material to be defined as input in ANSYS as in Table 2.1)

1. Shear transfer coefficients for an open crack.
2. Shear transfer coefficients for a closed crack.
3. Uniaxial tensile cracking stress.

4. Uniaxial crushing stress (positive).

Typical shear transfer coefficients range from 0.0 to 1.0, with 0.0 representing a smooth crack (complete loss of shear transfer) and 0.9 representing a rough crack (no loss of shear transfer). The shear transfer coefficients for open and closed cracks were determined using the work established in Kachlakev et al. (2001). Convergence problems occurred when the shear transfer coefficient for the open crack dropped below 0.2. No deviation of the response occurs with the change of the coefficient. Therefore, the coefficient for the open crack was set to 0.3. The uniaxial cracking stress was based upon the modulus of rupture. This value is determined using,

$$f_r = 0.7\sqrt{f'_c} \quad (MPa) \tag{2.6}$$

The uniaxial crushing stress in this model is based on the uniaxial unconfined compressive strength $f'_c$, and is denoted by $f_t$. It is entered as -1 to turn off the crushing capability of the concrete element as suggested in Kachlakev et al. (2001). Convergence problems have been repeated when the crushing capability was turned on.

The biaxial crushing stress refers to the ultimate biaxial compressive strength $f'_{cb}$. The ambient hydrostatic stress state is denoted as $\sigma_h$ and is defined as

$$\sigma_h = \frac{1}{3}(\sigma_{xp} + \sigma_{yp} + \sigma_{zp}) \tag{2.7}$$

where $\sigma_{xp}$, $\sigma_{yp}$, and $\sigma_{zp}$ are the principal stresses in the principal directions. The biaxial crushing stress under the ambient hydrostatic stress state refers to the ultimate compressive strength for a state of biaxial compression superimposed on the hydrostatic stress state $f_1$. The uniaxial crushing stress under the ambient hydrostatic stress state refers to the ultimate compressive strength for a state of uniaxial compression superimposed on the hydrostatic stress state $f_2$. The failure surface can be defined with a minimum of two constants: $f_t$ and $f'_c$. The remainder of the variables in the concrete model are left to default value based on the following equations.

$$f'_{cb} = 1.2f'_c \;\; ; \;\; f_1 = 1.45f'_c \;\; ; \;\; f_2 = 1.725f'_c \tag{2.8}$$

LINK180 and REIN264 elements are used for all of the steel reinforcement in Model A and B respectively. Both elements are assumed to be bilinear isotropic based on the Von Mises failure criteria. The bilinear model requires the yield stress $f_y$ as well as the hardening modulus of the steel to be defined. All the material properties were converted into SI units and have been entered into ANSYS following the values in Table 2.1.

| Element Type | Material Properties | |
|---|---|---|
| SOLID65 | Linear isotropic | |
| | EX | $2.8\times10^{10}$ Pa |
| | PRXY | 0.3 |
| | Density | 2400 kg/m$^3$ |
| | Multilinear isotropic | |
| | Strain | Stress |
| | 0.00036 | $9.8\times10^{6}$ Pa |
| | 0.0006 | $1.5\times10^{7}$ Pa |
| | 0.0013 | $2.8\times10^{7}$ Pa |
| | 0.0019 | $3.2\times10^{7}$ Pa |
| | 0.00243 | $3.3\times10^{7}$ Pa |
| | Concrete | |
| | Open shear transfer coefficient | 0.3 |
| | Closed shear transfer coefficient | 0.9 |
| | Uniaxial cracking stress | $3.6\times10^{6}$ Pa |
| | Uniaxial crushing stress | $-6.9\times10^{3}$ Pa |
| Link 180 REINF264 | Linear isotropic | |
| | EX | $2.0\times10^{11}$ Pa |
| | PRXY | 0.3 |
| | Density | 7850 kg/m$^3$ |
| | Bilinear | |
| | Yield stress | $4.1\times10^{8}$ Pa |
| | Tangent modulus | $2.0\times10^{7}$ Pa |
| SOLID45 | Linear isotropic | |
| | EX | $2.0\times10^{11}$ Pa |
| | PRXY | 0.3 |
| | Density | 7850 kg/m$^3$ |

Table 2.1: Material properties for Models A and B.

**Modelling**

For the nonlinear static analysis, a steel plate is used between the load and the top surface

of the RC and prestressed RC beam. This is used to ensure the proper transition of the load into the beam, and to prevent local failure due to concentration of the load into one node of the beam before reaching its actual failure. Subsequently, a 3D solid element SOLID45 is used for a steel plate supporting the load on the beam. The element is defined by eight nodes having three degrees of freedom at each node: translations in the X, Y and Z directions. The element has plasticity, creep, swelling, stress stiffening, large deflection and large strain capabilities ANSYS (2013). The geometry and node locations are shown in Figure 2.7.

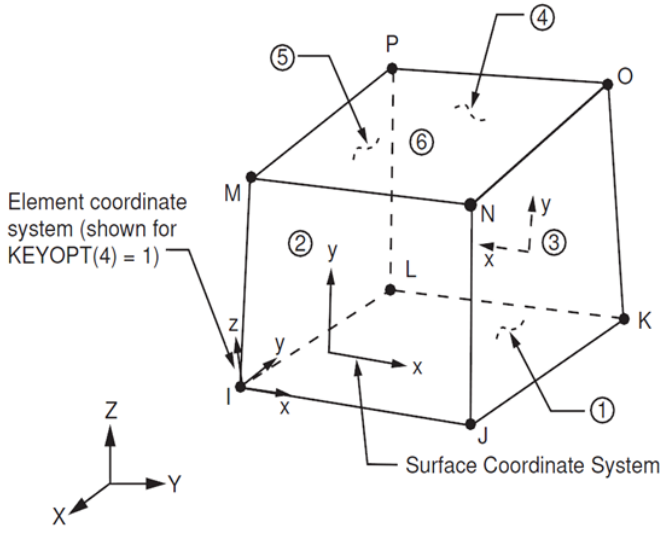


Figure 2.7: SOLID45 geometry and nodes locations ANSYS (2013).

The beam and plate, onto which the loading is directly applied, are modelled as volumes that are meshed with the solid elements. Both beams are modelled in ANSYS as shown in Figure 2.8 and Figure 2.9.

The material, reinforcement cross section and reinforcement offset distance from the concrete solid element sides are defined (the offset distance is 0.5). To obtain good results from the SOLID65 element, the use of a rectangular mesh is recommended. Therefore, the mesh was set up such that square or rectangular elements were created for both models. The dimension and size of each model mesh is chosen in such a way that the reinforcements in each model are at the same locations inside the beam, as shown in Figure 2.10. The longitudinal mesh size is set to 0.01 m. No mesh of the reinforcement is needed because individual elements are created in the modelling through the nodes created by the mesh of the concrete volume in Model A, or by assigning the base element for Model B.

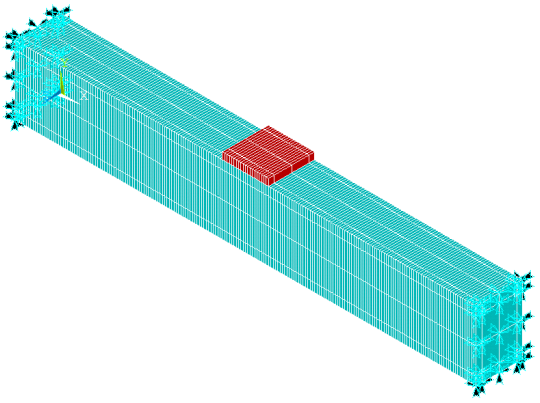

Figure 2.8: RC beam model (A) using LINK180 elements with supporting load plate and fixed boundaries.

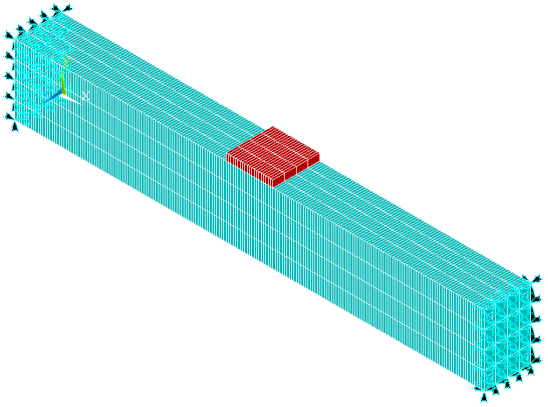

Figure 2.9: RC beam model (B) using REINF264 elements with supporting load plate and fixed boundaries.

The size and the mesh of the steel plate should be consistent with the nodes in the concrete portion of both models. The steel plate dimensions were chosen as 200×200×30 mm, and it is positioned in the middle of the beam. The coincident nodes between the concrete and the plate need to be merged. Furthermore, displacement boundary conditions are needed to constrain the model to get a solution. The beam was modelled with fully fixed constraints. As a result, nodes at each end of the beam are constrained as a fixed support by setting the displacements UX, UY and UZ to zero.

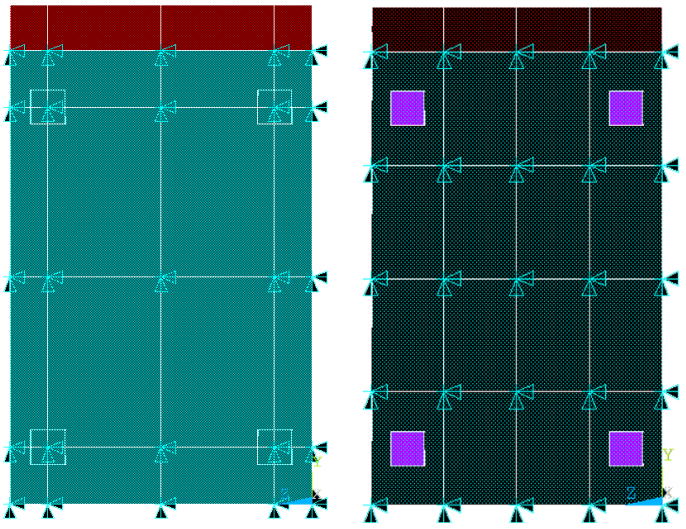

Figure 2.10: RC beam model cross-section using LINK180 (left) and REINF264 (right) elements with supporting load plate on top surface and fixed boundaries in ANSYS.

## 2.3 Finite Element modelling of prestressed RC beams using embedded reinforcements

In the majority of the literature, concrete is modelled using SOLID65 elements, and the steel reinforcements and prestressed tendon represented via LINK8 or LINK180. This approach requires the coupling between the linked reinforcements and nearby concrete element nodes for the transfer of the prestress. However, in this study, steel rebars are modelled via REINF264 elements as embedded reinforcements to ensure the transfer of the prestress effect from steel reinforcement to the surrounding concrete with no use of coupling elements. Similarly to other studies, the prestress effect will be modelled via an initial strain in the tendon elements, corresponding to tendon tensile forces, in a preliminary load stage. The initial strain value will be calculated based on steel reinforcement material properties and the prestress force applied. Then, this value is defined for the bottom layer reinforcement before any further application and analysis takes place in ANSYS.

Saiidi et al. (1994) investigated the prestress force effect on the natural frequencies of vibration of concrete bridges. A lab experiment was performed to measure changes in dynamic modal properties by adjusting the prestress forces applied to the test structure. The simply supported beam was reinforced longitudinally and in the transverse direction. Using the Fast Fourier Transformation technique (FFT), the first two frequencies of the bending mode were obtained for each in-situ prestress-force case as listed in Table 2.4. The listed frequencies are the averaged values.

The frequencies found experimentally by Saiidi et al. (1994) were compared to finite analysis results using ANSYS. A finite element dynamic analysis using ANSYS of the Saiidi beam was conducted by Li and Zhang (2011). Saiidi's beam was modelled in FE using SOLID65 element for concrete. The LINK8 element was used to simulate regular reinforcing steel and the LINK10 element was employed to simulate the prestress wire, since it has the feature of uniaxial tension only. The applied prestressing force was introduced by an initial strain value, and transfer to the prestressing force from prestressed wire to concrete is achieved by coupling elements. The predicted frequencies are listed in Table 2.4.

Here, the prestressed RC section is a replica of the section tested in Saiidi et al. (1994) and shown in Figure 2.11. The beam is 3.66 m long with four steel non-prestressed reinforcements of 9.525 mm diameter at each corner. In addition, a prestressed strand is located in the middle of the cross section with a diameter of 12.7 mm. This strand is prestressed via an initial strain value in ANSYS corresponding to the prestress force defined in Saiidi et al. (1994). The El Masri model does not contain stirrups, but the Saiidi beam model included 12 stirrups. The total mass of these stirrups is very small compared to the total mass of the structure. Therefore, no significant effect will result on the dynamic performance of the beam without stirrups. The length of the element was set to 0.01 m. The beam is modelled as simply supported at both ends. The material properties for concrete and steel reinforcement are shown in Table 2.2.

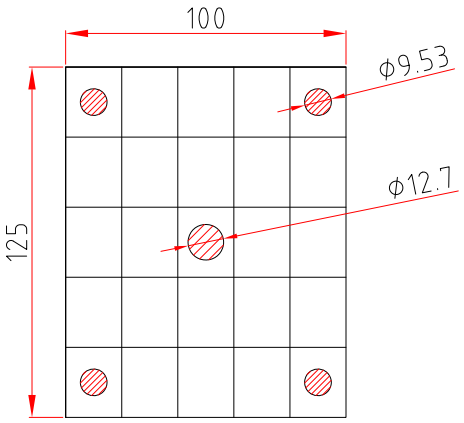


Figure 2.11: Prestressed RC beam model cross section with details of embedded steel reinforcements (mm).

| **Material properties** | **Concrete** | **Steel** |
|---|---|---|
| Young Modulus $E$ (Pa) | $21.52\times10^9$ | $200\times10^9$ |
| Poisson ratio $\upsilon$ | 0.18 | 0.3 |
| Density $\rho$ (kg/m$^3$) | 2400 | 7850 |

Table 2.2: Material properties for concrete and steel.

## 2.4 Nonlinear static analysis of RC beams

The two approaches using linked and embedded reinforcements are compared under static loading through nonlinear analysis in ANSYS. The force P applied at the steel plate is located across the entire centreline of the plate with a maximum value of 100 kN.

The Solution Controls command dictates the use of a non-linear solution for the finite element model. The Analysis Option defines the use of static analysis with small displacement. For the Time control, the automatic stepped option was chosen with a maximum of 1000 substeps and a minimum of one substep calculation. Results were output at every substep. The Newton-Raphson method of analysis was applied by the FE solver to compute the nonlinear response. The application of the loads up to failure was done incrementally, as required by the Newton-Raphson procedure. After the analysis was completed, the deflection of the mid bottom node of the beam was plotted against the load increment for both models.

As illustrated in Figure 2.12, the deflection due the load P for Models A and B are almost identical up to a load of approximately 40 kN. Above this value, the two deflection curves start to deviate, and the deflection of Model B is slightly smaller than Model A. At a higher load, the mesh of the cross section becomes a crucial factor. The cross section meshes are not exactly the same; it is coarser for Model A. For this reason, one might expect that at higher load values the deflection between the models are not as close as it was for lower loads. Despite this behaviour, the differences between the two model deflections are not too significant at high loads, and under small linearised dynamic response they should be able to be considered as equivalent representations. This is to be investigated in the next section.

## 2.5 Linear dynamic analysis of RC and prestressed RC beams

### RC beams

The two approaches, using linked and embedded reinforcements, were compared for dynamic mode calculations through linear analysis in ANSYS. For this analysis, the two beams were modelled in the same manner as before. Block Lanczos was selected for the full mode extraction method, and the number of modes extracted was set to 50. The natural frequency values were then plotted for each model, as shown in Figure 2.13. From visual inspection of this graph, one can observe that the natural frequencies for both models using either LINK180 or REINF264 as the reinforcement correlate well. As

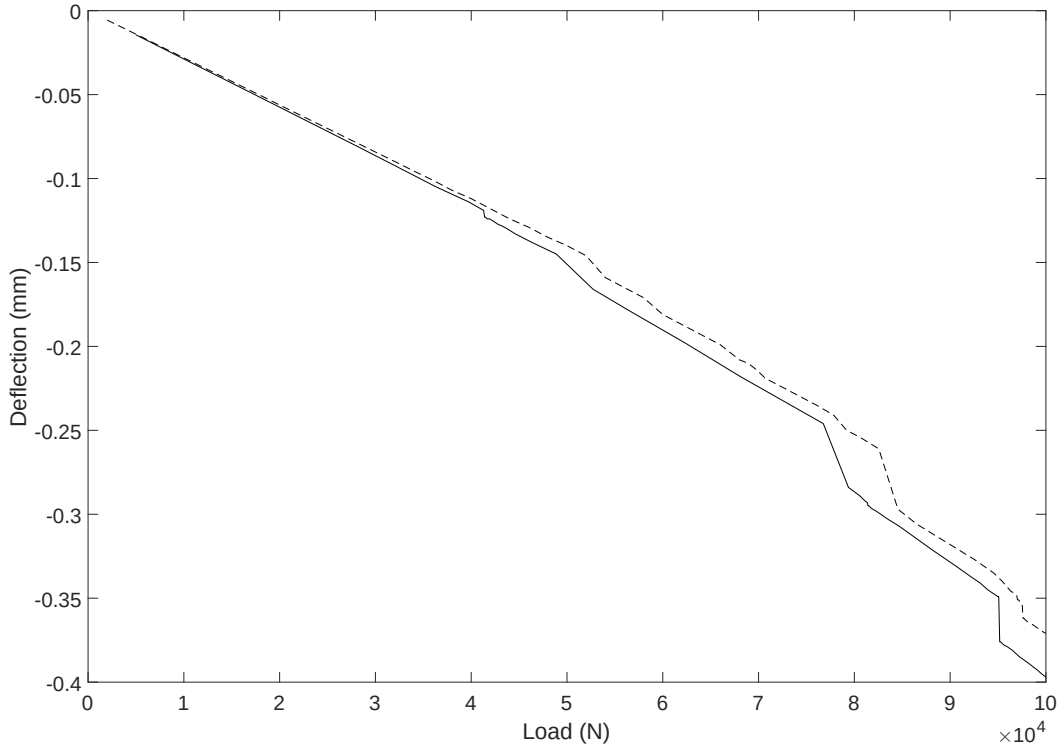


Figure 2.12: Deflection versus load applied midspan for a fixed RC beam when the nonlinear static solver is applied.

Two alternative representations of the reinforcements were used respectively: LINK180 (—) and REINF264 (- - -) elements in ANSYS (2013).

a result, one would expect similar dynamic behaviour for both model representations under small loads.

Hence, from both analyses it was decided that the RC model with embedded reinforcement would be employed in this project due to several advantages. First, the embedded rebars model requires a less fine mesh, since they are assigned in the concrete solid element. Therefore, the total number of degrees of freedom is minimised as well as the time required for analysis, calculations and extraction of the results. Secondly, since the reinforcement bar is embedded inside the solid element, no slip effect needs to be considered and full bond between the two materials is assured. Subsequently, no additional COMBIN elements need to be created between the steel rebars and the solid concrete at shared nodes, as are recommended when modelling with LINK elements in order to ensure no slip effect between the two materials.

### Prestressed RC beams

Up to this point the reinforcements were considered unstressed. The Block Lanczos method was selected for a full mode extraction in order to update the model matrices with the prestress effect. At each step, the initial strain inside the reinforcements was modified with respect to the change in the prestressed force. The strain value is the

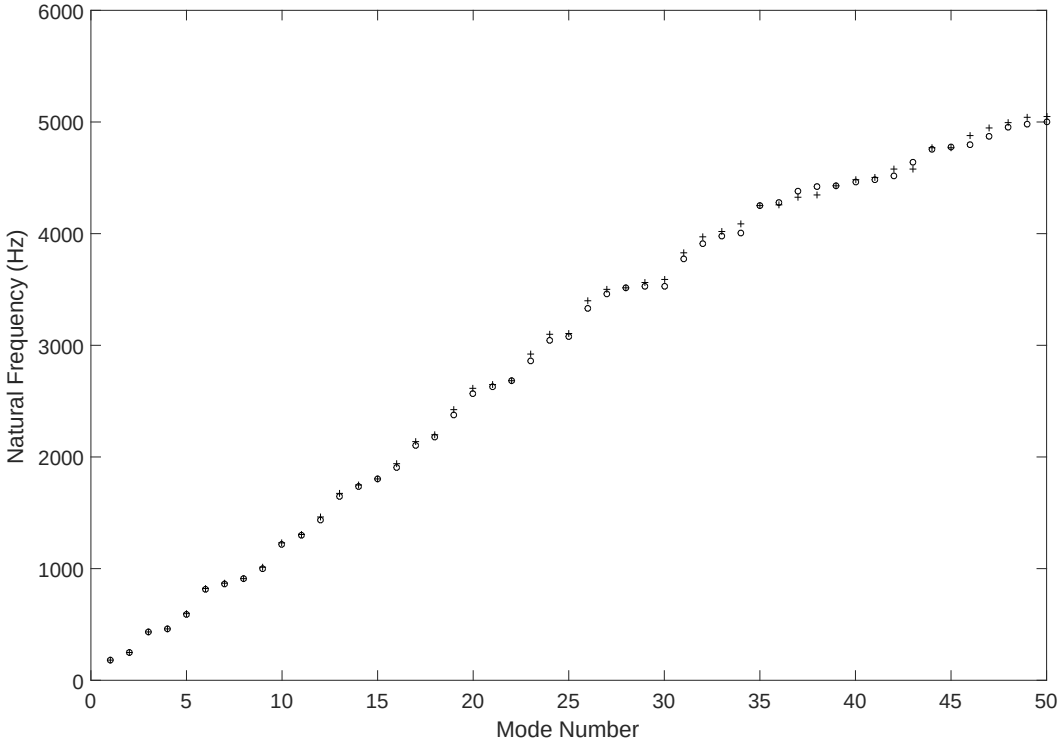


Figure 2.13: Natural frequencies of a fixed RC beam.
LINK180 (○), REINF264 (+).

ratio of the stress value resulting from the prestressed force on the cross sectional area of the strand over the Young's Modulus of steel $E_s$. The values of initial strain for each step are listed in Table 2.3. The linear dynamic analysis is repeated at each step and the first two frequencies of the bending modes were recorded.

| **Load case** | **Prestressed force (kN)** | **Initial strain values** |
|---|---|---|
| 1 | 0 | 0 |
| 2 | 15.71 | $6.04\times10^{-4}$ |
| 3 | 27.05 | $1.04\times10^{-3}$ |
| 4 | 36.49 | $1.40\times10^{-3}$ |
| 5 | 57.25 | $2.20\times10^{-3}$ |
| 6 | 91.26 | $3.51\times10^{-3}$ |
| 7 | 121.46 | $4.67\times10^{-3}$ |
| 8 | 130.91 | $5.04\times10^{-3}$ |
| 9 | 132.8 | $5.11\times10^{-3}$ |

Table 2.3: Initial strain values with respect to the prestressed force.

The first two bending natural frequencies were extracted from ANSYS at each prestressing force listed in Table 2.4. The percentage differences in the natural frequencies of Li and Zhang (2011) and this current thesis (El Masri results) versus the experimentally determined values by Saiidi et al. (1994) are presented in Table 2.5.

| In situ prestress force (kN) | Experimental frequency | Saiidi et al. (1994) | FE model frequency | Li and Zhang (2011) | FE model frequency | El Masri |
|---|---|---|---|---|---|---|
| | Mode 1 | Mode 2 | Mode 1 | Mode 2 | Mode 1 | Mode 2 |
| 0 | 11.41 | 43.99 | 11.674 | 43.990 | 11.978 | 47.682 |
| 15.71 | 12.09 | 44.11 | 12.526 | 49.213 | 12.316 | 48.024 |
| 27.05 | 13.47 | 44.89 | 13.059 | 51.306 | 12.557 | 48.273 |
| 36.49 | 12.89 | 44.69 | 13.428 | 52.754 | 12.751 | 48.475 |
| 57.25 | 13.63 | 45.62 | 14.050 | 55.193 | 13.172 | 48.923 |
| 91.26 | 14.72 | 46.32 | 14.677 | 57.649 | 13.834 | 49.647 |
| 121.46 | 14.72 | 45.86 | 14.973 | 58.809 | 14.395 | 50.279 |
| 130.91 | 14.97 | 46.10 | 15.031 | 59.035 | 14.569 | 50.479 |
| 132.8 | 15.07 | 45.87 | 15.040 | 59.073 | 14.602 | 50.517 |

Table 2.4: Natural frequency comparison from different models, published results and the current thesis (El Masri) for a simply beam reported by Saiidi.

| **Case** | **% Difference, Li and Zhang (2011)** | | **% Difference, El Masri** | |
|---|---|---|---|---|
| | Mode 1 | Mode 2 | Mode 1 | Mode 2 |
| 1 | 2.3 | 0 | 5 | 8.4 |
| 2 | 3.6 | 11.6 | 1.9 | 8.9 |
| 3 | -3.1 | 14.3 | -6.8 | 7.5 |
| 4 | 4.2 | 18.0 | -1.1 | 8.5 |
| 5 | 3.1 | 21.0 | -3.4 | 7.2 |
| 6 | -0.3 | 24.5 | -6.0 | 7.2 |
| 7 | 1.7 | 28.2 | -2.2 | 9.6 |
| 8 | 0.4 | 28.1 | -2.7 | 9.5 |
| 9 | -0.2 | 28.8 | -3.1 | 10.1 |

Table 2.5: Percentage differences for the predicted natural frequencies in this study against Saiidi's experimental results.

Both Li's and the model herein show small differences compared to the experimental results by Saiidi et al. (1994). For the first bending mode natural frequency, Li's model produced a smaller error than El Masri. However, for the second bending mode natural frequency, El Masri showed significantly lower error than the Li model. In addition, one needs to confirm the transfer of the prestress effect from the steel reinforcement to the surrounding concrete. Using the LINK elements, this requirement is accomplished by coupling the shared nodes with the solid element. However, using the embedded reinforcement, the degrees of freedom and connectivity of the REINF264 element are identical to those of the base element that is the SOLID65 element, and therefore no coupling methods have to be applied. Subsequently, the prestressed RC model with REINF264 reinforcement was adopted for later use in this research.

## 2.6 Finite Element modelling of damping

Damping is one of the most important factors for the evaluation of the structural dynamic forced response. High damping means that the vibrational energy is dissipated in the material reducing the resonant vibration response. Thus, internal damping is an important property for structures. In this section, ways in which damping can be incorporated in finite element models are briefly presented.

Here, structural or hysteretic damping is considered. The general form of this stiffness proportional damping is given by Petyt (1990) for multi-degree of freedom system as

$$\mathbf{M}\ddot{\boldsymbol{q}} + \mathbf{K}[1 + i\eta]\boldsymbol{q} = \boldsymbol{f} \tag{2.9}$$

This form of damping can only be applied when the excitation is harmonic. The complex term $[1 + i\eta]$ is obtained by replacing Young's Modulus $E$ by a complex one $E(1 + i\eta)$ while deriving the element stiffness matrix, where $\eta$ is the material loss factor.

For simplicity purposes, a constant damping ratio will be used to specify an equivalent damping value which structural damping would produce for the model at resonance. In this thesis, the input constant damping ratio $\zeta$ is set to half the value of the loss factor $\eta$, and will be defined as an input in ANSYS using the DMPRAT command.

## 2.7 Conclusions

Since both RC models using linked and embedded reinforcement act similarly in either their static or dynamic behaviour, the model with embedded reinforcements will subsequently be employed in this thesis due to several advantages.

First, the model requires less nodes by using embedded rebars since they are built into the concrete solid element. Therefore, the number of total degrees of freedom compared to using linked elements will decrease as well as the analysis time and calculation computation. Second, since the reinforcement bar is embedded inside the solid element, no slip effect needs to be considered and a full bond between the two materials is guaranteed. Therefore, no additional COMBIN elements need to be created between the steel rebars and the concrete solid shared nodes, as is recommended when modelling with LINK elements to ensure no slip effect between the two materials. Third, for prestressed and post-tensioned RC model, one needs to confirm the transfer of the prestress effect from the steel reinforcement to the surrounding concrete. Using the LINK elements, this approach is accomplished by coupling the shared nodes with the solid element. However, using the embedded reinforcement, the degrees of freedom and connectivity of the REINF264 element are identical to those of the base element that is the SOLID65, and therefore no coupling methods need to be applied.

Furthermore, damping is one of the most important factors for the evaluation of the structural dynamic response. For simplicity purposes, a constant hysteretic loss factor is used. The associated value for concrete dissipation is selected via results published in the previous literature.

# Chapter 3

# Modelling of waves in RC beams

## 3.1 Introduction

Vibration based methods are popular to detect the damage remotely in RC structures. In this research, guided waves are employed to detect possible damage of the rebars in deep RC beams. In this chapter, deep RC beams are considered. Subsequently, for comparison the Timoshenko beam solutions are evaluated numerically for their corresponding dispersion relationships.

Due to the complex cross section of RC beams, the Timoshenko beam wave solution is not expected to be an accurate representation especially at high frequencies. As a result, another approach is needed. For this the Wave Finite Element (WFE) method is selected as it is well suited to identify the wave characteristics within the RC waveguide.

In this chapter, the formulation of the WFE method is presented. The complex cross section of the waveguide is initially modelled via an FE package as described in Chapter 2. Then, the dynamic stiffness matrix of a small length of the assumed periodic structure is evaluated using the extracted mass and stiffness matrices. The dynamic stiffness matrix can be rearranged to form a transfer matrix relating the forces and degrees of freedom at one end of the waveguide to the same quantities at the other end. By applying the periodicity condition, the free wave propagation characteristics are then obtained from the transfer matrix. In addition, causes of the numerical errors and ill conditioning are investigated and solutions to reduce these errors are suggested and implemented.

Finally, having established and obtained the WFE free wave solutions, one can consider calculation of the forced response. By applying a wave approach, the forced response is computed by determining the amplitudes of the directly excited waves, calculating the boundary reflection and subsequently superimposing the wave amplitudes at the response point in question.

## 3.2 Timoshenko beam and dispersion solutions

Euler-Bernoulli beam theory is based on the assumption that plane cross sections perpendicular to the beam axis remain plane and perpendicular to this axis even after deformation. This theory assumes that transverse shear strains are zero, and therefore it is valid only for thin beams undergoing small amplitude and relatively long wavelength bending. However, when dealing with deep beams, the effect of the transverse shear strain cannot be neglected. Timoshenko Beam theory is an extension of Euler-Bernoulli beam theory, where shear deformation and rotatory inertia are introduced and thus it is applicable for deep beams Wang (1995).

For an Euler-Bernoulli beam, the bending wave number (phase change per unit length in rad/m) is given by the following dispersion relationship Mace (1984)

$$k_b = \sqrt[4]{\frac{\rho A \omega^2}{EI}} = \frac{2\pi}{\lambda_b} \tag{3.1}$$

where $A$ is the cross-sectional area, $\rho$ is the density, $\omega$ is the angular frequency, $E$ is the Young's Modulus, $I$ is the second moment of area of the cross section and $\lambda_b$ is the free bending wavelength at this frequency. There are four solutions: two wavenumbers are strictly real, and the other two are strictly imaginary. The real wavenumbers are associated with the propagating waves, and the imaginary wavenumbers are associated with the near-field or evanescent waves that decay exponentially with distance from the boundary or a disturbance.

For a Timoshenko beam, the differential equation of motion is given by Mei and Mace (2005)

$$\rho A \frac{\partial^2 y(x,t)}{\partial^2 t} + EI \frac{\partial^4 y(x,t)}{\partial^4 x} - \rho I (1 + \frac{E}{\kappa G}) \frac{\partial^4 y(x,t)}{\partial^2 t \partial^2 x} + \frac{\rho^2 I}{\kappa G} \frac{\partial^4 y(x,t)}{\partial^2 t} = 0 \tag{3.2}$$

where $y(x,t)$ is the flexural deflection of the Timoshenko beam, $G$ is shear modulus, and $\kappa$ is a shear correction factor dependent upon the beam cross section. The solution of Equation 3.2 is written as

$$y(x,t) = (C_1 e^{-jk_1 x} + C_2 e^{jk_1 x} + C_3 e^{-jk_2 x} + C_4 e^{jk_2 x}) e^{j\omega t} \tag{3.3}$$

where $k_1$, $k_2$ are the wavenumbers and $\omega$ is angular frequency.

The corresponding dispersion relationship for the Timoshenko beam is given by

$$k^2 = \frac{1}{2EI} \left( \pm \sqrt{\left(\rho I - \frac{\rho EI}{\kappa G}\right)\omega^4 + 4\rho AEI\omega^2} + \rho I \left(1 + \frac{E}{\kappa G}\right)\omega^2 \right) \tag{3.4}$$

The solution of Equation 3.4 provides one pair of real wavenumbers that are related to propagating waves. The second pair is imaginary at low frequency and linked to

evanescent waves. The cut-on frequency is the frequency limit where the second pair become real and thus associated with propagating waves. This mode of transition at a cut-on frequency can be found by setting Equation 3.4 to zero, such as

$$\omega_c = \sqrt{\frac{\kappa GA}{\rho I}} \tag{3.5}$$

First, one considers a Timoshenko beam with the following dimensions and material properties: $\rho$ is equal to 2400 kg/m$^3$, the cross sectional area of the beam is of a height 0.3 m and width 0.2 m, $E$ is equal to $4 \times 10^{10}$ Pa and $L$ is the total length of beam of 2 m. The shear modulus $G$ is defined as $\frac{E}{2(1+\nu)}$ with $\nu$ as the Poisson ratio of 0.18. The shear correction factor $\kappa$ is defined using the cross section dimensions as in Gruttman and Wagner (2001). Then, Equation 3.4 is solved and the dispersion curve is plotted in Figure 3.1. One can notice the real wavenumber solution valid over all of the frequency range associated with the propagating wave. The evanescent wave starts cutting on at 4450 Hz, where its associated wavenumber becomes real.

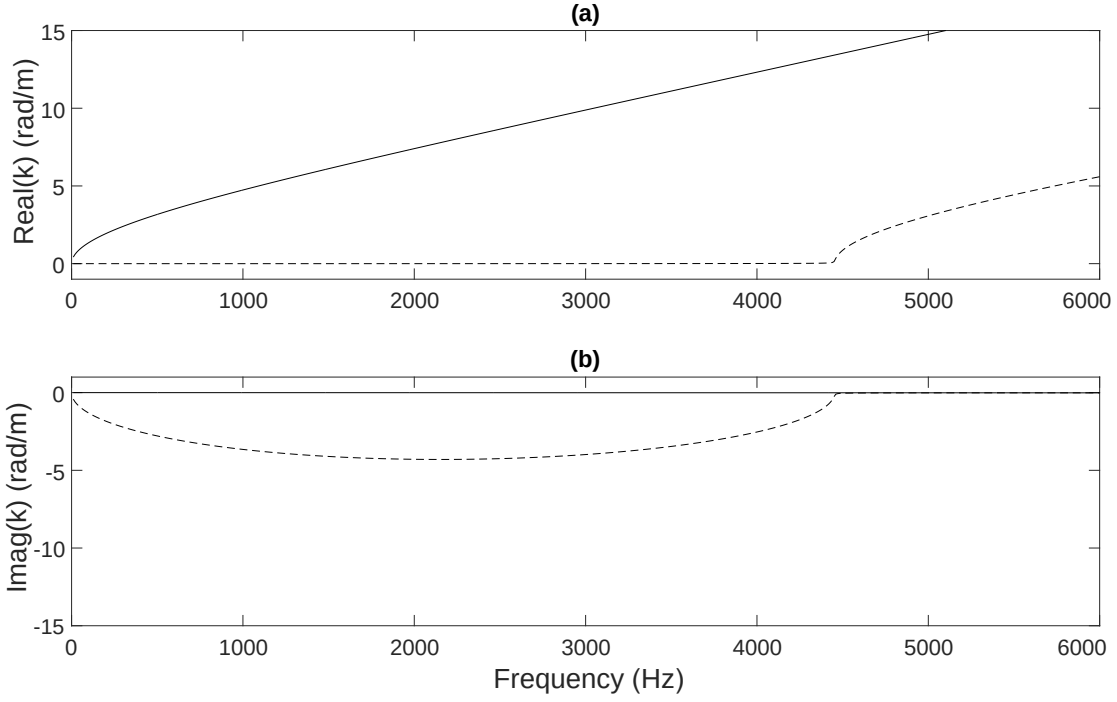


Figure 3.1: Dispersion curve of flexural waves in a Timoshenko beam.

(a): real wavenumber of propagating wave (—), real part of wavenumber of evanescent wave with cut-on frequency of 4450 Hz (- - -), (b): imaginary part of wavenumber of propagating wave (—), imaginary wavenumber of evanescent wave (- - -).

## 3.3 Formulation of the Wave Finite Element Method

In this section, the WFE method is reviewed. Causes of numerical errors and ill conditioning are investigated. Suggestions using concatenating elements and conditioning of the eigenvalue problem are presented to reduce these errors.

### 3.3.1 Transfer matrix

Consider a segment of short length $\Delta$ of a uniform waveguide as shown schematically in Figure 3.2. Commercial FE packages are used first to model this segment and to extract the required mass and stiffness matrices. The only constraint required in FE is that the nodes and their associate degrees of freedom (DOFs) are ordered identically on the left and right sides of the segment. The extracted matrices are employed to develop the associated dynamic stiffness matrix. Time harmonic motion $e^{i\omega t}$ is implicit throughout this thesis and suppressed for brevity. The equation of motion for the section by Duhamel et al. (2006) is

$$\mathbf{D}\boldsymbol{q} = \boldsymbol{f} \tag{3.6}$$

where

$$\mathbf{D} = \mathbf{K} + j\omega\mathbf{C} - \omega^2\mathbf{M} \tag{3.7}$$

$\boldsymbol{q}$ and $\boldsymbol{f}$ are $(2n \times 1)$ vectors of the nodal DOFs and forces respectively, while $n$ is the number of DOFs on each side of the segment. Here, only one segment in length is considered. Condensation of internal nodes is required as per Section 3.5 if they are present. $\mathbf{K}$, $\mathbf{C}$ and $\mathbf{M}$ are the stiffness, damping and mass matrices extracted from FE. $\mathbf{D}$ is the dynamic stiffness matrix and $\omega$ is the angular frequency. The dynamic stiffness matrix can be partitioned to reflect the influence of the left and right nodes of the segment. Equation 3.6 can be expressed as

$$\begin{bmatrix} \mathbf{D}_{LL} & \mathbf{D}_{LR} \\ \mathbf{D}_{RL} & \mathbf{D}_{RR} \end{bmatrix} \begin{bmatrix} \boldsymbol{q}_L \\ \boldsymbol{q}_R \end{bmatrix} = \begin{bmatrix} \boldsymbol{f}_L \\ \boldsymbol{f}_R \end{bmatrix} \tag{3.8}$$

The subscripts $L$ and $R$ are designated for the left and right sides of the segment.

Consider a series of segments of the waveguide as shown in Figure 3.2. Continuity of displacement and force equilibrium of adjacent sections give

$$\begin{bmatrix} \boldsymbol{q}_L^{N+1} \\ \boldsymbol{f}_L^{N+1} \end{bmatrix} = \begin{bmatrix} \boldsymbol{q}_R^{N} \\ -\boldsymbol{f}_R^{N} \end{bmatrix} \tag{3.9}$$

For each segment, the transfer matrix $\mathbf{T}$ can then be defined as

$$\mathbf{T} \begin{bmatrix} \boldsymbol{q}_L^{N} \\ \boldsymbol{f}_L^{N} \end{bmatrix} = \begin{bmatrix} \boldsymbol{q}_L^{N+1} \\ \boldsymbol{f}_L^{N+1} \end{bmatrix} \tag{3.10}$$

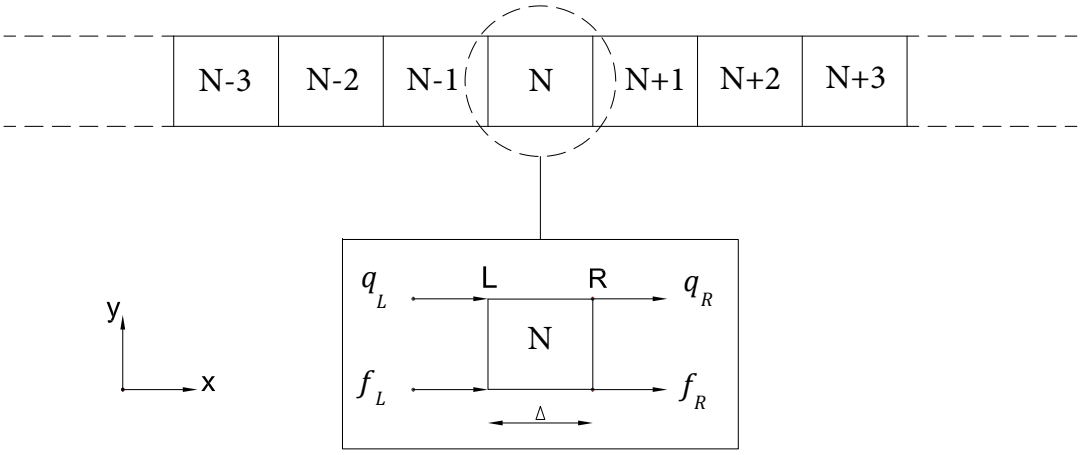


Figure 3.2: Structure with periodic elements: an N cell or segment of length $\Delta$ is shown with the internal forces and displacements vectors.

The periodic conditions for the displacements and the equilibrium condition at the junction of two successive elements are $\boldsymbol{q}_R = \lambda\ \boldsymbol{q}_L$ and $\boldsymbol{f}_R = -\lambda\ \boldsymbol{f}_L$ where the propagation constant

$$\lambda_j = e^{-ik_j\Delta} \tag{3.11}$$

relates the right and left displacements and forces where $k$ is the unknown wavenumber.

Equation 3.8 can be rearranged, and the free wave motion along the x-axis of the segment is therefore described in the form of an eigenvalue problem

$$\mathbf{T}\begin{Bmatrix}\boldsymbol{q}_L\\ \boldsymbol{f}_L\end{Bmatrix} = \lambda\begin{Bmatrix}\boldsymbol{q}_L\\ \boldsymbol{f}_L\end{Bmatrix} \tag{3.12}$$

Subsequently, one can define the transfer matrix $\mathbf{T}$ as

$$\mathbf{T} = \begin{bmatrix} -\boldsymbol{D}_{\boldsymbol{LR}}^{-1}\boldsymbol{D}_{\boldsymbol{LL}} & \boldsymbol{D}_{\boldsymbol{LR}}^{-1} \\ -\boldsymbol{D}_{\boldsymbol{RL}} + \boldsymbol{D}_{\boldsymbol{RR}}\boldsymbol{D}_{\boldsymbol{LR}}^{-1}\boldsymbol{D}_{\boldsymbol{LL}} & -\boldsymbol{D}_{\boldsymbol{RR}}\boldsymbol{D}_{\boldsymbol{LR}}^{-1} \end{bmatrix} \tag{3.13}$$

### 3.3.2 Wave solutions

The transfer matrix eigenvalue problem in Equation 3.13 is solved at each frequency step to yield the propagation constants $\lambda_j$ and the corresponding wavenumbers $k_j$ as in Equation 3.11. The wavenumber can be purely real, purely imaginary or complex, associated with a propagating, a nearfield (evanescent) or an oscillating decaying wave respectively.

In Zhong (1995), it has been shown that that the eigenvalues of the transfer matrix occur in reciprocal pairs as $\lambda_j^+$ and $\lambda_j^- = 1/\ \lambda_j^+$. The corresponding wavenumbers are $k_j^+$ and $k_j^- = -\ k_j^+$ as the positive and negative going waves, respectively. Furthermore,

$\mathbf{\Phi}_j^+$ and $\mathbf{\Phi}_j^-$ are the associated positive and negative going right eigenvectors, where each wavemode is divided into displacement $\boldsymbol{q}$ and force $\boldsymbol{f}$ sub-vectors, i.e.

$$\mathbf{\Phi}_j = \begin{Bmatrix} \mathbf{\Phi}_q \\ \mathbf{\Phi}_f \end{Bmatrix}_j \tag{3.14}$$

The positive-going waves are characterized by $\mid \lambda_j^+ \mid < 1$ and the negative going waves by $\mid \lambda_j^+ \mid > 1$. . However, for $\mid \lambda_j^+ \mid = 1$, the associated waves are considered positive-going if they fulfil the condition $Re\left\{\boldsymbol{f}_{\boldsymbol{L}}^{\boldsymbol{H}}\, \dot{\boldsymbol{q}}_{\boldsymbol{L}}\right\} = Re\left\{i\omega \boldsymbol{f}_{\boldsymbol{L}}^{\boldsymbol{H}}\, \boldsymbol{q}_{\boldsymbol{L}}\right\} < 0$. This means that if the wave is travelling in the positive direction, then its amplitude should be deceasing. If its amplitude remains constant, then time average power transmission in the positive direction occurs. In the case of evanescent waves that do not transfer energy, they contribute to the input response at discontinuities/boundaries by giving rise to propagating and evanescent waves(Mace (1984)).

Subsequently, the wave modes associated with the eigenvectors which are the solutions of Equation 3.13 are grouped into positive and negative going waves

$$\mathbf{\Phi}^+ = [\mathbf{\Phi}_1^+ \cdots \mathbf{\Phi}_n^+] \;\; ; \;\; \mathbf{\Phi}^- = [\mathbf{\Phi}_1^- \cdots \mathbf{\Phi}_n^-] \;\; ; \;\; \mathbf{\Phi} = [\mathbf{\Phi}^+ \quad \mathbf{\Phi}^-] \tag{3.15}$$

One can obtain the left eigenvectors of the transfer matrix $\mathbf{T}$ as well (Equation 3.12). They can be partitioned and grouped as follows

$$\mathbf{\Psi}_j = \begin{Bmatrix} \mathbf{\Psi}_{\boldsymbol{f}} & \mathbf{\Psi}_{\boldsymbol{q}} \end{Bmatrix}_j \;\; ; \;\; \mathbf{\Psi}^{\pm} = \begin{bmatrix} \mathbf{\Psi}_1^{\pm} \\ \cdots \\ \mathbf{\Psi}_n^{\pm} \end{bmatrix} \;\; ; \;\; \mathbf{\Psi} = \begin{bmatrix} \mathbf{\Psi}^+ \\ \mathbf{\Psi}^- \end{bmatrix} \tag{3.16}$$

The left and right wavemodes are orthogonal, and can be normalised so that

$$\mathbf{\Psi}^+\mathbf{\Phi}^+ = \mathbf{I} \;\; ; \;\; \mathbf{\Psi}^-\mathbf{\Phi}^- = \mathbf{I} \tag{3.17}$$

A useful consequence of this normalisation is to avoid inverting matrices that can lead to numerical problems (Waki et al.). This can be accomplished by premultiplying the intended matrix by the normalised right eigenvectors. This benefit is due to the property that

$$\mathbf{\Psi}\mathbf{T}\mathbf{\Phi} = diag(\lambda_j) \tag{3.18}$$

However, at higher frequencies, numerical errors can affect this orthogonality assumption. A simple orthogonality check was carried out to check this especially at higher frequency. This helped in identifying the number of retained wave modes at each frequency. Thus, only $m$ pairs of positive and negative going waves are retained based on a user-defined criterion at each frequency step considering least decaying evanescent waves. As a result, the size of the model will be smaller and the calculation time reduced.

The partitions of the left and right eigenvectors can be used to form the positive and negative going wave components as displacement and force matrices

$$\boldsymbol{\Phi}_q^+ = [\boldsymbol{\Phi}_{q,1}^+ \cdots \boldsymbol{\Phi}_{q,n}^+] \;\; ; \;\; \boldsymbol{\Psi}_q^+ = \begin{bmatrix} \boldsymbol{\Psi}_{q,1}^+ \\ \cdots \\ \boldsymbol{\Psi}_{q,n}^+ \end{bmatrix} \tag{3.19}$$

$$\boldsymbol{\Phi}_q^- = [\boldsymbol{\Phi}_{q,1}^- \cdots \boldsymbol{\Phi}_{q,n}^-] \;\; ; \;\; \boldsymbol{\Psi}_q^- = \begin{bmatrix} \boldsymbol{\Psi}_{q,1}^- \\ \cdots \\ \boldsymbol{\Psi}_{q,n}^- \end{bmatrix} \tag{3.20}$$

$$\boldsymbol{\Phi}_f^+ = [\boldsymbol{\Phi}_{f,1}^+ \cdots \boldsymbol{\Phi}_{f,n}^+] \;\; ; \;\; \boldsymbol{\Psi}_f^+ = \begin{bmatrix} \boldsymbol{\Psi}_{f,1}^+ \\ \cdots \\ \boldsymbol{\Psi}_{f,n}^+ \end{bmatrix} \tag{3.21}$$

$$\boldsymbol{\Phi}_f^- = [\boldsymbol{\Phi}_{f,1}^- \cdots \boldsymbol{\Phi}_{f,n}^-] \;\; ; \;\; \boldsymbol{\Psi}_f^- = \begin{bmatrix} \boldsymbol{\Psi}_{f,1}^- \\ \cdots \\ \boldsymbol{\Psi}_{f,n}^- \end{bmatrix} \tag{3.22}$$

The transformations between the physical domain, where the motion is described in terms of $\boldsymbol{q}$ and $\boldsymbol{f}$, and the wave domain, where the motion is described in terms of the wave amplitudes $\mathbf{a}^+$ and $\mathbf{a}^-$ travelling in the positive and negative directions respectively, are accomplished via

$$\begin{Bmatrix} \boldsymbol{q}_L \\ \boldsymbol{f}_L \end{Bmatrix} = \begin{bmatrix} \boldsymbol{\Phi}_q^+ & \boldsymbol{\Phi}_q^- \\ \boldsymbol{\Phi}_f^+ & \boldsymbol{\Phi}_f^- \end{bmatrix} \begin{Bmatrix} \mathbf{a}^+ \\ \mathbf{a}^- \end{Bmatrix} \tag{3.23}$$

Near a discontinuity, there will be evanescent waves created from an incident propagating wave. The inclusion of these wave modes is fundamental for scattering analysis.

## 3.4 Numerical errors in the WFE method

The WFE method suffers from some numerical and ill conditioning errors. They include FE discretization errors and errors due to round-off of the inertia terms. These issues and methods to reduce their effects are presented in this section.

### 3.4.1 Finite element discretization error

The FE discretization error becomes large when the phase change over the length of a segment $\Delta$ increases. There are always numerical errors since the FE modelling is an approximate representation of a system. In the usual application of FEA, 6 or more linear shape function elements are generally needed for each wavelength to represent the system vibrational motion accurately Waki et al. (2009b). The phase change over an

element is recommended to obey

$$| k\Delta | \leq 1 \;\; i.e. \;\; \frac{\Delta}{\lambda} \leq \pi \tag{3.24}$$

For small FE discretisation errors, this condition should be fulfilled both across the cross-section of a waveguide and in the direction of the wave propagation. On the other hand, FE discretisation errors depend as well on the shape function used in the formulation of an element. For instance, even for the same values of $k\Delta$, errors in the WFE results using a linear shape function for the displacement are higher than those using a cubic polynomial shape function.

Propagating waves carry power and it is important to predict propagating waves accurately. The length of the section $\Delta$ should therefore be determined to satisfy the condition in Equation 3.24 at the maximum frequency of interest, where the propagating wavenumber typically takes its maximum value. In this project, the length of the section $\Delta$ is chosen to satisfy this condition in order for all propagating wavenumbers to be accurately predicted.

On the other hand, numerical errors and inaccuracies can be also due to a poor discretisation of the cross-section rather than the choice of the segment length. This is particularly crucial at higher frequencies. Here, a convergence analysis can assist in finding an efficient mesh size for the cross section. A modal analysis was carried out on the cross-section for different mesh sizes and the associated natural frequencies of mode shapes above 10 KHz are listed in Table 3.1. One can notice that the values of the natural frequencies start to converge when the number of segments per one side is 4, whilst further refinement of the mesh does not make a significant difference to the values. Subsequently, the mesh size equal to four segments per side was selected for representing the RC cross sections.

| **Number of segments/one side** | **Frequency 1 (kHz)** | **Frequency 2 (kHz)** |
|---|---|---|
| 2 | 10.5 | 11.3 |
| 4 | 12.5 | 13.8 |
| 6 | 12.7 | 13.8 |
| 8 | 12.7 | 13.9 |

Table 3.1: Natural frequencies of the free-free RC cross section occurring after 10 kHz associated with different mesh size for a beam length of 2 m.

### 3.4.2 Round-off of the inertia terms

An upper bound for the length $\Delta$ of the element can be decided from the FE discretization error in Equation 3.24, considering the maximum wavenumber of interest in the frequency range analysed. On the other hand, the lower bound of $\Delta$ may be defined

considering round-off of the inertia terms. In the WFE method, the round-off error can be significant specifically when $\mathbf{D} = \mathbf{K}$ - $\omega^2$ $\mathbf{M}$ is evaluated numerically. For very small $\Delta$, and in particular at low frequencies, some effective significant figures of the inertia terms will be rounded-off since $\mathbf{K}$ might be very large compared to $\omega^2$ $\mathbf{M}$. The criterion for the smallest permissible value of $\Delta$ should therefore be determined to satisfy

$$log_{10}(\frac{\mathbf{K}_{ii}}{\omega^2 \mathbf{M}_{ii}}) < \alpha_{ii} \quad i = 1, \cdots, n \tag{3.25}$$

Using the double precision calculations for accurate results, $\alpha_{ii} < 16$ is chosen at the minimum frequency of interest.

### 3.4.3 Condensation of internal nodes in WFE

For periodic structures, the condensation of internal nodes is necessary for some applications to decrease the size of the structure and thus limit the size of the matrices which need to be processed. Another reason to apply this condensation in WFE at each chosen frequency is to reduce the errors related to the FE discretisation and the roundoff due to inertia. For uniform structural waveguides, the equation of motion of an element is given by

$$\mathbf{M}\ddot{\boldsymbol{q}} + \mathbf{C}\dot{\boldsymbol{q}} + \mathbf{K}\boldsymbol{q} = \boldsymbol{f} \tag{3.26}$$

Steady state time-harmonic motion is assumed. The DOFs are composed into sets corresponding to the $L$ (left), $R$ (right) and $I$ (interior) nodes. Assuming no external forces are being applied to the internal nodes, one has

$$\begin{bmatrix} \mathbf{D}_{LL} & \mathbf{D}_{LR} & \mathbf{D}_{LI} \\ \mathbf{D}_{RL} & \mathbf{D}_{RR} & \mathbf{D}_{RI} \\ \mathbf{D}_{IL} & \mathbf{D}_{IR} & \mathbf{D}_{II} \end{bmatrix} \begin{bmatrix} \boldsymbol{q}_L \\ \boldsymbol{q}_R \\ \boldsymbol{q}_I \end{bmatrix} = \begin{bmatrix} \boldsymbol{f}_L \\ \boldsymbol{f}_R \\ \boldsymbol{0} \end{bmatrix} \tag{3.27}$$

which can be written as

$$\begin{bmatrix} \mathbf{D}_{MM} & \mathbf{D}_{MI} \\ \mathbf{D}_{IM} & \mathbf{D}_{II} \end{bmatrix} \begin{bmatrix} \boldsymbol{q}_M \\ \boldsymbol{q}_I \end{bmatrix} = \begin{bmatrix} \boldsymbol{f}_M \\ \mathbf{0} \end{bmatrix} \;\; ; \;\; \boldsymbol{q}_M = \begin{bmatrix} \boldsymbol{q}_L \\ \boldsymbol{q}_R \end{bmatrix} \;\; and \;\; \boldsymbol{f}_M = \begin{bmatrix} \boldsymbol{f}_L \\ \boldsymbol{f}_R \end{bmatrix} \tag{3.28}$$

where the subscript $M$ is denoted by master nodes (Left and Right). Using the second row of Equation 3.28, one can write

$$\begin{bmatrix} \boldsymbol{q}_M \\ \boldsymbol{q}_I \end{bmatrix} = \begin{bmatrix} \boldsymbol{I} \\ \mathbf{D}_{II}^{-1}\mathbf{D}_{IM} \end{bmatrix} \boldsymbol{q}_M = \boldsymbol{R}\boldsymbol{q}_M \tag{3.29}$$

where $\boldsymbol{I}$ is the identity matrix, and by using the $\boldsymbol{R}$ matrix, Equation 3.27 becomes

$$\boldsymbol{R}^T \begin{bmatrix} \mathbf{D}_{MM} & \mathbf{D}_{MI} \\ \mathbf{D}_{IM} & \mathbf{D}_{II} \end{bmatrix} \boldsymbol{R}\boldsymbol{q}_M = \boldsymbol{f}_M \tag{3.30}$$

This equation is essential to derive the reduced mass, stiffness and damping matrices by using them instead of $\mathbf{D}$ in the transfer matrix such that the interior nodes are eliminated. After removing the internal nodes, Equation 3.27 becomes like Equation 3.8 which is frequency dependent. For example, the reduced mass matrix is shown below as

$$\boldsymbol{R}^T\boldsymbol{M}\boldsymbol{R} = \boldsymbol{M}_{MM} - \boldsymbol{D}_{MI}\boldsymbol{D}_{II}^{-1}\boldsymbol{M}_{IM} - \boldsymbol{M}_{MI}\boldsymbol{D}_{II}^{-1}\boldsymbol{D}_{IM} + \boldsymbol{D}_{MI}\boldsymbol{D}_{II}^{-1}\boldsymbol{M}_{II}\boldsymbol{D}_{II}^{-1}\boldsymbol{D}_{IM} \quad (3.31)$$

## 3.5 Conditioning of the eigenvalue problem

Apart from FE discretisation errors and errors due to the round-off of inertia terms, ill-conditioning of the eigenvalue problem develops when using the transfer matrix $\mathbf{T}$ having formed the eigenvalue problem in Equation 3.12. Ill-conditioning arises when inverting the $\mathbf{D}_{LR}$ matrix. Therefore, methods for improving the conditioning of the eigenvalue problem are described in this section. In particular, Zhong′s method is introduced as the conditioned eigenvalue problem Zhong (1995). The method was used for better conditioning of the transfer matrix in different WFE applications such as in Waki et al. (2009b) and (2009a).

Zhong′s method is applied to formulate the eigenvalue problem represented via the transfer matrix $\mathbf{T}$. The application of singular value decomposition (SVD) is proposed to determine the eigenvectors more accurately and to avoid inverting the $\mathbf{D}_{LR}$ matrix.

The method starts from a reformulation of Equation 3.10 into the relationships for the displacement vectors alone. After some matrix operations using the periodicity condition, the eigenvalue problem becomes

$$\begin{bmatrix} \mathbf{0} & \mathbf{D}_{LR} \\ -\mathbf{D}_{RL} & \mathbf{0} \end{bmatrix} \begin{bmatrix} \boldsymbol{\Phi}_{q,i} \\ \boldsymbol{\lambda}\boldsymbol{\Phi}_{q,i} \end{bmatrix} = (\lambda_i + \frac{1}{\lambda_i}) \begin{bmatrix} (\mathbf{D}_{LR} - \mathbf{D}_{RL}) & -(\mathbf{D}_{LL} + \mathbf{D}_{RR}) \\ (\mathbf{D}_{LL} + \mathbf{D}_{RR}) & (\mathbf{D}_{LR} - \mathbf{D}_{RL}) \end{bmatrix} \begin{bmatrix} \boldsymbol{\Phi}_{q,i} \\ \boldsymbol{\lambda}\boldsymbol{\Phi}_{q,i} \end{bmatrix} \quad (3.32)$$

This eigenvalue problem has repeated eigenvalues of $\lambda + 1/\lambda$. In addition, the repeated eigenvectors are considered as a linear combination of the original displacement eigenvectors given by Equation 3.14. Then, the force eigenvectors can be found from the first row of Equation 3.8 together with Equation 3.11

$$\boldsymbol{\Phi}_{f,i} = (\mathbf{D}_{LL} + \boldsymbol{\lambda_i}\mathbf{D}_{LR})\boldsymbol{\Phi}_{q,i} \quad (3.33)$$

Numerical issues concerning the determination of the eigenvectors and an application of singular value decomposition to improve numerical difficulties are described in detail by Waki et al. (2009b).

## 3.6 Forced response via WFE

In this section, the forced response is formulated using the wave approach applied to the WFE solutions. First, the amplitudes of directly excited waves are computed. Then, the reflection coefficient matrix is defined for boundaries. Subsequently, the total wave amplitude is computed using the result of wave superposition at a specific point in the waveguide.

Considering first an infinite waveguide, the external force in applied and decomposed in the physical domain. By applying continuity for the displacements and equilibrium of forces, one can write (see Appendix A for details)

$$\begin{bmatrix} \boldsymbol{\Phi}_q^+ & -\boldsymbol{\Phi}_q^- \\ \boldsymbol{\Phi}_f^+ & -\boldsymbol{\Phi}_f^- \end{bmatrix} \begin{bmatrix} \mathbf{e}^+ \\ \mathbf{e}^- \end{bmatrix} = \begin{bmatrix} \mathbf{0} \\ \boldsymbol{f}_{ext} \end{bmatrix} \tag{3.34}$$

where $\mathbf{e}^+$ and $\mathbf{e}^-$ are column vectors of positive and negative going directly excited wave amplitudes, respectively. $\boldsymbol{f}_{ext}$ is the external force vector. By rearranging Equation 3.34, the directly excited wave amplitudes are defined by

$$\begin{bmatrix} \mathbf{e}^+ \\ \mathbf{e}^- \end{bmatrix} = \begin{bmatrix} \boldsymbol{\Phi}_q^+ & -\boldsymbol{\Phi}_q^- \\ \boldsymbol{\Phi}_f^+ & -\boldsymbol{\Phi}_f^- \end{bmatrix}^{-1} \begin{bmatrix} \mathbf{0} \\ \boldsymbol{f}_{ext} \end{bmatrix} \tag{3.35}$$

Due to matrix inversion, numerical errors related to ill conditioning occur. However, one can benefit from the orthogonality of the left and right eigenvectors of the transfer function as in Equation 3.18 to reduce these errors. By premultiplying Equation 3.34 by the left eigenvector matrix,

$$\begin{bmatrix} \boldsymbol{\Psi}_f^+ & -\boldsymbol{\Psi}_q^+ \\ \boldsymbol{\Psi}_f^- & -\boldsymbol{\Psi}_q^- \end{bmatrix} \begin{bmatrix} \boldsymbol{\Phi}_q^+ & -\boldsymbol{\Phi}_q^- \\ \boldsymbol{\Phi}_f^+ & -\boldsymbol{\Phi}_f^- \end{bmatrix} \begin{bmatrix} \mathbf{e}^+ \\ \mathbf{e}^- \end{bmatrix} = \begin{bmatrix} \boldsymbol{\Psi}_f^+ & -\boldsymbol{\Psi}_q^+ \\ \boldsymbol{\Psi}_f^- & -\boldsymbol{\Psi}_q^- \end{bmatrix} \begin{bmatrix} \mathbf{0} \\ \boldsymbol{f}_{ext} \end{bmatrix} \tag{3.36}$$

one can obtain

$$\begin{bmatrix} \boldsymbol{\Psi}^+\boldsymbol{\Phi}^+ & \mathbf{0} \\ \mathbf{0} & -\boldsymbol{\Psi}^-\boldsymbol{\Phi}^- \end{bmatrix} \begin{bmatrix} \mathbf{e}^+ \\ \mathbf{e}^- \end{bmatrix} = \begin{bmatrix} \boldsymbol{\Psi}_q^+ \boldsymbol{f}_{ext} \\ \boldsymbol{\Psi}_q^- \boldsymbol{f}_{ext} \end{bmatrix} \tag{3.37}$$

By applying the orthogonality relations in Equation 3.17 and 3.18, Equation 3.37 becomes

$$\mathbf{e}^+ = \boldsymbol{\Psi}_q^+ \boldsymbol{f}_{ext} \;\; ; \;\; \mathbf{e}^- = -\boldsymbol{\Psi}_q^- \boldsymbol{f}_{ext} \tag{3.38}$$

One can notice that Equation 3.38 does not require matrix inversion which results in reducing chances of numerical errors. In addition, $m$ pairs of positive and negative going waves are retained for which their imaginary wavenumbers are small. This due to the fact that rapidly decaying waves offer a small contribution to the total response.

In a finite waveguide, the waves are reflected at the boundaries. The boundary matrix $\mathbf{r}$ relates the wave change at the boundaries between the incident and reflected waves as

$$\mathbf{a}^- = \mathbf{r}\mathbf{a}^+ \tag{3.39}$$

where $\mathbf{a}^+$ and $\mathbf{a}^-$ are column vectors of incident and reflected wave amplitudes at boundary, respectively. In general, as shown in Harland et al. (2001), the boundary condition can be expressed as

$$\mathbf{A}\boldsymbol{f} + \mathbf{B}\boldsymbol{q} = \mathbf{0} \tag{3.40}$$

where $\mathbf{A}$ and $\mathbf{B}$ are frequency dependent matrices that involve the stiffness, damping, etc. The displacement $\boldsymbol{q}$ and force $\boldsymbol{f}$ vectors can be related to wave amplitudes as in Equation 3.23. As a result, the boundary matrix is refined as

$$\mathbf{r} = -(\mathbf{A}\boldsymbol{\Phi}_{\boldsymbol{f}}^- + \mathbf{B}\boldsymbol{\Phi}_{\boldsymbol{q}}^-)^{-1}(\mathbf{A}\boldsymbol{\Phi}_{\boldsymbol{f}}^+ + \mathbf{B}\boldsymbol{\Phi}_{\boldsymbol{q}}^+) \tag{3.41}$$

The diagonal of the boundary matrix $\mathbf{r}$ represents the reflection coefficients relating the incident and reflected waves at the boundary. However, the off-diagonal terms in $\mathbf{r}$ represent wave mode conversion. In other words, when one wave type of the incident wave is scattered to another wave type. Subsequently, if $\mathbf{r}$ is a diagonal matrix, the incident wave at a boundary gets reflected with no wave mode conversion. In addition, when only $m$ waves are retained for the solution, a pseudo matrix inverse is applied in Equation 3.41.

After travelling a distance $x$ in the waveguide, the propagation matrix $\boldsymbol{\tau}$ relates the wave amplitudes as

$$\boldsymbol{\tau}(\boldsymbol{x}) = \boldsymbol{diag}(\boldsymbol{e}^{-\boldsymbol{i}\boldsymbol{k}_1^+\boldsymbol{x}}, \cdots, \boldsymbol{e}^{-\boldsymbol{i}\boldsymbol{k}_m^+\boldsymbol{x}}) \tag{3.42}$$

To ensure good conditioning, only $m$ waves are retained for the solution where the elements corresponding to high-order waves being nearly zero in the $\boldsymbol{\tau}(x)$ matrix. Subsequently, the magnitudes of the elements of the propagation matrix $\boldsymbol{\tau}(x)$ are $\leq 1$.

To compute the forced response at any point in the waveguide, wave superposition is considered. For a finite waveguide illustrated in Figure 3.3, the wave amplitudes $\mathbf{a}^+$ and $\mathbf{a}^-$ are the result of the directly excited waves $\mathbf{e}^+$ and $\mathbf{e}^-$, in addition to travelling waves from left and right side $\mathbf{g}^+$ and $\mathbf{g}^-$ as

$$\mathbf{a}^+ = \mathbf{e}^+ + \mathbf{g}^+ \;\; ; \;\; \mathbf{g}^- = \mathbf{e}^- + \mathbf{a}^- \tag{3.43}$$

By applying wave propagation and boundary matrices, one can express the $\mathbf{a}^+$ waves as

$$\mathbf{a}^+ = \mathbf{e}^+ + \boldsymbol{\tau}(x_e)\mathbf{r}_L\boldsymbol{\tau}(x_e)\mathbf{g}^- \tag{3.44}$$

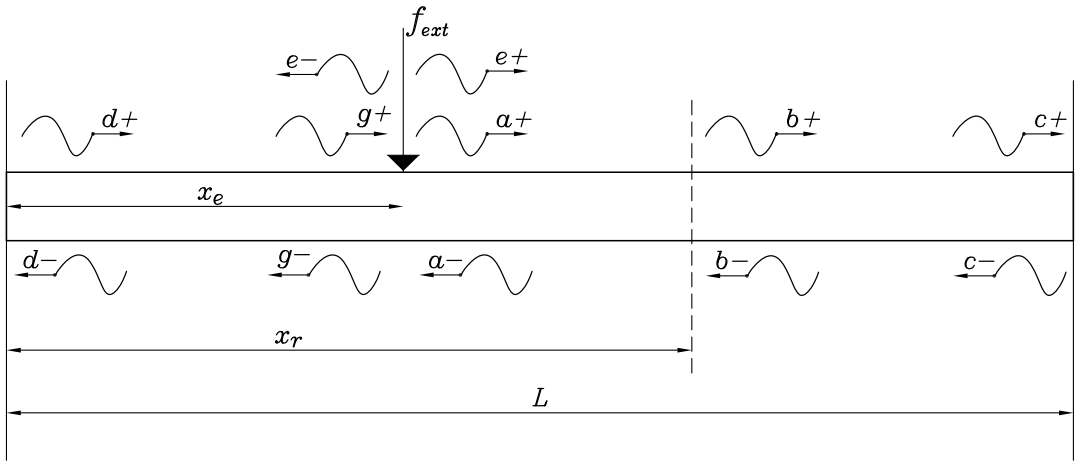


Figure 3.3: Wave amplitudes in finite structure.

By using Equation 3.43 and rearranging Equation 3.44,

$$\mathbf{a}^+ = \mathbf{e}^+ + \boldsymbol{\tau}(x_e)\mathbf{r}_L\boldsymbol{\tau}(L)\mathbf{r}_R\boldsymbol{\tau}(L-x_e)\mathbf{a}^+ + \boldsymbol{\tau}(x_e)\mathbf{r}_L\boldsymbol{\tau}(x_e)\mathbf{e}^- \tag{3.45}$$

then,

$$\mathbf{a}^+ = \{\mathbf{I} - \boldsymbol{\tau}(x_e)\mathbf{r}_L\boldsymbol{\tau}(L)\mathbf{r}_R\boldsymbol{\tau}(L-x_e)\}^{-1}\{\mathbf{e}^+ + \boldsymbol{\tau}(x_e)\mathbf{r}_L\boldsymbol{\tau}(x_e)\mathbf{e}^-\} \tag{3.46}$$

where $L$ is the total length of the waveguide, and $x_e$ is the position of the excitation force. In addition, $\mathbf{r}_L$ and $\mathbf{r}_R$ are the boundary matrices of the left and right boundary, respectively. Next, the negative going wave amplitude $\mathbf{a}^-$ can be related to the positive going wave $\mathbf{a}^+$ as

$$\mathbf{a}^- = \boldsymbol{\tau}(L-x_e)\mathbf{r}_R\boldsymbol{\tau}(L-x_e)\mathbf{a}^+ \tag{3.47}$$

Then, the transfer response can be obtained at position $x_r$ by

$$\mathbf{b}^+ = \boldsymbol{\tau}(x_r - x_e)\mathbf{a}^+ \tag{3.48}$$

and

$$\mathbf{b}^- = \boldsymbol{\tau}(L-x_r)\mathbf{r}_R\boldsymbol{\tau}(L-x_r)\mathbf{b}^+ \tag{3.49}$$

Finally, the total displacement at a point $x_r$ of the waveguide is expressed as

$$\mathbf{q} = \sum_{i=1}^{n}(\mathbf{b}_i^+\boldsymbol{\Phi}_{qi}^+ + \mathbf{b}_i^-\boldsymbol{\Phi}_{qi}^-) \tag{3.50}$$

## 3.7 Conclusions

In this chapter, the formulation of the WFE approach was presented. The method starts from the dynamic stiffness matrix of a short section of the waveguide that can be modelled using conventional FE. By applying the periodicity condition, the eigenvalue problem is formed from the transfer matrix of the rearranged elements in the dynamic stiffness matrix. In addition, causes of WFE numerical errors such as FE discretisation and the round-off of inertia terms errors were discussed. A solution to reduce ill-conditioning errors associated with inverting the $\mathbf{D}_{LR}$ matrix was also presented.

The forced response was presented using the wave approach via the WFE solution as nodal displacements and forces for an infinite waveguide. Then, the wave amplitudes in finite structures were identified by applying wave propagation and reflection coefficients of boundaries.

# Chapter 4

# Simulations of waves in RC beams

## 4.1 Introduction

The WFE formulation was introduced in the previous chapter. The method is now applied to RC waveguides to obtain the wave characteristics.

Reinforced concrete, prestressed and post-tensioned reinforced concrete segments are modelled via finite element. Then, the associated mass and stiffness matrices are extracted and processed via WFE to obtain the dynamic stiffness matrix for each model. Later, the eigenvalue problem based on the transfer matrix $\mathbf{T}$ is formed.

In order to track the calculated eigenvalues/eigenvectors at different frequencies, a Wave Assurance Criterion (WAC) is applied to the extracted eigenvectors. Next, the wavenumbers corresponding to waves in damaged and undamaged segments are evaluated and plotted in the form of dispersion curves. Damage is subsequently introduced as a diameter reduction of one rebar. Furthermore, the normalised wave mode shapes are plotted for undamaged waveguides.

Subsequently, the effects of the concrete properties and rebar diameter reduction on the computed dispersion relations are investigated. In addition, the WFE free wave solution is used to calculate the forced response in finite RC beams which is compared with conventional FE.

## 4.2 RC, prestressed and post-tensioned RC models

RC, prestressed and post-tensioned RC segments are first modelled in ANSYS before applying the WFE approach. The undamaged reinforced concrete section is modelled using 16 SOLID65 elements, with the dimensions and properties shown in Table 4.1.

The length $\Delta$ of the element is set equal to 0.01 m, the total number of DOFs $n$, is 150, and a hysteretic damping value equal to $\eta = 0.004$ is chosen for both models.

| **Material properties** | **Concrete** | **Steel** |
|---|---|---|
| Young Modulus E (Pa) | $40\times10^9$ | $200\times10^9$ |
| Poisson ratio $\nu$ | 0.18 | 0.3 |
| Density $\rho$ (kg/m$^3$) | 2400 | 7850 |

Table 4.1: Material properties of concrete and steel in FE.

The reinforcements are modelled via the embedded approach as described in Chapter 2 using REINF264 elements. The damaged reinforced concrete section is modelled in the same way as for the undamaged section except that the area of the damaged reinforced rebar at the right bottom corner is reduced to represent a loss of thickness due to corrosion. In this model, the corroded rebar is taken to have a diameter equivalent to a 36% reduction compared to the intact one. Both damaged and undamaged sections are shown in Figure 4.1.

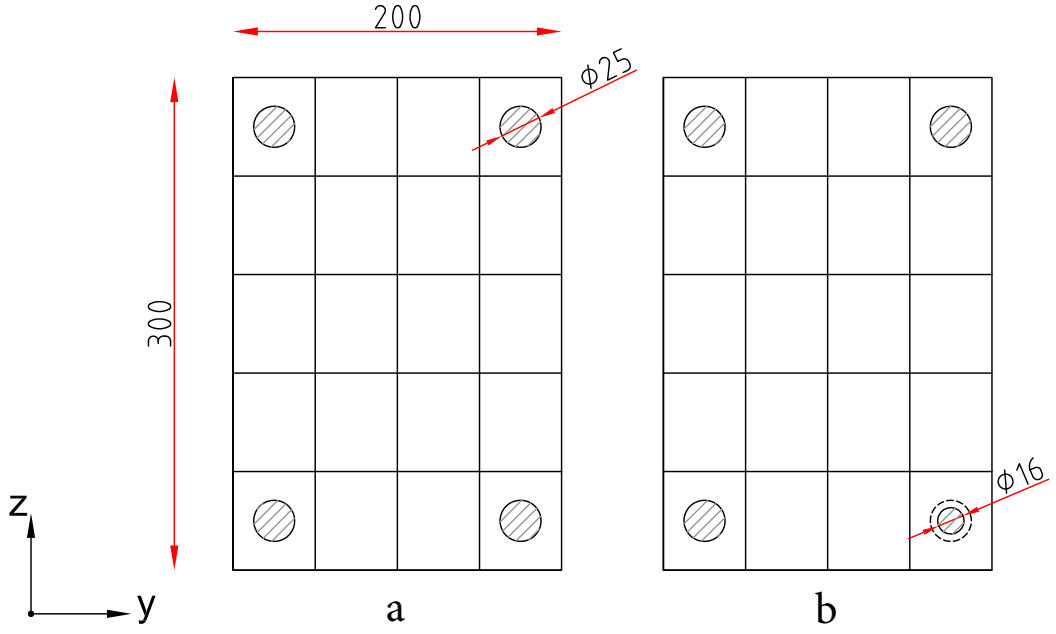


Figure 4.1: FE mesh of RC cross section: (a) undamaged and (b) damaged. Dimensions in mm.

The prestressed RC section is first modelled in ANSYS using SOLID65 elements for concrete and REINF264 elements for the embedded reinforcement as shown in Figure 4.2(a). The prestressing effect is modelled via an initial strain in the tendon elements, corresponding to tendon tensile forces in a preliminary load stage. The initial strain value is calculated based on the steel reinforcement material properties and the prestress force

applied. In this model, one can assume that the tensile prestress force of the steel reinforcement is equal to 70 percent of its ultimate tensile strength ($0.4 \times 10^9$ Pa). This force is used to prestress both the damaged and undamaged rebars. Thus the stress value used to calculate the initial strain for the damaged rebar is higher than that for the undamaged one, since the cross sectional area is smaller for the same amount of prestress force. Subsequently, $\varepsilon_1 = 0.0014$ and $\varepsilon_2 = 0.0036$ are the initial longitudinal strain values for the undamaged and damaged rebars respectively. In this model, the damaged reinforcement included the bottom right rebar. The RC section details for the damaged and undamaged prestress RC and material properties are similar to those of conventional RC model defined previously.

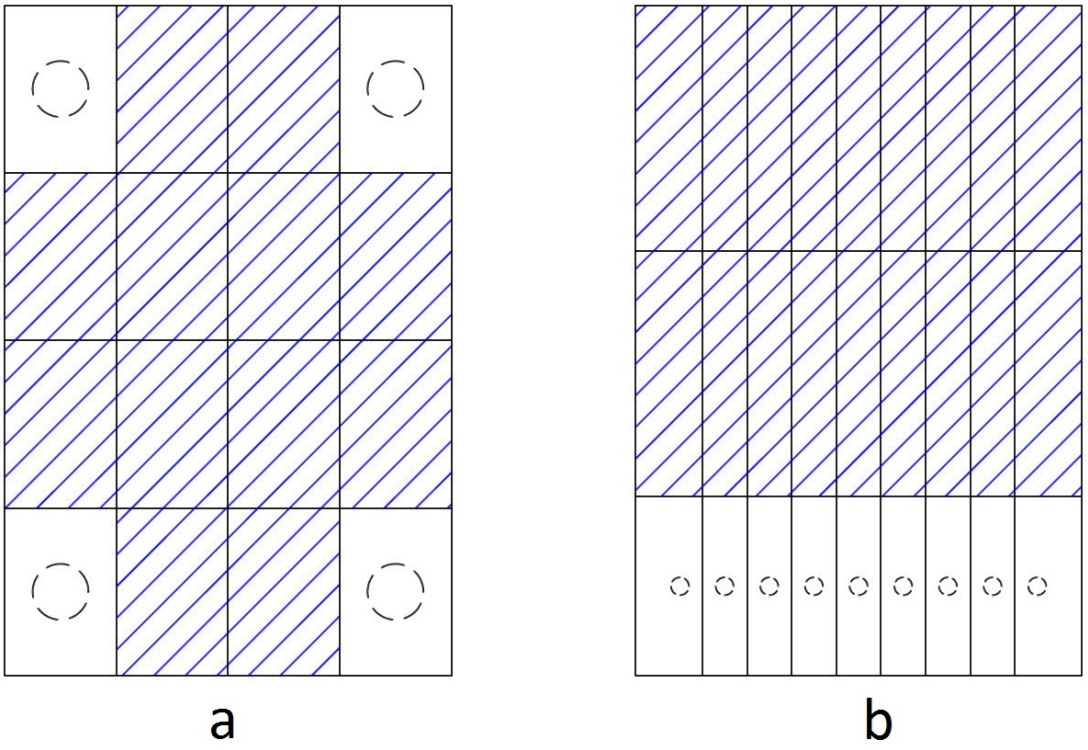


Figure 4.2: RC and prestressed RC section (a), post-tensioned RC section (b) with the surrounded concrete (patterned area).

In the case of the post-tensioned concrete segment, the model involves reinforcements as small diameter tendons placed in the bottom layer of concrete as in Figure 4.2(b). The undamaged reinforcement has a diameter representing an 8 mm steel bar. Similarly, for the RC section, the damaged rebar in post-tensioned model is reduced by 36% of its area compared to the undamaged one. In addition, $\varepsilon_1 = 0.0014$ and $\varepsilon_2 = 0.0023$ are the initial strain values for the undamaged and damaged rebars respectively. In this model, the damaged reinforcements were included in all of the bottom layer reinforcement where the strain values were assigned. The length $\Delta$ of element is equal to 0.01 m, the total number of DOFs $n$ is 240, and hysteretic damping value is $\eta = 0.004$ is chosen for both models. The difference between the models is shown in Figure 4.2 where the surrounding

concrete is highlighted as the patterned area. One would expect some differences in the dynamic behaviour of the post-tensioned RC since the majority of concrete is separated from the bottom layer of the reinforcement.

The mass and stiffness matrices were extracted using the ANSYS software for both the damaged and undamaged sections, and then post-processed using WFE. There are 150 different wavenumbers in accordance with the number of DOFs for RC and prestressed RC, and there are 240 different wavenumbers in accordance with the post-tensioned RC model. However, most of these wavenumbers have a significant imaginary part corresponding to highly attenuated waves, and therefore need to be eliminated. In these models, only the wave modes associated with $\mid Im\ (k\ \Delta) \mid \leq 0.3$ are retained at each frequency step. This corresponds to an attenuation of 10 dB along the element length in the propagating direction.

## 4.3 Wave mode tracking

The eigenvalues and associated eigenvectors were calculated at each frequency step. However, a new problem arises to ensure and compare the correlation of the calculated eigenvalues/eigenvectors between frequencies.

To solve this issue, as the eigenvalue ordering was not necessarily consistent at different frequencies, the Wave Assurance Criterion (WAC) presented in Houillon et al. (2005) was used to order of the eigenvalues/eigenvectors between each small increment in frequency. This takes advantage of the fact that the eigenvectors capture a spatial similarity of the other corresponding eigenvector at the previous frequency. The WAC value is given by

$$\mathbf{WAC}(\omega_j, \omega_{j+1}) = \frac{(\Phi_j^H \Phi_{j+1}^H)^2}{(\Phi_j^H \Phi_j)(\Phi_{j+1}^H \Phi_{j+1})} \tag{4.1}$$

where $\omega_j$ and $\omega_{j+1}$ are the frequency of the $j$th and $j$+1 steps, and $\Phi_j$ is the eigenvector related with the $j$th step.

The WAC equation uses two consecutive eigenvectors to give a value between 0 and 1. Based on this, the closer the value of WAC is to 1, the more the consecutive pair of eigenvectors are related to the same wave mode. Using this criterion, one can choose if the calculated eigenvectors are associated with the same wave mode or not. By choosing only the positive travelling wavenumbers, the WAC configuration is plotted for two values of frequency of the associated eigenvectors at $f_1 = 1000$ Hz and $f_2 = 2000$ Hz as in Figure 4.3 for an RC beam.

The WAC plot demonstrates the correlation of the related eigenvectors, that is shown by the strength of the values plotted on the diagonal of the WAC with values equal or very close to 1. The corresponding eigenvectors belong to the same type of wave. This is

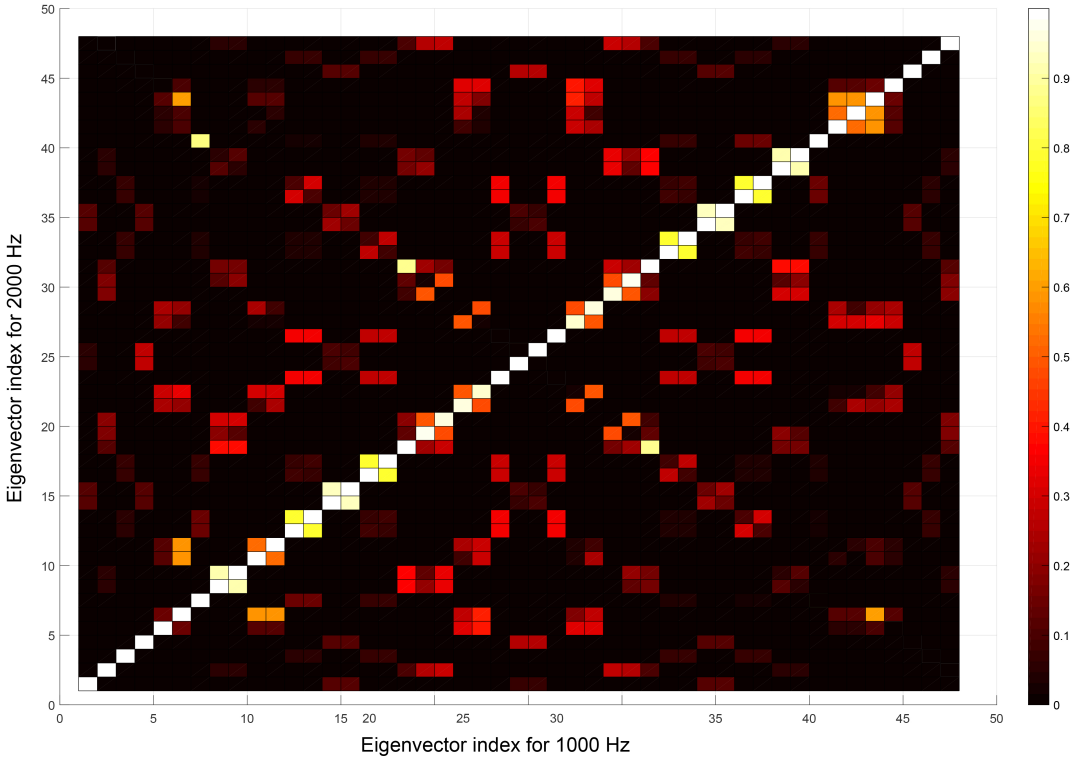


Figure 4.3: Wave Assurance Criterion (WAC) plot for eigenvectors at 1000 Hz and 2000 Hz for an RC beam.

required to join the corresponding discrete points plotted in the dispersion curves. Apart from the diagonal, the WAC values are between 0 and 0.3, where the eigenvectors are not well correlated. The WAC plot is essential to check the uniqueness of the correlation of two consecutive eigenvalues/eigenvectors where only one set of the WAC values equals to 1 is shown.

## 4.4 Dispersion relations and wave mode shapes

One of the contributions of this research involves the solution and production of the dispersion curves and mode shapes of RC sections. Previous work only involved analytical and experimental calculation of limited wave modes wavenumbers. For instance, Zerwer et al. (2006) used the formulation by Aalami (1973) in order to compute the dispersion curves and mode shapes associated with the first ten modes for uncracked and unreinforced concrete beam. The cross section of the concrete member was divided into linear triangular elements in the x-y plane and steady state wave motion was assumed along the length of the bar in the z-direction. However, the present research involves all of the wave modes associated with the DOFs for damaged and undamaged RC, prestressed and post-tensioned RC. Here, only the dispersion relations associated with the propagating

and evanescent wave modes are plotted for comparison purposes. However, other wave modes are illustrated and listed in detail separately.

First, the effect of the concrete strength on the dispersion curves is examined. Different undamaged RC sections are modelled with different concrete properties. The strength of concrete increases with time due to the continuous concrete hydration while most of this strength is gained in the first 28 days after casting. The compressive strength of concrete is directly proportional to its Young's Modulus. Subsequently, two undamaged RC sections are modelled with different Young's Modulus values. The associated dispersion curves are plotted in Figure 4.4. Due to the increase in the concrete stiffness, the wavenumbers decrease especially at high frequencies and the cut-on frequencies shift to the right.

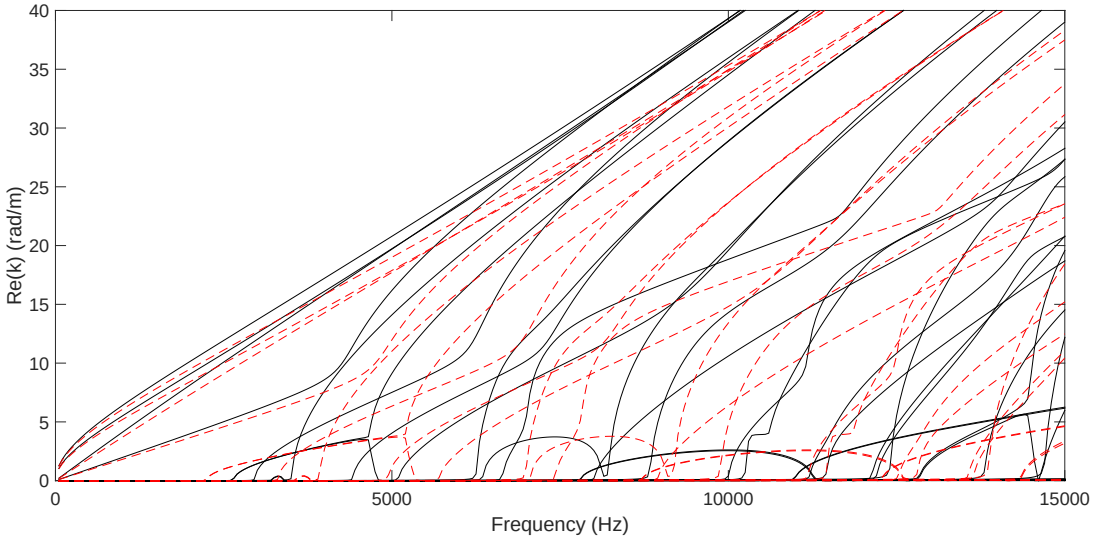


Figure 4.4: Dispersion curves for the real part of the wavenumbers for an undamaged RC with different concrete properties.

$E_c = 2.0 \times 10^{10}$ Pa (-), $E_c = 2.5 \times 10^{10}$ Pa (– – –).

Second, the effect of steel reinforcement on wave modes is investigated. Two undamaged segments are modelled using ANSYS. One is modelled with concrete only, and the second is modelled as reinforced concrete. Next, the associated stiffness and mass matrices are extracted and rearranged to formulate the transfer matrix for each waveguide. Solutions are calculated for each eigenvalue problem. The wave modes were evaluated within the frequency range of 1 to 15 kHz with a frequency step of 50 Hz. Dispersion curves for concrete and RC waveguides are shown in Figure 4.5. One can notice the small changes between the two sets of wavenumber values. However, the wavenumber values of RC are higher than the ones for concrete especially at high frequencies. This is due to the added mass of the reinforcement rebars present. The most distinctive difference in the wavenumbers between the concrete and RC section occurs at lower frequency, where the

latter are complex and have a high imaginary part. Consequently, they are considered highly attenuated within this frequency range of interest.

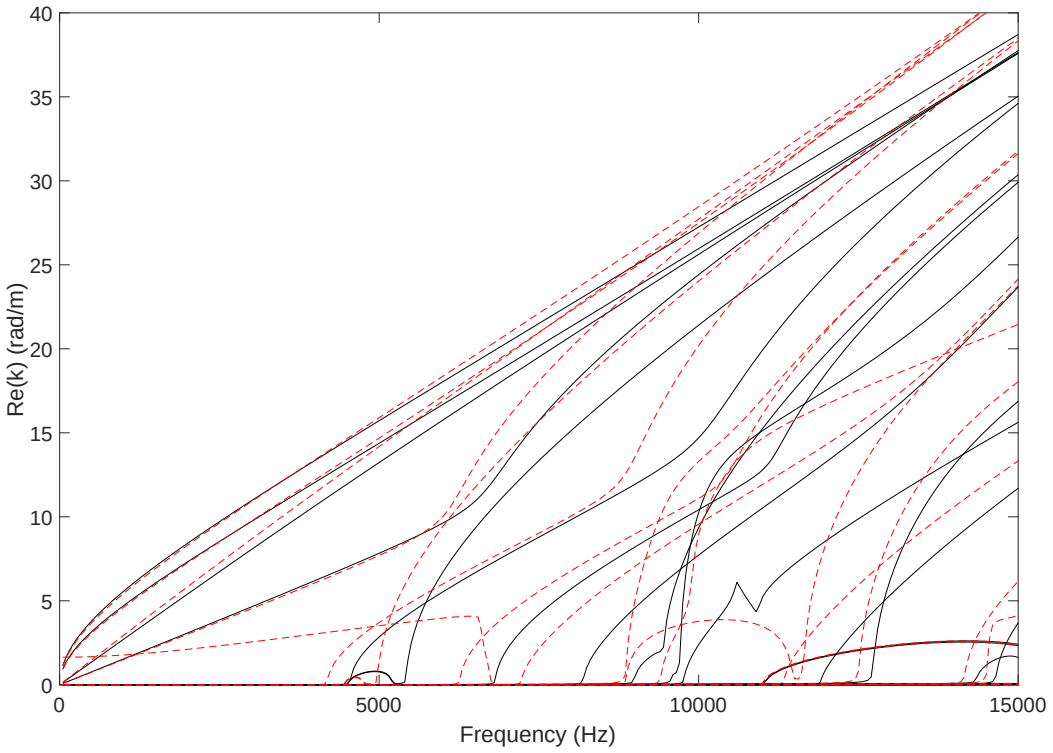


Figure 4.5: Dispersion curves for the real part of the wavenumbers for wave modes in a concrete and reinforced concrete beam.

Concrete section (—), RC section (– – –).

In Figure 4.4 and Figure 4.5, the real wavenumbers plotted can be associated with wave modes that are either propagating, evanescent or complex. The propagating wave modes are presented as purely real wavenumber over the whole frequency range. The evanescent ones are presented as purely real wavenumber after they cut-on. However, the complex wave modes are associated with real and imaginary part over the whole frequency range (the imaginary part is plotted at a later stage). In addition, one can notice the numerical artefact that is the shallow gradient at cut-on caused largely (but not entirely) by limited frequency resolution.

Also, in Figure 4.4 and Figure 4.5, there are some real wavenumbers that increase from and then decrease back to zero. Waves with such positive and the negative group velocities have been discovered in other solids such as layered media, shells and cylinders as in Tamm et al. (2017).

Third, the effect of damage in RC is investigated. Two segments of damaged and undamaged RC are modelled. Then, the WFE approach is applied over the same frequency range. The dispersion curves relating to wave modes of the damaged and undamaged

RC waveguides are shown in Figure 4.6. It can be seen that only a slight change exists between the wavenumbers associated with the damaged and undamaged RC waveguides. The cut-on frequencies are shifted to the right i.e. to higher frequencies once damage is present. The effect on these wavenumbers of the rebar diameter reduction as loss due to stiffness or mass are investigated in detail in the next chapter.

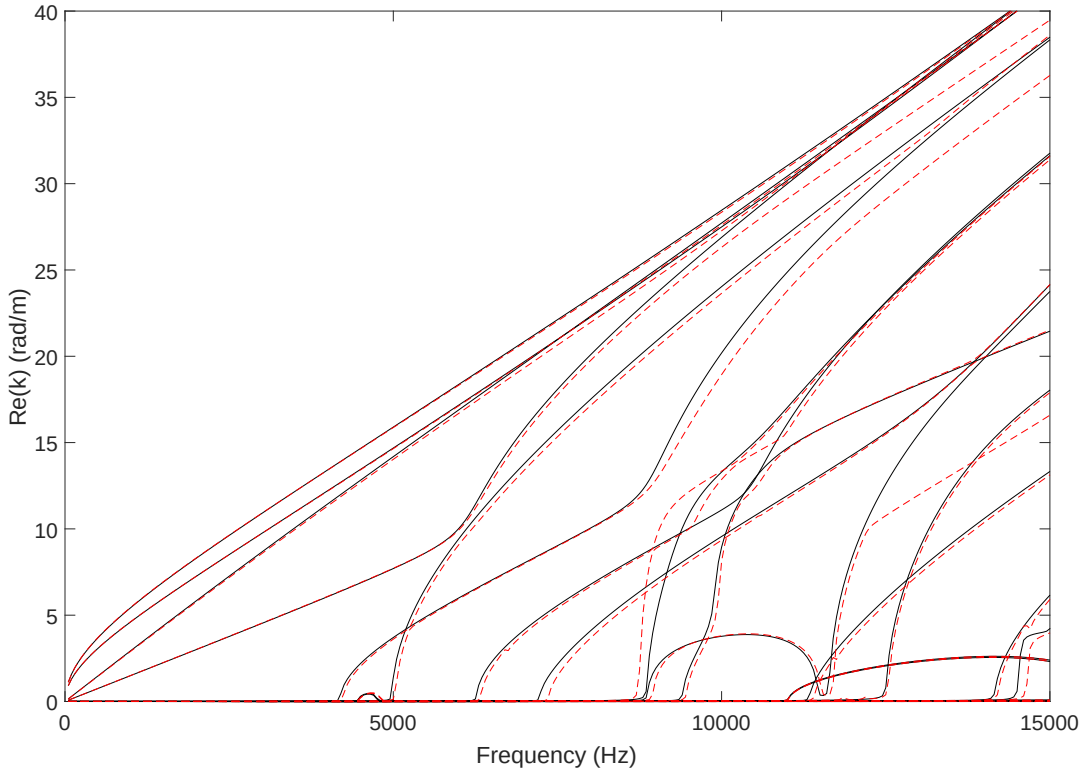


Figure 4.6: Dispersion curves for the real part of the RC wavenumbers for wave modes.

Undamaged section (—), damaged section (– – –).

The dispersion curves related to the least attenuated waves are selected for both the damaged and undamaged waveguides. In other words, only the wave modes associated with $\mid Im\ (k\Delta) \mid \leq 0.3$ are retained at each frequency step. Figure 4.7 shows the dispersion curves for those modes that can propagate over the whole frequency band for the RC segment. Only the real part of the wavenumbers is plotted. Mode 1 is associated with axial motion, mode 2 with torsional displacements around the x-axis, and modes 3 and 4 with bending in the vertical and transverse directions respectively. Figure 4.8 presents the dispersion curves of the waves that are evanescent at low frequency. This means that before a specific frequency associated with each wave mode, its wavenumber is purely imaginary. Starting from this specific frequency, the wavenumber becomes purely real. This frequency is called the cut-on frequency. Figure 4.9 illustrates the dispersion curves of the complex modes at low frequency for both waveguides, where

the wavenumber is complex below the cut-on frequency. Above cut-on, the wavenumber becomes purely real.

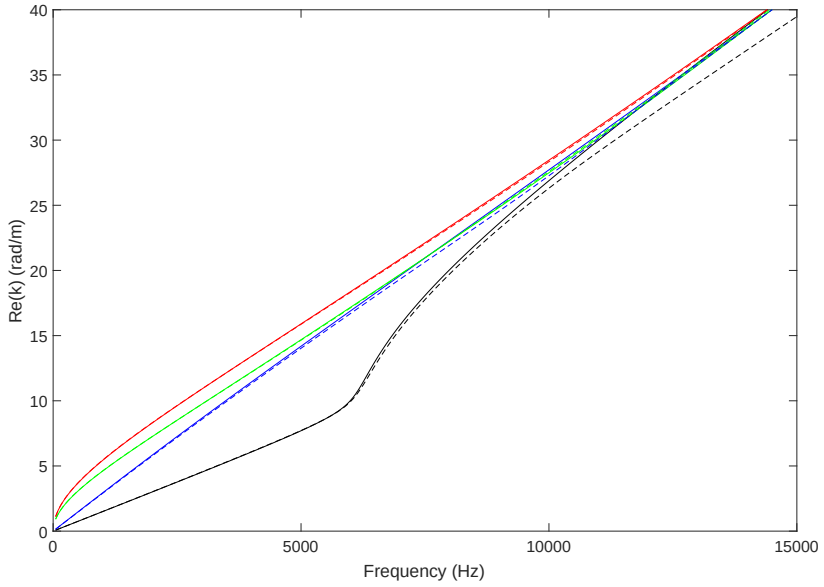


Figure 4.7: Dispersion curves for the real part of the wavenumbers for propagating wave modes in an RC beam.

Undamaged section (—), damaged section (- - -): mode 1 axial (-), mode 2 torsional (–), mode 3 bending (–) and mode 4 bending transversal (–).

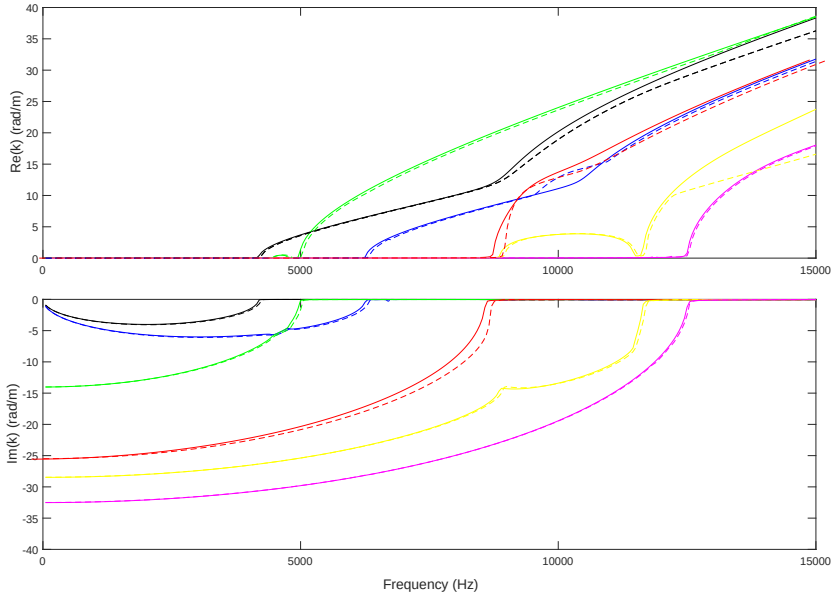


Figure 4.8: Dispersion curves for the real and imaginary parts for the RC wavenumbers for evanescent wave modes.

Undamaged section (—), damaged section (- - -): E4200 (-), E5000 (–), E6300 (–), E8700 (–), E11700 (–), E12500 (–). E stands for an evanescent wave with its associated cut-on frequency in Hz.

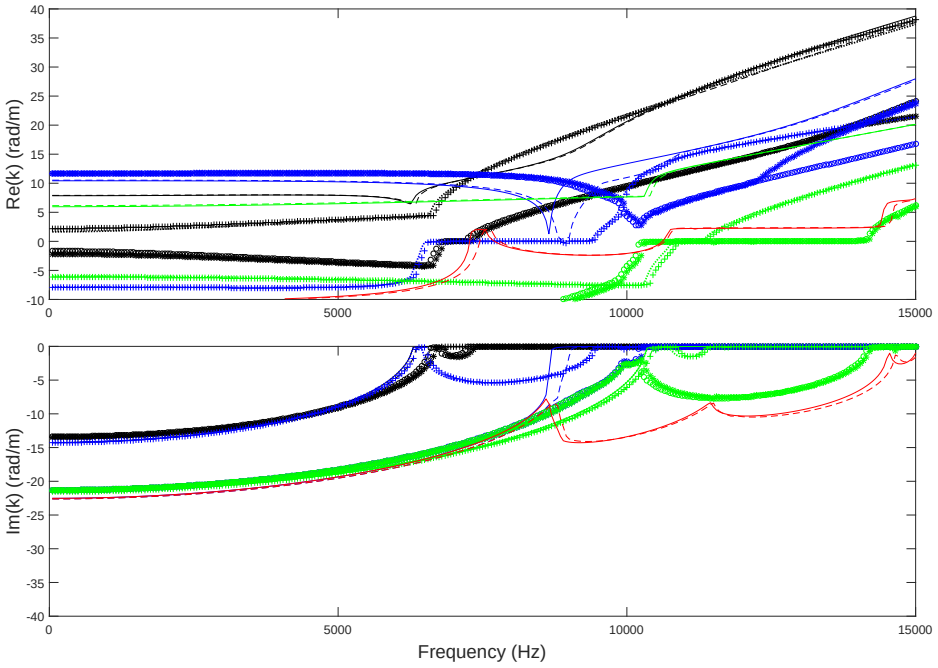


Figure 4.9: Dispersion curves for the real and imaginary parts for the RC wavenumbers for complex wave modes.

C6300 in undamaged RC (—), C6300 in damaged RC (- - -), C6600 in undamaged RC ($\cdots$), C6600 in damaged RC (+), C7250 in undamaged RC ($\circ$), C7250 in damaged RC ($*$), C8750 in undamaged RC ($-$), C8750 in damaged RC ($- - -$), C9450 in undamaged RC ($\cdots$), C9450 in damaged RC (+), C10250 in undamaged RC ($\circ$), C10250 in damaged RC ($*$), C10400 in undamaged RC ($-$), C10400 in damaged RC ($- - -$), C11400 in undamaged RC ($\cdots$), C11400 in damaged RC (+), C14200 in undamaged RC ($\circ$), C14200 in damaged RC ($*$), C14500 in undamaged RC ($-$), C14500 in damaged RC ($- - -$). C stands for a complex wave with its associated cut-on frequency in Hz.

Fourth, the effect of the prestress in the embedded reinforcements on the dynamic properties of RC is investigated. The dispersion curves for RC waveguides with and without prestress are shown in Figure 4.10. By comparing these dispersion curves, one can notice that prestress has a small effect on the wavenumbers of the waveguide. Due to the prestress effect in increasing the stiffness matrix of the segment and maintaining the mass matrix invariant, the wavenumbers are shifted to the right compared to the ones present for the RC section. Due to the similarity between the dispersion relations of RC and prestressed RC, only RC beams are considered from this point forward in this research for simulations and experimental validations.

Fifth, the dispersion curves relating to all wave modes of damaged and undamaged post-tensioned RC waveguides are illustrated in Figure 4.11. One can notice the change in the dispersion relations compared to the RC section. In addition, only a slight change exists

between the wavenumbers associated with the damaged and undamaged post-tensioned RC waveguides. The cut-on frequencies of the evanescent wave modes are shifted to the right.

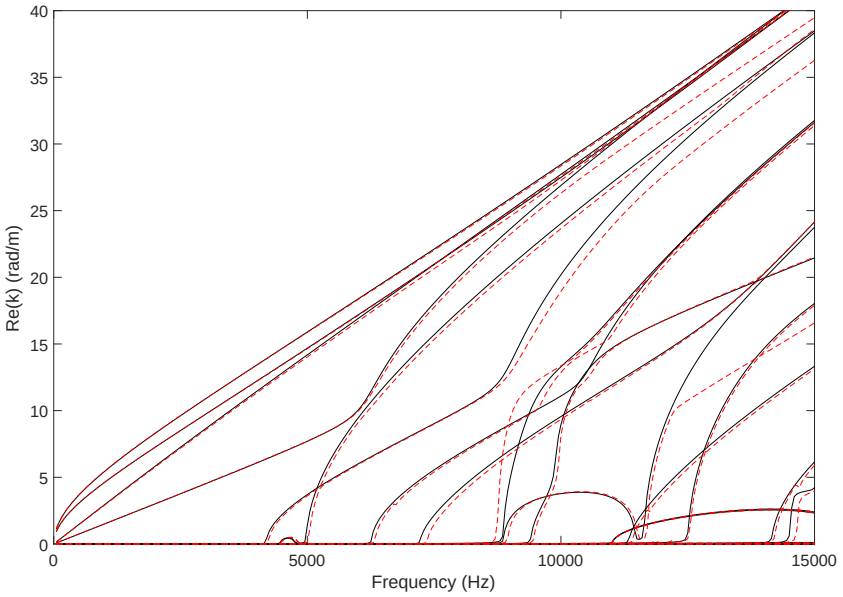


Figure 4.10: Dispersion curves for the real part for the wavenumbers of wave modes and the effect of prestress.

RC section (—), prestress RC section (– – –).

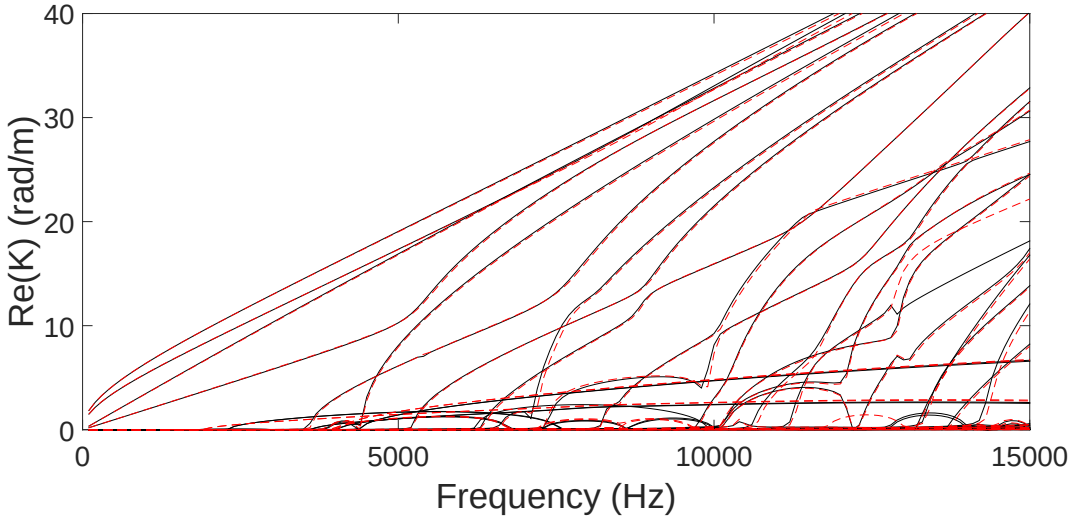


Figure 4.11: Dispersion curves for the real part of the wavenumbers of wave modes for the post-tensioned RC.

Undamaged section (—), damaged section (– – –).

In all of the above cases, only a slight change is observed between the wavenumbers associated with the concrete and RC sections, damaged and undamaged sections, RC,

prestressed and post-tensioned RC. This due to the fact that the majority of the structural stiffness is governed by the concrete rather than the reinforcement rebars.

After solving the eigenvalue/eigenvector problem, one can plot the wave mode shapes by extracting the nodal displacements from Equation 3.14. The wavemodes are complex, but only the real part of the displacements is plotted rather than the amplitude for simplicity. The imaginary parts were not very significant. The objective here is to validate the wave mode shapes and to visualise the cross section deformation especially for higher order modes. The nodal displacements in the Y and Z directions of propagating wave mode shapes in the undamaged RC section are plotted in Figure 4.12. The axial mode shows zero displacements in the selected directions since it occurs it the X direction.

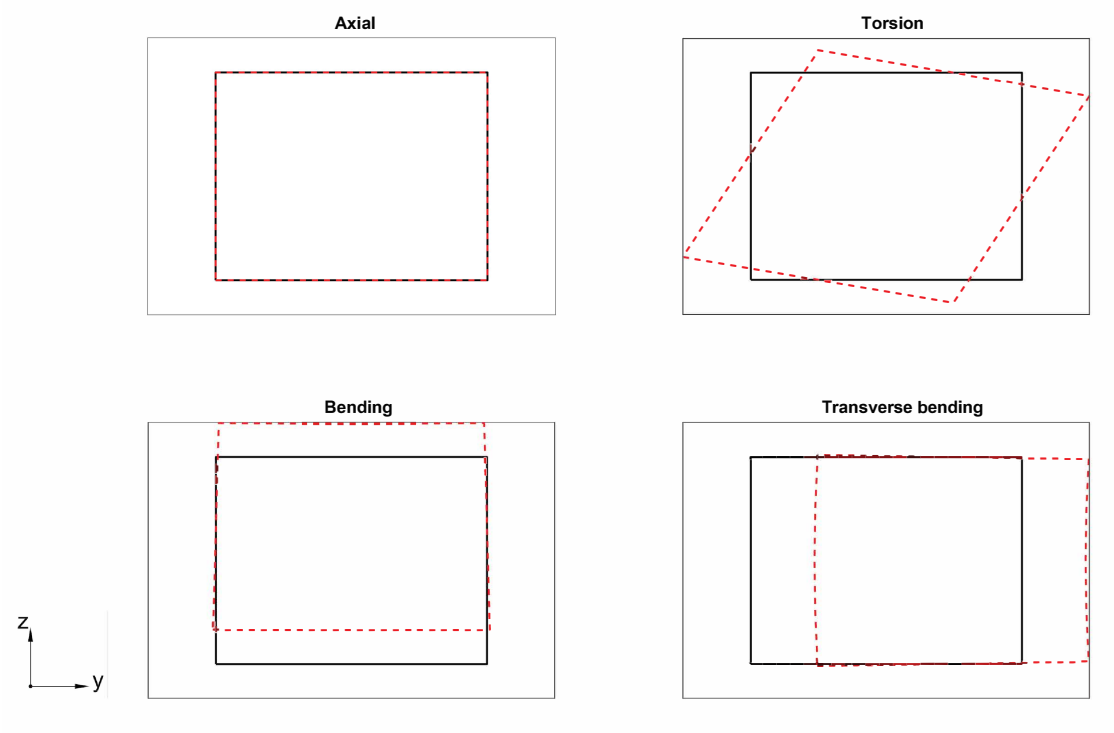


Figure 4.12: Nodal displacements in the plane of the beam cross section, i.e. in the Y and Z directions for selected propagating wave modes in an undamaged RC section.

Undeformed section (—), deformed section (– – –) at 1000 Hz.

Similarly, the selected evanescent wave modes in the undamaged RC section are plotted in Figure 4.13. For E4200 and E6300, the wave modes have no displacements in these directions. Then, their major nodal displacements occur in X direction (same as the propagation direction). In contrast, the remaining evanescent wave modes (i.e. E5000, E8700, E11700 and E 12500) have shown high nodal displacements in the Y and Z directions. Subsequently, they are cross sectional modes where the majority of their displacements occur in the cross section of the waveguide.

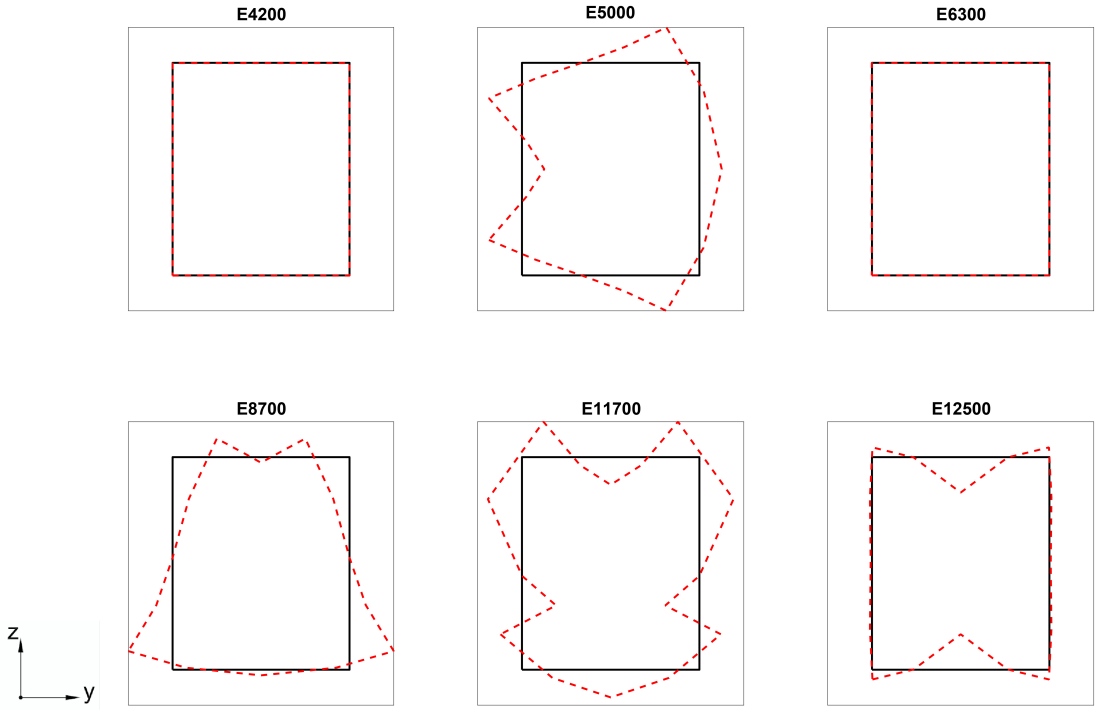


Figure 4.13: Nodal displacements in the plane of the beam cross section, i.e. in the Y and Z directions for selected evanescent wave modes in an undamaged RC section.

Undeformed section (—), deformed section (– – –). E stands for evanescent with its associated cut-on frequency.

In addition, the nodal displacements in the Y and Z directions of selected complex wave modes in an undamaged RC section are plotted in Figure 4.14. For the C7250, C10400, C11400, and C14200 wave modes there are no displacements in these directions; their major nodal displacements occur in the X direction. However, the remaining complex wave mode (i.e. C6300, C6600, C8750, C9450, C10250 and C14500) have shown high nodal displacements in the Y and Z directions. Subsequently, they are cross sectional modes where the majority of their displacements occur in the cross section of the waveguide.

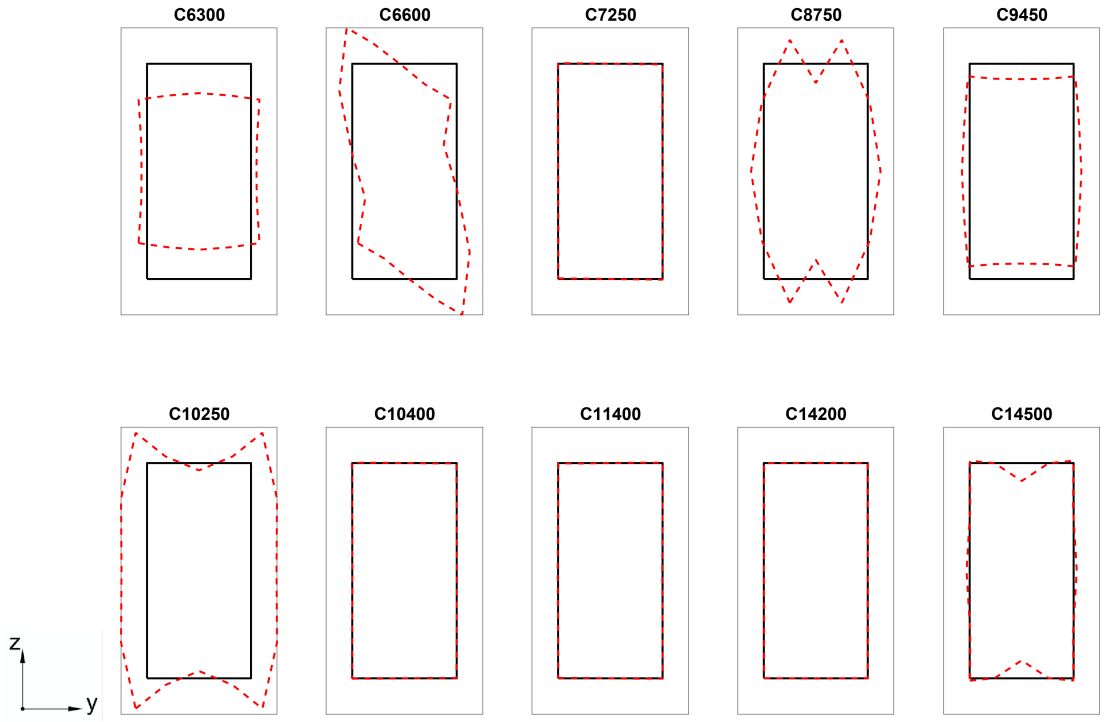


Figure 4.14: Nodal displacements in Y and Z directions of selected complex wave modes in undamaged RC section.

Undeformed section (—), deformed section (– – –). C stands for complex with its associated cut-on frequency.

## 4.5 FE and WFE forced response

In this section, the forced response of an undamaged cantilever RC beam is computed via FE and WFE for comparison and validation purpose. The RC structure is modelled in full FE with SOLID65 elements of length $\Delta$ 10mm with REINF264 embedded reinforcements. Each segment has 25 nodes at each face with three translational DOFs per node. Thus, there are 75 DOFs on each side of the segment. The total length of the beam is $L = 2$ m with fixed boundaries at the left end and free at the right end as shown in Figure 4.15. Thus, the full FE model contains 15075 DOFs. Harmonic analysis was selected with a frequency range from 0 to 15 kHz with a frequency step of 50 Hz. The excitation force is located at $x_e = 0.3$ m from the left boundary. The vertical FRF on of the top middle node at $x_r = 0.5$ m is selected.

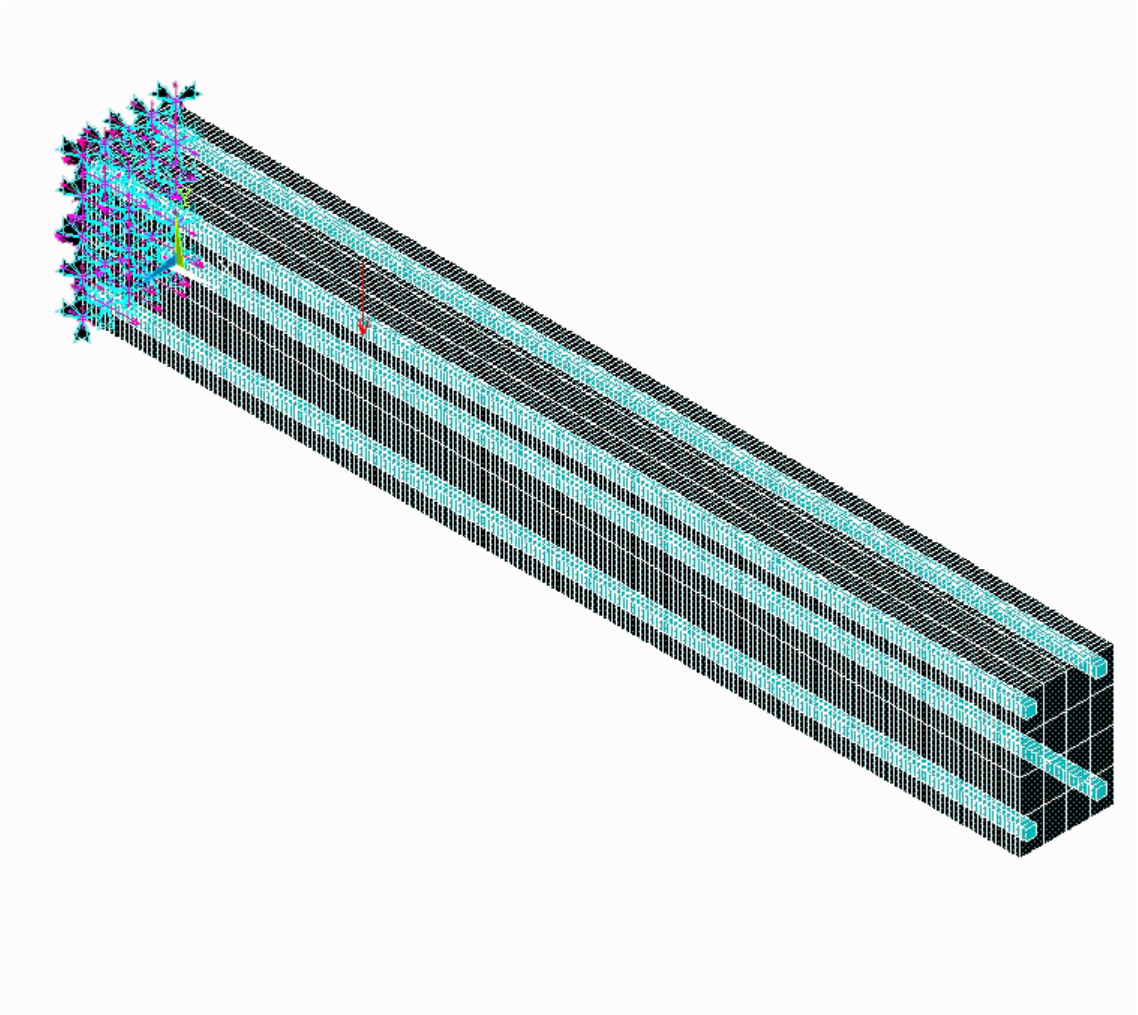

Figure 4.15: FRF in ANSYS for an RC cantilever beam model.

For the WFE section, there are only 75 DOFs at each end. First, the free wave propagation is solved via the transfer matrix in Equation 3.13. Then, the eigenvalue solution has 75 pairs of positive and negative going waves. Most of the wave modes obtained are strongly decaying waves at each frequency and their contribution to the response is negligible. Therefore, only those wave modes for which $\mid \mathrm{Im}(k\Delta) \mid \leq 0.3$ were retained at each step frequency. Then, the directly excited waves $\mathbf{e}^{+}$ and $\mathbf{e}^{-}$ are calculated using Equation 3.38.

The boundary matrices need to be identified using Equation 3.41. For the left fixed boundary, $\mathbf{A} = \mathbf{0}$ and $\mathbf{B} = \mathbf{I}$. However, for the right free boundary, $\mathbf{B} = \mathbf{0}$ and $\mathbf{A} = \mathbf{I}$. After solving for the boundary matrices, one can estimate the waves amplitudes at $x_r = 0.5$ m of the top middle node as per Equation 3.48 and 3.49. Finally, the total displacement can be obtained by superposing all of the wave amplitudes considered using Equation 3.50.

The WFE forced response predictions are then compared with those of the full FE model of the beam. The FRF vertical response of both models is plotted in Figure 4.16. Perfect agreement is seen between the two responses. Subsequently, the potential of WFE as a concise and efficient approach to estimate the forced response is validated. In the next chapters, the forced response using WFE solution is applied instead of solving a full FE model since the WFE solution is already available.

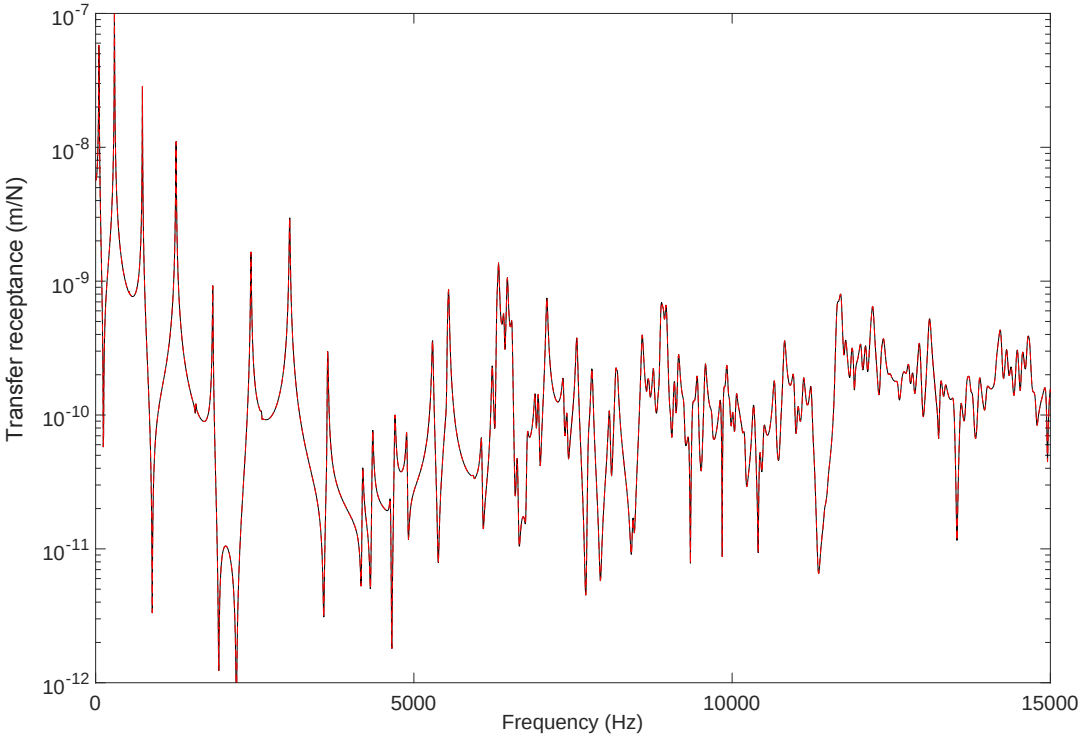


Figure 4.16: FRF vertical response of the cantilever RC beam at $x_r = 0.5$ m. Excitation is at $x_e = 0.3$ m.

FE (—), WFE (– – –).

## 4.6 Conclusions

The WFE method was applied to damaged and undamaged RC, prestressed and post-tensioned RC beams and the dispersion relations were identified. The effect of the concrete strength on the wavenumbers was investigated first. An increase in the concrete stiffness leads to a decrease in the wavenumbers especially at high frequencies. In addition, the cut-on frequencies increase. In contrast, adding steel reinforcements to concrete beam leads to an increase in the wavenumbers especially at high frequencies, and the corresponding cut-on frequencies decrease. This is due to the added mass of the reinforcement rebars with minimal effect on the overall RC beam stiffness.

Damage introduced by reducing the diameter of one rebar results in a small shift in the values of the wavenumbers. They become lower especially at higher frequencies, with higher values for the corresponding wave mode cut-on frequencies compared to the undamaged case. The least attenuated wave modes are selected and grouped as either propagating, evanescent or complex.

The prestressed effect introduced as initial strain in the embedded reinforcements results in a negligible effect on the dispersion relations. Subsequently, only RC beams are considered in this research for further simulations and experimental validation. Similar to conventional RC, damage introduced in the post-tensioned RC section results in small changes in the dispersion relations. This is due to the fact that the majority of the structural stiffness is governed by the concrete rather than the reinforcement rebars.

By using the wave mode solutions represented as eigenvectors, one can plot the wave mode shapes by using the nodal displacement results. Most of the evanescent and complex modes have shown cross sectional dominant displacements in the Y and Z directions.

Frequency response functions (FRFs) predicted using both the full FE and WFE models are compared. The full FE model contains 15075 DOFs, however the WFE model only contains 75 DOFs on each end of the segment. Both responses align perfectly, and therefore the WFE forced response approach is selected for the subsequent simulations of the response of damaged RC beams and the identification of damage via simulations.

# Chapter 5

# Wave scattering due to simulated damage in RC beams

## 5.1 Introduction

Structural and serviceability failures of reinforced concrete cause different damages scenarios within the structure. Although structural failures are shown through large cracks and deformations, serviceability damages are typically presented through small surface cracks and increased deflections of the structure. For this reason, the visibility of the damage has more potential for the structural damage identification, and therefore the probability of detection is higher compared to serviceability damage.

The principal origin of premature corrosion of steel reinforcement is due to exposure by chloride ions. The corroded layer between the steel reinforcement and the concrete causes changes in the tensile stresses due to contraction and expansion. Once these stresses exceed the concrete tensile capacity, cracks start to form from the steel reinforcement toward the surface of the concrete (PCA (2002)). For this reason, corrosion of reinforced concrete is considered as a long-term damage scenario, and it is challenging to detect the early rate of corrosion when surface cracking is not yet visible. In the corrosion scenario of the steel reinforcement, the reflection and transmission properties for propagating waves at a damage interface are advantageous, especially during the early stage of corrosion development. The reflection and transmission properties of a damage of finite size are hence considered in this chapter.

The WFE approach using the internal nodal displacements and forces can be used to couple damaged and undamaged waveguides, and subsequently to predict the reflection and transmission coefficients due to a defect. In this chapter, numerical simulations representing a finite length damage are considered. Two approaches are presented to couple the damaged and undamaged waveguides. These are namely the WFE-FE-WFE

and WFE-WFE-WFE approaches. Results will be produced and compared, and one methodology will be subsequently selected to obtain the scattering matrices associated with damage. In addition, the effect of the loss of rebar stiffness versus mass is investigated by examination of the kinetic and potential energies of the rebars. Then, a suitable and damage sensitive criterion is selected for potential damage detection technique.

## 5.2 Coupling of waveguides

Damage or discontinuities in structures give rise to scattering of incident waves, which is potentially of use for damage inspection. One can model the damaged and undamaged waveguides as two semi-infinite beams, and couple the waves at the interface of the junction. This model is denoted here as the WFE-WFE approach. When considering the total scattering caused by a discontinuity of finite length, coupling of a finite damage section to undamaged waveguides is a more appropriate model. In this case, the finite section can be modelled either in FE or WFE. In this section, both approaches are introduced and applied to an RC model. Results are compared and one coupling approach is selected for further simulations.

### 5.2.1 Coupling of waveguides using WFE-FE-WFE approach

As presented in Renno and Mace (2013), one can model the undamaged waveguides as two semi-infinite beams via WFE, and the finite length of the damaged section via FE, and couple the sections representing the undamaged waveguides using the continuity and equilibrium conditions at the interfaces with the FE damaged section. This approach is known as the WFE-FE-WFE approach, and it is presented in this section with the associated scattering matrix due to simulated damage as shown Figure 5.1.

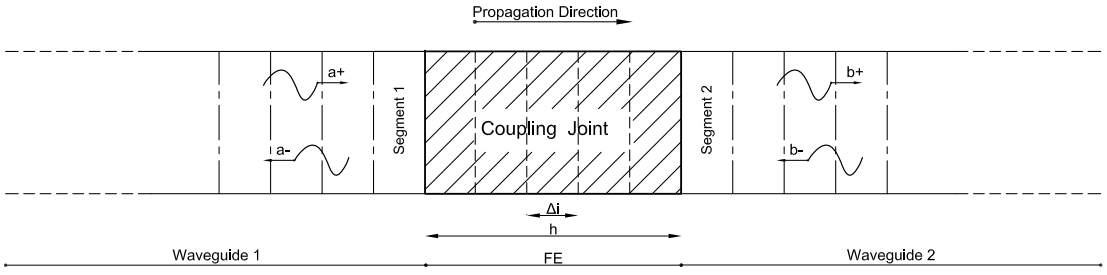


Figure 5.1: The interface between wave finite elements (Sections 1 and 2) connected to a finite element model of the coupling joint.

First, the damaged section is modelled via FE of finite length $h$ and with elements of length $\Delta_i$, i.e. here there are $h/\Delta_i$ elements in the length direction of the section. Let $\mathbf{D}_c$ be the dynamic stiffness matrix of the coupling joint, which is given in terms of its

mass $\mathbf{M}_c$, damping $\mathbf{C}_c$ and stiffness $\mathbf{K}_c$ matrices as follows (Kessentini et al. (2016))

$$\mathbf{D}_c = -\omega^2 \mathbf{M}_c + j\omega \mathbf{C}_c + \mathbf{K}_c \tag{5.1}$$

The left and right interface nodes of the finite section are expressed by $l$ and $r$ respectively. Internal nodes are denoted by $i$. A block matrix formulation of the matrix $\mathbf{D}_c$ can be written as

$$\mathbf{D}_c = \begin{bmatrix} \mathbf{D}_{ll} & \mathbf{D}_{li} & \mathbf{D}_{lr} \\ \mathbf{D}_{il} & \mathbf{D}_{ii} & \mathbf{D}_{ir} \\ \mathbf{D}_{rl} & \mathbf{D}_{ri} & \mathbf{D}_{rr} \end{bmatrix} \tag{5.2}$$

The dynamic stiffness matrix $\mathbf{D}_c$ of the coupling element is condensed to eliminate the internal nodes onto the nodes situated on the left and right faces. The dynamic condensation at every frequency $\omega$ is presented in Waki et al. (2009b). The condensed matrix can be denoted as

$$\mathbf{D}_c^* = \begin{bmatrix} \mathbf{D}_{ll} - \mathbf{D}_{li}\mathbf{D}_{ii}^{-1}\mathbf{D}_{il} & \mathbf{D}_{lr} - \mathbf{D}_{li}\mathbf{D}_{ii}^{-1}\mathbf{D}_{ir} \\ \mathbf{D}_{rl} - \mathbf{D}_{ri}\mathbf{D}_{ii}^{-1}\mathbf{D}_{il} & \mathbf{D}_{rr} - \mathbf{D}_{ri}\mathbf{D}_{ii}^{-1}\mathbf{D}_{ir} \end{bmatrix} \tag{5.3}$$

The dynamic stiffness matrix $\mathbf{D}_c^*$ of the coupling joint relates the displacements and forces on the interfaces with the two WFE modelled sections as

$$\mathbf{D}_c^* \begin{Bmatrix} \boldsymbol{q}_l^c \\ \boldsymbol{q}_r^c \end{Bmatrix} = \begin{Bmatrix} \boldsymbol{f}_l^c \\ \boldsymbol{f}_r^c \end{Bmatrix} \tag{5.4}$$

Two coupled waveguide segments 1 and 2 belonging respectively to waveguides 1 and 2 are modelled via WFE. Let $\boldsymbol{a}^+$ and $\boldsymbol{b}^-$ be the amplitudes of the waves incident on the coupling joint interface, and $\boldsymbol{a}^-$ and $\boldsymbol{b}^+$ be the amplitudes of the waves reflected by the coupling joint interface. Vectors $\boldsymbol{q}$ and $\boldsymbol{f}$ are defined in the wave domain by Equation 3.23. For waveguides 1 and 2

$$\begin{Bmatrix} \boldsymbol{q}_r^1 \\ \boldsymbol{q}_l^2 \\ \boldsymbol{f}_r^1 \\ \boldsymbol{f}_l^2 \end{Bmatrix} = \begin{bmatrix} \boldsymbol{\Phi}_{q_1}^+ & \mathbf{0} & \boldsymbol{\Phi}_{q_1}^- & \mathbf{0} \\ \mathbf{0} & \boldsymbol{\Phi}_{q_2}^+ & \mathbf{0} & \boldsymbol{\Phi}_{q_2}^- \\ \boldsymbol{\Phi}_{f_1}^+ & \mathbf{0} & \boldsymbol{\Phi}_{f_1}^- & \mathbf{0} \\ \mathbf{0} & \boldsymbol{\Phi}_{f_2}^+ & \mathbf{0} & \boldsymbol{\Phi}_{f_2}^- \end{bmatrix} \begin{Bmatrix} \boldsymbol{a}^+ \\ \boldsymbol{b}^- \\ \boldsymbol{a}^- \\ \boldsymbol{b}^+ \end{Bmatrix} \tag{5.5}$$

where $\boldsymbol{\Phi}_{q,f}^+$ and $\boldsymbol{\Phi}_{q,f}^-$ are now defined by concatenating the relevant vectors for individual waveguides 1 and 2 after the application of WFE as follows

$$\boldsymbol{\Phi}_q^{inc} = \begin{pmatrix} \boldsymbol{\Phi}_{q_1}^+ & \mathbf{0} \\ \mathbf{0} & \boldsymbol{\Phi}_{q_2}^+ \end{pmatrix} \quad \boldsymbol{\Phi}_q^{ref} = \begin{pmatrix} \boldsymbol{\Phi}_{q_1}^- & \mathbf{0} \\ \mathbf{0} & \boldsymbol{\Phi}_{q_2}^- \end{pmatrix} \quad \boldsymbol{\Phi}_f^{inc} = \begin{pmatrix} \boldsymbol{\Phi}_{f_1}^+ & \mathbf{0} \\ \mathbf{0} & \boldsymbol{\Phi}_{f_2}^+ \end{pmatrix} \quad \boldsymbol{\Phi}_f^{ref} = \begin{pmatrix} \boldsymbol{\Phi}_{f_1}^- & \mathbf{0} \\ \mathbf{0} & \boldsymbol{\Phi}_{f_2}^- \end{pmatrix} \tag{5.6}$$

By implementing the continuity and force equilibrium conditions, the nodal DOFs and forces at the interfaces are equal to those of the undamaged waveguides on each side,

i.e.

$$\begin{pmatrix} \boldsymbol{q}_l^c \\ \boldsymbol{q}_r^c \end{pmatrix} = \begin{pmatrix} \boldsymbol{q}_r^1 \\ \boldsymbol{q}_l^2 \end{pmatrix} \quad ; \quad \begin{pmatrix} \boldsymbol{f}_l^c \\ \boldsymbol{f}_r^c \end{pmatrix} = \begin{pmatrix} \boldsymbol{f}_r^1 \\ \boldsymbol{f}_l^2 \end{pmatrix} \tag{5.7}$$

The scattering matrix $\mathbf{S}$ is defined as

$$\begin{pmatrix} \boldsymbol{a}^+ \\ \boldsymbol{b}^- \end{pmatrix} = \mathbf{S} \begin{pmatrix} \boldsymbol{a}^- \\ \boldsymbol{b}^+ \end{pmatrix} \tag{5.8}$$

By combining Equation 5.5 to 5.7, then

$$\mathbf{S} = -(-\mathbf{D}_c^* \boldsymbol{\Phi}_q^{ref} + \boldsymbol{\Phi}_f^{ref})^{-1}(-\mathbf{D}_c^* \boldsymbol{\Phi}_q^{inc} + \boldsymbol{\Phi}_f^{inc}) \tag{5.9}$$

The scattering matrix $\mathbf{S}$ is a block matrix, where the diagonal matrices comprise the reflection coefficients and the off-diagonal matrices contain the transmission coefficients. In these models, the reflection coefficients of the damaged section are of interest. Once again, if a reduced number of waves is retained then the matrix to be inverted in Equation 5.9 is not square and pseudo-inversion is required Renno and Mace (2013). However, since the inversion of this matrix can cause ill-conditioning errors, appropriate use of the left eigenvector matrix $\boldsymbol{\Psi}$ from Equation 3.16 and the orthogonality condition from Equation 3.17 can eliminate these numerical errors. As a result, one can premultiply Equation 5.9 by matrix $\boldsymbol{\Psi}_q^{ref}$ defined as

$$\boldsymbol{\Psi}_q^{ref} = \begin{bmatrix} \boldsymbol{\Psi}_{q_1}^- & \mathbf{0} \\ \mathbf{0} & \boldsymbol{\Psi}_{q_2}^- \end{bmatrix} \tag{5.10}$$

Subsequently, the scattering matrix $\mathbf{S}$ becomes

$$\mathbf{S} = -\boldsymbol{\Psi}_q^{ref}(-\mathbf{D}_c^* \boldsymbol{\Phi}_q^{ref} + \boldsymbol{\Phi}_f^{ref})^{-1} \boldsymbol{\Psi}_q^{ref}(-\mathbf{D}_c^* \boldsymbol{\Phi}_q^{inc} + \boldsymbol{\Phi}_f^{inc}) \tag{5.11}$$

Given this WFE-FE-WFE coupling approach, which has been presented, the undamaged waveguides can be modelled as two semi-infinite beams via WFE, and the finite size of the damaged joint waveguide via FE. In principle, due to the generality of the FE modelled section, a large number of damage scenarios can be considered.

### 5.2.2 Coupling of waveguides using a WFE-WFE-WFE approach

Since the damaged waveguide is uniform, another approach to couple the damaged and undamaged waveguides can be applied via a WFE-WFE-WFE model. The two undamaged waveguides are modelled as before as two semi-infinite beams via WFE. Unlike the WFE-FE-WFE approach, the finite damaged waveguide length is modelled using WFE. Coupling of the waveguides is achieved by applying the continuity and equilibrium conditions at each junction. The approach is presented in this section and the associated scattering matrix due to changes in the waveguide properties is formulated.

The interfaces between the semi-infinite sections and the damage section are compatible, since for convenience they can be chosen to have the same nodal meshes and DOFs on the common cross-sections. In order to obtain the scattering matrix due to the finite damage section, one should get the scattering matrix at each junction of the waveguides as shown in Figure 5.2. A segment of length $\Delta_i$ is taken to represent each of the waveguides. Sections 1 and 3 represent the undamaged waveguide, and section 2 represents the damaged waveguide. Each section is modelled via WFE. Using the solution of the WFE as nodal displacement and forces, the scattering matrices at Junctions 1 and 2 are first obtained. Then, the total scattering matrix due to the finite length of the coupling element is developed and confirmed.

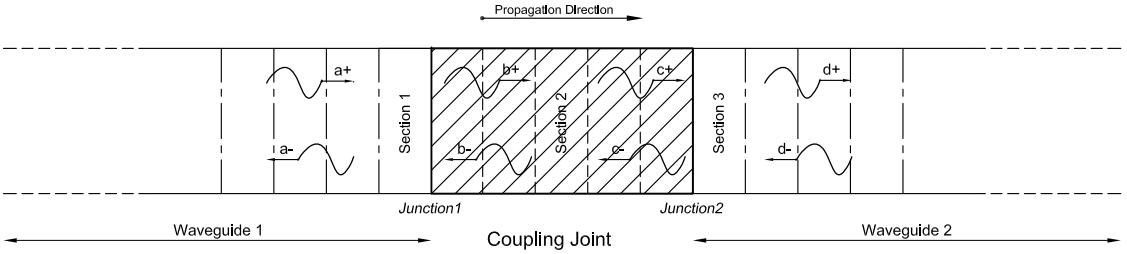


Figure 5.2: The interface between wave finite elements waveguides: Sections 1, 2 and 3.

At Junction 1, $\boldsymbol{a}^-$ and $\boldsymbol{b}^+$ are the amplitudes of the wave modes reflected by the coupling element interface. $\boldsymbol{a}^+$ and $\boldsymbol{b}^-$ are the amplitudes of the wave modes incident onto the coupling element interface. Furthermore, $\boldsymbol{\Phi}^+$ and $\boldsymbol{\Phi}^-$ are negative going right eigenvectors, where each wavemode is divided into displacement $\boldsymbol{q}$ and force $\boldsymbol{f}$ sub-vectors.

The displacements and forces in waveguides 1 and 2 are given by

$$\boldsymbol{q}_1 = \boldsymbol{\Phi}^+_{q_1}\boldsymbol{a}^+ + \boldsymbol{\Phi}^-_{q_1}\boldsymbol{a}^- \;\; ; \;\; \boldsymbol{f}_1 = \boldsymbol{\Phi}^+_{f_1}\boldsymbol{a}^+ + \boldsymbol{\Phi}^-_{f_1}\boldsymbol{a}^- \tag{5.12}$$

$$\boldsymbol{q}_2 = \boldsymbol{\Phi}^+_{q_2}\boldsymbol{b}^+ + \boldsymbol{\Phi}^-_{q_2}\boldsymbol{b}^- \;\; ; \;\; \boldsymbol{f}_2 = \boldsymbol{\Phi}^+_{f_2}\boldsymbol{b}^+ + \boldsymbol{\Phi}^-_{f_2}\boldsymbol{b}^- \tag{5.13}$$

Both waveguides are modelled such that positive going waves are travelling to the right. In addition, the continuity of displacements and equilibrium of forces at junction 1 are given by

$$\boldsymbol{q}_1 = \boldsymbol{q}_2 \;\; ; \;\; \boldsymbol{f}_1 = \boldsymbol{f}_2 \tag{5.14}$$

By applying Equation 5.14 into Equation 5.12 and 5.13

$$\begin{bmatrix} -\boldsymbol{\Phi}^-_{q_1} & \boldsymbol{\Phi}^+_{q_2} \\ -\boldsymbol{\Phi}^-_{f_1} & \boldsymbol{\Phi}^+_{f_2} \end{bmatrix} \begin{Bmatrix} \boldsymbol{a}^- \\ \boldsymbol{b}^+ \end{Bmatrix} = \begin{bmatrix} \boldsymbol{\Phi}^+_{q_1} & -\boldsymbol{\Phi}^-_{q_2} \\ \boldsymbol{\Phi}^+_{f_1} & -\boldsymbol{\Phi}^-_{f_2} \end{bmatrix} \begin{Bmatrix} \boldsymbol{a}^+ \\ \boldsymbol{b}^- \end{Bmatrix} \tag{5.15}$$

The scattering matrix $\mathbf{S}_1$ at Junction 1 is defined as

$$\begin{Bmatrix} \boldsymbol{a}^- \\ \boldsymbol{b}^+ \end{Bmatrix} = \mathbf{S}_1 \begin{Bmatrix} \boldsymbol{a}^+ \\ \boldsymbol{b}^- \end{Bmatrix} \tag{5.16}$$

Then

$$\mathbf{S}_1 = \begin{bmatrix} -\boldsymbol{\Phi}^-_{q_1} & \boldsymbol{\Phi}^+_{q_2} \\ -\boldsymbol{\Phi}^-_{f_1} & \boldsymbol{\Phi}^+_{f_2} \end{bmatrix}^{-1} \begin{bmatrix} \boldsymbol{\Phi}^+_{q_1} & -\boldsymbol{\Phi}^-_{q_2} \\ \boldsymbol{\Phi}^+_{f_1} & -\boldsymbol{\Phi}^-_{f_2} \end{bmatrix} \tag{5.17}$$

The scattering matrix $\mathbf{S}_1$ is a block matrix where the diagonal matrices comprise the reflection coefficients, and the off-diagonal matrices contain the transmission coefficients. Subsequently, the scattering matrix $\mathbf{S}_1$ is defined as

$$\mathbf{S}_1 = \begin{bmatrix} \mathbf{R}_{12} & \mathbf{T}_{21} \\ \mathbf{T}_{12} & \mathbf{R}_{21} \end{bmatrix} \tag{5.18}$$

where $\mathbf{R}$ and $\mathbf{T}$ are the reflection and transmission matrices at the junction. In addition, the subscripts 1 and 2 are used to indicate the reflection and transmission matrices when the wave is incident from waveguide 1 to 2 respectively.

Using the same procedure and definitions, the scattering matrix $\mathbf{S}_2$ at Junction 2 is defined as

$$\mathbf{S}_2 = \begin{bmatrix} -\boldsymbol{\Phi}^-_{q_2} & \boldsymbol{\Phi}^+_{q_3} \\ -\boldsymbol{\Phi}^-_{f_2} & \boldsymbol{\Phi}^+_{f_3} \end{bmatrix}^{-1} \begin{bmatrix} \boldsymbol{\Phi}^+_{q_2} & -\boldsymbol{\Phi}^-_{q_3} \\ \boldsymbol{\Phi}^+_{f_2} & -\boldsymbol{\Phi}^-_{f_3} \end{bmatrix} \tag{5.19}$$

with

$$\mathbf{S}_2 = \begin{bmatrix} \mathbf{R}_{23} & \mathbf{T}_{32} \\ \mathbf{T}_{23} & \mathbf{R}_{32} \end{bmatrix} \tag{5.20}$$

The matrices $\mathbf{S}_1$ and $\mathbf{S}_2$ may suffer from ill conditioning error when inverting the inner matrices. Alternatively, a numerical implementation is proposed where the orthogonality of the left and right vectors is used as per Equation 3.17. Thus, premultiplying Equation 5.12 by the left eigenvector matrix

$$\begin{bmatrix} \boldsymbol{\Psi}^+_{f_1} & \boldsymbol{\Psi}^+_{q_1} \\ \boldsymbol{\Psi}^-_{f_1} & \boldsymbol{\Psi}^-_{q_1} \end{bmatrix} \begin{Bmatrix} \boldsymbol{q}_1 \\ \boldsymbol{f}_1 \end{Bmatrix} = \begin{bmatrix} \boldsymbol{\Psi}^+_{f_1} & \boldsymbol{\Psi}^+_{q_1} \\ \boldsymbol{\Psi}^-_{f_1} & \boldsymbol{\Psi}^-_{q_1} \end{bmatrix} \begin{bmatrix} \boldsymbol{\Phi}^+_{q_1} & \boldsymbol{\Phi}^-_{q_1} \\ \boldsymbol{\Phi}^+_{f_1} & \boldsymbol{\Phi}^-_{f_1} \end{bmatrix} \begin{Bmatrix} \boldsymbol{a}^+ \\ \boldsymbol{a}^- \end{Bmatrix} \tag{5.21}$$

Then, Equation 5.21 becomes

$$\begin{bmatrix} \boldsymbol{\Psi}^+_{f_1} & \boldsymbol{\Psi}^+_{q_1} \\ \boldsymbol{\Psi}^-_{f_1} & \boldsymbol{\Psi}^-_{q_1} \end{bmatrix} \begin{Bmatrix} \boldsymbol{q}_1 \\ \boldsymbol{f}_1 \end{Bmatrix} = \begin{bmatrix} \mathbf{I} & \mathbf{0} \\ \mathbf{0} & \mathbf{I} \end{bmatrix} \begin{Bmatrix} \boldsymbol{a}^+ \\ \boldsymbol{a}^- \end{Bmatrix} \tag{5.22}$$

Therefore,

$$\begin{Bmatrix} \boldsymbol{q}_1 \\ \boldsymbol{f}_1 \end{Bmatrix} = \begin{bmatrix} \boldsymbol{\Psi}^{+\,*}_{f_1} & \boldsymbol{\Psi}^{+\,*}_{q_1} \\ \boldsymbol{\Psi}^{-\,*}_{f_1} & \boldsymbol{\Psi}^{-\,*}_{q_1} \end{bmatrix} \begin{Bmatrix} \boldsymbol{a}^+ \\ \boldsymbol{a}^- \end{Bmatrix} \tag{5.23}$$

Subsequently, Equation 5.17 and 5.19 become

$$\mathbf{S}_1 = \begin{bmatrix} -\boldsymbol{\Psi}^{+\,*}_{q_1} & \boldsymbol{\Psi}^{+\,*}_{f_2} \\ -\boldsymbol{\Psi}^{-\,*}_{q_1} & \boldsymbol{\Psi}^{-\,*}_{f_2} \end{bmatrix}^{-1} \begin{bmatrix} \boldsymbol{\Psi}^{+\,*}_{f_1} & -\boldsymbol{\Psi}^{+\,*}_{q_2} \\ \boldsymbol{\Psi}^{-\,*}_{f_1} & -\boldsymbol{\Psi}^{-\,*}_{q_2} \end{bmatrix} \tag{5.24}$$

$$\mathbf{S}_2 = \begin{bmatrix} -\boldsymbol{\Psi}^{+\,*}_{q_2} & \boldsymbol{\Psi}^{+\,*}_{f_3} \\ -\boldsymbol{\Psi}^{-\,*}_{q_2} & \boldsymbol{\Psi}^{-\,*}_{f_3} \end{bmatrix}^{-1} \begin{bmatrix} \boldsymbol{\Psi}^{+\,*}_{f_2} & -\boldsymbol{\Psi}^{+\,*}_{q_3} \\ \boldsymbol{\Psi}^{-\,*}_{f_2} & -\boldsymbol{\Psi}^{-\,*}_{q_3} \end{bmatrix} \tag{5.25}$$

After solving the scattering matrices at each junction, the total scattering matrix due to the coupling damage element is derived based on the reflection and transmission matrices of each junction. It is assumed that $\boldsymbol{d}^-$ is zero since it is a semi-infinite beam (the Sommerfeld radiation condition). Using Equation 5.16,

$$\boldsymbol{a}^- = \mathbf{R}_{12}\boldsymbol{a}^+ + \mathbf{T}_{21}\boldsymbol{b}^- \tag{5.26}$$

Let $\mathbf{F}$ be the propagation matrix between the two edges of the coupling element of length $h$, and $k_3$ are the wavenumbers associated with it. Then,

$$\mathbf{F} = \begin{bmatrix} e^{-i(k_2^+)h} & \cdots & 0 \\ \vdots & \ddots & \vdots \\ 0 & \cdots & e^{-i(k_n^+)h} \end{bmatrix} \tag{5.27}$$

Next, $\mathbf{b}^-$ is defined as

$$\boldsymbol{b}^- = \mathbf{F}\boldsymbol{c}^- = \mathbf{F}\mathbf{R}_{23}\boldsymbol{c}^+ = \mathbf{F}\mathbf{R}_{23}\mathbf{F}\boldsymbol{b}^+ \tag{5.28}$$

with

$$\boldsymbol{b}^+ = \mathbf{T}_{12}\boldsymbol{a}^+ + \mathbf{R}_{21}\boldsymbol{b}^- \tag{5.29}$$

then,

$$\boldsymbol{b}^- = \mathbf{F}\mathbf{R}_{23}\mathbf{F}[\mathbf{I} - \mathbf{R}_{21}\mathbf{F}\mathbf{R}_{23}\mathbf{F}]\mathbf{T}_{12}\boldsymbol{a}^+ \tag{5.30}$$

Substituting Equation 5.30 into Equation 5.26

$$\boldsymbol{a}^- = \mathbf{R}_T\boldsymbol{a}^+ \;\; ; \;\; \mathbf{R}_T = \mathbf{R}_{12} + \mathbf{T}_{21}\mathbf{F}\mathbf{R}_{23}\mathbf{F}[\mathbf{I} - \mathbf{R}_{21}\mathbf{F}\mathbf{R}_{23}\mathbf{F}]\mathbf{T}_{12} \tag{5.31}$$

Subsequently, $\mathbf{R}_T$ is the net reflection matrix due to the full finite length of the coupling element.

Using Equation 5.20,

$$\boldsymbol{d}^+ = \mathbf{T}_{23}\mathbf{F}\boldsymbol{b}^+ \tag{5.32}$$

$$\boldsymbol{d}^+ = \mathbf{T}_T\boldsymbol{a}^+ \;\; ; \;\; \mathbf{T}_T = \mathbf{T}_{23}\mathbf{F}[\mathbf{I} - \mathbf{R}_{21}\mathbf{F}\mathbf{R}_{23}\mathbf{F}]\mathbf{T}_{12}\boldsymbol{a}^+ \tag{5.33}$$

where $\mathbf{T}_T$ is the net transmission matrix due to the full finite length of the coupling element.

Subsequently, the full scattering matrix of the coupling element is given by

$$\begin{Bmatrix} \boldsymbol{a}^- \\ \boldsymbol{d}^+ \end{Bmatrix} = \begin{bmatrix} \mathbf{R}_T \\ \mathbf{T}_T \end{bmatrix} \left\{ \boldsymbol{a}^+ \right\} \tag{5.34}$$

### 5.2.3 Comparison and discussions

Both coupling methods have been simulated. Results such as the magnitude of the reflection coefficients are compared. In addition, the advantages and limitations of each approach are presented and discussed. Finally, one approach is chosen to get the scattering matrices for different damage scenarios.

The undamaged and damaged RC sections were modelled as described in Section 4.2. The undamaged reinforced concrete section is modelled using 16 SOLID65 elements. The element length is $\Delta_i = 0.01$ m for all waveguides, the total number of DOFs $n$ is 150, and a hysteretic damping value of 0.004 is chosen for both models. However, for the damaged coupling section, the total length is $h = 0.2$ m. The reinforcements are modelled via the embedded approach using REINF264 elements. The damaged reinforced concrete section is modelled in the same way as for the undamaged section, except that the area of the damaged reinforced rebar at the bottom right corner is reduced to represent a loss of thickness due to corrosion. In this model, the corroded rebar is taken to have a diameter equivalent to a 36% reduction compared to the intact one. Both damaged and undamaged sections are shown in Figure 4.1. The scattering matrix for each approach was calculated, and the magnitude of the reflection coefficients of all propagating modes are plotted in Figure 5.3.

In the WFE-FE-WFE coupling approach, a single FE model is needed for both undamaged and damaged sections. For the finite damaged joint, an FE model is needed for each different damage scenario. The damage is modelled with different rebar diameter reduction. Subsequently, the FE approach uses a dynamic condensation to eliminate internal nodes for each damage scenario. In this example, the nodes comprising 20 elements were needed to be condensed into left and right DOFs. Calculation and ill-conditioning errors related to dynamic condensation arise with the increased number of DOFs in the model. As a result, a proper element length and Zhong's approach are required to decrease the effect of these errors. After defining the WFE solutions of the undamaged section and the dynamic condensed matrix of the finite coupling element, both waveguides can be coupled and the net scattering matrix calculated using Equation 5.11. To eliminate ill-conditioning errors due to matrix inversion, a multiplication by the right eigenvectors is used. The magnitude of the diagonal of reflection matrix is then plotted as shown in Figure 5.3.

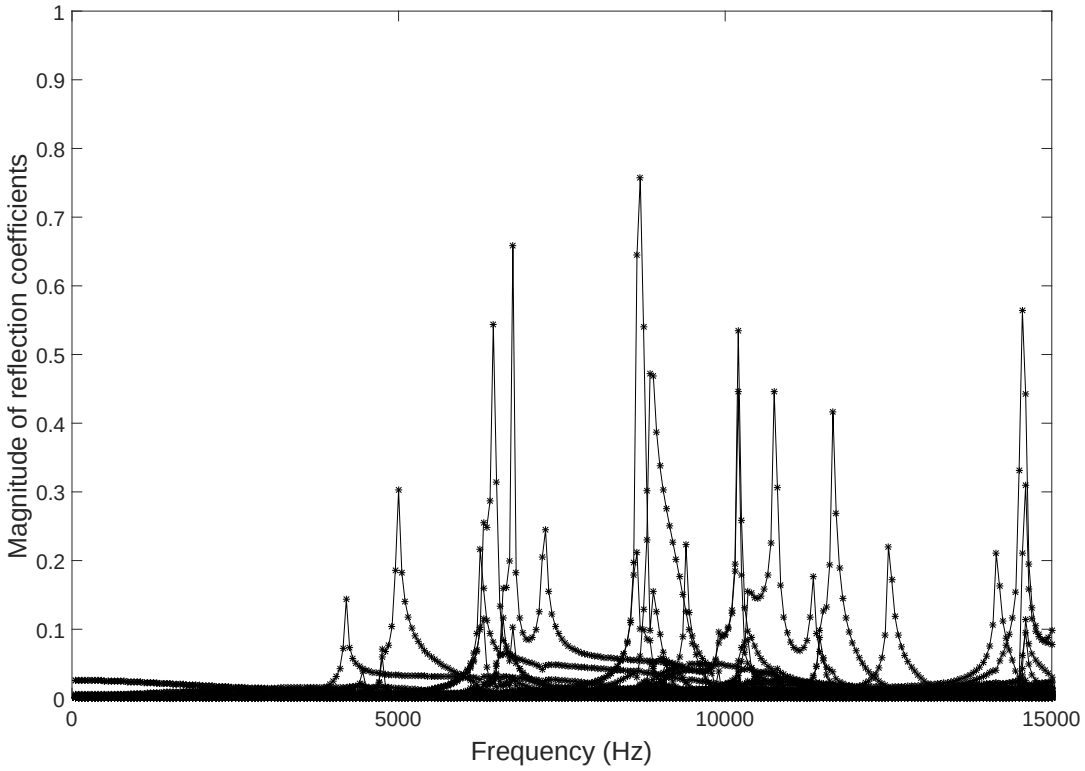


Figure 5.3: Magnitude of the reflection coefficients due to simulated damage in RC beam.

36% reduction of one of steel diameter over a length $h = 0.2$ m and element size of 0.01 m. WFE-FE-WFE approach (—), WFE-WFE-WFE approach ($*$).

However, in the WFE-WFE-WFE coupling approach, an FE model of the section is needed for both the undamaged and damaged segment. For the damaged element, only one FE model is sufficient to model one reduction of diameter at a time for different damaged lengths. In this example, an element of length 0.01 m is modelled to represent each waveguide respectively. After extracting the associated mass and stiffness matrices of each FE model, the WFE approach is applied for both damaged and undamaged sections. Since the element length is small, no dynamic condensation is needed for the damaged section since no internal nodes exist. As a result, calculation and ill-conditioning errors related to dynamic condensation are not present. However, a proper segment length is required. This length should be not too small with respect to the shortest wavelength to avoid round off errors, nor too large to reduce discretization errors. After defining the WFE solutions for all of the waveguides, the damaged and undamaged sections are coupled first at the junctions as per Equation 5.24 and 5.25. One should check the matching of the wave modes between the waveguides at a junction. For these reasons, the WAC approach was applied between the wave modes in the waveguides in order to make sure that the wave modes are listed in the same order for each waveguide at each frequency step. Similarly to WFE-FE-WFE, errors related to ill-conditioning occur and can be reduced via pre-multiplication by the right eigenvectors. The net

scattering matrix is calculated using Equation 5.31, and the magnitudes of the terms in the diagonal of the reflection matrix are then plotted and compared to the ones via WFE-FE-WFE as shown in Figure 5.3.

It can be seen that both methods give exactly the same solution. Subsequently, the WFE-WFE-WFE approach was chosen to be used in the next section where scattering matrices are to be calculated for different damage scenarios. The advantage of this approach is summarised by the fact that it evaluates the phase change over different finite lengths between the two undamaged waveguides and it is only necessary to model one FE model, as used for example for the diameter reduction of one rebar.

## 5.3 Scattering due to damage in RC beams

In this section, different damage scenarios for corrosion of steel reinforcement are considered in RC members. Corrosion is modelled as a percentage reduction in a reinforcement diameter. Moreover, this reduction is localised over a small length in order to represent the pitting corrosion effect. As a result, the damaged part is considered as a coupling element localised between two undamaged waveguides.

For each RC model, a damage scenario is selected and the WFE-WFE-WFE approach is applied. The scattering matrix is then calculated accordingly with the magnitude of the reflection coefficients plotted. Furthermore, the least attenuated modes are selected as potential modes sensitive to the damage. In addition, the effect of the loss of the rebar stiffness and mass is compared based on the rebar kinetic and strain energies.

### 5.3.1 Scattering properties of RC beams

Both undamaged and damaged RC sections are modelled as described in Section 4.2. The element length is $\Delta_i = 0.01$m for all waveguides. However, for the damaged coupling section, the total length is h = 0.05 m, and the damage is represented by a 36% and 60% diameter reduction in one of the bottom reinforcement debars. Then, the length of the damage is increased to $h = 0.2$ m for the 36% damage case.

In Figure 5.4, the magnitude of the reflection coefficients associated with a 36% and 60% rebar diameter reduction over a length $h = 0.2$ m are plotted. The magnitude of the reflection coefficients of wave modes are high at specific frequencies and related to the increase in the extent of the damage. Next, the effect of the damage length is investigated. In Figure 5.5, the magnitude of the reflection coefficients due to simulated 36% damage is plotted for different damage length $h$. These magnitudes increase with an increase in the damage length.

In Figure 5.6, $d$ is the intact diameter of the rebar, $a$ is the diameter reduction and $h$ is the damage length. In all cases, $a$ x $h$ is kept constant. It simulates a loss of material at each stage. In Figure 5.7, the effects of diameter reduction and the increase of damage length on the magnitude of reflection coefficients are compared. The magnitude of the highest reflection coefficients at cut-on frequencies are selected and plotted. One can observe the increase in the magnitude of the reflection coefficients with respect to the greater diameter reduction. This means that the wave modes are more sensitive to the change in the rebar diameter rather than its length. Subsequently, attention is more focused on the damage represented by the rebar diameter reduction.

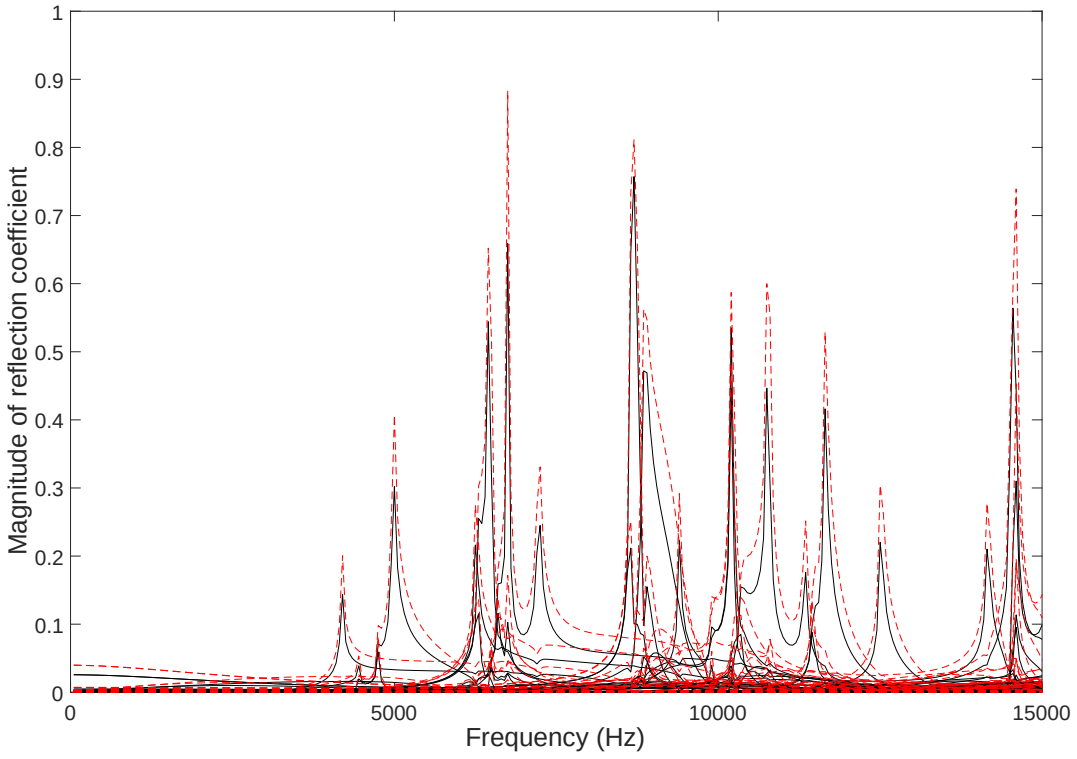


Figure 5.4: Magnitude of the RC reflection coefficients due to simulated damage length $h = 0.2$ m.

Rebar diameter reduction: 36% (—), 60% (– – –).

The magnitude of the reflection coefficients of the least attenuated wave modes is selected and plotted for the 60% damage over a length $h = 0.2$ m. The magnitude of the reflection coefficients of fundamental wave modes (axial, torsional, bending and transverse bending) are plotted in Figure 5.8. These reflections are negligible and therefore the fundamental wave modes are not sensitive to this type of damage due to rebar diameter reduction. However, high magnitudes of the reflection coefficients are associated with some evanescent and complex wave mode shapes as seen in Figure 5.9 and Figure 5.10. Not all evanescent and complex wave modes defined in Section 4 have shown high magnitude of reflection coefficients. The peaks of these reflection coefficients are at the cut-on frequency of these wave modes. This is due to the shift between the wavenumbers in

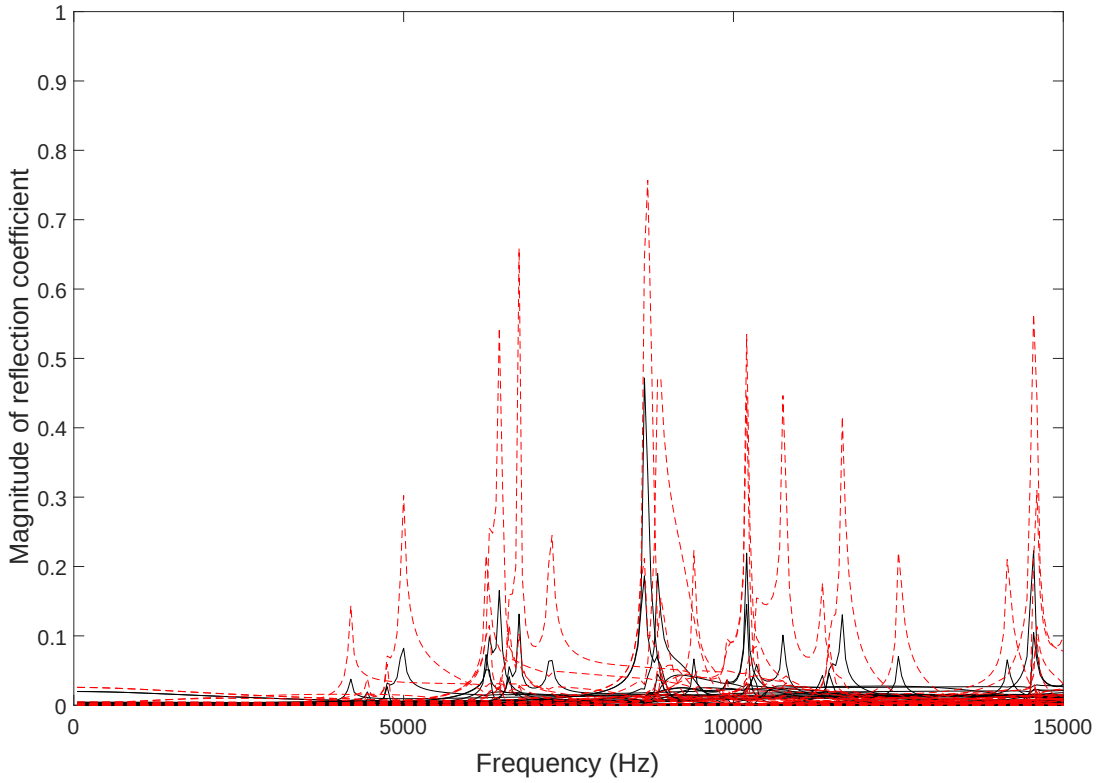


Figure 5.5: Magnitude of the RC reflection coefficients due to simulated $a$ as 36% diameter reduction.

Damage length $h$: 0.05 m (—), 0.2 m (– – –).

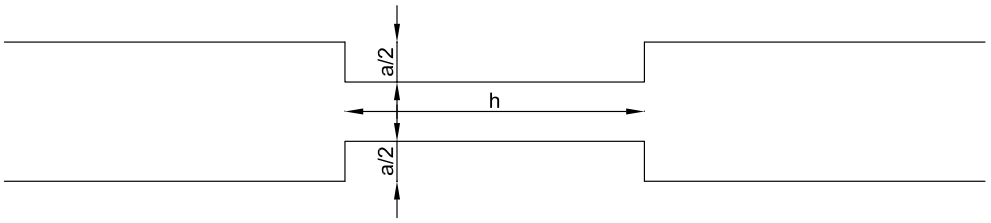


Figure 5.6: Damaged rebar details with $d$ is rebar diameter, $a$ is rebar reduction and $h$ is the damage length.

the damaged and undamaged waveguides of the evanescent and complex wave modes, seen in Figure Figure 4.8 and Figure 4.9. These wave modes start propagating in the undamaged waveguide before the damaged one in this frequency range. Subsequently, the high reflection coefficients are present in narrow frequency bands. In addition, the magnitude of these reflection coefficients associated with this damage scenario are listed in Table 5.1.

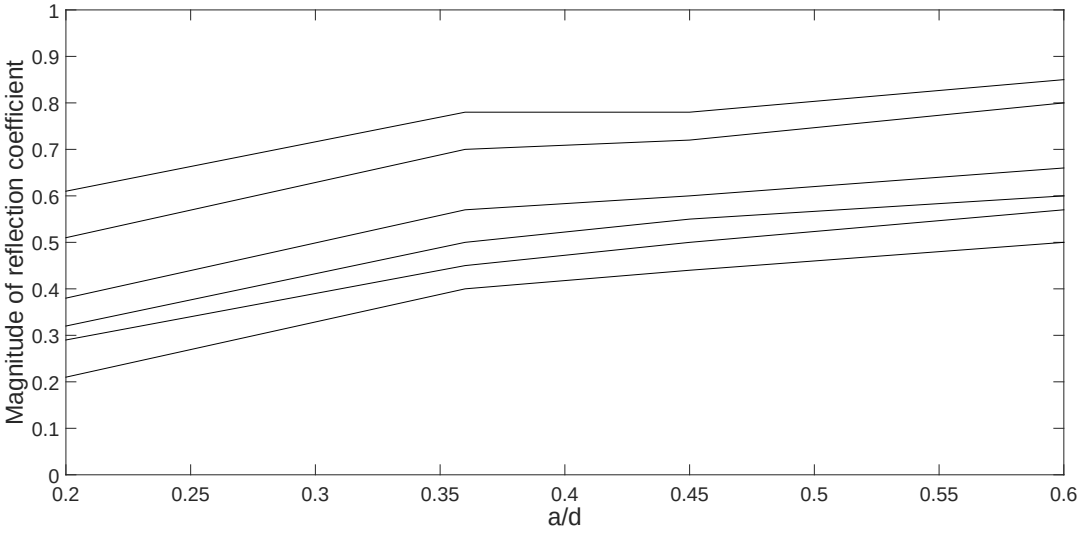


Figure 5.7: Variation of the magnitude of the reflection coefficient associated with wave modes at cut-on with respect to the damage depth ratio whilst keeping the product diameter reduction times length ($a \times h$) a constant.

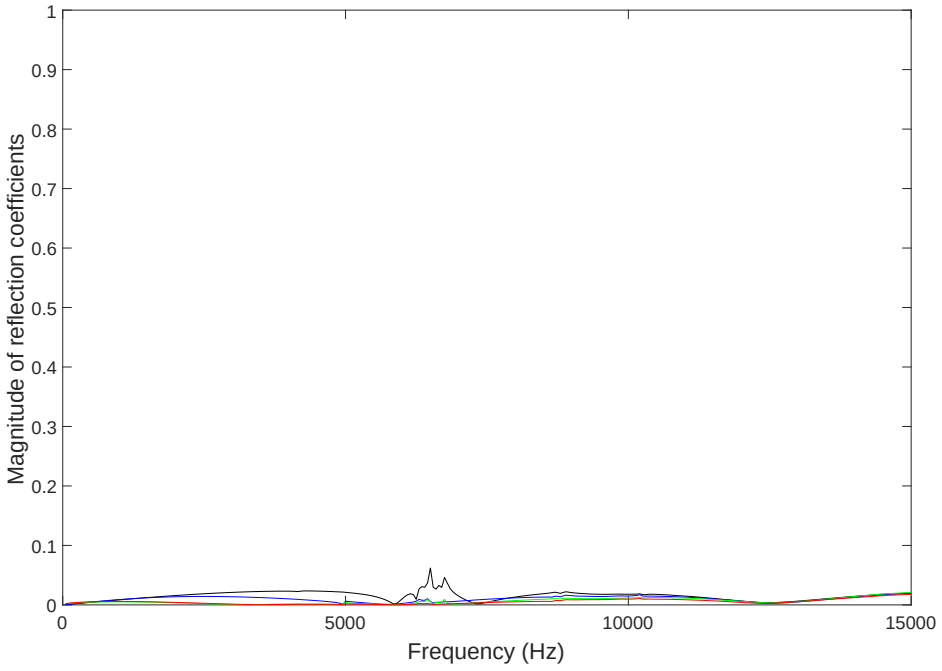


Figure 5.8: Magnitude of the reflection coefficients of fundamental wave modes in an RC section with a 60% single rebar diameter reduction damage over a length $h$ =0.2 m.

Axial (—), torsional (– –), bending(– –), bending transversal (– –).

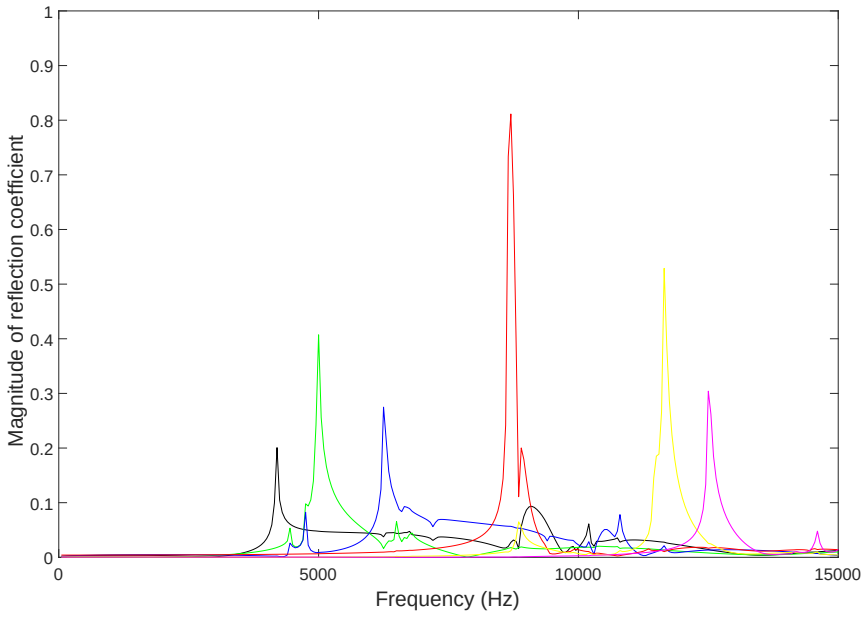


Figure 5.9: Magnitude of the reflection coefficients of evanescent wave modes in an RC section with a 60% single rebar diameter reduction damage over a length $h$ =0.2 m.

E4200 (-), E5000 (−), E6300 (−), E8700 (−), E11700 (−), E12500 (−). E stands for evanescent with their associated cut-on frequency.

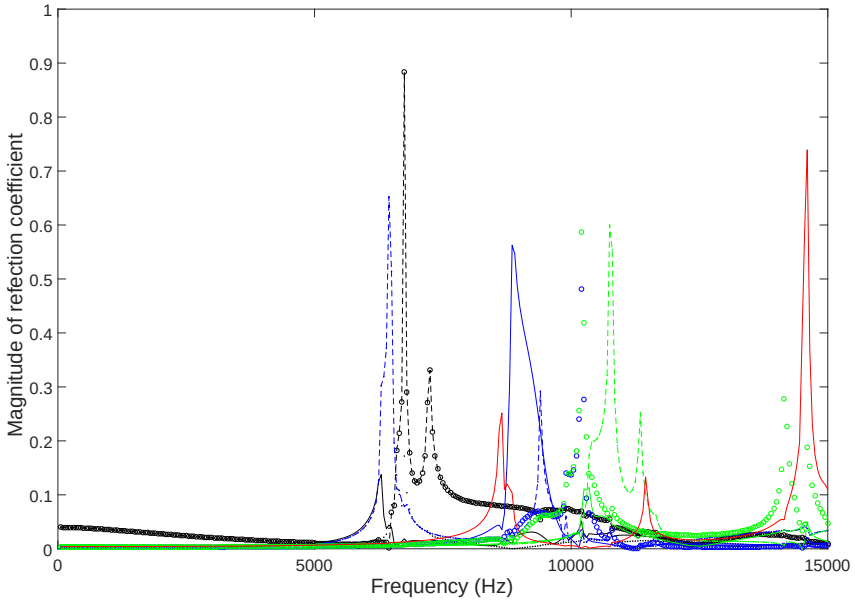


Figure 5.10: Magnitude of the reflection coefficients of complex wave modes in an RC section with 60% single rebar diameter reduction damage over a length $h$ =0.2 m.

C6300 (-), C6600 (· · ·), C7250 (- - -), C8750 (−), C9450 (− − −), C10250 ($o$), C10400 (−), C11400 (− − −), C14200 ($o$), C14500 (−). C stands for complex wavenumbers with their associated cut-on frequency.

| **Wave description** | **Cut-on frequency (Hz)** | **Reflection coefficient** |
|---|---|---|
| Axial | - | 0 |
| Torsional | - | 0 |
| Bending | - | 0 |
| Bending transversal | - | 0 |
| E4200 | 4200 | 0.2 |
| E5000 | 5000 | 0.4 |
| E6300 | 6300 | 0.27 |
| C6300 | 6300 | 0.1 |
| C6600 | 6600 | 0.17 |
| C7250 | 7200 | 0.33 |
| E8700 | 8700 | 0.8 |
| C8750 | 8800 | 0.6 |
| C9450 | 9450 | 0.3 |
| C10250 | 10250 | 0.48 |
| C10400 | 10400 | 0.1 |
| C11400 | 11400 | 0.25 |
| E11700 | 11700 | 0.53 |
| E12500 | 12500 | 0.3 |
| C14200 | 14200 | 0.27 |
| C14500 | 14500 | 0.74 |

Table 5.1: Characteristics of the least attenuated waves in an RC beam associated with 60% rebar reduction damage for length h = 20 cm. E refers to evanescent waves and C refers to complex waves

### 5.3.2 The effect of loss in rebar stiffness and mass

The rebar potential energy $E_p$ is related to its stiffness, and its kinetic energy $E_k$ is related to its mass. Subsequently, the potential and kinetic energies of the embedded reinforcement were computed via conventional FE and compared to the total energies in the RC cross section.

Modal analysis was applied to the undamaged RC beam. Wave modes associated with high reflection are listed in Table 5.1. Then, the modal kinetic and potential energies associated with the concrete and reinforcement elements were extracted for each wave mode. The energy ratio of the reinforcement to the total beam elements is computed. In Figure 5.11 the percentage of the kinetic energy of the reinforcements evaluated at cut-on frequencies is plotted for each wave mode. The magnitude of the reflection coefficients increases with the rebars' increased kinetic energy. Similarly, the magnitude of the reflection coefficients increases with the rebars' percentage potential energy as seen in Figure 5.12. However, the kinetic energy ratio is much more significant and dominant. Therefore, the effect of the rebar mass is more significant than its stiffness.

In other words, the reflection coefficients are more sensitive to the loss of mass of the rebar compared to changes in its stiffness.

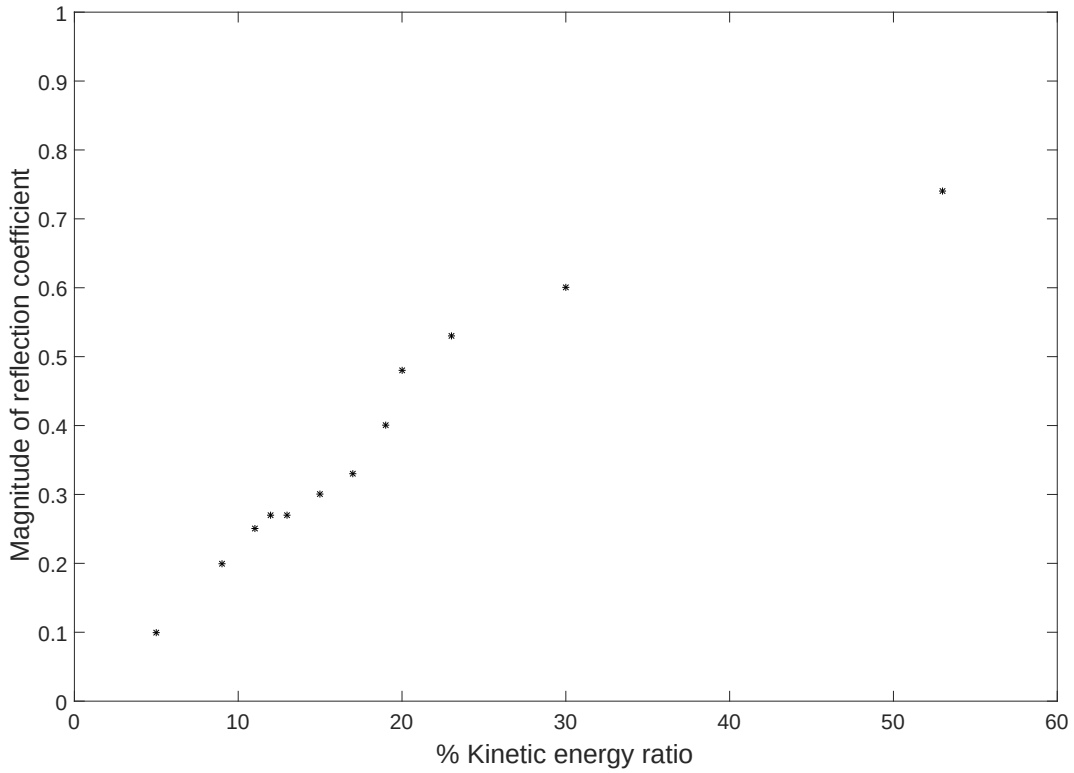


Figure 5.11: Magnitude of the reflection coefficients for fundamental wave modes in an RC section with respect to percentage of kinetic energy associated with the rebars at cut-on frequencies.

### 5.3.3 Discussion and damage criteria

The scattering matrices were formulated for the damaged model. The damage was modelled as a diameter reduction over a specific length to simulate the pitting corrosion of the reinforcement. One would expect a decrease in the diameter of the rebar to increase the magnitude of the reflection coefficients. For this reason, only the smallest detectable damage was modelled for each model respectively. This is why the damage was only limited to a decrease in the rebar diameter equal to 40% or 60%. Full rebar reduction was not considered, since its effect can be seen from external visual inspection of the outer surface of the concrete and therefore it does not need an internal detection method in the first place.

It can be seen from Table 5.1 that the reflection coefficient corresponding to different modes are sensitive at different levels to the rebar diameter reduction. When damage is present, the majority of the nodal displacements in the least attenuated modes possessing high reflection are in the transverse Y and Z directions. In addition, the maximum

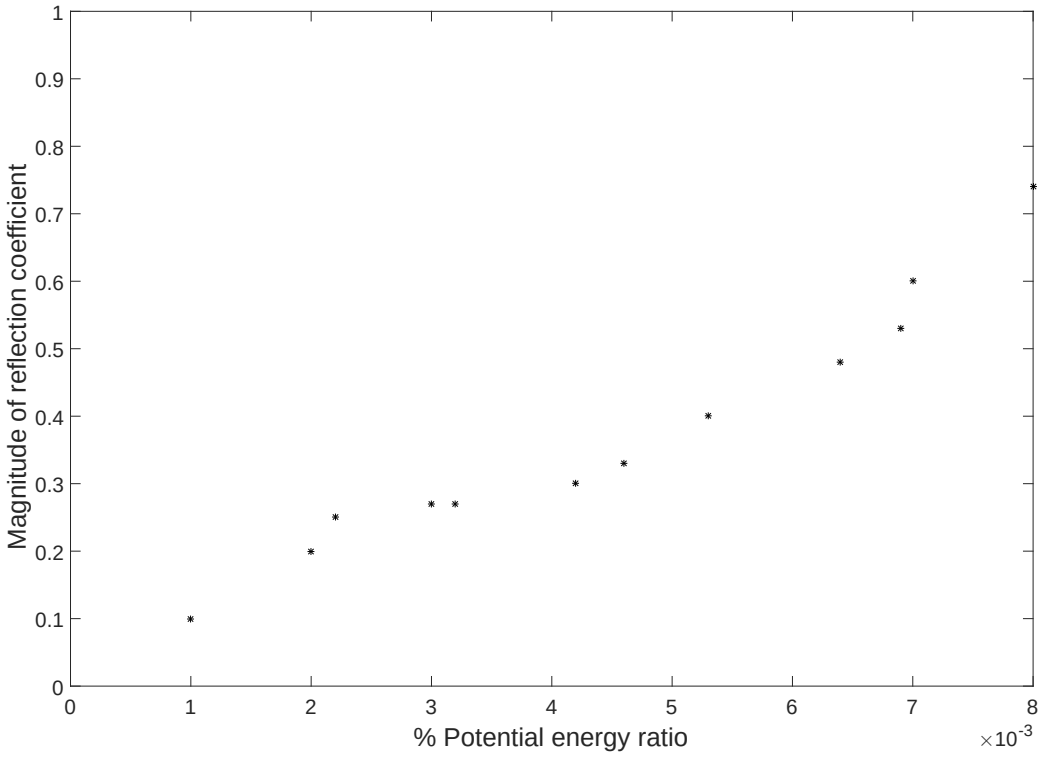


Figure 5.12: Magnitude of the reflection coefficients of fundamental wave modes in an RC section with respect to percentage of potential energy associated with the rebars at cut-on frequencies.

displacement is located at the corners and in the middle side surface of the beam cross section. This configuration gives a possibility to specify a damage criterion associated with the measurement of the side displacements in these directions. The challenge is to separate the displacement due to the defined mode at its cut-on frequency from all other modes excited at this particular frequency.

## 5.4 Conclusions

To summarise, a WFE-WFE-WFE coupling approach has been presented, where the undamaged waveguides were modelled as two semi-infinite beams, and the finite size of the damaged joint waveguide has been modelled via WFE. Then, the waveguides were coupled using the continuity and equilibrium conditions at each junction. Subsequently, the total scattering matrix was formed as a combination of reflection and transmission coefficients due to the finite length of the damaged coupling element.The WFE-WFE-WFE approach was compared to the WFE-FE-WFE approach. Both gave similar results due to rebar diameter reduction. Due to many advantages such as its flexibility for extending the length of the damage, the WFE approach was selected for subsequent simulations.

For each RC model, damage scenarios with different diameter reduction and damage length were selected to represent corrosion. The magnitude of the reflection coefficients were found to be more sensitive to the change in the rebar diameter rather than the damage length. This is related to the physics of the strength of the wave reflection at the interface between the original and reduced rebar sections. From simulation, it has been shown that the effect of the rebar diameter reduction is primarily governed by the mass reduction which is more significant than the length over which the rebar reduction has taken place. In addition, the rebar kinetic energy at the cut-on frequencies is dominant in comparison to their potential energy. Therefore, the effect of rebars' loss in mass is more significant on the magnitude of the reflection compared to its stiffness.

Furthermore, the least attenuated modes were selected as potential modes sensitive to the damage and the associated nodal displacements were shown in Figure 4.13 and Figure 4.14 in Chapter 4. The majority of the nodal displacements for these least attenuated modes with high reflection are in the Y and Z directions. This configuration gives a possibility for a defined damage criterion associated with the measurement of the corner displacements in these directions. This will be an area for experimental investigation and validation presented in the next chapter.

# Chapter 6

# Damage identification using cut-on waves

## 6.1 Introduction

The ultimate aim of this research is to define a damage identification algorithm for steel reinforced concrete beams that does not require direct contact with the reinforcements. In the previous chapter, it was seen that guided waves have high reflection coefficients at their cut-on frequencies due to damage modelled by loss of rebar thickness. In practice, one cannot reliably estimate these magnitudes from forced response measurements on the surface unless all the dispersion relations for all contributing wavetypes are known.

One is interested only in frequencies where strong reflections occur, i.e. near the cut-on frequencies, close to which the wavenumber is small. It is thus proposed that for this purpose the amplitudes of the positive and negative going waves near cut-on can be estimated using the Wave Amplitude Decomposition method in Halkyard and Mace (1995) using an assumed small wavenumber value i.e. exact knowledge of the dispersion curve would be unnecessary.

To evaluate the algorithm, it is first applied to infinite RC beams, where the estimated wave amplitudes are compared with the exact solution. In order to test and validate its robustness, the technique is then applied to finite beams with different boundaries namely perfectly reflecting, fixed and coupled to another beam. In addition, a parametric study is presented which considers the effect of the value of the wavenumber adopted and transducer spacing. A change in the estimated wave amplitudes along the length of the beam is then proposed as a potential damage localisation technique. Subsequently the benefits, accuracy and limitations of the approach are discussed.

## 6.2 Wave Amplitude Decomposition approach

The Wave Amplitude Decomposition (WAD) approach is adapted here to estimate the wave amplitudes in the RC beams where only values at wave cut-on are of interest. First, the feasibility of this method is tested using simulations, where a parametric study is applied in a noise free environment.

In a waveguide, the WAD method has been employed to identify the positive and negative going wave amplitudes at a specific point. Halkyard and Mace (1995) applied the WAD method to an experimental uniform beam undergoing flexural vibration in order to evaluate intensity, energy density and reflection coefficients. Optimisation of the condition number of the WAD matrix showed preferable transducer separations for better results. Subsequently, Mace and Halkyard (2000) applied the WAD method to digitally filtered outputs of an array of the sensors in the frequency domain followed by a reconstruction in the time domain. Compared to other methods, numerical simulations of the measurements were presented and the approach was shown to be reasonably insensitive to sensor miscalibration and measurement noise. Later, Muggleton et al. (2007) estimated the reflection and transmission coefficients of a joint when a pipe is undergoing flexural vibration. The wave amplitudes of fundamental modes were identified via the WAD approach as applied to experimental data. So, the WAD method has been demonstrated on flexural and other fundamental wave types present in a thin beam. However, in this research, the approach was applied to a deep non-homogeneous beam where multiple and complicated wave types can coexist.

One can assume a set of measurements from $n$ transducers at $n$ locations on a waveguide, where there are $m$ wave components to be estimated. The output responses (displacement, velocity or acceleration) are related to the wave amplitudes by

$$\mathbf{W} = \mathbf{\Lambda}\mathbf{A} \tag{6.1}$$

where

$$\mathbf{W} = \begin{Bmatrix} W(x_1) \\ W(x_2) \\ \vdots \\ W(x_n) \end{Bmatrix}; \mathbf{\Lambda} = \begin{bmatrix} e^{-ik_1x_1} & \dots & e^{-ik_mx_1} & e^{ik_1x_1} & \dots & e^{ik_mx_1} \\ e^{-ik_1x_2} & \dots & e^{-ik_mx_2} & e^{ik_1x_2} & \dots & e^{ik_mx_2} \\ \vdots & & \vdots & \vdots & & \vdots \\ e^{-ik_1x_n} & \dots & e^{-ik_mx_n} & e^{ik_1x_n} & \dots & e^{ik_mx_n} \end{bmatrix}; \mathbf{A} = \begin{Bmatrix} \boldsymbol{A}^+ \\ \boldsymbol{A}^- \end{Bmatrix} \tag{6.2}$$

$\mathbf{W}$ is an $n\times1$ vector comprising FRFs relating outputs at different points from $x_1$ to $x_n$ due to an excitation force. In addition, $\mathbf{\Lambda}$ is a propagation matrix of size $n\times2m$ which is dependent on the positive and negative going wavenumbers to be considered in the waveguide at each measurement location, and $\mathbf{A}$ is a $2m\times1$ vector comprising $\boldsymbol{A}^+$ and $\boldsymbol{A}^-$ as the $m$ positive and negative going wave amplitudes estimated at the mid point of the sensor array. In general, one needs to include all waves that contribute significantly

to the observed response and their wavenumbers should be estimated beforehand to evaluate the $\mathbf{\Lambda}$ matrix.

If the number of measurements is less than the number of wave components, i.e. $n < m$, the system is considered undetermined and additional conditions are required to compute the solution. In a determined system where the number of measurements matches the number of wave components, one can determine these wave amplitudes by

$$\mathbf{A} = \mathbf{\Lambda}^{-1}\mathbf{W} \tag{6.3}$$

In an overdetermined system, where $n > m$, the wave components can be found in a least squares manner as

$$\mathbf{A} = (\mathbf{\Lambda}^{H}\mathbf{\Lambda})^{-1}\mathbf{\Lambda}^{H}\mathbf{W} \tag{6.4}$$

where superscript $H$ indicates the conjugate transpose of a matrix. Normally the matrix is singular when the transducer spacing is an integer number of half-wavelengths. In this case, the matrix is ill-conditioned and may cause disproportionately large errors in the estimated wave amplitudes. Therefore, it is suggested that the transducer spacing must be less than half the shortest wavelength in the frequency range of interest for the method to identify the positive and negative going wave amplitudes correctly.

In addition, the number of transducers considered in the WAD approach has been discussed in the literature. In Halkyard and Mace (1995), when evanescent waves are ignored and only two propagating waves are considered, only two transducers are required to compute the wave amplitudes. However, if in addition a single evanescent wave is considered, then three or more transducers are required. Furthermore, where two evanescent waves are present then at least four transducers are necessary in the array to evaluate the wave amplitudes. It has also been shown that the condition number of matrix $\mathbf{\Lambda}$ deteriorates with an increasing number of unknown wave components.

Regarding the transducers' positions, the condition number of matrix $\mathbf{\Lambda}$ is dependent on the position of the centre of the transducer array when evanescent waves are considered (see Halkyard and Mace (1995)). The closer the transducers are to the excitation force or discontinuity, the higher is the condition number. Therefore, one tends to select the transducer positions in the far-field.

## 6.3 Wave amplitude estimation at cut-on

For the purpose of detecting reflections from regions of damage, one is interested only in estimating wave amplitudes near the cut-on frequencies close to which the wavenumber is small. First though, an *undamaged* infinite RC beam is considered, where the estimated WAD solutions from using a small wavenumber representing the wave modes cutting on are compared with the exact solutions.

At the cut-on of a wave, which corresponds to a cross-section resonance, it is assumed here that the wave dominates the response such that the contributions of all other waves are negligible. Furthermore, one could also assume the wavenumber is zero (real and imaginary parts) representing the value of the evanescent waves' wavenumber when they start cutting on, but then $\mathbf{\Lambda}$ becomes singular. To overcome this problem, a small value for the wavenumber is selected. Subsequently, the $\mathbf{\Lambda}$ matrix and $\mathbf{A}$ vector in the WAD Equation (6.2) can be reduced.

When a small real wavenumber value $k_s$ is selected, the $\mathbf{\Lambda}$ matrix is of size $n\times2$ comprising the positive and negative propagating waves as

$$\mathbf{\Lambda} = \begin{bmatrix} e^{-ik_s x_1} & e^{ik_s x_1} \\ \vdots & \vdots \\ e^{-ik_s x_n} & e^{ik_s x_n} \end{bmatrix} \tag{6.5}$$

The associated $\mathbf{A}$ vector is of size $2\times1$ comprising $A^+$ and $A^-$ as scalar values for the positive and negative propagating wave amplitudes respectively.

However, if the $k_s$ value is selected to be real and imaginary representing the wavenumber just before or after q cut-on frequency, the $\mathbf{\Lambda}$ matrix becomes of size $n\times4$ comprising the positive and negative propagating waves in addition to evanescent ones as

$$\mathbf{\Lambda} = \begin{bmatrix} e^{-ik_{sr} x_1} & e^{k_{si} x_1} & e^{ik_{sr} x_1} & e^{-k_{si} x_1} \\ \vdots & \vdots & \vdots & \vdots \\ e^{-ik_{sr} x_n} & e^{k_{si} x_n} & e^{ik_{sr} x_n} & e^{-k_{si} x_n} \end{bmatrix} \tag{6.6}$$

where $k_{sr}$ and $k_{si}$ are the real and imaginary wavenumbers, respectively. The associated $\mathbf{A}$ vector is of a size $4\times1$ comprising $\boldsymbol{A}^+$ and $\boldsymbol{A}^-$ as positive and negative propagating/evanescent going wave amplitudes, respectively.

This reduced WAD approach was then applied to the response of an infinite undamaged beam. The infinite undamaged RC beam is modelled in WFE as a small segment with the material properties as given in Table 4.1. The steel rebars are 25 mm in diameter. The WFE solutions are employed to calculate the forced response from exact wave amplitudes at $x_r = 0.375$ m. Since no boundaries are present, only the positive going wave amplitudes are calculated. In this model, one should apply the excitation force on the structure in a particular direction to excite specific waves. Figure 4.13 and Figure 4.14 show that the maximum displacement occurs in the Z direction in the middle of the top and bottom faces of the cross section for evanescent and complex wave modes respectively. Based on this observation, it is preferable to excite the beam in the Z-direction to excite these wavemodes, since typically only the top and bottom faces of the RC beams are accessible in real structures. The amplitude of the positive going wave was computed using a small value for the wavenumber $k_s = 0.1$ and $0.1 + 0.1\,i$ rad/m, with four transducers at 0.3 to 0.45 m from the excitation force. The estimated

and exact amplitudes of the least attenuated waves defined in Section 4.4 are illustrated in Figure 6.1.

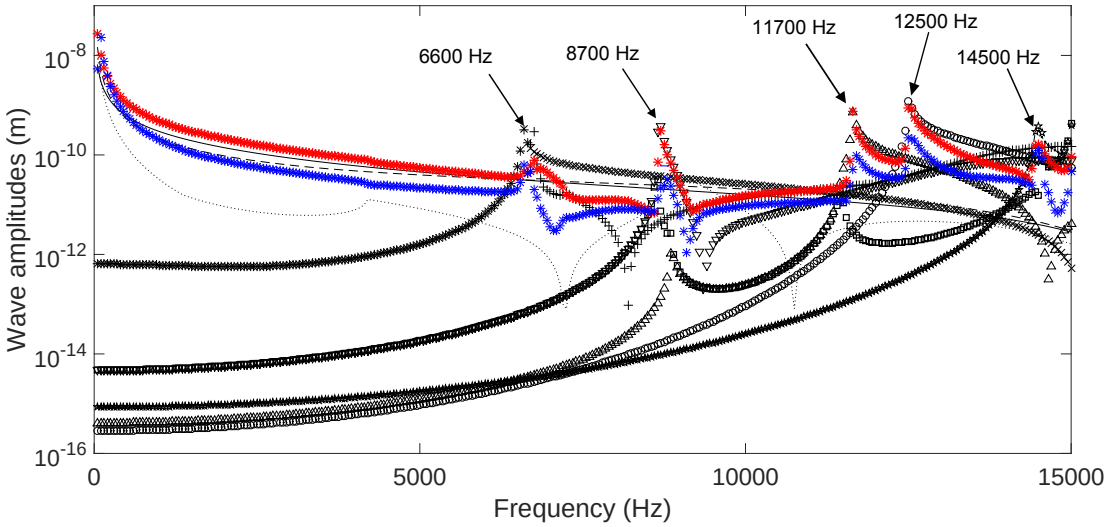


Figure 6.1: The amplitudes of the least attenuated waves in an infinite undamaged RC beam at $x_r = 0.375$ m.

WFE solution: torsion (—), bending (- - -), E4200 ($\cdots$), C6600 ($\times$), C7250 ($+$), E8700 ($\triangledown$), E11700 ($\triangle$), E12500 ($\circ$), C14500 ($\star$), C15000 ($\square$); WAD solution: using $k_s = 0.1$ rad/m ($*$), using $k_s = 0.1 + 0.1\ i$ rad/m ($*$).

Using a small real wavenumber, the estimated wave amplitude was estimated using Equation 6.5 and is depicted by the red markers in Figure 6.1. It can be seen that it aligns with the exact solution at the peaks corresponding to the cut-on frequencies of 8700, 11700 and 12500 Hz. However, these peaks are not captured well at 6600 and 14500 Hz. This is due to the fact that a small real wavenumber of 0.1 rad/m representing the waves cutting on is present at the cut-on frequencies of 8700, 11700 and 12500 Hz as in Figure 4.8 for the evanescent waves E8700, E11700 and E12500 wave modes. In contrast, this value of wavenumber is not correct for the complex waves C6600 and C14500 at their cut-on frequencies as shown in Figure 4.9. This means that the WAD approach correctly identifies the response at the cut-on frequencies associated with the small real trial wavenumber used but only for evanescent not complex waves. This is essential for the later application of the algorithm, since high reflection coefficients exist at these frequencies when damage is present.

Using a small complex wavenumber, the estimated wave amplitude was estimated using Equation 6.6 and is depicted by the blue markers in Figure 6.1. One can notice that it lacks the correct peak at all cut-on frequencies compared to the exact solution. This means that the use of a small complex wavenumber does not detect the response of the evanescent waves at their cut-on frequencies. Subsequently, a real wavenumber value of $k_s = 0.1$ rad/m was selected for the damage detection algorithm since it correctly

estimates the response near the cut-on frequencies, at which the reflection coefficients are sensitive to loss of rebar thickness.

## 6.4 The damage identification algorithm for infinite and semi-infinite RC beams

Damage introduced as a rebar diameter reduction produced high reflection at the cut-on frequencies of evanescent waves as shown in Chapter 5. Using the simulated RC beam forced response, one could obtain these coefficients by using the full WAD approach with a priori knowledge of all the wavenumbers present. However, since one is only interested in the wave amplitudes at the cut-on frequencies, it is an inverse problem that can be simplified if only one wavetype is dominant.

In Section 6.3, it has been shown that using a small real wavenumber detects the correct wave amplitudes near the cut-on frequencies of 8700, 11700 and 12500 Hz. Having computed the positive and negative going wave amplitudes from the forced response using the WAD approach, these values can be compared to identify the presence or absence of the damage. Here only the solution near the cut-on frequency is of interest.

One can estimate the positive and negative wave amplitudes in a waveguide using the reduced WAD approach presented in Section 6.3. Then, a damage identification metric can be defined simply as the ratio of negative to positive going wave amplitudes. The variability of this ratio with respect to the absence/presence of damage and beam boundaries are discussed in this section.

Considering first an infinite damaged RC beam in Figure 6.2, $a^+$ is the incident wave at the damage interface, $a^-$ and $b^+$ are the reflected and transmitted waves respectively. When no damage is present in the beam, only the positive going waves are present. Hence, the ratio of the amplitudes of the negative to positive going waves $|\frac{a^-}{a^+}|$ is equal to 0. However, when damage exists in the beam, this ratio $|\frac{a^-}{a^+}| = R_{T12}$ is less than 1 but greater than zero. This is due to the presence of the damage, where $R_{T12}$ is the reflection coefficient relating the incident and reflected waves travelling from waveguide 1 to 2 as presented in Section 5.2.2.

Subsequently, when damage is introduced as a loss of rebar thickness, $|R_{T12}| > 0$ near the cut-on frequency. Away from the latter, $|R_{T12}| \approx 0$. Then, a plot of the wave amplitude ratio $|\frac{a^-}{a^+}|$ resembles that as shown in Figure 6.3, where the peak is greater than zero only near the cut-on frequency. In Figure 6.4, the ratio of negative to positive wave amplitudes in an infinite RC beam is plotted at cut-on frequencies for different loss of thickness of a single rebar with length $h$ of 0.2 m. It can be seen that the ratio increases with the level of damage. However, the E8700 wave mode is more sensitive to lower damage than the E11700 and E12500 wave modes cutting on.

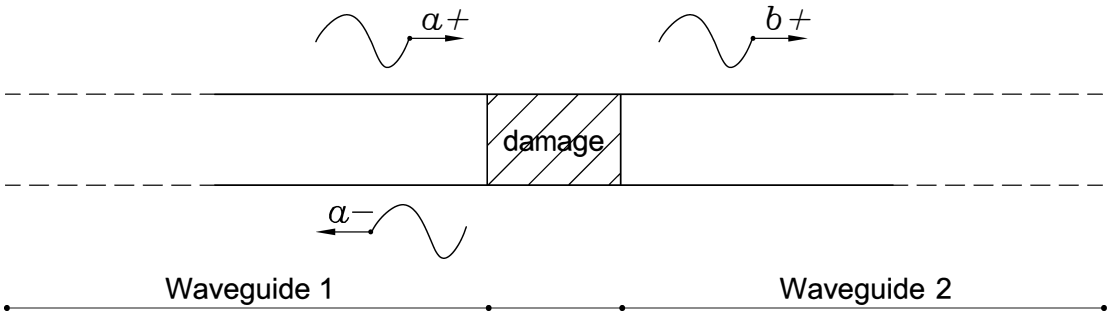


Figure 6.2: Wave amplitudes of infinite beam with damage.

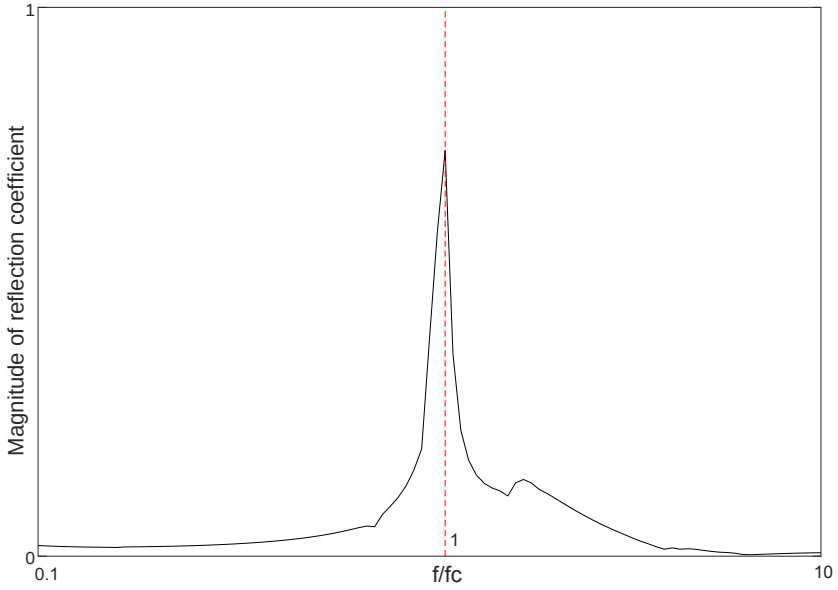


Figure 6.3: The magnitude of teh reflection coefficient for waves in an infinite beam incident on a reduced diameter (damaged) semi-infinite length beam plotted against non-dimensionalised frequency. The cut-on frequency of a wave in the undamaged (no reduced rebar diameter)RC beam – – –)

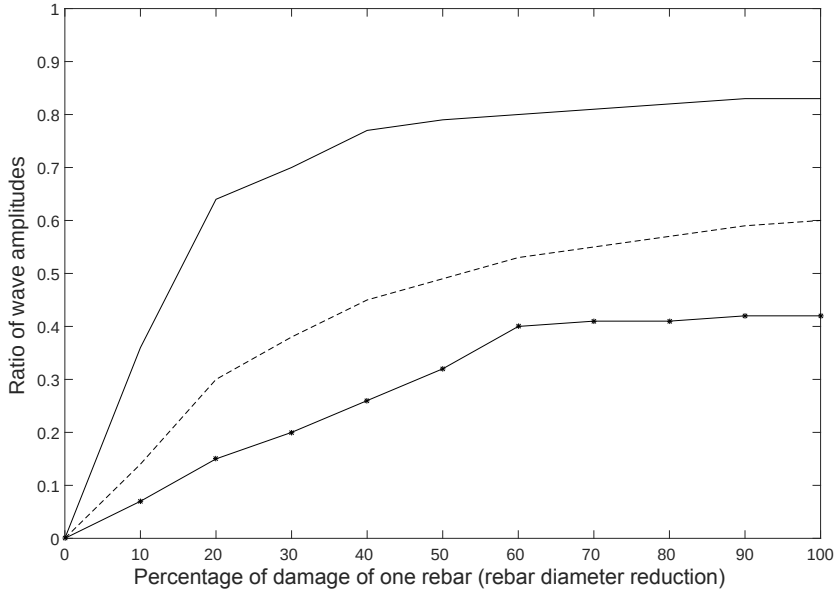


Figure 6.4: Ratio of negative to positive wave amplitudes at cut-on frequencies in infinite RC beam with different damage extents.

E8700 (—), E11700 (- - -), E12500 (-∗-).

Consider next a semi-infinite damaged beam with right boundary as shown in Figure 6.5. $a^+$ is the incident wave travelling from waveguide 1 to 2 at the damage interface, $a^-$ and $b^+$ are the reflected and transmitted waves defined as

$$a^- = R_{T_{12}} a^+ \;\; ; \;\; b^+ = T_{T_{12}} a^+ \tag{6.7}$$

$c^-$ is the transmitted wave travelling from waveguide 2 to 1. Therefore, the total negative going wave amplitude is $|a^- + c^-|$.

When no damage is present in the semi-infinite beam, the amplitude of the positive going wave should be equal to the negative going one provided that the far boundary is perfectly reflecting i.e. $|a^+| = |c^-|$ with $a^- = 0$. Hence, the practically observable ratio of the amplitudes of the negative to positive going waves $|\frac{a^- + c^-}{a^+}|$ is equal to 1. In this chapter, perfectly reflecting boundaries are defined as those with unity diagonal reflection matrices, i.e. full reflection with neither phase change nor mode conversion.

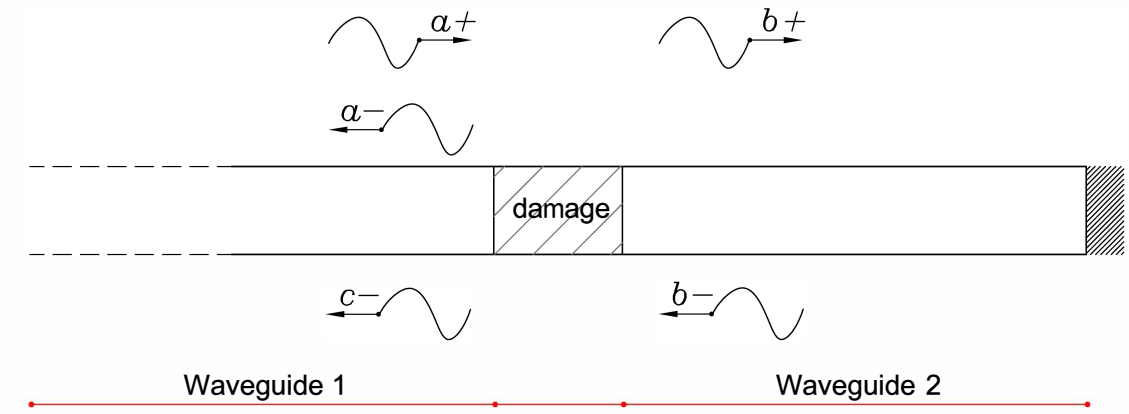


Figure 6.5: Wave amplitudes in semi-infinite beam with loss of rebar thickness as damage scenario.

However, when damage exists, the amplitude ratio of the negative to positive going waves can be written as

$$|\frac{a^- + c^-}{a^+}| \leq |\frac{a^-}{a^+}| + |\frac{c^-}{a^+}| \tag{6.8}$$

$c^-$ is related to the incident wave as (see Appendix B for details)

$$c^- = (T_{T_{21}}[\mathbf{I} - \tau(L_2) r_R \tau(L_2) R_{T_{21}}]^{-1} \tau(L_2) r_R \tau(L_2) T_{T_{12}}) a^+ \tag{6.9}$$

where $T_{T21}$ is the transmission coefficient for the wave travelling from waveguide 2 to 1, $\tau$ is the propagation matrix value, $L_2$ is the beam length after the damage, $r_R$ is the right boundary scattering value and $T_{T12}$ is the transmission coefficient relating the wave amplitude travelling from waveguide 1 to 2 (Section 5.2.2).

Then, by using Equation 6.7 and 6.9, one can write

$$|\frac{a^-}{a^+}| = R_{T_{12}} \;\; ; \;\; |\frac{c^-}{a^+}| = T_{T_{21}}[\mathbf{I} - \tau(L_2) r_R \tau(L_2) R_{T_{21}}]^{-1} \tau(L_2) r_R \tau(L_2) T_{T_{12}} \tag{6.10}$$

Consider a semi-infinite RC beam with a perfectly reflecting right boundary. The beam is damaged with 60 % diameter reduction over a length of 20 cm. In Figure 6.6, the ratio of exact wave amplitudes using Equation 6.10 are plotted for different wave modes. At the cut-on frequencies, the ratio of the combined total negative to positive wave amplitudes $|\frac{a^-+c^-}{a^+}|$ is dominated by the contribution due to the $|\frac{a^-}{a^+}| = |R_{T12}|$ value. Away from the cut-on frequency, $|R_{T12}|$ is $\approx 0$ and $|\frac{c^-}{a^+}|$ is given by Equation 6.10.

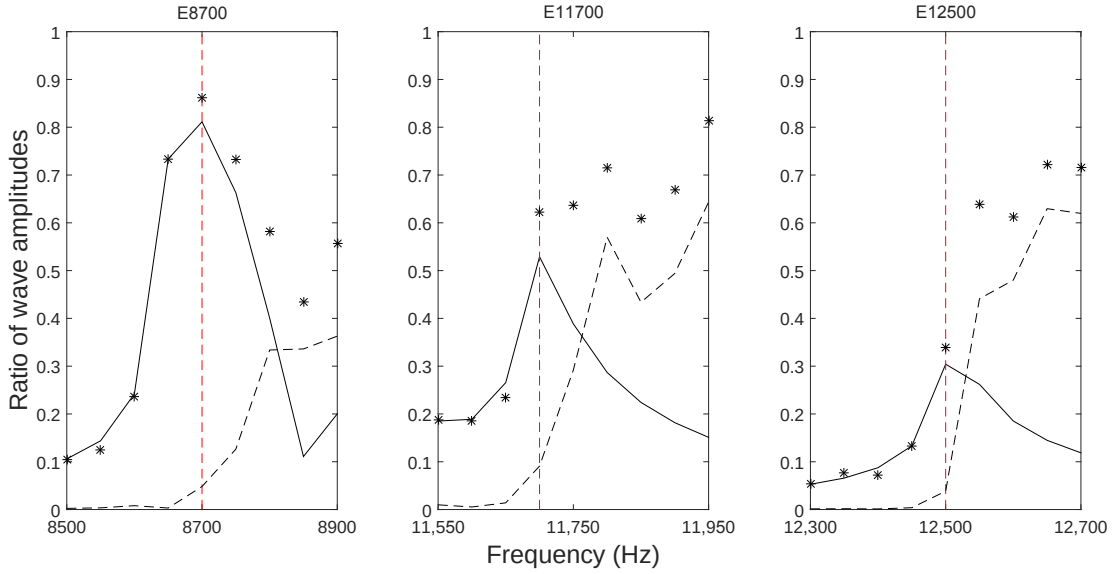


Figure 6.6: Ratio of the negative to positive wave amplitudes in a semi-infinite beam with a perfectly reflecting right boundary and 60 % loss of rebar thickness.

Ratio of wave amplitudes: $|\frac{a^-}{a^+}| = |R_{T12}|$ (—), $|\frac{c^-}{a^+}|$ (- - -), $|\frac{a^-+c^-}{a^+}|$ (∗). Cut-on frequencies (– – –).

By applying the damage algorithm using a small real wavenumber, the plot of the ratio of the estimated wave amplitudes should resemble Figure 6.7. At the cut-on frequency, the ratio is close to the value of $|R_{T12}|$. At other frequencies, the amplitudes of the positive and negative going waves are equal and the amplitude ratio is very close to 1.

Considering the case of a semi-infinite RC beam with perfectly reflecting right boundary, the ratio of wave amplitudes can be estimated for different extents of the damage at the cut-on frequencies. This is illustrated is Figure 6.8. When there is no damage in the RC beam, the ratio of positive to negative going wave amplitudes is 1 when considering the application of a small wavenumber in the WAD solution. Further demonstration of this statement is presented in simulation in Section 6.6.

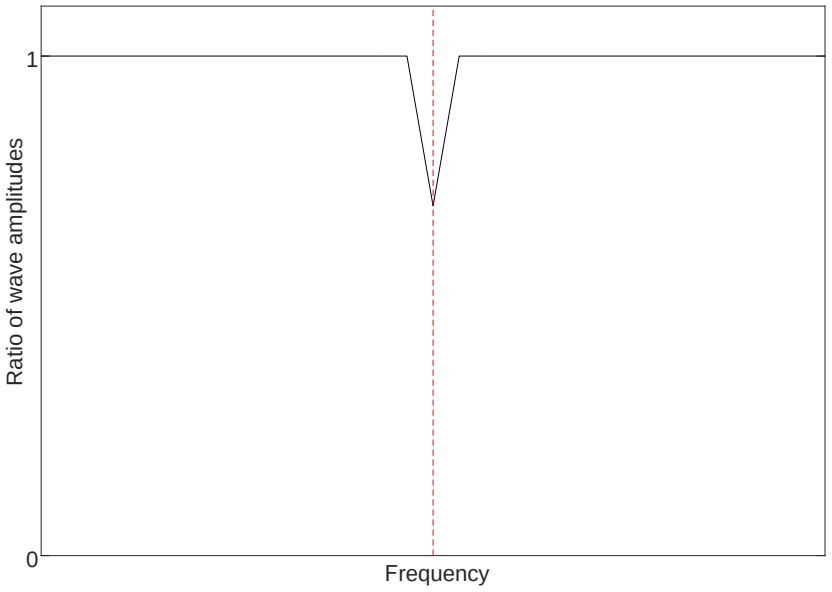


Figure 6.7: Ratio of the negative to positive wave amplitudes in a semi-infinite beam, with right boundary, due to loss of rebar diameter as a damage scenario when considering the application of a small wavenumber in the WAD solution. Cut-on frequency (– – –)

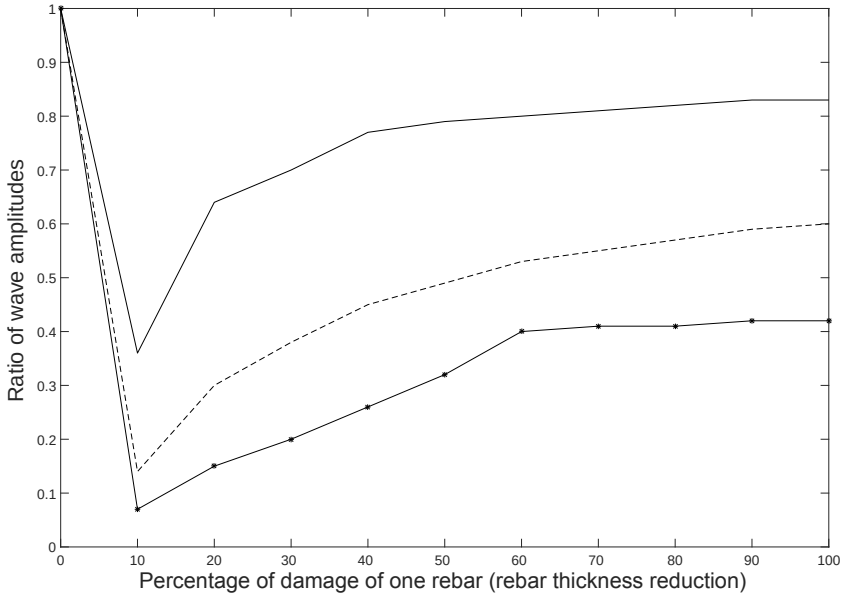


Figure 6.8: Ratio of negative to positive wave amplitudes at cut-on frequencies in semi-infinite RC beam with different extents of damage.

E8700 (—), E11700 (- - -), E12500 (-∗-).

When damage is present in one rebar, this ratio starts to decrease until the damage is 10% and is similar for the wave types plotted. This due to the small values of the reflection coefficients associated with this small damage scenario. After which the ratio starts increasing to become fairly constant for damage greater than 60%. However,

between 10% and 60% damage, the ratio is distinct for different wave types. For very small damage, less than 5 % rebar diameter reduction, the waves propagate past the reduction and reflect off the finite end and so the reflection coefficient is close to unity. As the damage increases to 10 % reduction, a small reflection occurs as the incident wave propagates past the damage but then the wave gets trapped between the damage and the end of the beam. As the level of rebar diameter reduction or equivalently damage increases still further, higher reflection occurs in the incident wave due to the change in impedance at the first reflection between the damaged and undamaged sections. Then, the wave reflection is independent of the finite end and similar to the reflection from a damaged section in the middle of an infinite length RC beam.

The aim here not to have full rebar reduction since its effect can be seen from external visual inspection of the outer surface of the concrete and therefore it does not need an internal detection method in the first place as explained earlier in Section 5.3.3. Here, as the amount of damage increases so the ratio of wave amplitudes increases again. This means that the ratio of wave amplitudes may not be effectively used to convey the extent of rebar reduction when the latter is too small or too large.

## 6.5 Damage identification on finite RC beams with perfectly reflecting boundaries

The damage identification technique is now applied to finite damaged and undamaged RC beams where the boundaries are perfectly reflecting at both ends. This is to validate the algorithm accuracy when no mode conversion is present at the boundaries. In addition, the effect of transducer spacing on the estimated wave amplitudes from the WAD approach is investigated.

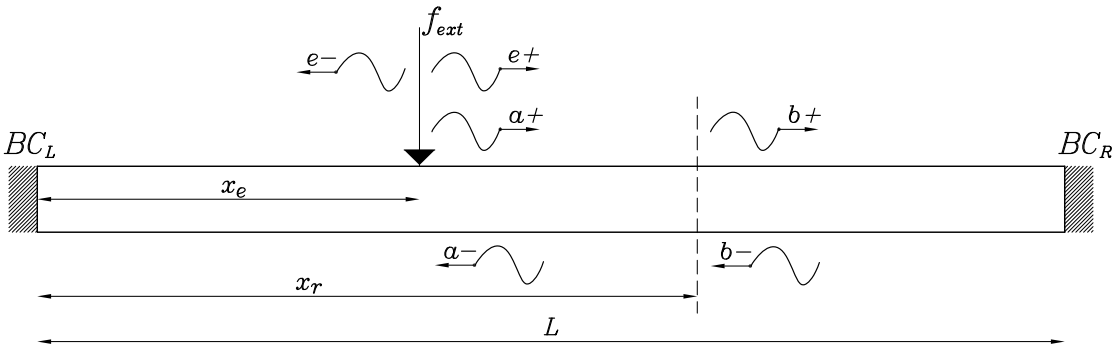


Figure 6.9: Forced response and wave amplitudes of a finite RC beam with perfectly reflecting left and right boundaries.

The forced response setup of a finite RC beam with left and right boundaries $BC_L$ and $BC_R$ is considered as shown in Figure 6.9. $BC_L$ and $BC_R$ are considered to be perfectly

reflecting and so no wave mode conversion occurs. The negative and positive going waves are related by the term $\boldsymbol{\tau}(L - x_r)\mathbf{r}_R\boldsymbol{\tau}(L - x_r)$ as shown in Equation 3.49. In the absence of damping, the propagation matrix $\boldsymbol{\tau}(L - x_r)$ is a phase change between the two positions $L$ and $x_r$. As a result, the negative and positive going waves are related based on the reflection coefficient matrix of the right boundary $\mathbf{r}_R$. The model material properties are given in Table 4.1. The undamaged diameter of the steel rebars is 25 mm and the total length of the beam is $L = 2$ m. The excitation force is at a distance $x_e = 0.3$ m from the left boundary.

The finite damaged RC beams were then modelled with 40% and 60% rebar diameter reduction with perfectly reflecting boundaries. The damage detection algorithm is applied using the following: the small wavenumber $k_s = 0.1$ rad/m, four transducers at 0.3 to 0.45 m from the excitation force. The ratio of the negative to positive estimated wave amplitudes is plotted for the damaged and undamaged beams in Figure 6.10. The undamaged beam shows a constant reflection ratio value of 1 over the frequency range, due to the absence of damage and wave mode conversion at the boundaries.

However, the damaged models show a reflection ratio of less than 1 near the cut-on frequencies of 8700, 11700 and 12500 Hz. The values of this ratio agree approximately with the magnitudes of the reflection coefficients due to damage as per the illustration presented in Section 6.4. Away from these cut-on frequencies, the ratio of the negative to positive estimated wave amplitudes is near 1. This is due to the fact that no wave mode conversion occurs at the boundaries and the change in the wave amplitudes is only present at the cut-on frequencies.

Next, a parametric simulation investigates the effect of the transducer spacing. Normally the $\boldsymbol{\Lambda}$ matrix is singular when the transducer spacing is an integer number of half-wavelengths. The matrix is then ill-conditioned and may cause errors in the calculated wave amplitudes. Therefore, it is suggested that the transducer spacing must be less than half the shortest wavelength for the method to correctly identify the positive and negative going wave amplitudes.

However, the use of a small real wavenumber results in higher imaginary parts in the $\boldsymbol{\Lambda}$ matrix (dominated by $e^{-ikx}$) and therefore deteriorates its condition number. In order to improve the conditioning of the $\boldsymbol{\Lambda}$ matrix, whilst using a small real wavenumber, one can modify the transducer spacing. Here, four transducers (denoted as transducers 1 to 4) are used with different array lengths and spacing. In Figure 6.11, the condition number of the $\boldsymbol{\Lambda}$ matrix is plotted against the various array length for $k_s = 0.1$ rad/m.

When a uniform spacing is applied, the transducer spacing is a constant value of the array length divided by 4. However, when non-uniform spacing is used, the position of each transducer (denoted from 1 to 4) is retrieved from Figure 6.12. Here, transducers 2 and 3 have been shifted by the same absolute amounts and so the transducer separation is almost uniform for longer arrays. For instance, for an array length of 0.6 m, transducer

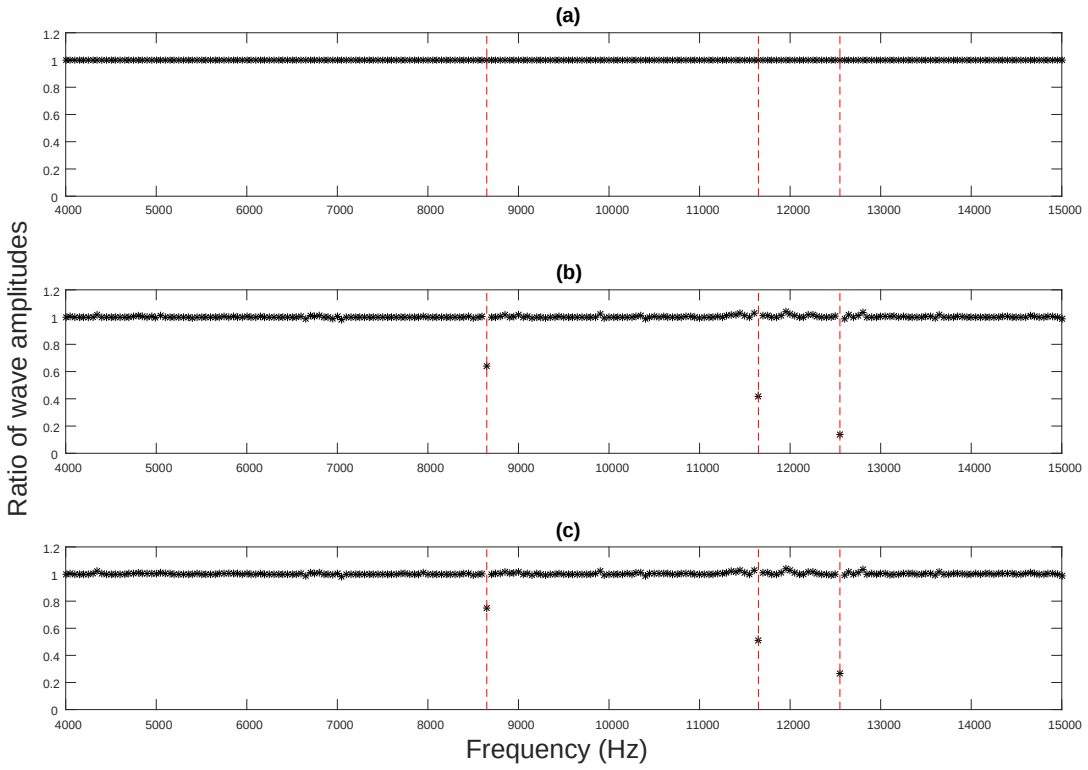


Figure 6.10: The ratio of the estimated negative to positive wave amplitudes for damaged and undamaged RC beams with perfectly reflecting boundaries.

(a): undamaged RC beam, (b): 40% damaged RC beam, (c): 60% damaged RC beam. Cut-on frequencies (– – –).

2 is located at 0.18 m, transducer 3 is located at 0.42 m and transducer 4 at 0.6 m from transducer 1.

For these reasons, the use of non-uniform transducer spacing improves the conditioning of the $\mathbf{\Lambda}$ matrix whilst using a smaller array length as shown in Figure 6.11. Therefore, a non-uniform transducer spacing with a small array length was subsequently selected for implementing the damage detection algorithm.

The condition number decreases with increased transducer spacing. This agrees with the discussion in Mace and Halkyard (2000). Therefore, larger transducer spacing is recommended for better results. However, transducer spacing selection is limited when it comes to damaged beams. Based on previous discussions and findings, one is interested in estimating the positive and negative going wave amplitudes spatially on the beam on one side of the damage.

Since the damage location is considered unknown, it is advisable to select a smaller transducer spacing that leads to a smaller array length that does not interfere or overlap with the damage location.

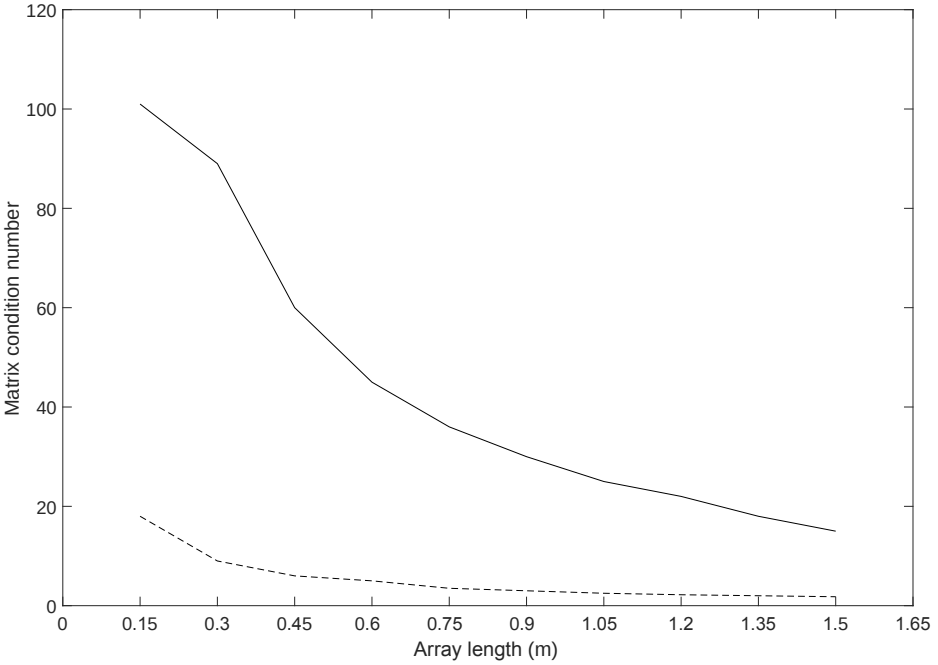


Figure 6.11: Condition number of propagating matrix for four transducers array length for undamaged RC beam.

Wavenumber $k_s = 0.1\ rad/m$: uniform spacing (—), non-uniform spacing (- - -).

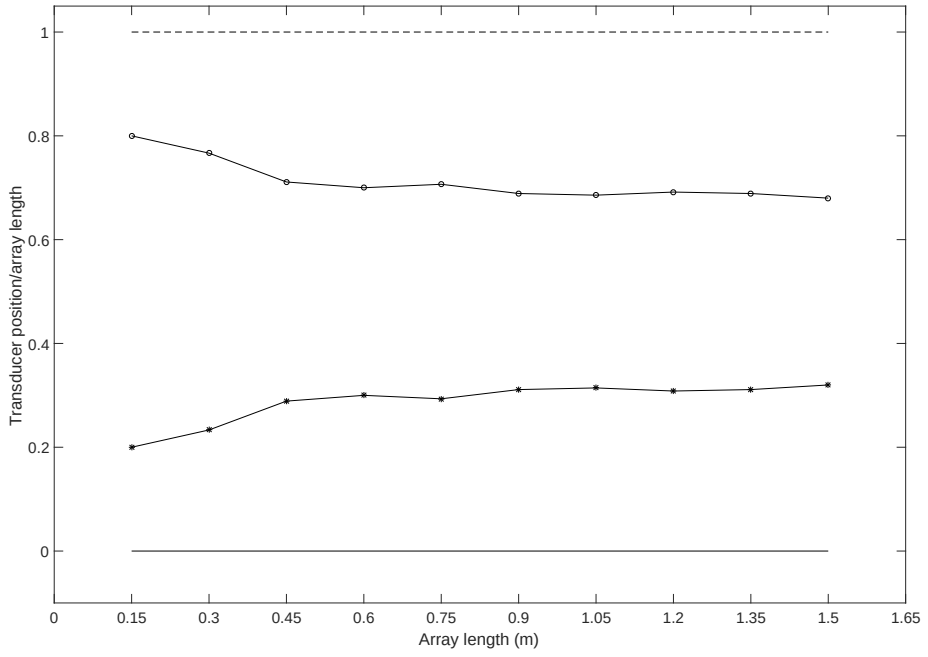


Figure 6.12: Transducer position with respect to array length when non-uniform spacing is applied. Transducer 1 is taken as the origin of various positions.

Transducer notation: 1 (—), 2 (- $*$ -), 3 (- $\circ$ -) and 4 (- - -).

## 6.6 Damage identification on RC beams with fixed boundaries

So far, the damage identification algorithm has been demonstrated on damaged and undamaged RC beams with perfectly reflecting boundaries. In this section, its robustness and potential to detect damage in the presence of mode conversion is investigated.

First, both beam's ends $BC_L$ and $BC_R$ are considered to be fully fixed at all the interface nodes. The corresponding reflection coefficients $\mathbf{r}_L$ and $\mathbf{r}_R$ are calculated using Equation 3.41. In this situation, these matrices are not diagonal matrices and wave mode conversion is present. First, the effect of the fixed boundary on exact wave amplitudes is investigated. Since the negative and positive going waves are related by the reflection coefficient matrix of the right boundary $\mathbf{r}_R$, the magnitudes of these coefficients for each of the least attenuated are plotted in Figure 6.13 showing that these coefficients are not constant over the frequency range. However, their magnitudes are close to 1 for the evanescent waves only at their associated cut-on frequencies. Elsewhere non-equal wave amplitudes of positive and negative going waves occur as illustrated in Figure 6.14. Consequently, even when no damage is present, the magnitude of the positive and negative going waves are not similar due to the boundary conditions which represent wave mode conversion.

Next, the same RC beam as in Table 4.1 is modelled for with fixed boundaries for three cases namely undamaged, damaged with 40 % and damaged with 60 % diameter reduction of one of the rebars. For a finite waveguide with no discontinuity, the forced response includes the following steps as mentioned in Section 3.6. The magnitudes of the directly excited waves due to the external point excitation are computed. The reflection matrices due to the boundaries are calculated and all of the equations governing the propagating waves are assembled. Then, the physical response at a specific point is evaluated via superposition of the waves. When a discontinuity is present, the same procedure is employed except that one needs to compute and add the reflection matrices of the discontinuity to the system of equations. The details of these computations are found in Appendix B.

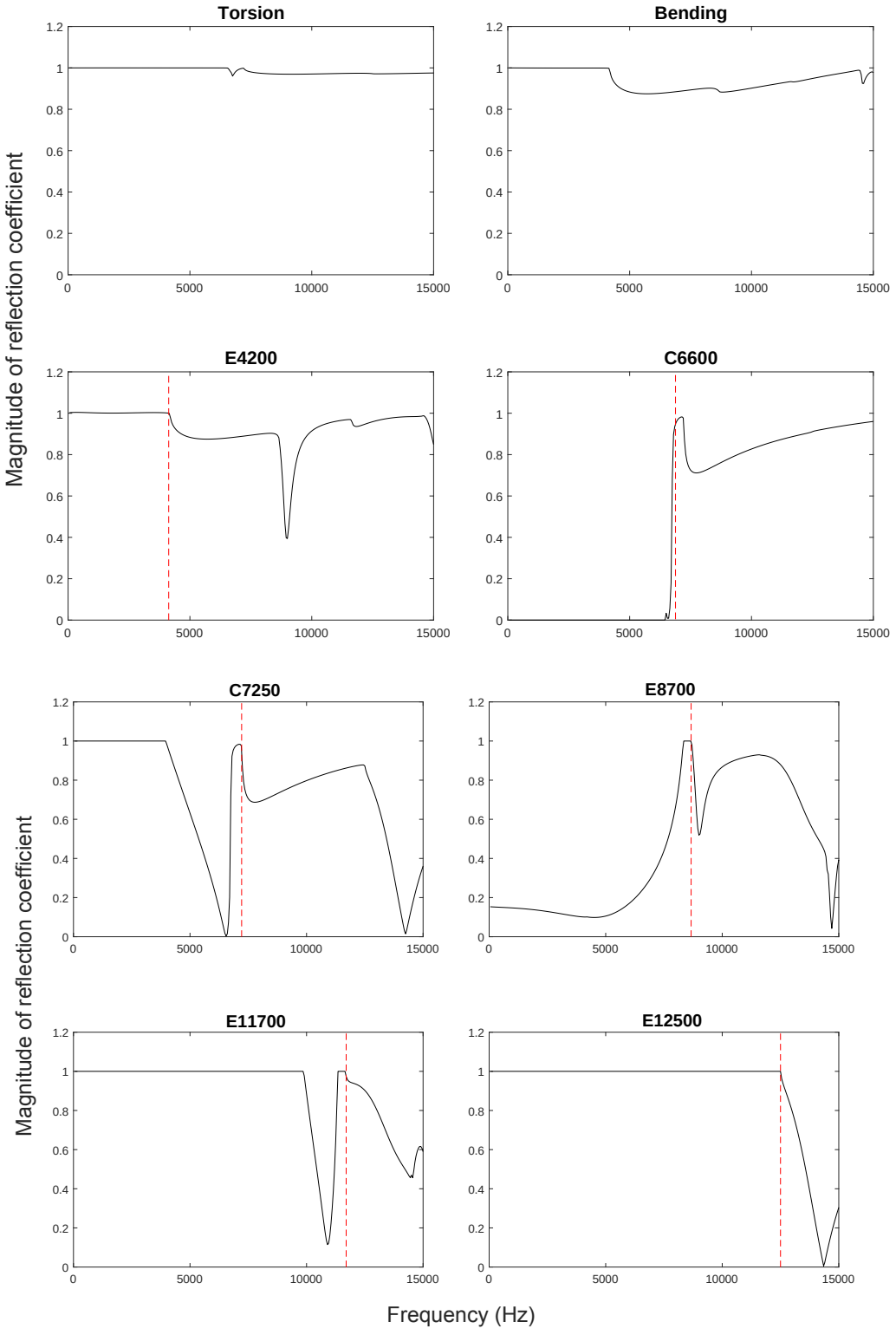


Figure 6.13: Magnitude of the reflection coefficients of the least attenuated waves in a finite RC beam due to fixed BCs.

Reflection coefficients(—), cut-on frequencies (– – –).

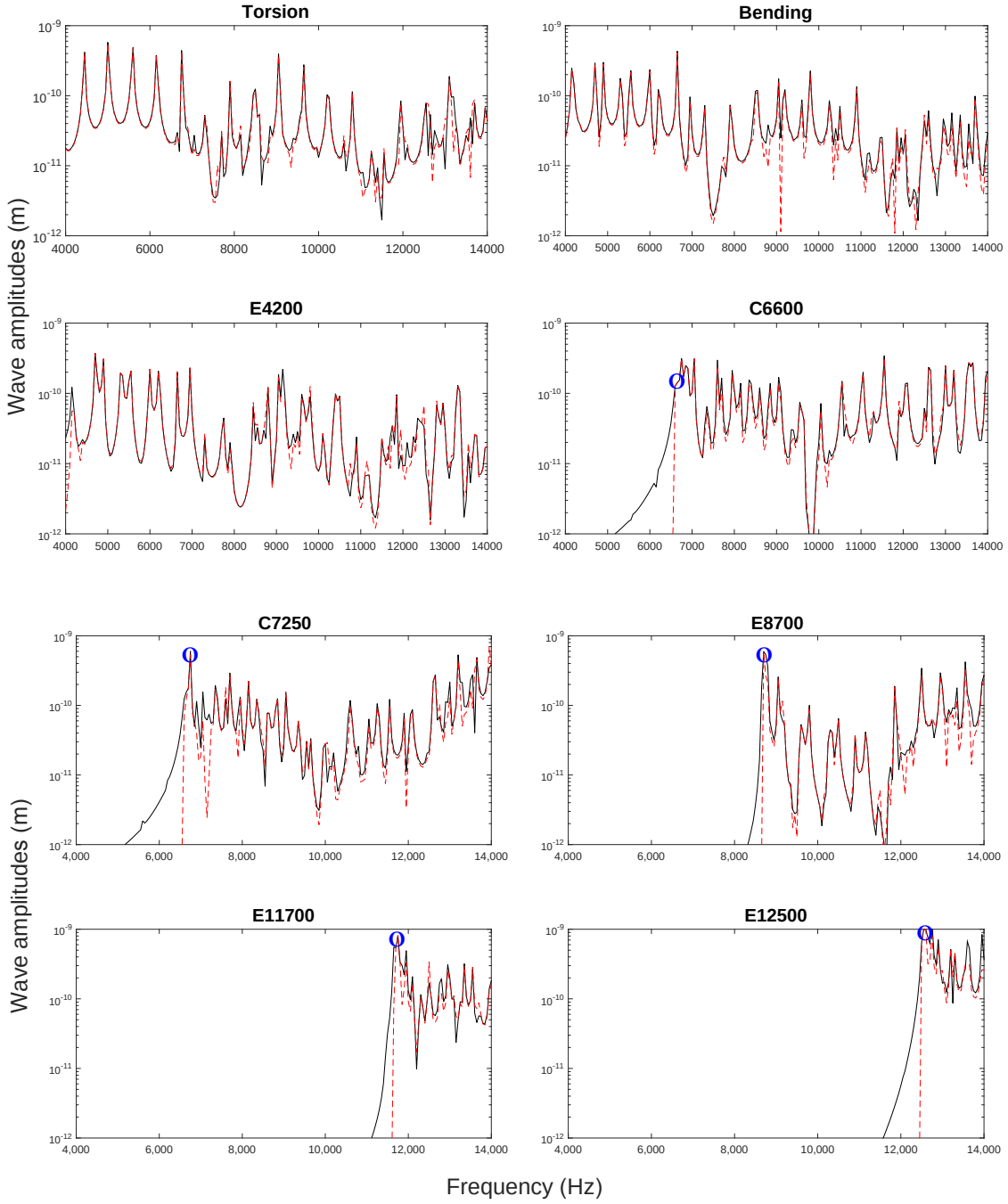


Figure 6.14: Least attenuated wave amplitudes in a finite RC beam with fixed BCs.

Positive going waves (—), negative going waves (– – –), response at cut-on frequency (○).

The WAD approach is applied to the three beams with the following parameters: $k_s = 0.1$ rad/m, with four non-uniformly spaced transducers at 0.3 to 0.45 m from the excitation force at 0.3 m. The estimated positive and negative wave amplitudes are identified. Considering first the undamaged finite RC beam, the amplitudes of the evanescent and

estimated waves are plotted in Figure 6.15. The estimated wave amplitudes align with the exact solution when this wavenumber value is correct, i.e. at the cut-on frequencies. Away from the cut-on, the use of the small real wavenumber is not correct and the estimated wave amplitudes follow the peaks of the dominant solution. However, this does not mean that the estimated wave amplitudes are equal to the exact solution since the wavenumber value is not applicable in this case. As demonstrated in Figure 6.15, the positive and negative wave amplitudes are equal away from the cut-on frequencies despite the fact that the exact ones (not fully shown for clarity) are different due to wave mode conversion at the boundaries as illustrated in Figure 6.14. This is advantageous to the algorithm, since only changes in the wave amplitudes at the cut-on frequencies are detected when the application of the small real wavenumber is correct. Subsequently, the ratio of the negative to positive estimated wave amplitudes is 1 for the fixed-fixed undamaged beam.

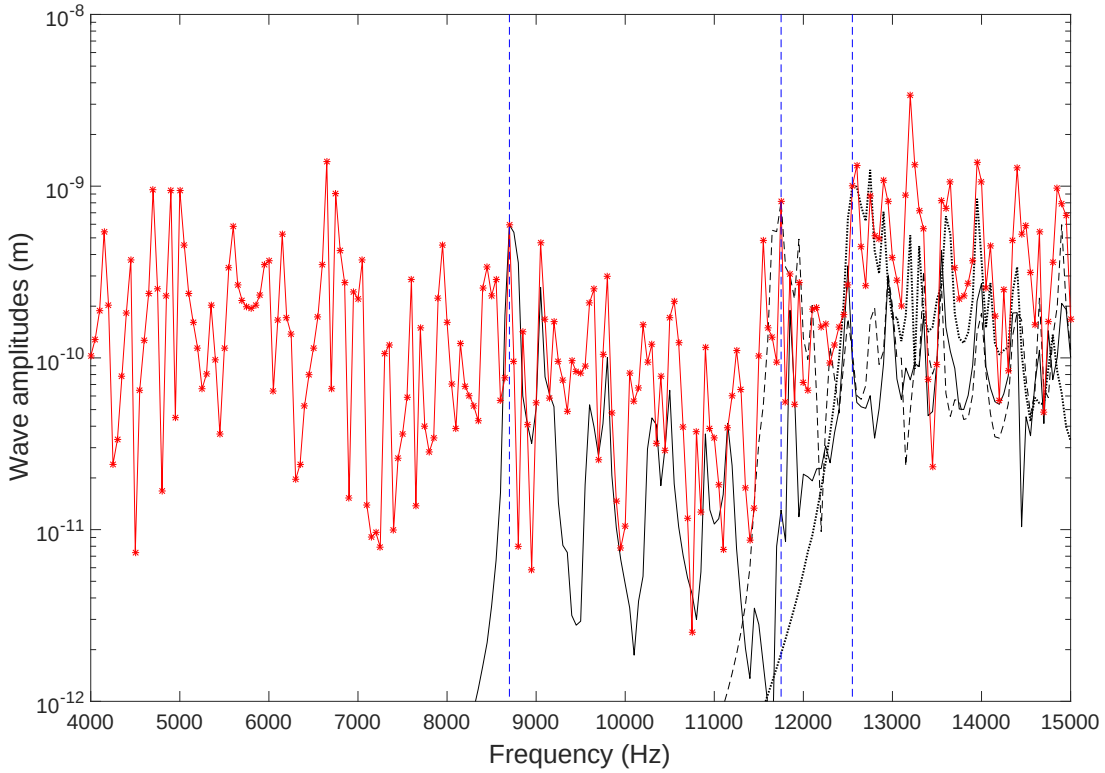


Figure 6.15: The wave amplitudes of the evanescent and estimated waves for undamaged fixed RC beam .

WFE solution: E8700 (—), E11700 (- - -), E12500 ($\cdots$); WAD solution using $k_s = 0.1$ rad/m: positive going wave ($-$), negative going wave ($*$); Cut-on frequencies ($- - -$).

In contrast, damaged models show a reflection ratio less than 1 near the cut-on frequencies of 8700 , 11700 and 12500 kHz as shown in Figure 6.16. The dips in the ratio at the cut-on frequencies is in accordance with the reflection coefficients, due to the presence of the damage predicted in Table 5.1 for the evanescent waves. Here, the term 'larger dips' is used to mean those reflection amplitude ratios being closer to zero, and 'small dips'

is small deviation of the ratio from 1. Higher reduction in the rebar diameter leads to higher reflection coefficients, and therefore to a smaller dip. Subsequently, values of the dip for the 40% damaged RC beam are lower than the 60% ones since lower magnitudes of reflection coefficients are associated with the extent of the damage. Similarly by comparing the dips for the same RC beam, the evanescent waves with the higher magnitude of the reflection coefficients tend to have small dips in the ratio (as seen in Figure 6.8).

The dips in the ratio of the wave amplitudes due to damage at cut-on frequencies clarify the advantages of the damage detection algorithm. First, a pre-simulation of the actual structure including a pre-investigation of the material properties is not required. Second, no prior knowledge of the wavenumbers and cut-on frequencies is necessary. One can simply apply the method taking into account the position and number of transducers and look for the minimum values of the ratio of the wave amplitudes. Thus, an intact beam model is not needed for application of the methodology or comparison with the results of predictions. Third, one can link the extent of the damage to the size of the dips. Greater damage represented by rebar diameter reduction is associated with a smaller dip since the wave amplitude ratio at the cut-on frequencies is dominated by the cut-on wave reflection coefficients, which tend to 1 with the increased amount of damage. In this case, it is only true when damage is between 10% and 60% diameter reduction. Apart from that, the ratio of the wave amplitudes is not very distinctive as shown in Figure 6.8.

## 6.7 Damage localisation

In this section, the ability of the algorithm to locate damage is tested via simulation. The forced response is computed as displacement along the top surface of the 60% damaged rebar finite RC beam. These responses are then applied via WAD in order to calculate the positive and negative going waves. The RC beam is divided into *Zones* 1 to 4 as shown in Figure 6.17. Each *Zone* contains 4 transducers with non uniform spacing. *Zone* 1 starts at 0.3 m from the excitation force, and *Zone* 3 is associated with the damage section. The ratio of the negative to positive going wave amplitudes is estimated by an array of simulated responses in each *Zone* and then plotted in Figure 6.18.

One can notice that the wave amplitude ratio in *Zone* 2 is less than 1 near the cut-on frequencies of 8700, 11700 and 12500 Hz. This due to the presence of the measurement array before the damage as shown in Figure 6.17. The dips have shown approximately similar values in *Zone* 1 (Figure 6.16) and 2. This is due to the fact that using a small real wavenumber in the WAD approach only detects the response near the cut-on frequencies that is independent of transducer location. On the other hand, the ratio of the wave amplitudes is almost 1 for *Zone* 3 and 4: For *Zone* 3, all the transducers are in the damaged part. The positive and negative wave amplitudes are related to the reflection

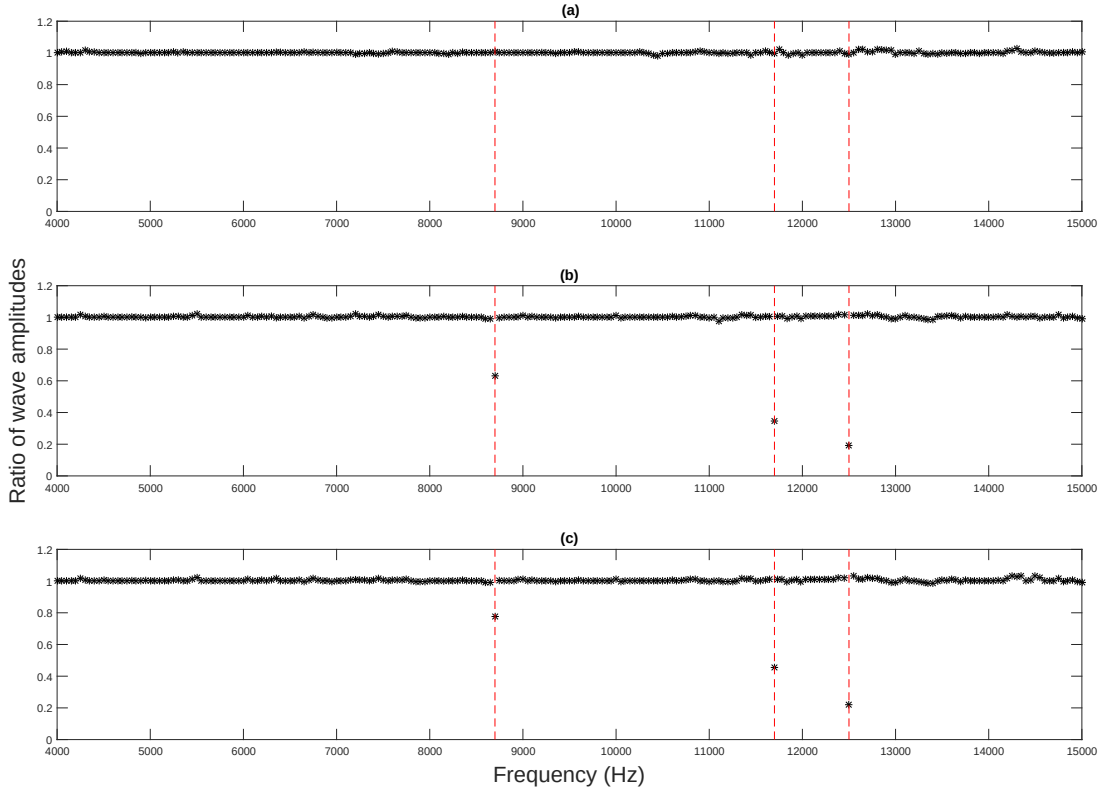


Figure 6.16: Ratio of negative to positive estimated wave amplitudes for damaged and undamaged RC beams with fixed boundaries.

(a): undamaged RC beam, (b): 40% damaged RC beam, (c): 60% damaged RC beam. Cut-on frequencies (– – –).

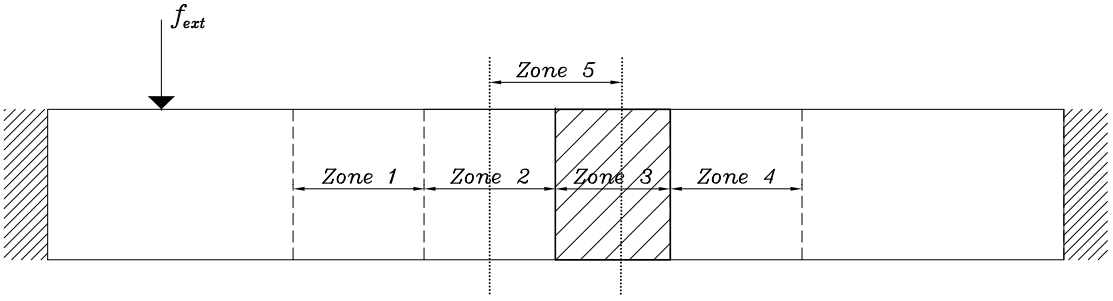


Figure 6.17: Finite damaged RC beam with *Zones* 1 to 5 associated with the group of transducers considered. *Zone* 3 is associated with the damage section.

coefficients due to the interface change between the undamaged and damaged parts and to the right fixed boundary. Since the reflection coefficients of the latter are known, one can apply the WFE-WFE coupling approach to identify these coefficients at the interface as shown in Table 6.1. The evanescent waves have reflection coefficients near 1 at their cut-on frequencies due to the interface change between the damaged and undamaged. In addition, these waves possess reflection coefficients of 1 near their cut-on frequencies due to the fixed boundary. Subsequently, the ratio of wave amplitudes is 1 when the

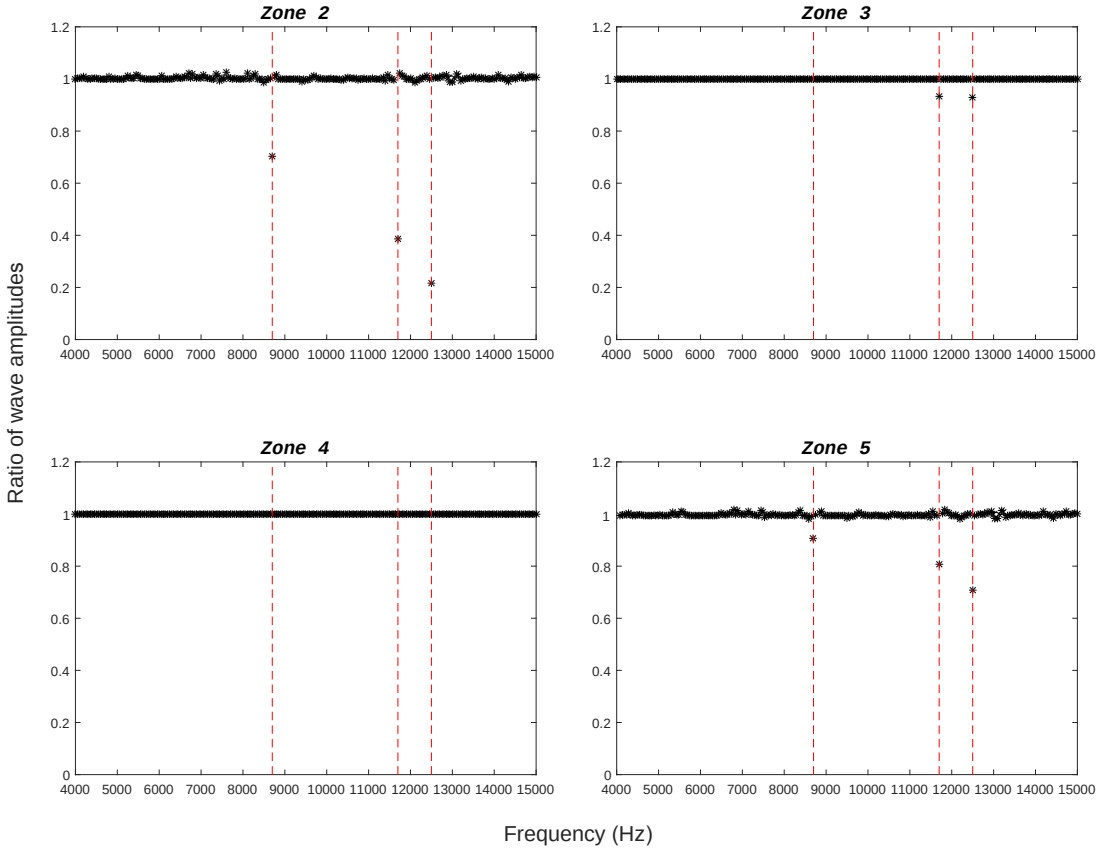


Figure 6.18: The ratio of the wave amplitudes of the negative to positive going waves with 60% diameter rebar reduction in different zones.

transducers are within the damaged length. For *Zone* 4, all the transducers are after the damaged part. Therefore, the positive and negative going waves are related only via the scattering matrix of the right fixed boundary. Another *Zone* can be considered

| **Wave description** | **Cut-on frequency (Hz)** | **Reflection coefficient** |
|---|---|---|
| Torsional | - | 0 |
| Bending | - | 0 |
| E4200 | 4200 | 0.86 |
| C6600 | 6600 | 0.2 |
| C7250 | 7200 | 0.9 |
| E8700 | 8700 | 1.0 |
| E11700 | 11700 | 0.9 |
| E12500 | 12500 | 0.9 |

Table 6.1: Least attenuated waves' reflection coefficients due to interface change.

where the transducers chosen are located in the damaged and undamaged parts. For instance, one can select 4 transducers to stagger the interface between the damaged and undamaged zones as in *Zone* 5 in Figure 6.17. In this case, the transducers are positioned between 0.3 and 0.45 m from the excitation force with non-uniform spacing. Despite dips being present at the cut-on frequencies, their values are less than the ones

associated with *Zones* 1 and 2. This is due to the fact that only two transducers are located before the damaged part to pick up the associated reflected waves.

The use of the damage detection algorithm along the beam length gives an estimation of the damage location. If no damage exists, the ratio of negative to positive wave amplitudes is 1. However, when damage exists, this ratio is less than 1 at the cut-on frequencies of excited evanescent waves if the measurements are located before the damage. One can locate the damage by tracking down the value of the dips at the cut-on frequencies. If the ratio of the wave amplitudes exhibit values less than 1, then the transducers are before the damage. Once the ratio is 1, this means that the transducers are at or after the damage location. To locate the damage more precisely, one can check the position where the dips gets closer to 1 due to the location of transducers between the interface of the damaged and undamaged waveguides. Alternatively, one can use other methods (like ultrasound) that are more precise in assessing the site of the damage once it has been generally located.

## 6.8 Damage detection algorithm applied to coupled RC beams

In real civil engineering structures, RC beams are connected together in order to ensure the distribution of the loads. So far, the damage detection algorithm approach has been demonstrated only on single uniform beams. In this section, the algorithm is tested on coupled RC beams where both connected beams share similar or different damping. The aim is to demonstrate the potential and identify some of the limitations of the method when applied to connected beams.

The coupled RC beam model involves the modelling of two attached beams in FE as shown in Figure 6.19. The two beams share the same material properties, damping and dimensions as in Section 4.2 . All the boundary nodes are modelled as fixed. The two beams share the same nodes at the interface in order to ensure good coupling between them. One interest is in how the wave type conversion occurs between the two beams. Therefore, the vibration mode shapes are plotted for fundamental modes in Figure 6.20. For example, the axial motion in the original beam is converted into transverse bending motion in the attached beam.

A harmonic solution is applied to the original beam over the frequency range from 0 to 15 kHz with a frequency step of 3 Hz. Using the WAD approach, the positive and negative going wave amplitudes are computed. In all cases, $k_s = 0.1$ rad/m is employed as the wavenumber value for the WAD, with the transducers positioned at non-uniform spacing between 0.3 and 0.45 m from the excitation point. The first model includes no damage in the original beam. In Figure 6.21, the ratio of negative to positive going wave

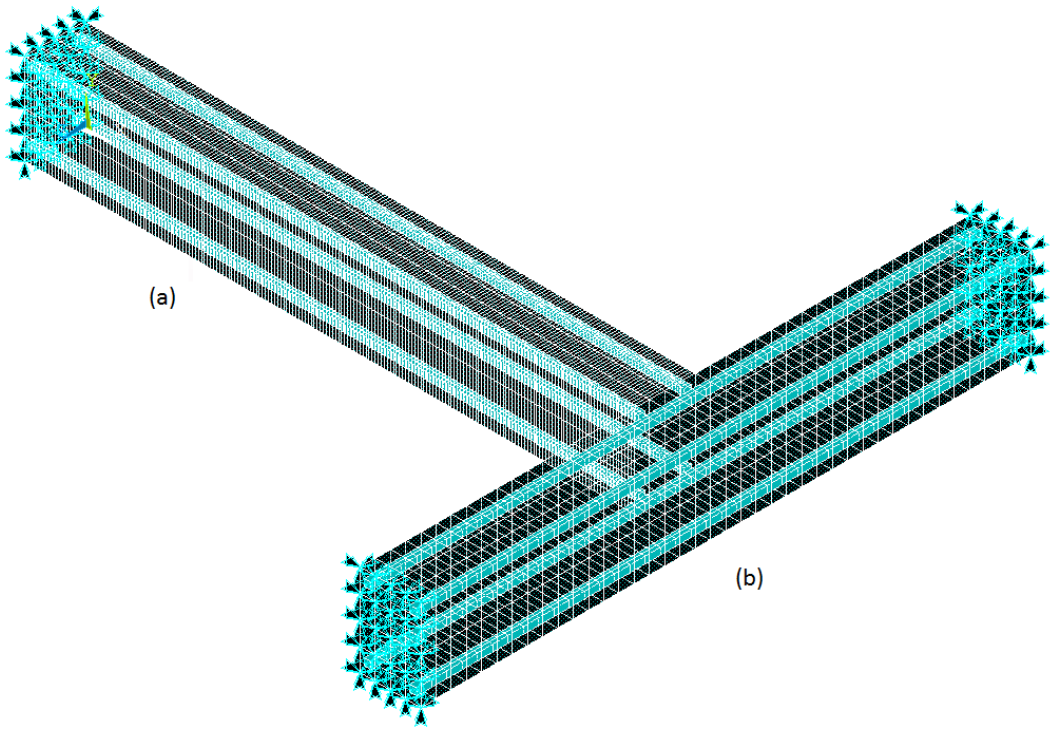


Figure 6.19: Built-in RC beam model in FE with fixed boundaries.
(a): original beam, (b): attached beam.

amplitudes is plotted for the undamaged original beam. The ratio is less than 1 at the cut-on frequencies of 8700, 11700, and 12500 Hz. Since the RC beam is undamaged, one can attribute the reason for these values to the attached beam, where wave reflections and conversions are present. Since these values are present at the cut-on frequencies, one can conclude that the magnitude of the reflection coefficients at these frequencies is not 1 for their associated wave type.

In addition, one can plot the vertical receptance of a point on the top surface of the original and attached beams while exciting the original beam. In Figure 6.22, the FRFs due to a point force of a point associated with the original and attached beam are plotted. One can notice the absence of the peak in the receptance of the point associated with the attached beam at the cut-on frequencies of 8700, 11700, and 12500 Hz. This is due to the mode conversion between the two attached beams, that leads to wave amplitude ratios less than 1 at these cut-on frequencies despite the absence of damage.

Similarly, the damage identification algorithm is applied to the damaged original RC beam (a) as in Figure 6.19. In Figure 6.21, the ratio of negative to positive going wave amplitudes is plotted for a 40% and 60% damaged RC beam with attached beam at the right boundary. One observes a change in the values of the dips associated with

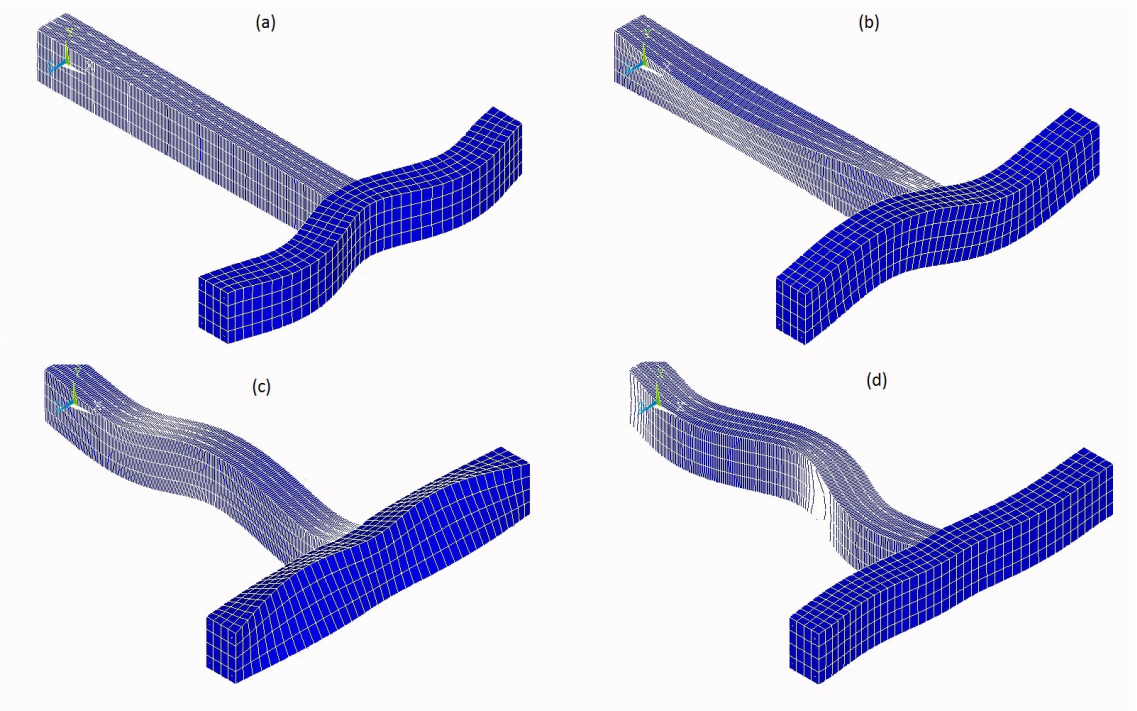


Figure 6.20: Fundamental mode shapes of coupled RC beams modelled in FE with fixed boundaries.

(a):axial to transverse bending, (b): torsional to bending, (c): bending to torsional, (d): transverse bending to axial.

the presence of the damage and its extent at 8.7, 11.7, and 12.5 kHz. This due to the superposition effect of the damage and the mode conversion at the right boundary.

As discussed in Section 6.6, dips not associated with the presence of damage are observed when the the boundary is not perfectly reflecting at the cut-on frequencies. Subsequently, this imposes a limitation to the damage identification algorithm associated with the requirement of an intact model. However, one can examine the variation of the ratio of wave amplitudes with respect to the transducers within the *Zones* considered in the WAD approach as in Figure 6.17. The 60% damaged RC beam with attached beam at the right boundary is selected for this simulation. In Figure 6.23, the ratio of negative to positive going waves associated with each *Zone* is plotted. Since the measurements in *Zone* 2 are before the damage location, the dips at the cut-on frequencies are associated with both damage and the attached beam at the right boundary. That is why the dip locations and levels are similar to the ones in *Zone* 1.

However, once the measurements are in the damage location as in *Zone* 3, the dips at the cut-on frequencies are superimposed due to the effect of the interface between the damaged and undamaged sections, and the right boundary wave mode conversion. This is why the greater dips occur in comparison to the previous *Zone*. Then, after the damage location as in *Zone* 4, the values of the dips are associated with the right boundary only. Subsequently, the dips get smaller and changes are only associated

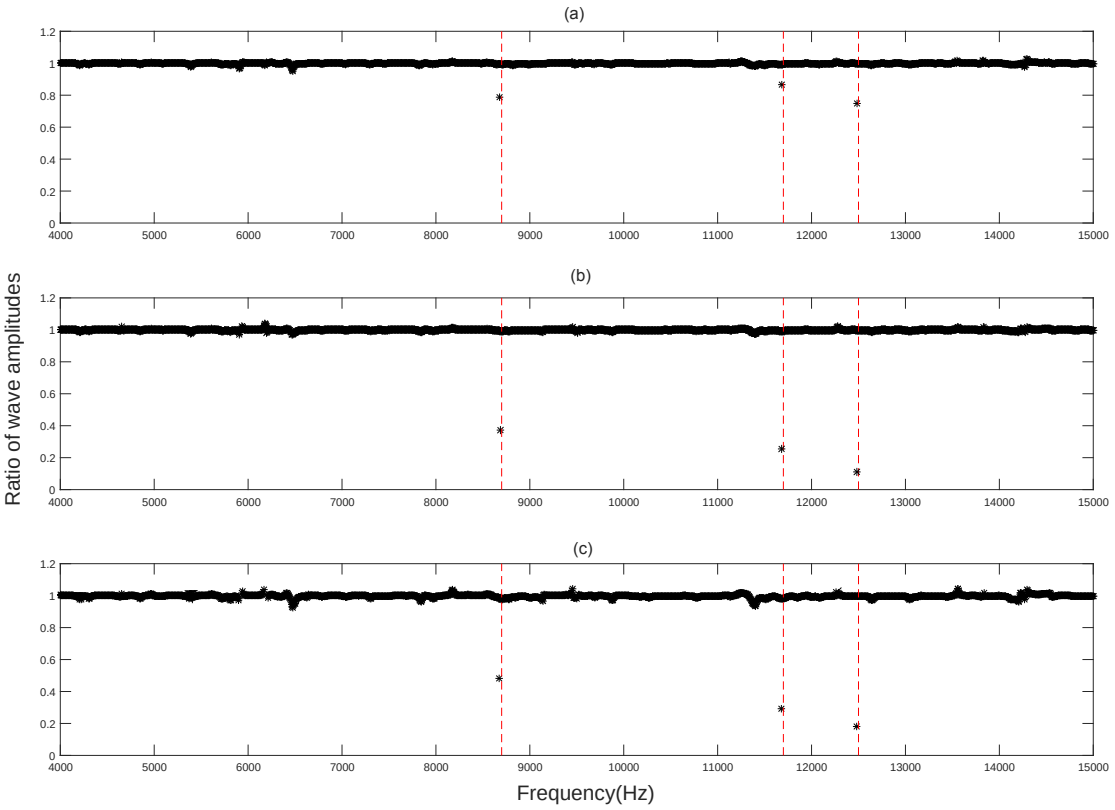


Figure 6.21: Ratio of estimated negative to positive going wave amplitudes for undamaged and damaged coupled RC beams.

(a): undamaged RC beam, (b): 40% damaged RC beam, (c): 60% damaged RC beam. Cut-on frequencies (– – –).

with the cut-on frequencies of 11700 and 12500 Hz in comparison with ones in *Zone* 3. In this case, their levels are in accordance with the undamaged coupled RC beam as in Figure 6.21, since all the transducers are after the damage. However, *Zone* 5 is associated with transducers positioned before and after the damage interface. The dips are present at the same cut-on frequencies as for *Zones* 1 and 2 but with smaller values. This is due to the fact that only the transducers located before the damage pick up the associated reflected waves.

The use of the damage detection algorithm along the length of the beam gives an estimation for the damage location, and helps in identifying if the right boundary is not fully reflecting at the cut-on frequencies. One can locate the damage by tracking down the values of the dips. If the values of the dips remain similar all along the beam length, this means that the beam is undamaged and therefore the dips are associated with the right boundary effect. However, if these values change along the beam length then the beam is damaged. The damage location is associated with the sudden change of these values. Subsequently, the presence of an intact model is not required in order to identify experimentally the presence of the damage.

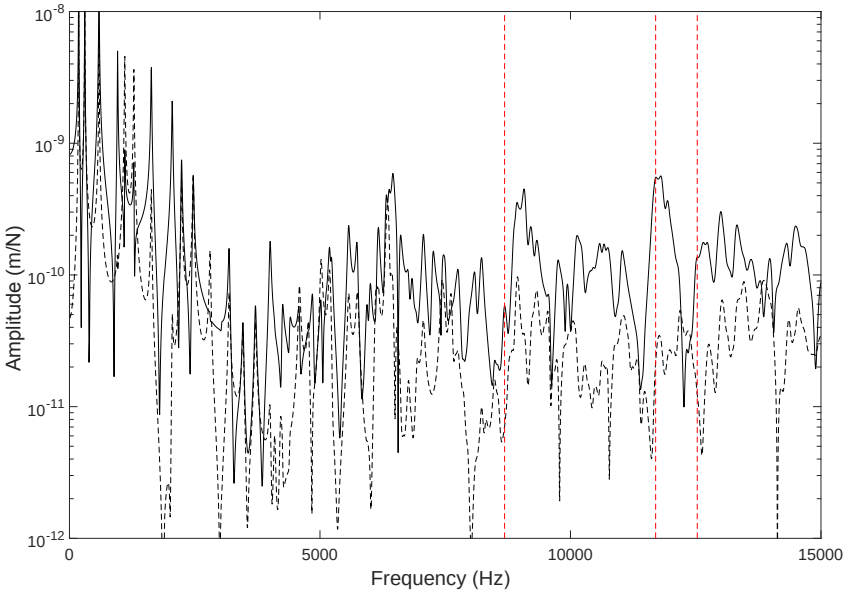


Figure 6.22: Magnitude of receptance at a point on the top surface of the RC beams.

original beam (—), attached beam (- - -). Cut-on frequencies (– – –).

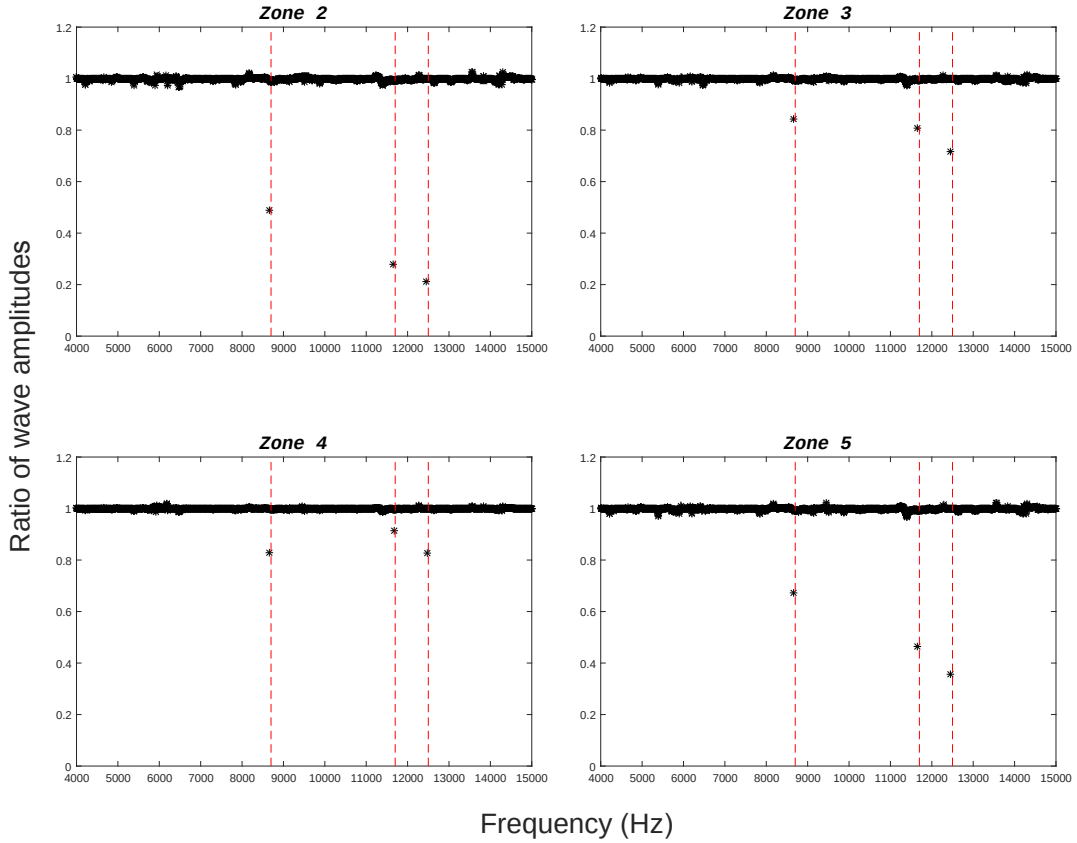


Figure 6.23: The ratio of the amplitudes of negative to positive going waves in a coupled RC beam with 60% diameter rebar reduction in different *Zones*.

The previous results are associated with the attached beams having the same damping. Therefore, one might be interested in investigating the effect of higher damping in the attached beam on the positive and negative going wave amplitudes. This is to model the effect of radiation damping when the RC beam is connected to various beams. The following model includes modelling the transverse beam with higher damping than the original one. In Figure 6.24, the ratio of negative to positive wave amplitude is plotted for the undamaged, 40% and 60% damaged RC beam with higher damping in the attached beam at the right boundary. In all cases, the overall ratio of the wave amplitudes dropped from 1. The presence of higher damping in the attached beam reduces the amplitude of all the reflected waves at all frequencies. In addition, the dips associated with the right boundary and the damage are present at the same frequency as the model with similar damping, except that their levels are shifted accordingly with the overall decrease in the ratio of the wave amplitudes.

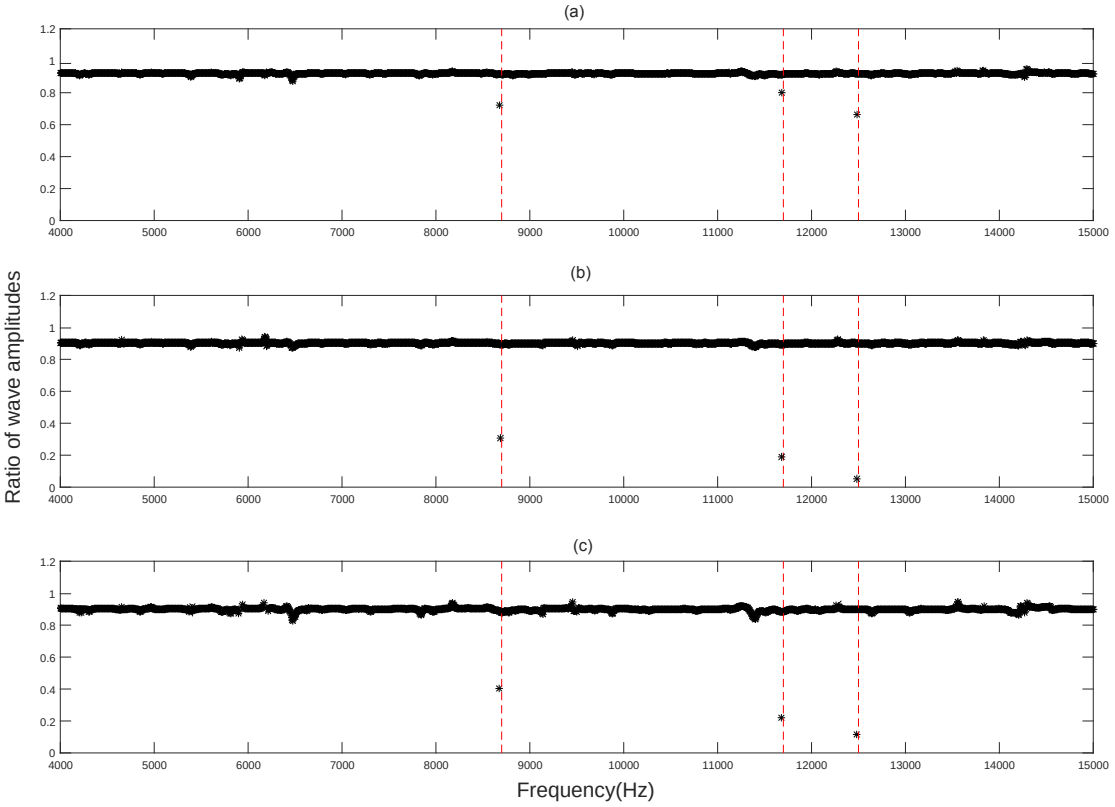


Figure 6.24: The ratio of the estimated negative to positive wave amplitudes for damaged and undamaged coupled in RC beams with higher damping in the attached beam.

(a): undamaged RC beam, (b): 40% damaged RC beam, (c): 60% damaged RC beam. Cut-on frequencies (– – –).

## 6.9 Conclusions

A damage identification algorithm has been introduced based on the ratio of the amplitudes of the reflected to incident waves. To determine the wave amplitudes, the WAD approach using the assumption of a small wavenumber can be employed to identify the evanescent waves cutting-on. The proposed technique is demonstrated via simulations and results are successful in identifying and locating the damage introduced as rebar diameter reduction.

The use of a real small wavenumber in the WAD approach gives correct peaks for the estimated wave amplitudes. They align with the exact solutions of the propagating and evanescent waves at they cut-on. This proves that the use of this value of $k_s$ detects the contribution of the dominant evanescent wave cutting on. The number of transducers is set based on findings in past literature. In addition, the transducer position was selected based on the decay of the evanescent wave amplitude to ensure good conditioning. On the other hand, the transducer spacing was selected to be non-uniform. This is essential to reduce the numerical errors due to bad conditioning when using a small real wavenumber,

Away from the cut-on frequencies, where the use of the small real wavenumber is not correct, the estimated wave amplitudes follow the peaks of the dominant solution without picking out the differences between the positive and negative wave amplitudes. This is advantageous, since only changes in the waves amplitudes at the cut-on frequencies are detected when the application of a small real wavenumber is correct. As a result, the ratio of wave amplitudes is less than one only when damage is present. The dips occur at the cut-on frequencies.

In finite RC beams, the ratio of the negative to positive wave amplitudes is close to 1 when no damage is present. In damaged beams, it is less than 1 near the cut-on frequencies. The levels of the dips are in approximate accordance with the magnitude of the reflection coefficients defined previously in Chapter 5. In the case of undamaged coupled RC beams, the ratio of wave amplitudes is less than 1 near cut-on frequencies due to wave mode conversion in the attached beam. The presence of the damage is superimposed on the original dips. In addition, the presence of higher damping in the attached beam reduces all the reflected wave types and subsequently the ratio is less than 1 over all the frequency range. Also, the dips get larger accordingly.

Application of the damage detection algorithm has shown many advantages compared to other wave damage detection techniques. First, a numerical model or simulation of the actual structure is not required. Second, no prior knowledge of the wavenumbers and cut-on frequencies is necessary. One can simply apply the method taking into account the position and number of transducers and look for the minimum values in the ratio of the wave amplitudes. Thus, an intact beam is not needed for comparison. Third, one

can link and correlate the extent of the damage to the minimum values in the estimated wave amplitude ratio.

# Chapter 7

# Experimental validation

## 7.1 Introduction

In the previous chapter a damage identification algorithm was proposed and validated through simulations without added noise. In this chapter, it is tested via an experimental implementation. The damage identification algorithm is applied to undamaged as well as damaged RC beams to check for false positive diagnoses.

First, the specimen properties are introduced, i.e. properties of the concrete, steel reinforcements and formwork are given. Two of the steel rebars were manufactured with loss of thickness over a specific length representing the localised damage. Next, the experimental setup is introduced including the concrete surface finishing, boundary conditions, transducers and instrumental hammer selection for measuring the FRFs.

The dispersion curves were identified using a correlation technique Ferguson et al. (2002), although this is not required for implementation of the damage identification method. Then, the effect of concrete strength and the presence of damage on the estimated wavenumber values are analysed. In addition, the nodal displacements from surface measurements are plotted to validate the wave mode shapes at cut-on frequencies.

Data selection based on the measured coherence is discussed and the associated frequency forced response plotted at various positions along the RC beams. The damage detection algorithm is applied to the various RC beams. In addition, the potential and limitations of the method are discussed.

## 7.2 Fabrication of specimens

### 7.2.1 Concrete

This subsection involves the concrete mix design, concrete mixing and curing. Then, after the concrete has gained enough strength, its compressive strength can be measured and therefore its associated Young's Modulus estimated.

The concrete mix is composed of the following materials: high strength cement, water, sand and 10 mm aggregate. The proportions of each component are first defined by volume, and then by using the proper densities one can compute their masses for each batch. The total volume of each batch $V_b$ is selected based on the capacity of the mixer. In this case, the value of $V_b$ was selected to be 0.03 $m^3$.

Since one is interested in designing a high strength concrete, then the water/cement ($w/c$) ratio should be small and was selected to be a value of 0.27. This value is the ratio of the mass of free water to the mass of cement in the mix. The term free water refers to the net water remaining free in the mix after some is absorbed by the sand and aggregate. Therefore, the total volume of the water required for each mix is

$$V_w = V_{wf} + V_{wabs} \;\; ; \;\; V_{wf} = \rho_w(w/c \times W_c) \tag{7.1}$$

where $V_w$ is the total volume of water required for each batch, $V_{wf}$ is the volume of free water as a function of water density $\rho_w$, water cement ratio $w/c$ and cement mass $W_c$ and $V_{wabs}$ is the volume of water absorbed by sand and aggregates based on their water content and absorption rate to reach saturation.

The mix proportions were selected to be 1:1 per weight for cement and sand. Then one can select the volume for each component respectively by using the associated density. Using the ratio $w/c$, one can compute the value for $V_{wf}$. After taking samples of both sand and aggregate, one can identify their absorption rate and calculate $V_{wabs}$ accordingly. Next, the volume of the aggregate is the remainder of the total volume of the batch after subtracting the volume of all the other components. Next, all the quantities are scaled for a 0.03 $m^3$ batch. In addition, three RC beams are made and each is of total volume of 0.12 $m^3$ (0.2×0.3×2 m). Subsequently, a total of 12 concrete batches were required.

Despite the fact that the use of a small $w/c$ ratio results in high strength concrete, the workability of the mix is very low. Therefore, a small amount of superplasticizer is used for each batch to enhance the workability and ease the handling of the mix. The cycle for concrete mixing and levelling is presented in Figure 7.1. In addition, samples from each batch were taken for later testing. After the proper pouring and levelling of concrete into the formwork, the concrete beams were left for proper hardening and curing processes for 7 days.

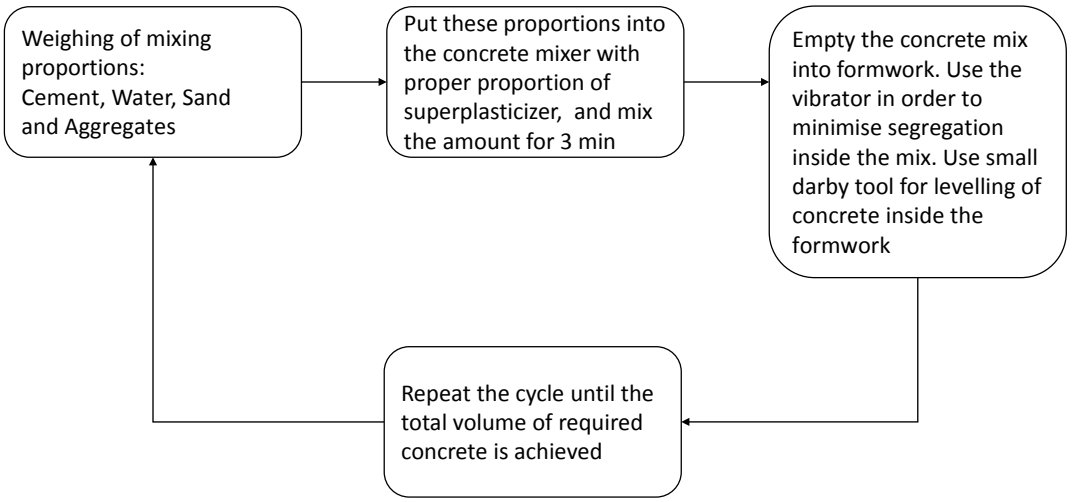


Figure 7.1: Cycle for concrete mixing and levelling.

Next, the beams were taken out of the frameworks. Cylindrical samples of the concrete mix were crushed in order to identify the concrete's compressive strength $f'_c$. The average strength was found to be 70 MPa. One can relate the concrete compressive strength $f'_c$ to its Young's Modulus $E_c$ in MPa using ACI (1995)

$$E_c = 4700\sqrt{f'_c} \tag{7.2}$$

Subsequently, the associated Young's Modulus of concrete at 28 days was found to be approximately $3.89\times10^{10}$ Pa.

### 7.2.2 Steel reinforcements

The concrete material is considered brittle and weak in tension. Therefore, horizontal steel reinforcements are essential to compensate for this weakness in the tension zones identified by internal moments due to the external loads applied to the beam. In contrast, the shear force applied due to that load should be resisted by both the concrete and the vertical reinforcements (stirrups).

Grade 60 steel reinforcements were used for each beam, which were separated into horizontal and vertical rebars as illustrated in Figure 7.2. Each beam comprises 4 horizontal rebars of length of 2 m, and of 10 stirrups spaced at 20 cm intervals. The undamaged horizontal rebars are of continuous 25 mm diameter and the damaged ones show a reduction to 16 mm and 10 mm respectively as shown in Figure 7.3. The horizontal and vertical reinforcements were tied together using steel fibres.

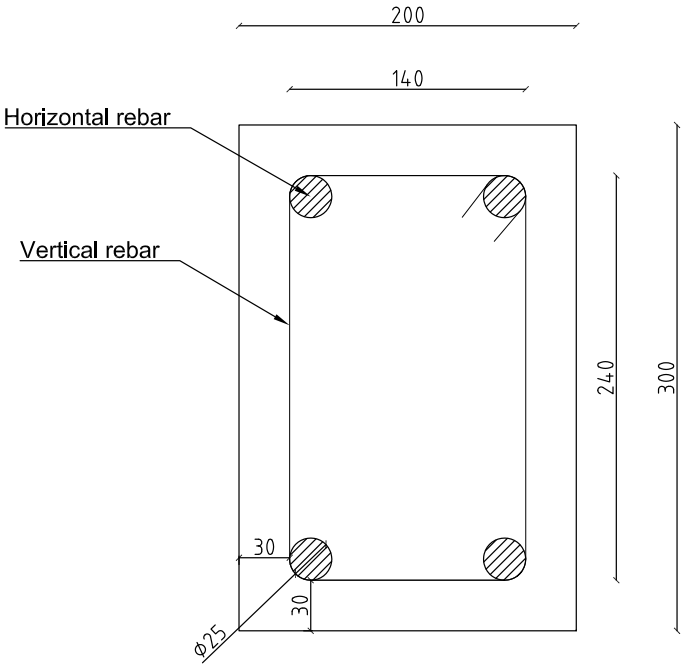


Figure 7.2: Cross section details of the RC beam reinforcement.

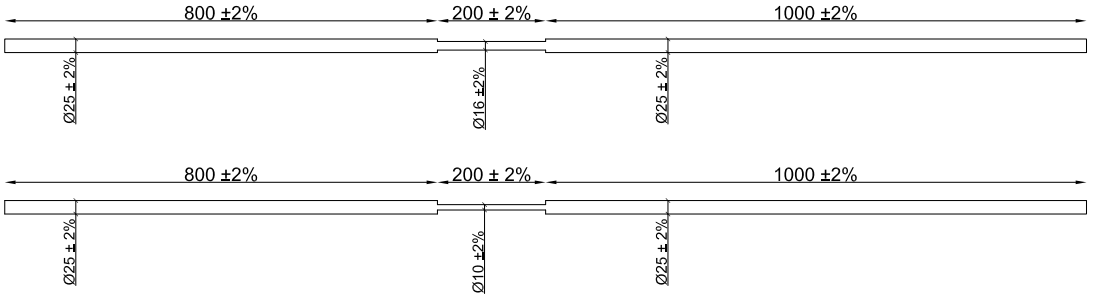


Figure 7.3: Details of damaged steel reinforcements.

In addition, a sufficient concrete cover is essential i.e. the distance between the horizontal steel reinforcements and the outer surface of concrete. The distance was set to be 30 mm and it was applied by fixing a concrete spacer of the same height at different positions along the length of the bottom two reinforcement rebars.

### 7.2.3 Formwork and placement of fresh concrete

The formwork were made using timber sheets. The design is illustrated in Figure 7.4. One can notice the double layer of timber in the bottom one third of the beam to resist the hydrostatic pressure of the concrete. For additional support, inclined timber ties were placed to ensure stability of the formwork.

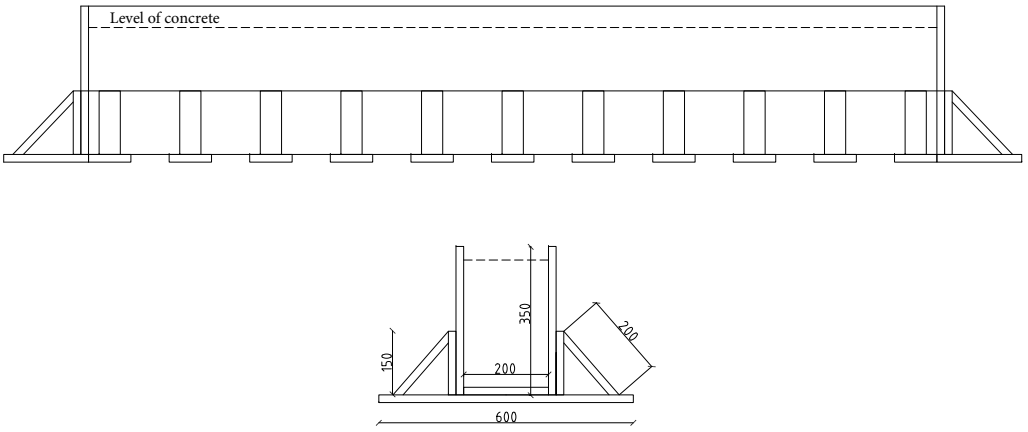


Figure 7.4: Formwork details.

Since the formwork is made of timber, one needs to make sure that the water mix is not absorbed by the formwork. Subsequently, an impermeable coating is applied on the inner surface of the formwork before pouring the concrete. In addition, this coating helps in the ease of removing the formwork after the concrete hardens.

A mechanical vibrator was used after each mix was poured to homogenise the concrete in the formwork. No vibration leads to air bubbles entrained in the concrete and a non-homogeneous texture to the beam. Excessive vibration leads to separation of the aggregate and mortar. For these reasons, an intermediate time of vibration took place to ensure the proper mixing of the new and old placement of concrete. Once the level of concrete was achieved in the formwork, a small darby tool was used for levelling the concrete. The details of the steel reinforcements' manufacturing, fixation and placement of concrete in the formwork are illustrated in Figure 7.5.

## 7.3 Experimental setup

This subsection involves concrete surface finishing, boundary conditions, transducers and hammer selection.

First, the concrete surface was dusty after it had hardened. To ensure good bonding of transducers on the surface of the beams, an acrylic resin based concrete seal was applied on all the external surfaces. The sealer formula is designed to penetrate deep into concrete to form a long lasting, dust free coating which repels water, oil and grease.

Second, each RC beam has a mass of approximately 300 kg. Therefore, it is hard to recreate fixed boundary conditions as introduced in the previous chapter. However, one can design the boundary at the edge of the RC beam as a roller. As illustrated in Figure 7.6, a steel plate was positioned first at the bottom surface of the concrete. This

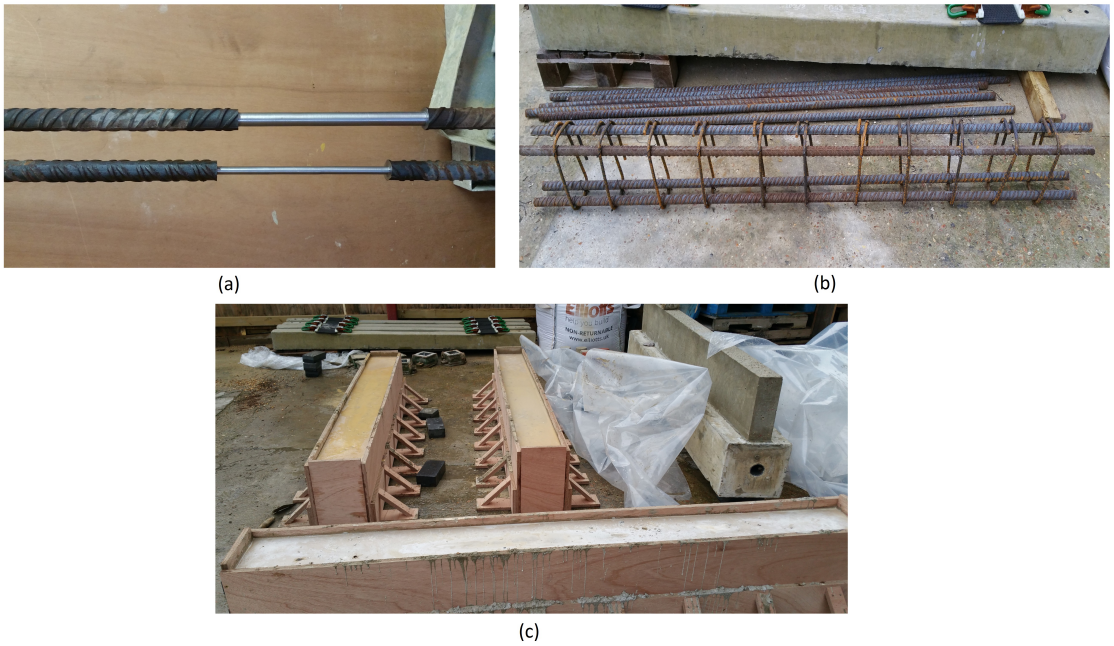


Figure 7.5: Steps of RC beam casting.

(a) damaged steel reinforcement bars, (b) horizontal and vertical steel reinforcements fixation, (c) placement of concrete in formwork.

was to protect this surface against any damage due to the direct contact with the steel rebar that acts as a roller. Then, the latter is positioned on top of a pad to stabilise it. This boundary configuration is applied at both ends of each RC beam.

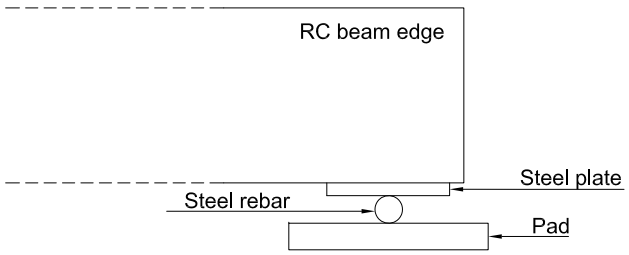


Figure 7.6: RC beam roller boundary details.

Deep RC beams are considered in this experiment to test over the frequency range of interest up to 13 kHz. A ceramic shear ICP accelerometer (PCB352C22) was used to measure the accelerance at different positions along the length of the RC beam. It was attached to the surface using an adhesive stud. In addition, it was powered by a simple constant current signal conditioner that gave a low-noise voltage output signal compatible with standard data acquisition equipment.

An ICP Impulse Force Test Hammer (PCB086C03) was used to excite the structure. The FRF measurements involved fixing the accelerometer at one location and impacting

the RC beam at various locations. The hammer size, length, tip material and velocity of impact determine the amplitude and frequency content of the impulse force. The impact cap on the hammer generally determines the impact energy content. Based on the force spectra of an impact, one can select the appropriate tip to use. A hard tip shows the least reduction at higher frequencies and so it is subsequently used.

## 7.4 Estimation of wavenumbers and wave mode shapes

The damage identification algorithm does not require estimation of the wavenumbers of free wave propagation in the waveguide. It has been shown that by using a small real wavenumber the amplitudes of the dominant wave near cut-on frequencies can be estimated. Despite the fact that it is not a requirement for the approach, estimation of the wavenumbers is beneficial to identify the cut-on frequencies and compare and validate the numerical WFE model results. In addition, the surface displacements are plotted to validate the predicted wave mode shapes at cut-on frequencies.

A wavenumber estimation technique that uses spatial arrays of data is advantageous, because the same measurements can also be employed for the damage identification algorithm as the next step. Ferguson et al. (2002) proposed a correlation technique for the estimation of wavenumbers in two-dimensional structures. However, one can apply the same approach for a one-dimensional structure by modifying the equations accordingly.

The formulation of this correlation technique for propagation of a single wave in a one-dimensional structure is given below

$$\hat{W}(k_{tx},\omega) = \int_{-l_x/2}^{l_x/2} w(x,\omega) e^{-ik_{tx}x} dx \tag{7.3}$$

where $\hat{W}(k_{tx},\omega)$ is a correlation coefficient at a trial wavenumber $k_{tx}$ with frequency $\omega$. $l_x$ is the length of the spatial array and $x$ is the spatial location on structure where the response $w$ is measured. The correlation coefficient will have peak values at particular wavenumbers $k_{tx}$. Then, the $k_{tx}$ value with the highest correlation coefficient at each frequency step is plotted as the dominant wavenumber.

For discrete response measurements, the correlation coefficient in Equation 7.3 can be approximated by an expression evaluated by the summation over the discrete measurement locations.

$$\hat{W}(k_{tx},\omega) \approx \frac{l_x}{N} \sum_{i=1}^{N} w(x_i,\omega) e^{-ik_{tx}x_i} \tag{7.4}$$

The correlation technique was applied to the three beams. One is interested in analysing the effect of the concrete strength and damage on the estimated wavenumbers. In all

cases, the impact excitation was positioned at $x_e = 0.3$ m, and the frequency forced response measurements were at 20 positions from $x_r = 0.5$ to 1.5 m (including the damaged zone). The trial wavenumber was selected within the range of 0 to 50 rad/m with a step size of 0.2 rad/m.

First, the undamaged RC beam is considered to test the effect of the reinforced concrete on the estimated wavenumbers. Sets of forced response measurements were collected after different concrete ageing periods: 7, 14 and 28 days. In addition, concrete cylinders were crushed on the same days to compute the strength and therefore identify the concrete Young's Modulus as per Equation 7.2 and presented in Table 7.1. In Figure 7.7, the estimated wavenumbers are plotted for each concrete age in days. The slopes of the dispersion curves become lower and the cut-on frequencies of the evanescent waves are shifted to the right with the increase in the concrete age and strength. This is due to the increased concrete Young's Modulus related to its compressive strength with respect to time.

| **Days** | **Compressive strength (MPa)** | **Young's Modulus (Pa)** |
|---|---|---|
| 7 | 48 | $3.25\times\ 10^{10}$ |
| 14 | 63 | $3.7\times\ 10^{10}$ |
| 28 | 70 | $3.89\times\ 10^{10}$ |

Table 7.1: Concrete samples compressive strength and Young's Modulus variability with respect to the concrete age in days.

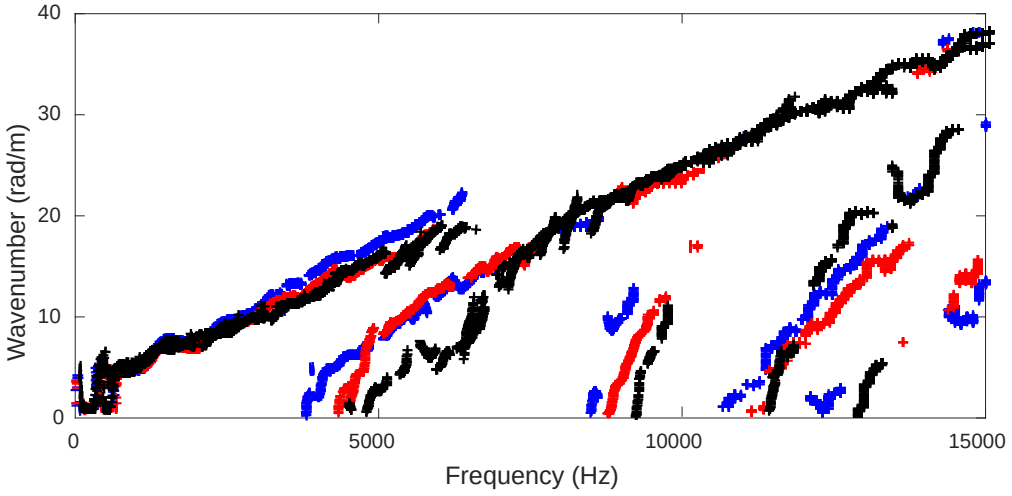


Figure 7.7: Estimated wavenumbers of the undamaged RC beam at different concrete ages.

7 days (∗), 14 days (∗), 28 days (∗).

Second, the damaged and undamaged beams were considered to test the effect of the rebar diameter reduction on the estimated wavenumbers. In Figure 7.8, the predicted

(from Chapter 3) and estimated wavenumbers using the correlation technique on the damaged and undamaged beams after 28 days are plotted. One can notice the good agreement between the predicted and the estimated wavenumbers: bending, E4950, E8700, E11700, and E12500. The correlation technique shows that the evanescent waves are the ones dominant near their cut-on frequencies since the dominant $k_{tx}$ values associated with high correlation coefficient are present at these frequencies. On the other hand, there is a slight change between the estimated wavenumbers when damage is present. This means that one can still estimate the correct wavenumbers values even if such damage is present.

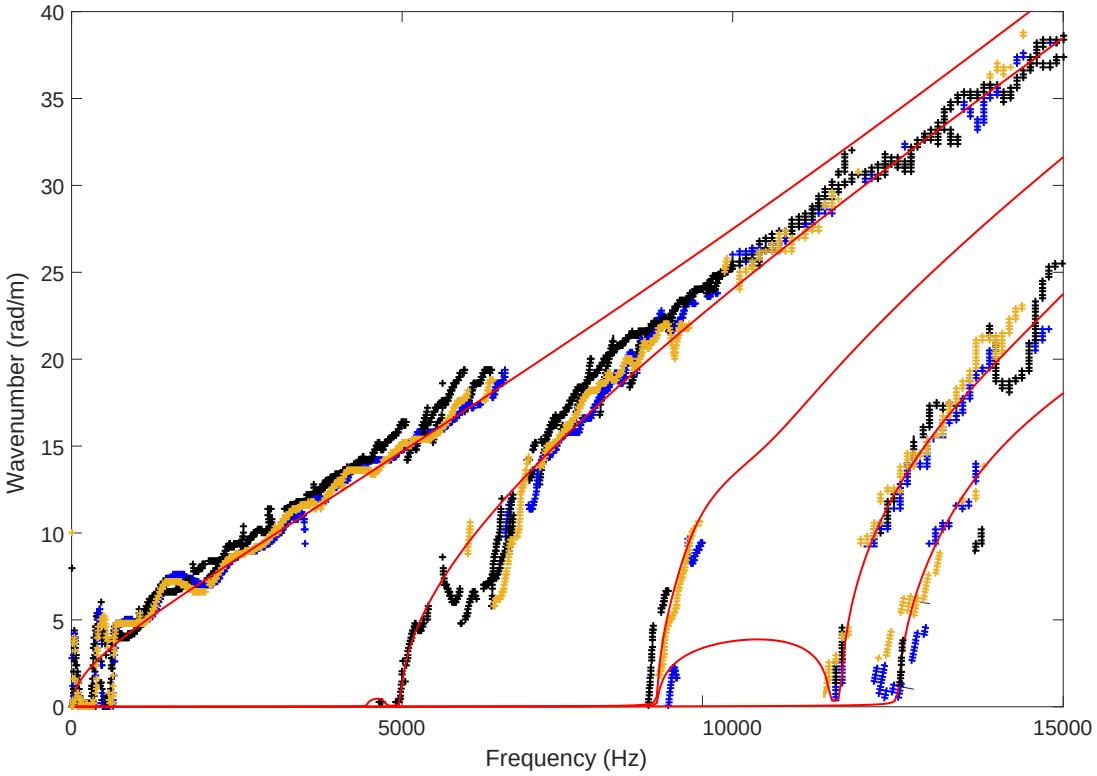


Figure 7.8: Predicted and estimated wavenumbers for the damaged and undamaged RC beams after 28 days.

WFE wavenumbers of undamaged model (−), undamaged beam (+), 40% damaged (+), 60% damaged (+).

Next, FRF measurements were taken on the top and side surfaces of the undamaged RC beam as shown in Figure 7.9. Since uniaxial transducers were used, the top surface measurements were only in the Z direction, and the side ones were only in the Y direction. Then, wave mode shapes associated with cut-on frequencies were plotted. The top surface displacements at cut-on frequencies in the Z direction are illustrated in Figure 7.10. The corresponding side surface displacements in the Y direction are illustrated in Figure 7.11. Good agreement is seen between the experimental and WFE predicted

wave mode shapes (in the Z and Y direction separately). This means that these cut-on frequencies correspond to the correct wave modes of interest.

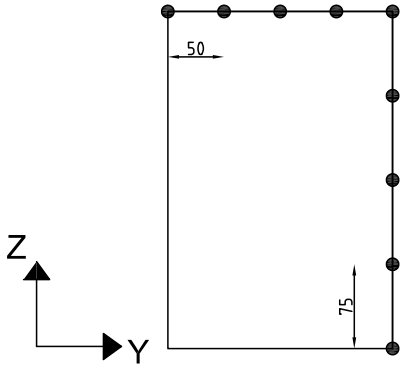


Figure 7.9: Transducers surface measurement location and coordination. Spacing in mm.

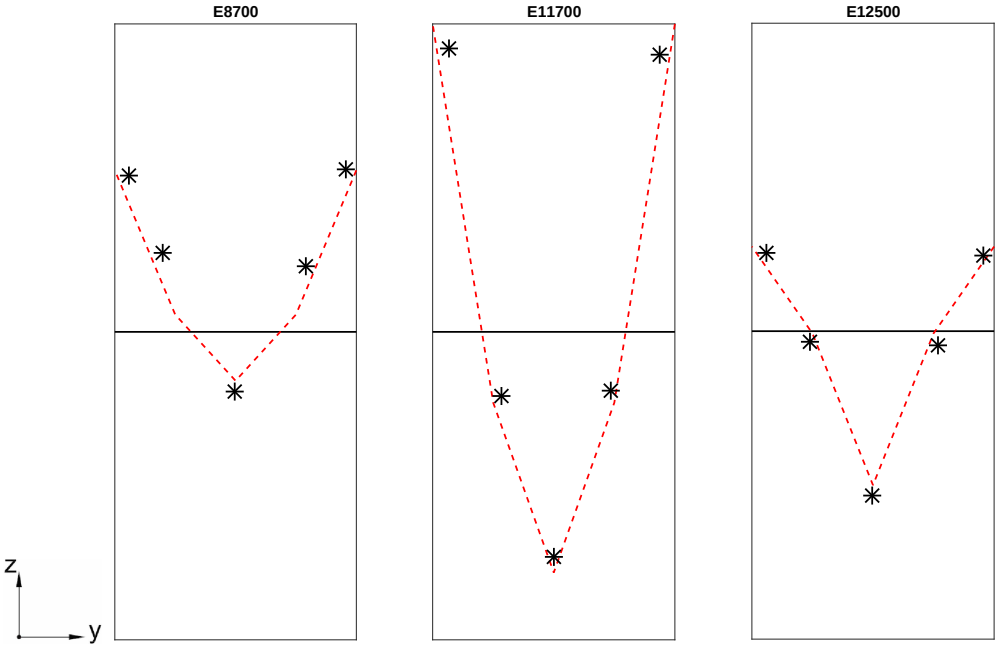


Figure 7.10: Nodal displacements in the Z direction of selected evanescent wave modes at cut-on frequencies on the top surface of undamaged RC beam.

Undeformed section (—), WFE deformed section (– – –), experimental deformed section (∗). E denotes evanescent with its associated cut-on frequency.

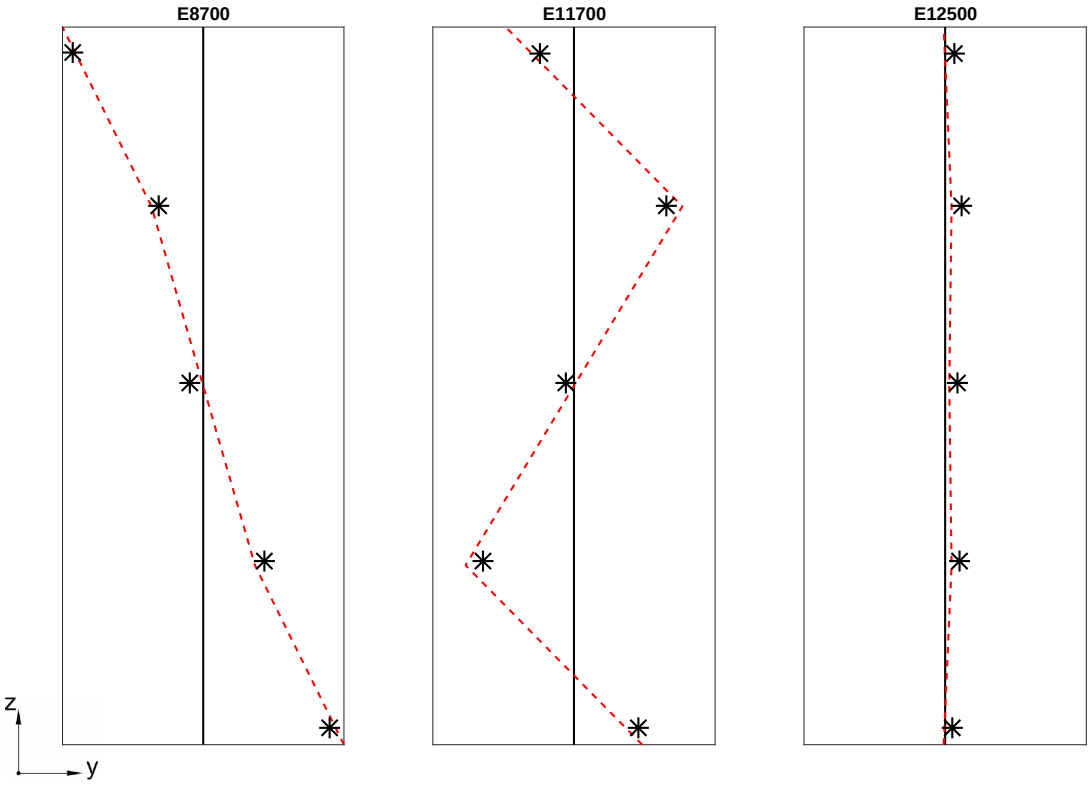


Figure 7.11: Nodal displacements in the Y direction of selected evanescent wave modes at cut-on frequencies on the side surface of undamaged RC beam.

Undeformed section (—), WFE deformed section (– – –), experimental deformed section (∗). E denotes evanescent with its associated cut-on frequency.

## 7.5 Validation of the damage identification algorithm

In this section, the damage identification algorithm is validated experimentally. The WAD approach is applied with the previously identified parameters on damaged and undamaged RC beams. In all cases, $k_s = 0.1$ rad/m is employed as the wavenumber value with the transducers non-uniformly spaced between 0.3 and 0.45 m from the excitation force. The potential for locating the damage is demonstrated.

The measurement setup is as follows. A frequency span of 20 kHz was selected with frequency resolution of 3.125 Hz. A rectangular window was chosen and each FRF is estimated from three averages. One expects to have a better resolution than the numerical solution since the frequency step is smaller. This is due to the limitation of solving the eigenvalue problem associated with the WFE method, where a larger frequency step is required to ensure correct tracking of the eigenvalues/eigenvectors sequence.

The coherence is related to the FRF, and it varies from zero to one and is a function of frequency. Only the response points associated with coherence values of greater or equal to 0.9 are considered. For instance, the FRF at four positions on the undamaged

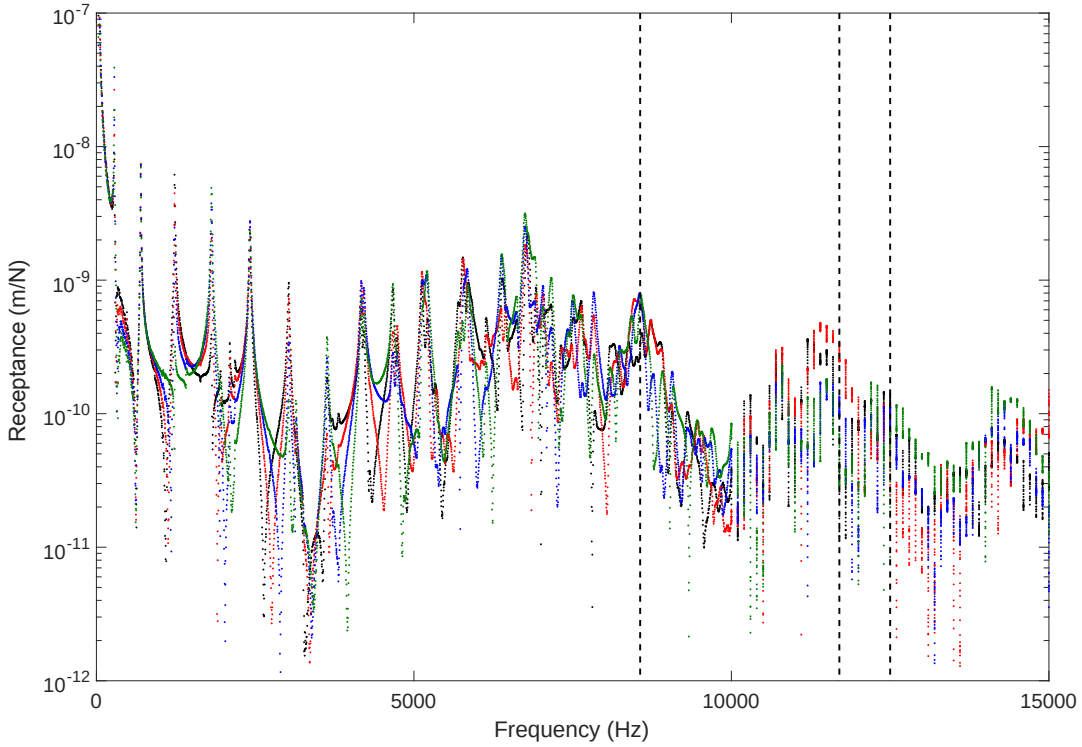


Figure 7.12: Forced response FRF as displacements of the undamaged RC beam at $x_r = 0.6$ to 0.75 m.

FRF response ($\cdots$), cut-on frequencies of interest (- - -).

beam at $x_r = 0.6$ to 0.75 m are illustrated in Figure 7.12. The number of data points considered in the response starts to drop after 10 kHz, due to elimination of points corresponding to lower coherence values. The peaks associated with the response at the cut-on frequencies of interest are highlighted.

The damage identification algorithm was applied via the WAD approach on the RC beams as discussed in Chapter 6. The accelerance associated with coherence values greater or equal to 0.9 were considered. In Figure 7.13, the ratio of the negative to positive wave amplitudes is plotted for the undamaged, 40% and 60% damaged RC beams. For the undamaged RC beam, the wave amplitude ratio is approximately 1 over all of the frequency range. Subsequently, this gives an indication that the RC beam is undamaged. In addition, one expects the presence of mode conversion at the boundaries. However, based on the findings of Chapter 6 and since no dips are present in the ratio plot, the evanescent waves are fully reflected at their cut-on frequencies.

However, for the damaged beams, dips are present at 8800, 11700 and 12500 Hz. They indicate the presence of the damage. Their values are correlated with the extent of the damage; they are smaller dips with the increased diameter reduction based on the findings of the previous chapter. In addition, one can notice a slight shift in the frequencies

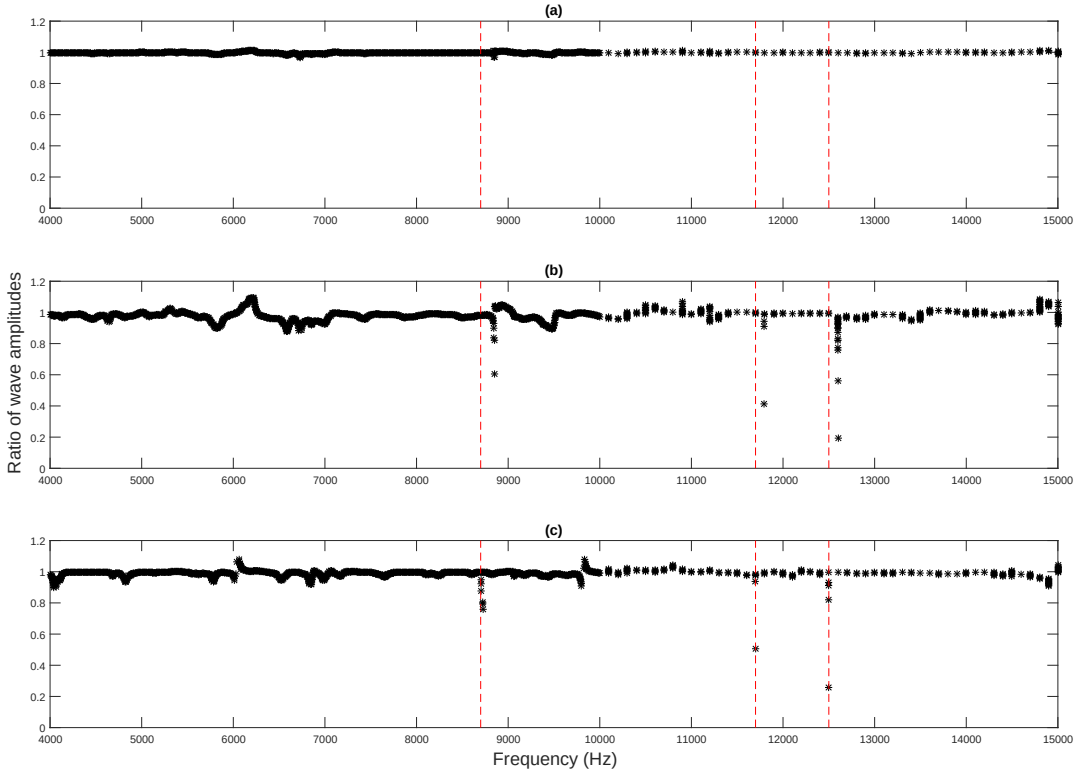


Figure 7.13: Ratio of negative to positive estimated wave amplitudes for damaged and undamaged experimental RC beams.

(a): undamaged RC beam, (b): 40% damaged RC beam, (c): 60% damaged RC beam. Cut-on frequencies (– – –).

of the dips. This are associated with the small changes in the concrete's Young's Modulus between the three beams. Due to the small difference in the stiffness of the three RC beams associated with the concrete mix design, small shifts in the cut-on frequencies occur accordingly.

On the other hand, if measurements on the undamaged beam are unavailable for comparison, one would question whether these dips are associated with damage or wave mode conversion at the boundary. Subsequently, the 60% damaged RC beam is selected for quantification of the ratio of wave amplitudes in different zones. If the dip is unchanged over the beam length, this means that the dips are associated with mode conversion occurring at the right boundary. However, if the dip gets smaller, this means that they are associated with the presence of the damage.

In Figure 7.14, the ratio of negative to positive going waves is plotted for each *Zone* as in Figure 6.17. By using a small real wavenumber, the computed wave amplitudes detect only the response of evanescent waves at their cut-on frequencies. In *Zone* 2, the dip values are similar to those in *Zone* 1 in Figure 7.13. This is due to the fact that at cut-on frequencies the magnitude of the negative going wave amplitude is independent of the position of the transducers. However, by getting closer to the damage zone, the

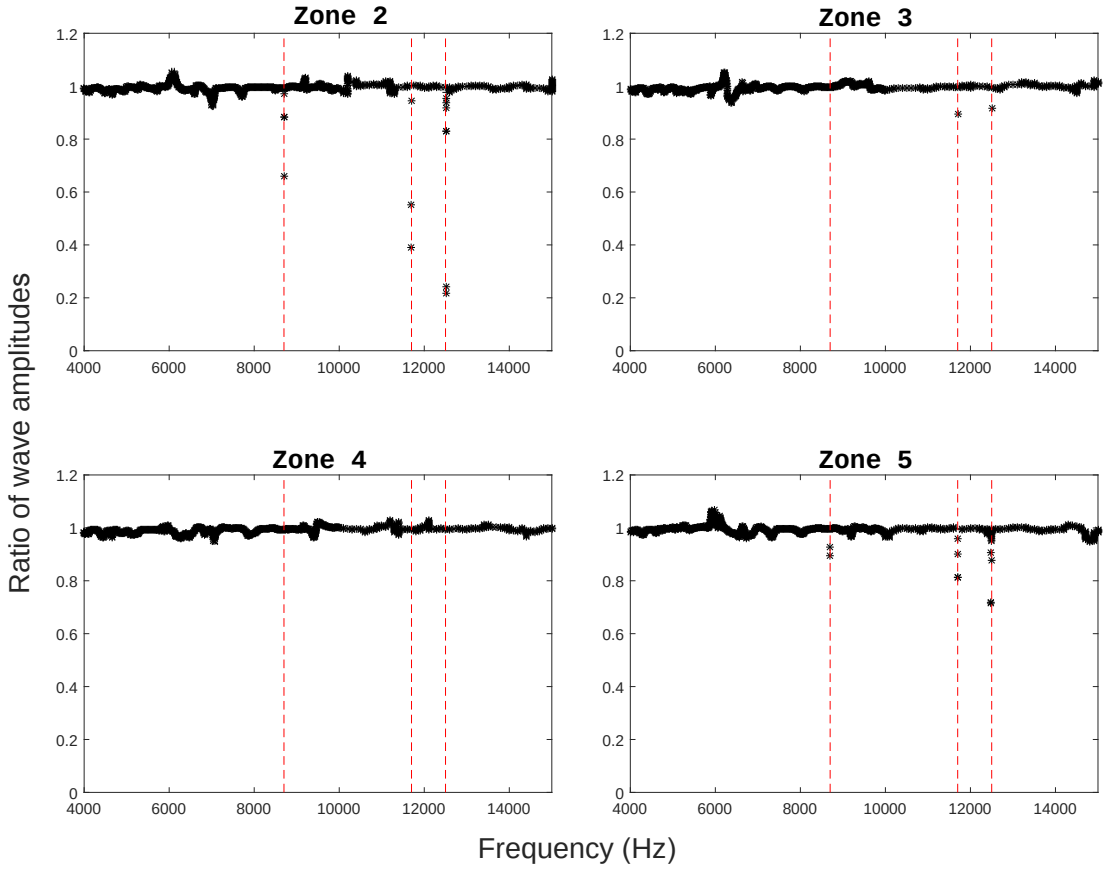


Figure 7.14: Ratio of amplitudes of negative to positive going waves in experimental RC beam with 60% diameter rebar reduction at different *Zones*. Damage occurs at *Zone* 5.

value of the dip gets smaller. After the damage zone, the algorithm only detects the wave reflection due to the boundaries. As shown before, although mode conversion exists at the boundary, perfect reflection occurs at the cut-on frequencies. Therefore, the ratio of the negative to positive wave amplitudes is closer to unity when measured after the damage location. The sudden change in the level of the dips can locate more precisely the damage location.

## 7.6 Conclusions

In this chapter, the damage identification algorithm was validated on damaged and undamaged RC beams through experimental investigation and implementation.

The estimated wavenumbers show the shift to higher frequencies with respect to the change of concrete strength with days. This is due to the increase of concrete Young's Modulus related to its compressive strength with respect to time. However, this is only

crucial for the early period in the life cycle of concrete. After 28 days from casting the mix, the rate of change of concrete strength becomes less significant.

In addition, the effect of damage on the estimated wavenumbers is considered. Good agreement is presented between the wavenumbers of both the damaged and undamaged RC beams and numerical (WFE) results. This means that one can correctly estimate wavenumbers even if the damage is present in the form of rebar diameter reduction. Also, the WFE model accurately produces the correct propagating wave characteristics as seen in the dispersion curves.

Furthermore, the wave mode shapes were plotted at cut-on frequencies. These experimental wave mode shapes are in good agreement with the WFE ones. Therefore, the wave modes measured at cut-on frequencies have been correctly identified.

Next, the damage identification algorithm was tested experimentally. For the undamaged beam, the ratio of the estimated negative to positive wave amplitudes is approximately 1 over the entire measured frequency range. Subsequently, this gives an indication that the RC beam is undamaged and that the right boundary is fully reflective at the cut-on frequencies. For the damaged RC beams, the ratio of the wave amplitudes exhibits dips at the cut-on frequencies. The values of these dips are correlated with the amount of damage. Furthermore, the change in the dips with respect to the response along the beam assists in identifying the damage location and the nature of the right boundary. If the dips are unchanged with measurement location, this means that mode conversion is occurring at the right boundary. In contrast, if the dip gets smaller, this means that damage is present in the beam. Subsequently, it can be seen that neither an intact beam or experimental data from an undamaged beam are required for the application of the algorithm and for changes in the RC beam to be identified.

# Chapter 8

# Conclusions

## 8.1 Summary of present work

Wave based methods showed potentials in detecting the damage remotely. Whilst many of these NDT techniques focused on the damage in rebars embedded reinforced concrete beams, they required access to these reinforcements. In this thesis, one is interested in developing guided wave technique that does not rely on contact with the rebars.

For better understanding of RC behaviour statically and dynamically, a proper FE model is required. The model with embedded reinforcement was employed in this project due to several advantages compared to the conventional models using LINK elements. After applying the WFE to a short section of the damaged and undamaged RC waveguides, the associated wavenumbers were computed and plotted as dispersion curves. In all cases, only a slight change was observed between the wavenumbers associated with the damaged and undamaged waveguides. This is due to the fact that the majority of the structural stiffness is governed by the concrete rather by the reinforcement rebars. In addition, the cut-on frequencies increased with the rebar diameter reduction. This means that evanescent wave modes start propagating in the undamaged waveguide at lower frequency than the damaged one. Furthermore, the least attenuated wave modes are selected and their mode shapes are plotted. The majority of the displacements were found in the cross sectional directions. In addition, WFE solutions for free wave propagation were employed to calculate the forced response in finite beams. Both solutions from FE and WFE align perfectly. However, the WFE model requires significantly fewer DOFs to compute the same forced response.

The WFE approach, using the internal nodal displacements and forces, can be used to couple damaged and undamaged waveguides, and subsequently to predict the reflection and transmission coefficients due to rebar diameter thickness reduction over a specific length. The WFE-WFE-WFE approach was applied to couple the damage and

undamaged waveguides. Then, the scattering matrix was calculated accordingly. The magnitude of the reflection coefficients was subsequently plotted. The least attenuated modes were selected as potential modes sensitive to the damage, and the associated nodal displacements were shown. The majority of the nodal displacements for these least attenuated modes with high reflection due to damage are in the cross sectional directions. This configuration gives a possibility for a defined damage criteria associated with post-processing the surface measurements.

A damage identification algorithm was introduced based on the ratio of reflected to incident wave amplitudes. To determine the latter, the WAD approach using the assumption of a small wavenumber can be employed to identify evanescent waves cutting on. This is essential since high reflection coefficients were found associated with the modes cutting on. The proposed techniques was successfully demonstrated via simulation in identifying and locating the damage as rebar diameter reduction in finite RC beams. The use of a small real wavenumber detected the contribution of a dominant evanescent wave at its cut-on frequency. Away from cut-on frequencies, where the use of the small real wavenumber is not correct, the estimated wave amplitudes follow the peaks of the dominant solution without picking out the differences between the positive and negative wave amplitudes. This is advantageous, since only changes in the wave amplitudes at the cut-on frequencies are detected when the application of a small real wavenumber is correct.

The WAD approach was subsequently demonstrated on simulated finite damaged and undamaged RC beams. It has been shown that the ratio of the negative to positive wave amplitudes is less than 1 near the cut-on frequencies. The levels of the dips were related to the magnitude of the reflection coefficients defined previously in Chapter 5. In built-in RC beams, when no damage is present, the ratio of wave amplitudes is less than 1 near cut-on frequencies due to wave mode conversion in the attached beam. The presence of the damage is superimposed on the original dips. Also, the presence of higher damping in the attached beam reduces all of the reflected wave types and subsequently the ratio is less than 1 over all the frequency range. Also, the dips get larger accordingly.

Application of the damage detection algorithm has shown many advantages compared to other wave damage detection techniques. First, a numerical model or simulation of the actual structure is not required. Second, no prior knowledge of the wavenumbers and cut-on frequencies is necessary. One can simply apply the method taking into account the position and number of transducers and look for the minimum values in the ratio of the wave amplitudes. Thus, an intact beam is not needed for comparison. Third, one can link the extent of the damage to the minimum values in the estimated wave amplitude ratio. Also, damage can be located by tracking the values of the dips along the length of the beam.

The damage identification algorithm was validated experimentally and successfully matched the simulation results. For the undamaged beam, the ratio of the estimated negative to positive wave amplitudes was approximately 1 all over the frequency range. Subsequently, this gives an indication that the RC beam is undamaged and that the right boundary is fully reflective at the cut-on frequencies. For the damaged RC beams, the ratio of the wave amplitudes exhibits dips at the cut-on frequencies. The values of these dips were related to the amount of damage. Furthermore, the change in the dips with respect to the response along the beam assists in identifying the damage location and the nature of the right boundary. If the dips are unchanged with measurement location, this means that mode conversion is occurring at the right boundary. In contrast, if the dip gets smaller, this means that damage is present in the beam. In conclusion, it can be seen that an intact model is not required for the application of the algorithm and for changes in the RC beam to be identified.

## 8.2 Suggestions for further research

In this thesis, the damage detection algorithm was successfully demonstrated and tested on finite RC beams with one damaged rebar. Possible further research related to the damage detection algorithm is proposed. This can be summarised as:

- Testing the algorithm limitations via simulation when more than one rebar is damaged and/or different damaged sections occurring occur along the same rebar.
- Testing the algorithm limitations via simulation when a different damage scenario is present, i.e. concrete cracks instead of rebar diameter reduction.
- The algorithm application on built in RC beams was demonstrated only via simulation. Experimental investigations can take place to validate the results when two or more RC beams are connected.
- Identify the potential of the identified method on other structural elements. For instance, the damage occurring in composite concrete beams and FRP (fiber reinforced polymer) RC beams.
- Consider extending the technique to more complex geometries such as circular or non-uniform beams, or other 1-D waveguide systems.

# Appendix A

# Theoretical details of the WFE solution and forced reponse

As seen in Figure A.1, the $N^{th}$ and $(N+1)^{th}$ waveguides are excited by the external force $\boldsymbol{f}_{ext}$. This gives arise to directly excited waves $\mathbf{e}^{+}$ and $\mathbf{e}^{-}$ as the positive and negative going wave amplitudes, respectively. The positive going waves are propagating to the right. The associated nodal displacements ($\boldsymbol{q}_R$ and $\boldsymbol{q}_L$) and forces ($\boldsymbol{f}_R$ and $\boldsymbol{f}_L$) of the right and left interfaces of $N^{th}$ and $(N+1)^{th}$ waveguides respectively.

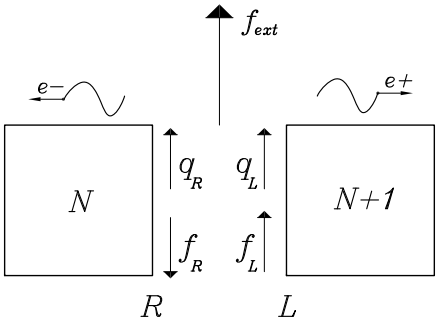


Figure A.1: Nodal displacements ($\boldsymbol{q}_R$ and $\boldsymbol{q}_L$) and forces ($\boldsymbol{f}_R$ and $\boldsymbol{f}_L$) of the right and left interfaces of $N^{th}$ and $(N+1)^{th}$ waveguides excited by the external force $\boldsymbol{f}_{ext}$. $\mathbf{e}^{+}$ and $\mathbf{e}^{-}$ are the positive and negative directly excited wave amplitudes.

Considering the continuity of displacements on the right and left sides of the $N^{th}$ and $(N+1)^{th}$ waveguides respectively, one can write

$$\boldsymbol{q}_L - \boldsymbol{q}_R = \mathbf{0} \tag{A.1}$$

By applying the equilibrium of forces on the right and left sides of the $N^{th}$ and $(N+1)^{th}$ waveguides respectively, one can write

$$\boldsymbol{f}_L - \boldsymbol{f}_R = \boldsymbol{f}_{ext} \tag{A.2}$$

As per Equation 3.23, one can relate the motion described in the physical domain using $\boldsymbol{q}$ and $\boldsymbol{f}$ with the wave domain described using the wave amplitudes $\mathbf{e}^+$ and $\mathbf{e}^-$. Then, Equation A.1 and A.2 become

$$\boldsymbol{\Phi}_{\boldsymbol{q}}^+\mathbf{e}^+ - \boldsymbol{\Phi}_{\boldsymbol{q}}^-\mathbf{e}^- = \mathbf{0} \;\; ; \;\; \boldsymbol{\Phi}_{\boldsymbol{f}}^+\mathbf{e}^+ - \boldsymbol{\Phi}_{\boldsymbol{f}}^-\mathbf{e}^- = \boldsymbol{f}_{ext} \tag{A.3}$$

Then, one can write Equation A.3 in matrix form as (similar to Equation 3.34)

$$\begin{bmatrix} \boldsymbol{\Phi}_{\boldsymbol{q}}^+ & -\boldsymbol{\Phi}_{\boldsymbol{q}}^- \\ \boldsymbol{\Phi}_{\boldsymbol{f}}^+ & -\boldsymbol{\Phi}_{\boldsymbol{f}}^- \end{bmatrix} \begin{bmatrix} \mathbf{e}^+ \\ \mathbf{e}^- \end{bmatrix} = \begin{bmatrix} \mathbf{0} \\ \boldsymbol{f}_{ext} \end{bmatrix} \tag{A.4}$$

# Appendix B

# Details of forced response of a finite beam with discontinuity

Consider a finite beam with discontinuity of length $h$ as shown in Figure B.1. $\boldsymbol{f}_{ext}$ is the external force. $\boldsymbol{e}^+$ and $\boldsymbol{e}^-$ are positive and negative going directly excited wave amplitudes, respectively. The latter wave amplitudes can be defined using Equation 3.38. $x_e$ is the position of the excitation force and $x_r$ is the response position associated with the positive and negative going wave amplitudes $\mathbf{d}^+$ and $\mathbf{d}^-$, respectively. $h$ is the length of the discontinuity, $L_1$ is the length of the beam before the discontinuity and $L_2$ is the length after it.

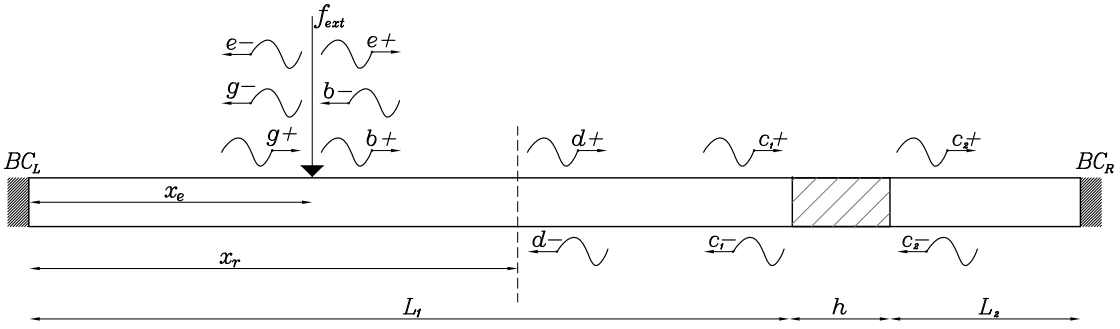


Figure B.1: Forced response on a finite beam with a discontinuity of length $h$ resulting in positive and negative going waves. $BC_L$ and $BC_R$ are the left and right boundaries.

$\boldsymbol{c}_1^-$ and $\boldsymbol{c}_2^-$ are the wave amplitudes reflected by the discontinuity. $\boldsymbol{c}_1^+$ and $\boldsymbol{c}_2^+$ are the amplitudes of the wave modes incident onto the coupling element interface. As per Section 5.2.2, one can write

$$\begin{Bmatrix} \boldsymbol{c}_1^- \\ \boldsymbol{c}_2^- \end{Bmatrix} = \begin{bmatrix} \mathbf{R}_{T_{12}} & \mathbf{T}_{T_{21}} \\ \mathbf{T}_{T_{12}} & \mathbf{R}_{T_{21}} \end{bmatrix} \begin{Bmatrix} \boldsymbol{c}_1^+ \\ \boldsymbol{c}_2^+ \end{Bmatrix} \tag{B.1}$$

where $\mathbf{R}_T$ and $\mathbf{T}_T$ are the net reflection and transmission matrices due to the discontinuity of length $h$ . The subscripts 1 and 2 are associated with the waveguides before and after the damage from left to right respectively.

The other wave amplitudes are defined as follows,

$$\begin{aligned} \boldsymbol{b}^+ &= \boldsymbol{a}^+ + \boldsymbol{g}^+ \\ &= \boldsymbol{a}^+ + \boldsymbol{\tau}(x_e)\mathbf{r}_L\boldsymbol{\tau}(x_e)\boldsymbol{g}^- \\ &= \boldsymbol{a}^+ + \boldsymbol{\tau}(x_e)\mathbf{r}_L\boldsymbol{\tau}(x_e)\boldsymbol{a}^- + \boldsymbol{\tau}(x_e)\mathbf{r}_L\boldsymbol{\tau}(x_e)b^- \\ &= \boldsymbol{a}^+ + \boldsymbol{\tau}(x_e)\mathbf{r}_L\boldsymbol{\tau}(x_e)\boldsymbol{a}^- + \boldsymbol{\tau}(x_e)\mathbf{r}_L\boldsymbol{\tau}(x_e)\boldsymbol{\tau}(L_1 - x_e)\boldsymbol{c}_1^- \end{aligned} \tag{B.2}$$

where $\boldsymbol{\tau}$ is the propagation matrix and $\mathbf{r}_L$ is the reflection coefficient matrix of the left boundary.

In addition, $\boldsymbol{c}_2^+$ is defined as

$$\boldsymbol{c}_2^+ = \boldsymbol{\tau}(L_2)\mathbf{r}_R\boldsymbol{\tau}(L_2)\boldsymbol{c}_2^- \tag{B.3}$$

where $\boldsymbol{c}_2^-$ is defined via Equation B.1. Then, Equation B.3 becomes

$$\boldsymbol{c}_2^+ = \boldsymbol{\tau}(L_2)\mathbf{r}_R\boldsymbol{\tau}(L_2)\mathbf{T}_{T_{12}}\boldsymbol{c}_1^+ + \boldsymbol{\tau}(L_2)\mathbf{r}_R\boldsymbol{\tau}(L_2)\mathbf{R}_{T_{21}}\boldsymbol{c}_2^+ \tag{B.4}$$

By combining the two equations defining $\boldsymbol{c}_2^+$ in Equation B.1 and B.4, one can write

$$\boldsymbol{c}_2^+ = [\mathbf{I} - \boldsymbol{\tau}(L_2)\mathbf{r}_R\boldsymbol{\tau}(L_2)\mathbf{R}_{T_{21}}]^{-1}\boldsymbol{\tau}(L_2)\mathbf{r}_R\boldsymbol{\tau}(L_2)\mathbf{T}_{T_{12}}\boldsymbol{c}_1^+ \tag{B.5}$$

Using Equation B.5 in the relation of $\boldsymbol{c}_1^-$ in Equation B.1,

$$\boldsymbol{c}_1^- = [\mathbf{R}_{T_{12}} + \mathbf{T}_{T_{21}}[\mathbf{I} - \boldsymbol{\tau}(L_2)\mathbf{r}_R\boldsymbol{\tau}(L_2)\mathbf{R}_{T_{21}}]^{-1}\boldsymbol{\tau}(L_2)\mathbf{r}_R\boldsymbol{\tau}(L_2)\mathbf{T}_{T_{12}}]\boldsymbol{c}_1^+ \tag{B.6}$$

However,

$$\boldsymbol{c}_1^+ = \boldsymbol{\tau}(L_1 - x_e)\boldsymbol{b}^+ \tag{B.7}$$

Substituting Equation B.7 in B.6,

$$\boldsymbol{c}_1^- = [\mathbf{R}_{T_{12}} + \mathbf{T}_{T_{21}}[\mathbf{I} - \boldsymbol{\tau}(L_2)\mathbf{r}_R\boldsymbol{\tau}(L_2)\mathbf{R}_{T_{21}}]^{-1}\boldsymbol{\tau}(L_2)\mathbf{r}_R\boldsymbol{\tau}(L_2)\mathbf{T}_{T_{12}}]\boldsymbol{\tau}(L_1 - x_e)\boldsymbol{b}^+ \tag{B.8}$$

Combining Equation B.2 and B.8, then rearranging for $\boldsymbol{b}^+$

$$\begin{aligned} \boldsymbol{b}^+ =& (\mathbf{I} - [\boldsymbol{\tau}(x_e)\mathbf{r}_L\boldsymbol{\tau}(x_e)\boldsymbol{\tau}(L_1 - x_e)[\mathbf{R}_{T_{12}} + \mathbf{T}_{T_{21}}[\mathbf{I} - \boldsymbol{\tau}(L_2)\mathbf{r}_R\boldsymbol{\tau}(L_2)\mathbf{R}_{T_{21}}]^{-1}\boldsymbol{\tau}(L_2)\mathbf{r}_R \\ & \boldsymbol{\tau}(L_2)\mathbf{T}_{T_{12}}]\boldsymbol{\tau}(L_1 - x_e)])^{-1}(\boldsymbol{a}^+ + \boldsymbol{\tau}(x_e)\mathbf{r}_L\boldsymbol{\tau}(x_e)\boldsymbol{a}^-) \end{aligned} \tag{B.9}$$

Then, the wave amplitudes at $x_r$ are computed via

$$\boldsymbol{d}^+ = \boldsymbol{\tau}(x_r - x_e)\boldsymbol{b}^+ \;\; ; \;\; \boldsymbol{d}^- = \boldsymbol{\tau}(L_1 - x_r)\boldsymbol{c}_1^- \tag{B.10}$$

# Appendix C

# REINF264 element shape functions in ANSYS

Use REINF264 with standard base elements 3-D link, beam, shell and solid elements to provide reinforcements. Here, shape functions are presented for REINF264 element.

For base element as linear 3D spar, beam, solid or shell, the shape functions of REINF264 are as (ANSYS (2013))

$$u = 1/2(u_I(1-s) + u_J(1+s)) \tag{C.1}$$

$$v = 1/2(v_I(1-s) + v_J(1+s)) \tag{C.2}$$

$$w = 1/2(w_I(1-s) + w_J(1+s)) \tag{C.3}$$

For base element as quadratic 3D beam, solid or shell, the shape functions of REINF264 are as (ANSYS (2013))

$$u = 1/2(u_I(-s+s^2) + u_J(s+s^2) + u_K(1-s^2)) \tag{C.4}$$

$$v = 1/2(v_I(-s+s^2) + v_J(s+s^2) + v_K(1-s^2)) \tag{C.5}$$

$$w = 1/2(w_I(-s+s^2) + w_J(s+s^2) + w_K(1-s^2)) \tag{C.6}$$

# References


B. Aalami. Waves in prismatic guides of arbitrary cross section. *Journal of Applied Mechanics*, 40(4):1067–1072, 1973. ISSN 0021-8936. 10.1115/1.3423127.

M.M. Abdel Wahab and G. De Roeck. Damage detection in bridges using modal curvatures: Application to a real damage scenario. *Journal of Sound and Vibration*, 226: 217235, 1999.

M. A. B. Abdo and M. Hori. A numerical study of structural damage detection using changes in the rotation of mode shapes. *Journal of Sound and Vibration*, 251(2): 227–239, 2002. ISSN 0022460X.

ACI. *Building code requirements for structural concrete : (ACI 318-95)*. Farmington Hills, MI : American Concrete Institute, 1995.

S. Al-Amin and R. Ahsan. Finite element modeling of reinforced concrete column under monotonic lateral loads. *International Journal of Computer Applications*, 42:0975–8887, 2012.

Inc. ANSYS. ANSYS mechanical APDL element reference. Report, 2013.

J. R. F. Arrud, K. M. Ahmida, and J.M. Ichchou, M. N. Mencik. Investigating the relations between the wave finite element and spectral element methods using simple waveguides. 2007.

ASNT. Introduction to nondestructive testing, 2015.

N. S. Badiger and K. M. Malipatil. Parametric study on reinforced concrete beam using ANSYS. *Civil and Environmental Research*, 6, 2014.

G. Burcu and G. Oguz. Structural health monitoring and damage assessment part i: A critical review of approaches and methods. *International Journal of Physical Sciences*, 8:1694–1702, 2013.

P. C. Chang, A. Flatau, and S. C. Liu. Review paper: Health monitoring of civil infrastructure. *Structural Health Monitoring*, 2(3):257–267, 2003. ISSN 14759217.

T.D. Chaudhari and S.K. Maiti. A study of vibration of geometrically segmented beams with and without crack. *International Journal of Solids and Structures*, 37:761–779, 2000.

R. O. Curadelli, J. D. Riera, D. Ambrosini, and M. G. Amani. Damage detection by means of structural damping identification. *Engineering Structures*, 30(12):3497–3504, 2008. ISSN 01410296.

L. Dahmani, A. Khennane, and S. Kacia. Crack identification in reinforced concrete beams using ANSYS software. *Strength of Materials,*, 42:232–240, 2010.

M. S. Darmawan. Pitting corrosion model for reinforced concrete structures in a chloride environment. *Magazine of Concrete Research*, 62(2):91–101, 2010.

M. Dilena and A. Morassi. The use of antiresonances for crack detection in beams. *Journal of Sound and Vibration*, 276:195–214, 2004. ISSN 0022460X.

D. Duhamel, B. R. Mace, and M. J. Brennan. Finite element analysis of the vibrations of waveguides and periodic structures. *Journal of Sound and Vibration*, 294:205–220, 2006. ISSN 0022460X.

D. Duhamel, B.R. Mace, and M.J. Brennan. Finite element analysis of the vibrations of waveguides and periodic structures. *ISVR Technical Memorandum 922*, August 2003.

E. El Masri, N.S. Ferguson, and T.P. Waters. Application of the wave finite element method to reinforced concrete structures with damage. *Journal of Physics: Conference Series, MOVIC2016: International Conference on Motion and Vibration Control*, 744: 012053, 2016a. ISSN 1742-6588 1742-6596.

E. El Masri, N.S. Ferguson, and T.P. Waters. Wave propagation in reinforced and prestressed concrete structures with damage. *Procedia Engineering, ISMA2016: Conference on Noise and Vibration Engineering. type = Journal Article*, 2016b.

E. El Masri, N.S. Ferguson, and T.P. Waters. Detecting damaged reinforcement bars in concrete structures using guided waves. *Procedia Engineering, EURODYN2017: X International Conference on Structural Dynamics*, pages 1882–1887, 12 2017.

P. Fanning. Nonlinear models of reinforced and post-tensioned concrete beams. *Electronic Journal of Structural Engineering*, 2, 2001.

C.R. Farrar and S.W. Doebling. Damage detection ii: field applications to large structures. *NATO Science Series*, 1999.

F. A. Fathelbab, M. S. Ramadan, and A. Al-Tantawy. Finite element modelling of strengthened simple beams using frp techniques: a parametric study. *Concrete Research Letters*, 2, 2011.

N.S. Ferguson, C.R. Halkyard, B.R. Mace, and K.H. Heron. The estimation of wavenumbers in two-dimensional structures. *ISMA2002: International Conference on Noise and Vibration Engineering, Leuven, Belgium*, page 7pp, 2002.

A. Ghods, M. R. Sohrabi, and M. Miri. Effect of rebar corrosion on the behavior of a reinforced concrete beam using modeling and experimental results. *Materials and technology*, 48:395–402, 2014.

F. Gruttman and W. Wagner. Shear correction factors in Timoshenko's beam theory for arbitrary shaped crosssections. page 199207, 2001.

P. Gudmundson. Eigenfrequency changes of structures due to cracks, notches or other geometrical changes. *Journal of the Mechanics and Physics of Solids*, 30:339–353, 1982.

C. R. Halkyard and B. R. Mace. Structural intensity in beams-waves, transducer systems and the conditioning problem. *Journal of Sound and Vibration*, 185(2):279–298, 1995. ISSN 0022-460X.

N. R. Harland, B. R. Mace, and R. W. Jones. Wave propagation, reflection and transmission in tunable fluid-filled beams. *Journal of Sound and Vibration*, 241(5):735–754, 2001. ISSN 0022460X.

L. Houillon, M. N. Ichchou, and L. Jezequel. Wave motion in thin-walled structures. *Journal of Sound and Vibration*, 281(3-5):483–507, 2005. ISSN 0022460X.

A. M. Ibrahim and M. S. Mahmood. Finite element modeling of reinforced concrete beams strengthened with frp laminates. *European Journal of Scientific Researc*, 30: 526–541, 2009.

M. N. Ichchou, J. M. Mencik, and W. Zhou. Wave finite elements for low and mid-frequency description of coupled structures with damage. *Computer Methods in Applied Mechanics and Engineering*, 198(15-16):1311–1326, 2009. ISSN 00457825.

P. Jayajothi, R. Kumutha, and K. Vijai. Finite element analysis of frp strengthened rc beams using ansys. *Asian Journal of Civil Engineering*, 14:631–642, 2013.

F. Jnaid and R. Aboutaha. Nonlinear finite element modeling of unbonded steel reinforced concrete beams. *International Journal of Civil, Environmental, Structural, Construction and Architectural Engineering*, 9:222–228, 2015.

N.R. Joshuva, S. Saibabu, P. E. Sakaria, K. N. Lakshmikandhan, and P. Sivakumar. Finite element analysis of reinforced and pre-tensioned concrete beams. *International Journal of Emerging Technology and Advanced Engineering*, 4:449–457, 2014.

D.I. Kachlakev, T. Miller, S. Yim, K. Chansawat, and T. Potisuk. Finite element modeling of reinforced concrete structures strengthened with frp laminates. *California Polytechnic State University, San Luis Obispo, CA and Oregon State University, Corvallis, OR for Oregon Department of Transportation*, 2001.

D. G. Kasper, D. C. Swanson, and K. M. Reichard. Higher-frequency wavenumber shift and frequency shift in a cracked, vibrating beam. *Journal of Sound and Vibration*, 312(1-2):1–18, 2008. ISSN 0022460X.

G. Kawiecki. Modal damping measurements for damage detection. *European COST F3 conference on system identification and structural health monitoring. Madrid, Spain*, pages 651–658, 2000.

A. Kessentini, M. Taktak, M. A. Ben Souf, O. Bareille, M. N. Ichchou, and M. Haddar. Computation of the scattering matrix of guided acoustical propagation by the wave finite element approach. *Applied Acoustics in Multiphysic systems*, 108:92100, 2016. ISSN 0003682X.

M. Kharrat, M. N. Ichchou, O. Bareille, and W. Zhou. Pipeline inspection using a torsional guided-waves inspection system. part 2: Defect sizing by the wave finite element method. *International Journal of Applied Mechanics*, 06(04):1450035, 2014. ISSN 1758-8251 1758-826X.

M. Kharrat, W. Zhou, O. Bareille, and M. Ichchou. Identification and sizing of defects in pipelines by the wave finite element method using torsional guided waves. *COMPDYN 2011, ECCOMAS Thematic Conference on Computational Methods in Structural Dynamics and Earthquake Engineering, Corfu, Greece*, 2011.

J. T. Kim and N. Stubbs. Crack detection in beam-type structures using frequency data. *Journal of Sound and Vibration*, 259(1):145–160, 2003. ISSN 0022460X.

J.T. Kim, J.H. Park, and B.J. Lee. Vibration-based damage monitoring in model plate-girder bridges under uncertain temperature conditions. *Engineering Structures*, 29(7): 1354–1365, 2007. ISSN 01410296.

U. Kim, P.R. Chakrabarti, and J.H. Choi. Nonlinear finite element analysis of unbonded post-tensioned concrete beams. *Challenges, Opportunities and Solutions in Structural Engineering and Construction Ghafoori*, 2010.

P. B. Kote, S. P. Patil, and K. Keshav Sangle. Finite element analysis of prestressed beam. *International Journal of Advance Foundation and Research in Science and Engineering*, 1, 2014.

S. K. Lee, B. R. Mace, and M. J. Brennan. Wave propagation, reflection and transmission in non-uniform one-dimensional waveguides. *Journal of Sound and Vibration*, 304(1-2):31–49, 2007. ISSN 0022460X.

Y. Lei and Z.P. Zheng. Review of physical based monitoring techniques for condition assessment of corrosion in reinforced concrete. *Mathematical Problems in Engineering*, 2013:1–14, 2013. ISSN 1024-123X 1563-5147.

S.P. Lele and S.K. Maiti. Modelling of transverse vibration of short beams for crack detection and measurement of crack extension. *Journal of Sound and Vibration*, 257: 559–583, 2002.

C. Q. Li, J. J. Zheng, W. Lawanwisut, and R. E. Melchers. Concrete delamination caused by steel reinforcement corrosion. *Journal of Materials in Civil Engineering ASCE*, 19:591–600, 2007.

D. Li, T. Ruan, and J. Yuan. Inspection of reinforced concrete interface delamination using ultrasonic guided wave non-destructive test technique. *Science China Technological Sciences*, 55:2893–2901, 2012. ISSN 1674-7321 1869-1900.

R. Li and Y. Zhang. Frequencies and modals analysis of prestressed concrete beam by ansys. *Advanced Materials Research*, 243-249:769–773, 2011. ISSN 1662-8985.

Choy F.K. Liang, R.Y. and J.L. Hu. Detection of cracks in beam structures using measurements of natural frequencies. *Journal of the Franklin Institute-Engineering and Applied Mathematics*, 328:505–518, 1991.

Hu J.L. Liang, R.Y. and F. Choy. Theoretical-study of crack-induced eigenfrequency changes on beam structures. *Journal of Engineering Mechanics-ASCE*, 118:384–396, 1992.

Y. Lu, J. Li, L. Ye, and D. Wang. Guided waves for damage detection in rebar-reinforced concrete beams. *Construction and Building Materials*, 47:370–378, 2013. ISSN 09500618.

B. R. Mace and C. R. Halkyard. Time domain estimation of response and intensity in beams using wave decomposition and reconstruction. *Journal of Sound and Vibration*, 230(3):561–589, 2000. ISSN 0022460X.

B.R. Mace. Wave reflection and transmission in beams. *Journal of Sound and Vibration*, 97:237–246, 1984.

B.R. Mace, D. Duhamel, M.J. Brennan, and L. Hinke. Finite element prediction of wave motion in structural waveguides. *Journal of the Acoustical Society of America*, 117: 2835–2843, 2005.

W. MacGregor. *Reinforced Concrete Mechanics and Design*. Pearson Education, Inc., Upper Saddle River, New Jersey, 6th edition, 2012.

E. Manconi and B. R. Mace. Wave characterization of cylindrical and curved panels using a finite element method. *Acoustical Society of America*, 125(1):154–63, 2009. ISSN 1520-8524.

E. Manconi, B. R. Mace, and R. Garziera. The loss-factor of pre-stressed laminated curved panels and cylinders using a wave and finite element method. *Journal of Sound and Vibration*, 332(7):1704–1711, 2013. ISSN 0022460X.

E. Manconi and B.R. Mace. Estimation of the loss factor of viscoelastic laminated panels from finite element analysis. *Journal of Sound and Vibration*, 329:3928–3939, 2010. ISSN 0022460X.

C. Mei and B.R. Mace. Wave reflection and transmission in timoshenko beams and wave analysis of timoshenko beam structures. *Journal of Vibration and Acoustics*, 127:382–394, 2005.

J. M. Mencik and M. N. Ichchou. Wave finite elements in guided elastodynamics with internal fluid. *International Journal of Solids and Structures*, 44(7-8):2148–2167, 2007. ISSN 00207683.

T. H. Miller, T. Kundu, J. Huang, and J. Y. Grill. A new guided wave-based technique for corrosion monitoring in reinforced concrete. *Structural Health Monitoring*, 12(1): 35–47, 2012. ISSN 1475-9217 1741-3168.

A. Morassi. Crack-induced changes in eigenparameters of beam structures. *Journal of Engineering Mechanics-ASCE*, 119:1798–1803, 1993.

A. Morassi. Identification of a crack in a rod based on changes in a pair of natural frequencies. *Journal of Sound and Vibration*, 242(4):577–596, 2001. ISSN 0022460X.

A. Morassi and M. Rollo. Identification of two cracks in a simply supported beam from minimal frequency measurements. *Journal of Vibration and Control*, 7:729739, 2001.

J. M. Muggleton, T. P. Waters, B. R. Mace, and B. Zhang. Approaches to estimating the reflection and transmission coefficients of discontinuities in waveguides from measured data. *Journal of Sound and Vibration*, 307:280–294, 2007. ISSN 0022460X.

S. Mustapha, Y. Lu, J. Li, and L. Ye. Damage detection in rebar-reinforced concrete beams based on time reversal of guided waves. *Structural Health Monitoring*, 13(4): 347–358, 2014. ISSN 1475-9217 1741-3168.

B.P. Nandwana and S.K. Maiti. Detection of the location and size of a crack in stepped cantilever beams based on measurements of natural frequencies. *Journal of Sound and Vibration*, 203:435–446, 1997.

Y. Q. Ni, X. G. Hua, K. Q. Fan, and J. M. Ko. Correlating modal properties with temperature using long-term monitoring data and support vector machine technique. *Engineering Structures*, 27(12):1762–1773, 2005. ISSN 01410296.

S.K. Padmarajaiah and A. Ramaswamy. A finite element assessment of flexural strength of prestressed concrete beams with fiber reinforcement. *Cement and Concrete Composites*, 24:229–241, 2002.

P. M. Pawar and R. Ganguli. Matrix crack detection in thin-walled composite beam using genetic fuzzy system. *Journal of Intelligent Material Systems and Structures*, 16:395–409, 2016. ISSN 1045-389X 1530-8138.

PCA. Types and causes of concrete deterioration. *Portland Cement Association*, IS536, 2002.

M. Petyt. *Introduction to Finite Element Vibration Analysis*. Cambridge University Press, 1990.

A. Rahai, F. Bakhtiari-Nejad, and A. Esfandiari. Damage assessment of structure using incomplete measured mode shapes. *Structural Control and Health Monitoring*, 14(5): 808–829, 2007. ISSN 15452255 15452263.

N.K. Raju. *Prestressed Concrete*. McGraw Hills, Fourth edition edition, 2007.

S.R. Ravi and G. P. Arulraj. Finite element modeling on behavior of reinforced concrete beam-column joints retrofitted with carbon fiber reinforced polymer sheets. *International Journal of Civil and Structural Engineering*, 1:576–582, 2010.

J. Renno and B. R. Mace. On the forced response of waveguides using the wave and finite element method. *Journal of Sound and Vibration*, 329(26):5474–5488, 2010. ISSN 0022460X.

J. Renno and B.R. Mace. Calculating the forced response of two-dimensional homogeneous media using the wave and finite element method. *Journal of Sound and Vibration*, 330:5913–5927, 2011. ISSN 0022460X.

J. Renno and B.R. Mace. Calculation of reflection and transmission coefficients of joints using a hybrid finite element/wave and finite element approach. *Journal of Sound and Vibration*, 332:2149–2164, 2013. ISSN 0022460X.

J. Renno, E. Manconi, and B.R. Mace. A finite element method for modelling waves in laminated structures. *Advances in Structural Engineering*, 16:61–76, 2013.

M. Saiidi, B. Douglas, and S. Feng. Prestress force effect on vibration frequency of concrete bridges. *Structural Engineering*, 10, 1994.

Z.Y. Shi, S.S. Law, and L.M. Zhang. Damage localization by directly using incomplete mode shapes. *Journal of Engineering Mechanics-ASCE*, 126:656–660, 2000.

S. P. Shone, B. R. Mace, and T. P. Waters. Reflection of waves from cracks in beams. *Key Engineering Materials*, 347:193–198, 2007.

S. P. Shone, B. R. Mace, and T. P. Waters. Locating damage in waveguides from the phase of point frequency response measurements. *Mechanical Systems and Signal Processing*, 23:405–414, 2009. ISSN 08883270.

K. Tamm, T. Peets, J. Engelbrecht, and D. Kartofelev. Negative group velocity in solids. *Wave Motion*, 71:127–138, 2017.

Y. Waki, B. R. Mace, and M. J. Brennan. Free and forced vibrations of a tyre using a wave/finite element approach. *Journal of Sound and Vibration*, 323(3-5):737–756, 2009a. ISSN 0022460X.

Y. Waki, B. R. Mace, and M. J. Brennan. Numerical issues concerning the wave and finite element method for free and forced vibrations of waveguides. *Journal of Sound and Vibration*, 327(1-2):92–108, 2009b. ISSN 0022460X.

C.M. Wang. Timoshenko beam-bending solutions in terms of Euler-Bernoulli solutions. *ASCE*, 121:763–765, 1995.

F. Wei and Q. Pizhong. Vibration-based damage identification methods: a review and comparative study. *Structural Health Monitoring*, 10:83–111, 2010. ISSN 1475-9217 1741-3168.

K.J. Willam and E.P. Warnke. Constitutive model for triaxial behaviour of concrete. *Seminar on Concrete Structures Subjected to Triaxial Stresses, International Association of Bridge and Structural Engineering Conference, Bergamo, Italy*, page 174, 1974.

A. Zerwer, M. A. Polak, and J. C. Santamarina. Detection of surface breaking cracks in concrete members using rayleigh waves. *Journal of Environmental & Engineering Geophysics*, 10(3):295–306, 2006. ISSN 1083-13631943-2658.

Z. Zheng, Y. Lei, and X. Xue. Numerical simulation of monitoring corrosion in reinforced concrete based on ultrasonic guided waves. *ScientificWorldJournal*, 2014:9, 2014.

S. Zhong, S.O. Oyadiji, and K. Ding. Response-only method for damage detection of beam-like structures using high accuracy frequencies with auxiliary mass spatial probing. *Journal of Sound and Vibration*, 311:1075–1099, 2008. ISSN 0022460X.

W.X. Zhong. On the direct solution of wave propagation for repetitive structures. *Journal of Sound and Vibration*, 181(3):485–501, 1995.

W. Zhou and M. Ichchou. Wave scattering by local defect in structural waveguide through wave finite element method. *Structural Health Monitoring*, 10(4):335–349, 2010a. ISSN 1475-9217 1741-3168.

W. J. Zhou and M. N. Ichchou. Wave propagation in mechanical waveguide with curved members using wave finite element solution. *Computer Methods in Applied Mechanics and Engineering*, 199(33-36):2099–2109, 2010b. ISSN 00457825.

W. J. Zhou, M. N. Ichchou, and O. Bareille. Finite element techniques for calculations of wave modes in one-dimensional structural waveguides. *Structural Control and Health Monitoring*, 18:737–751, 2011. ISSN 15452255.

Y. Zou, L. Tong, and G. P. Steven. Vibration-based model-dependent damage (delamination) identification and health monitoring for composite structures a review. *Journal of Sound and Vibration*, 230(2):357–378, 2000. ISSN 0022460X.